

**Application of the Schwinger Multichannel Method to Multichannel  
Studies of Electronically Inelastic Electron–Molecule Collisions**

Thesis by

Howard P. Pritchard

In Partial Fulfillment of the Requirements  
for the Degree of  
Doctor of Philosophy

California Institute of Technology  
Pasadena, California

1994

September, 1993

## ACKNOWLEDGMENTS

I wish to express my appreciation to my research advisor, Professor Vincent McKoy for his advice and support. I also wish to thank all of the members of our research group, but particularly to Qiyang Sun for his very useful ideas and stimulating discussions. I would also like to thank Dr. Earl Stoufflet for providing me some of the software used in writing this thesis. Most of all, I am grateful to Tsutomu Ohshima for making my time at Caltech a truly invaluable and rewarding experience.

## ABSTRACT

We have applied the Schwinger Multichannel Method(SMC) to the study of electronically inelastic, low energy electron–molecule collisions. The focus of these studies has been the assessment of the importance of multichannel coupling to the dynamics of these excitation processes. It has transpired that the promising quality of results realized in early SMC work on such inelastic scattering processes has been far more difficult to obtain in these more sophisticated studies.

We have attempted to understand the sources of instability of the SMC method which are evident in these multichannel studies. Particular instances of such instability have been considered in detail, which indicate that linear dependence, failure of the separable potential approximation, and difficulties in converging matrix elements involving recorelation or  $Q$ –space terms all conspire to complicate application of the SMC method to these studies. A method involving singular value decomposition(SVD) has been developed to, if not resolve these problems, at least mitigate their deleterious effects on the computation of electronically inelastic cross sections.

In conjunction with this SVD procedure, the SMC method has been applied to the study of the  $\text{H}_2$ ,  $\text{H}_2\text{O}$ , and  $\text{N}_2$  molecules. Rydberg excitations of the first two molecules were found to be most sensitive to multichannel coupling near threshold. The  $(3\sigma_g \rightarrow 1\pi_g)$  and  $(1\pi_u \rightarrow 1\pi_g)$  valence excitations of the  $\text{N}_2$  molecule were found to be strongly influenced by the choice of channel coupling scheme at all collision energies considered in these studies.

## TABLE OF CONTENTS

ACKNOWLEDGMENTS . . . . .	ii
ABSTRACT . . . . .	iii
TABLE OF CONTENTS . . . . .	iv
1. Application of the SMC Method to the Multichannel Problem . . . . .	1
1.1 The Variational Expression . . . . .	1
1.2 Numerical Properties of the $A^{(+)}$ Matrix . . . . .	9
1.3 Stability of the SMC Method for Multichannel Studies . . . . .	17
1.4 Conclusions . . . . .	62
References . . . . .	62
2. Computation of the Scattering Amplitude and Cross Sections . . . . .	65
3. Excitation of the $b^3\Sigma_u^+$ , $a^3\Sigma_g^+$ , and $c^3\Pi_u$ States of $H_2$ by Low Energy Electrons . . . . .	72
Introduction . . . . .	72
Computational Details . . . . .	75
Results and Discussion . . . . .	76
Observations and Conclusions . . . . .	89
References . . . . .	91
4. Electronic Excitation of $H_2O$ by Electron Impact . . . . .	94
Introduction . . . . .	94
Computational Details . . . . .	96

Results and Discussion . . . . .	102
Conclusions . . . . .	120
References . . . . .	121
5. Electronic Excitation of N <sub>2</sub> by Electron Impact . . . . .	125
Introduction . . . . .	125
Computational Details . . . . .	127
Results and Discussion . . . . .	131
Conclusions . . . . .	173
References . . . . .	174
Tables of Cross Sections . . . . .	178

## 1. Application of the SMC Method to the Multichannel Problem

### 1.1 The Variational Expression

The SMC functional of Takatsuka and McKoy, derived from a projected form of the Lippmann–Schwinger equation, has been successfully used to study a wide range of electron–molecule scattering processes [1–4]. In this work, we have attempted to exploit the multichannel capability of the method in studies of electronic excitation of molecules by low energy electron impact. In particular, we wished to ascertain the importance of inclusion of multiple channels in computing reliable cross sections for these electronically inelastic scattering events. Such cross section data are of great practical use in modeling a wide variety of natural phenomena and technological processes. Reliable theoretical methods are desirable as a supplement to direct experimental measurements of these cross sections. The difficulties attendant with carrying out such measurements at these low impact energies frequently lead to large uncertainties in the values obtained.

The purpose of this chapter is not to provide a full theoretical discussion of the SMC functional and its properties as such discussions can be found elsewhere. Rather, aspects of the method will be considered which have direct relevance to problems and difficulties encountered when realistic, large–scale multichannel calculations are attempted.

The Schrödinger equation for the  $N_0$  channel scattering problem for an  $N + 1$  electron system may be written as

$$(E - H)\Psi_m^{(+)} = 0, \quad m = 1, \dots, N_0 \quad (1.1)$$

where

$$H = H_{N+1} = H_t + V + T_{N+1}$$

and where  $\Psi_m^{(+)}$  is the  $N + 1$  electron wave function for the  $m^{\text{th}}$  open channel,  $V$  is the scattering electron–target molecule interaction potential,  $H_t$  is the Hamiltonian of the  $N$  electron target, and  $T_{N+1}$  is the kinetic energy operator for the scattering electron.

From this, one can then write the Lippmann–Schwinger equation for the problem [1],

$$\Psi_m^{(+)} = S_m + G^{(+)}V\Psi_m^{(+)} \quad (1.2)$$

in which  $S_m$  is the zero order eigenfunction and  $G^{(+)}$  the free particle Green's function with outgoing wave boundary conditions. A projection operator as defined by Takatsuka and McKoy [2], *viz.*

$$P = \sum_{m=1}^{N_0} |\Phi_m(1, 2, \dots, N)\rangle \langle \Phi_m(1, 2, \dots, N)| \quad (1.3)$$

is applied on both sides to yield a projected form of the Eq. 1.2

$$P\Psi_m^{(+)} = S_m + G_P^{(+)}V\Psi_m^{(+)} \quad (1.4)$$

A  $\frac{1}{\sqrt{N+1}}$  factor resulting from the normalization of  $N + 1$  and  $N$  electron wave functions is not explicitly indicated for clarity. The  $N$  electron projector operator (Eq. 1.3), defines the open–channel space in terms of  $N_0$  eigenfunctions of the target Hamiltonian. This operator is introduced in order to avoid having to include closed channels of the discrete spectrum of the target as well as its continuum states in the expansion of  $G^{(+)}$ . The need to include the target continuum states of  $G^{(+)}$  in Eq. 1.2 arises due to the antisymmetry requirement for  $\Psi_m^{(+)}$  [5].

The projected Lippmann–Schwinger equation (Eq. 1.4) cannot be used directly to construct a variationally stable functional as the component not involving  $VG_P^{(+)}V$  is not Hermitian. It has been shown in several places [1,2] that by manipulation of the expressions for the closed and open channel portion of the Hamiltonian one can construct a functional satisfying these requirements, viz.

$$\left[ \frac{1}{2}(PV + VP) - VG_P^{(+)}V + \frac{1}{2a} [\hat{H} - a(P\hat{H} + \hat{H}P)] \right] \Psi_m^{(+)} = VS_m \quad (1.5)$$

where  $S_m$  is again the solution for the unperturbed Hamiltonian as in Eq. 1.4 and  $\hat{H} = E - H$ . It is well-known that for an inhomogenous set of equations

$$A\vec{y} = \vec{b},$$

a variationally stable expression for the function  $\langle y|A|y \rangle$  is given by [3]

$$\tilde{Y} = \frac{\langle y|b \rangle \langle b|y \rangle}{\langle y|A|y \rangle}. \quad (1.6)$$

In the case of the scattering problem, we desire a variationally stable expression for the scattering amplitude, *i.e.*,  $-2\pi f_{mn} = \langle \Psi_m^{(-)} | A^{(+)} | \Psi_n^{(+)} \rangle$ . Comparison with Eq. 1.6 leads to a modified fractional form of the Schwinger variational functional

$$f_{mn} = -\frac{1}{2\pi} \frac{\langle S_m | V | \Psi_n^{(+)} \rangle \langle \Psi_m^{(-)} | V | S_n \rangle}{\langle \Psi_m^{(-)} | A^{(+)} | \Psi_n^{(+)} \rangle}. \quad (1.7)$$

$f_{mn}$  is the scattering amplitude for the  $m \rightarrow n$  scattering channel. The working formula for  $A^{(+)}$  is a rearrangement of the function in Eq. 1.5

$$(PV + VP) - VG_P^{(+)}V + \frac{1}{2a} \hat{H} - P\hat{H}_0P = A^{(+)} \quad (1.8)$$

where  $\hat{H}_0 = E - H_0$ , and  $H_0 = H_t + T_{N+1}$ , *i.e.*, the zeroeth order Hamiltonian. In this work,  $a = \frac{N+1}{2}$ . To obtain Eq. 1.8, one uses the fact that  $[\hat{H}_0, P] = 0$  and  $P^2 = P$ .

To evaluate this expression, the scattering wavefunction  $\Psi_m^{(+)}$  is expanded in terms of  $N + 1$  electron antisymmetrized Slater determinants generated by the outer product of the  $N_0$ ,  $N$  electron Slater determinants describing the target states (the ground state and designated hole( $\phi_j$ )-particle( $\phi'_j$ ) pairs) and an additional scattering function( $\chi_i$ ) not necessarily orthogonal to the target orbitals, *viz.*

$$\Psi_m^{(+)} = \sum_i \mathcal{A}_{N+1}(\phi_1 \bar{\phi}_1 \dots \phi_{N/2} \bar{\phi}_{N/2}) \lambda_i \quad (1.9a)$$

$$+ \sum_{i,j} \frac{\mathcal{A}_{N+1}}{\sqrt{2}} [(\phi_1 \bar{\phi}_1 \dots \phi_j \dots \phi_{N/2} \bar{\phi}_{N/2} \phi'_j) + (\phi_1 \bar{\phi}_1 \dots \bar{\phi}_j \dots \phi_{N/2} \bar{\phi}_{N/2} \bar{\phi}'_j)] \lambda_i \quad (1.9b)$$

$$+ \sum_{i,j} \frac{\mathcal{A}_{N+1}}{\sqrt{2}} [(\phi_1 \bar{\phi}_1 \dots \phi_j \dots \phi_{N/2} \bar{\phi}_{N/2} \phi'_j) - (\phi_1 \bar{\phi}_1 \dots \bar{\phi}_j \dots \phi_{N/2} \bar{\phi}_{N/2} \bar{\phi}'_j)] \lambda_i \quad (1.9c)$$

$$+ \sum_{i,j} \mathcal{A}_{N+1}(\phi_1 \bar{\phi}_1 \dots \bar{\phi}_j \dots \phi_{N/2} \bar{\phi}_{N/2} \phi'_j) \lambda_i \quad (1.9d)$$

For clarity of later discussions, each of the possible components of  $\Psi_m^{(+)}$  is explicitly indicated. (1.9a) are those terms constructed from the ground state configuration of the target, while (1.9b), (1.9c), and (1.9d) correspond to those combinations of Slater determinants constructed from singlet, triplet ( $m_s = 0$ ), and triplet ( $m_s = \pm 1$ ) target spin configurations, respectively. Using this expansion of the wavefunction, the matrix elements of  $A^{(+)}$  are evaluated, reducing Eq. 1.7 to one of solving a matrix inversion and multiplication problem,

$$-2\pi f_{mn} = \mathbf{T}_{mn} = \mathbf{b}_n^\dagger \cdot \mathbf{A}^{-1} \cdot \mathbf{b}_m \quad (1.10)$$

Presently, no continuum functions are included in the expansion of  $\Psi_m^{(+)}$ . The Green's function assures that  $L^2$  functions can suffice for the expansion (Eq. 1.9).

By expanding the orbitals of the target and scattering electron constituting the determinants in Eq. 1.9 in Cartesian Gaussian functions, all terms in Eq. 1.7 can be evaluated analytically except for those involving the  $VG_P^{(+)}V$  operator.

It should be noted that an expansion for  $\Psi_m^{(+)}$  of the type used in Eq. 1.9 implies that one can, in fact, accurately describe the electron-target potential by a separable potential approximation, *i.e.*,

$$V \approx V^N = \sum_{i,j}^N V|i\rangle\langle i|V^{-1}|j\rangle\langle j|V \quad (1.11)$$

The close connection between the use of separable potentials and the Schwinger variational expression for the scattering amplitude has been considered at length by many researchers [6-10]. Indeed, it can be shown that for a separable potential of rank N and a scattering wave function expanded in the same basis of N functions, expression Eq. 1.10 yields an exact solution for the potential [6]. Some researchers have attempted to demonstrate that the Schwinger variational method suffers from spurious resonances similar to those encountered when using the Kohn method with standing wave boundary conditions [11]. It was subsequently shown that what they had in fact proved is that a separable, energy dependent potential can be constructed with particular choices of basis functions such that  $V^{-1}$  in Eq. 1.11 is essentially singular [12]. Based on initial studies employing the SMC this seemed to be an unlikely event. Unfortunately, it has transpired in the course of numerous multichannel studies that essentially singular potentials readily occur, or at least behavior of Eq. 1.7 suggesting such an event is frequently observed.

The role of the projector operator in Eq. 1.7 needs also to be considered in order to interpret structures observed in cross sections obtained in multichannel

studies. Firstly, the distinction between this projector and the more commonly used Feshbach operator has been discussed elsewhere [13]. The relevance of these differences to the multichannel problem will be considered later. For the present discussion, however, these differences are not particularly pertinent. Of greater interest here is what this operator enables one to avoid, and more importantly, problems it does not address. The former can best be illustrated by applications of the Schwinger variational method in which such a projector is not employed.

The investigation of  $e^- \cdot H$  atom scattering of Bransden, Hewitt, and Plummer [14] affords such a case. In their study, the  $G^{(+)}$  term is expanded in terms of eigenstates of the  $H$  atom,

$$G^{(+)} = \sum_{m=1}^{N_0} \phi_m(\vec{r}_2) g_m^+(r_1, r'_1) \phi_m(\vec{r}_2) \quad (1.12)$$

with

$$g_m^+(r_1, r'_1) = -\frac{4}{\pi} \int_0^\infty dk \frac{\sin(kr_1) \sin(kr'_1)}{k_m^2 - k^2 + i\epsilon}$$

where for  $m = 1, 2$ , and  $3$ ,  $\phi_m(\vec{r}_2)$  are selected hydrogenic orbitals which diagonalize the hydrogen atom Hamiltonian and  $g^+(r_1, r'_1)$  is the free particle Green's function. In order to approximate the continuum portion of  $G^{(+)}$ , pseudostates of the type used in close coupling calculations [15] at energies exceeding the ionization threshold for the target ( $m > 3$ ) were employed in their study. The resulting branch points introduced along the positive  $E$ (or  $k$ ) axis lead to spurious resonances of the type observed in close coupling calculations just below the thresholds for the pseudostates representing the continuum. It was noted that the pseudoresonances arising in cross sections reported by Bransden *et al.* are inherently different from the spurious resonances intrinsic to the traditional, standing wave boundary conditions Kohn method. The projector in the  $A^{(+)}$  operator in the SMC scattering

amplitude (Eq. 1.7), by removing the need to approximate the Green's function using such pseudostate expansions, eliminates problems with resonances arising due to such an approximation of the Green's function. Rather, information concerning continuum states is contained in the terms involving the projected and unprojected Hamiltonian terms in  $A^{(+)}$ . As will be seen, it is unfortunately possible to unknowingly introduce pseudoresonances into  $A^{(+)}$  via unphysical states present in this continuum.

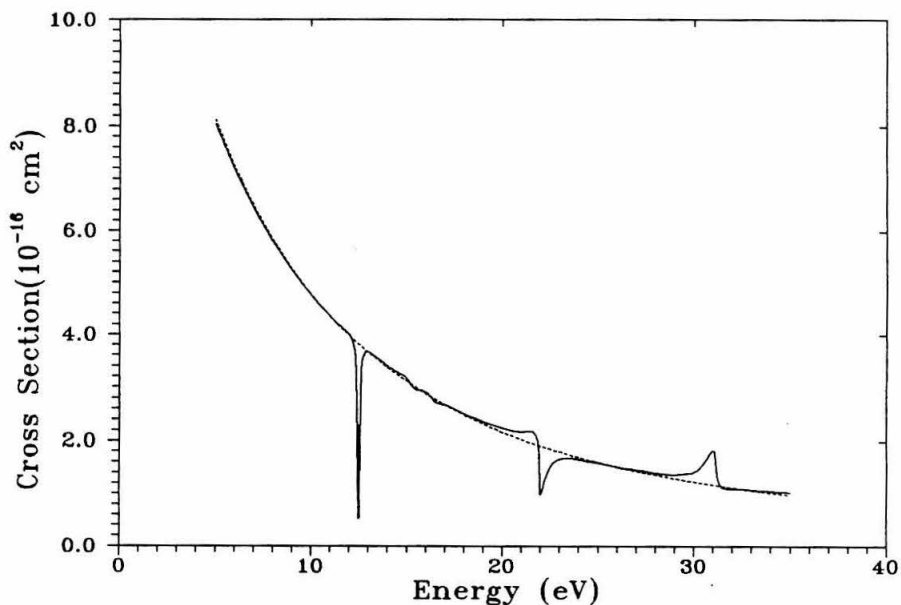


Figure 1.1  ${}^2\Sigma_g$  component of the integral elastic cross section for  $\text{H}_2$  in which a virtual excitation of the type  $[1\sigma_g \rightarrow 2\sigma_g]$  is included. The sharp feature at  $\sim 12.5$  eV is analogous to that discussed in [27]. The features above 20 eV were not reported therein. Dashed line indicates the pure static-exchange cross section.

Some early work involving the SMC indicated that the action of the projection operator (Eq. 1.3) was not correctly understood [16]. It is important to realize that

the function of the projector is to shift the problem of treating the target continuum states from the Green's function where they would be difficult to treat, to the full  $N+1$  electron Hamiltonian present in  $A^{(+)}$  where they can be tractably handled [2]. The other potential and Hamiltonian terms arise from the need, as mentioned above to insure that  $A^{(+)} + VG_P^{(+)}V$  is Hermitian, specifically to cancel the surface terms associated with the kinetic energy operator in  $\hat{H}$ . The projector does not remove effects of closed channels. Indeed, a straightforward, elastic scattering calculation including polarization shows that the SMC projector does not remove the effects of virtual excitations included in the expansion of  $\Psi_m^{(+)}$  which are not included as open channels in the  $P$  operator expansion (Eq. 1.3) on the open channels. See Figs. 1.1 and 1.2 below. These excitations lead to cusps and peaks in the cross sections of the open channels similar to structures observed in the closed coupled equations incorporating closed channel pseudostates in the expansion of the target wavefunction [15,17]. Of course, these are not observed well below the thresholds for the excitations (Eq. 1.9b,c,d) included in the expansion of  $\Psi_m^{(+)}$ . Such structure is analogous to the type of resonances observed in the calculations of Branchett *et al.* [18] for electronic excitation of the hydrogen molecule, where only a few channels were treated as open; although in their restricted VCI description of  $\Psi_m^{(+)}$  within the R-matrix sphere, terms were present corresponding to energetically open channels which were considered closed. As will be shown presently, the projector also does not remove resonances that may appear as a consequence of unphysical states present in the continuum owing both to a particular combination of single particle basis functions used to construct the Slater determinants in the expansion (Eq. 1.9), and to the correlation of the incident electron with the target electrons.

Finally, it should be noted that in contrast to the Kohn variational principle with standing wave boundary conditions, the Schwinger functional based on Eq.

1.2 has been shown to be free of spurious resonances [19]. As has been noted by Takatsuka and McKoy, the functional Eq. 1.7 is also free of such deficiencies [1], although it was noted that the spectrum of  $A^{(+)}$  was important in determining this property. In the following, it will be seen that in contrast to elastic scattering and most two state problems, multichannel calculations appear to frequently severely test some of the theoretical arguments pertaining to the behavior of  $A^{(+)}$  and the accurate evaluation of Eq. 1.10.

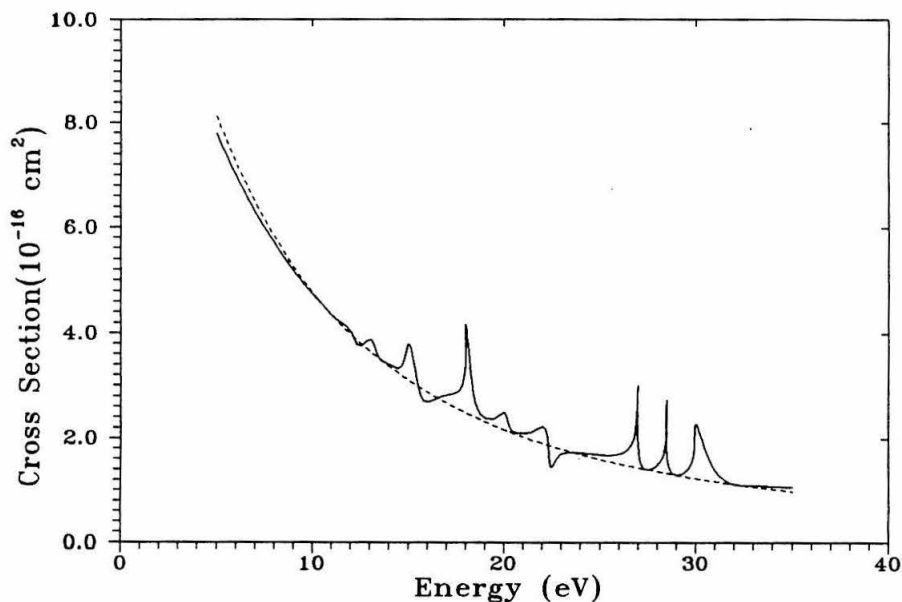


Figure 1.2. Same as in Fig. 1.1 except with an additional excitation  $[1\sigma_g \rightarrow 1\sigma_u]$  included in the expansion of  $\Psi_m^{(+)}$ .

## 1.2 Numerical Properties of the $A^{(+)}$ Matrix

### 1.2.1 The Green's Function

Of the elements in the variational expression (Eq. 1.7), the  $VG_P^{(+)}V$  component

of  $A^{(+)}$  is the most computationally intensive quantity to evaluate. Throughout this work, the numerical procedure developed by Winstead *et al.* [20] to calculate matrix elements involving this operator was employed. For linear molecules, a minimum of 26 angular points in the  $\theta$  (spherical coordinates) angular quadrature was typically used, whilst for nonlinear molecules, grids no sparser than  $14 \times 14$  angular points on each hemisphere of an off shell  $T$ -matrix component were used. Variations in the orientation and center of mass of the target molecule exhibit interesting convergence behavior in regards to these matrix elements. For nonlinear molecules, it has proven to be more effective to place the molecule away from the origin. For linear molecules oriented along the  $z$ -axis, convergence to results obtained using other molecular orientations could only be achieved by using a large number of  $\theta$  quadrature points per quadrature shell.

One property of this method of evaluating the  $VG_P^{(+)}V$  is worthy of some comment as it has been argued that, at least for linear molecules, using a discrete grid of points in  $k$ -space to evaluate the Green's function may lead to spurious resonances in multichannel studies owing to the fact that the quadrature can span many irreducible representations for a point symmetry group while the single particle functions of which the determinants used in the expansion of  $\Psi_m^{(+)}$  are comprised usually transform as a limited subgroup of these representations. That this is possible can be seen by considering the  $k$ -space representation of the principal value and residue components, viz.

$$\begin{aligned} \langle \Psi_m^{(-)} | VG_P^{(+)} V | \Psi_n^{(+)} \rangle &= i\pi \sum_{i=1, N_o} k_i \int d\Omega_{\vec{k}_i} \langle \Psi_m^{(-)} | V | \Phi_i \vec{k}_i \rangle \langle \vec{k}_i \Phi_i | V | \Psi_n^{(+)} \rangle \\ &+ \sum_{i=1, N_o} P \int_0^\infty dk \frac{2k^2}{k_i^2 - k^2} \int d\Omega_{\vec{k}_i} \langle \Psi_m^{(-)} | V | \Phi_i \vec{k}_i \rangle \langle \vec{k}_i \Phi_i | V | \Psi_n^{(+)} \rangle \quad (1.13) \end{aligned}$$

In the former so-called  $\alpha$ -insertion technique, where a set of  $L^2$  functions was used to evaluate both terms, the terms to be evaluated from Eq. 1.13 become

$$\begin{aligned} \sum_{i=1, N_o} k_i \int d\Omega_{\vec{k}_i} \langle \Psi_m^{(-)} | V | \Phi_i \vec{k}_i \rangle \langle \vec{k}_i \Phi_i | V | \Psi_n^{(+)} \rangle = \\ \sum_{i=1, N_o} \sum_{\alpha\beta} k_i \langle \Psi_m^{(-)} | V | \Phi_i \alpha \rangle \langle \beta \Phi_i | V | \Psi_n^{(+)} \rangle \int d\Omega_{\vec{k}_i} \langle \alpha | \vec{k}_i \rangle \langle \vec{k}_i | \beta \rangle. \end{aligned} \quad (1.14a)$$

$$\begin{aligned} \sum_{i=1, N_o} P \int_0^\infty dk \frac{2k^2}{k_i^2 - k^2} \int d\Omega_{\vec{k}_i} \langle \Psi_m^{(-)} | V | \Phi_i \vec{k}_i \rangle \langle \vec{k}_i \Phi_i | V | \Psi_n^{(+)} \rangle = \\ \sum_{i=1, N_o} \sum_{\alpha\beta} \langle \Psi_m^{(-)} | V | \Phi_i \alpha \rangle \langle \beta \Phi_i | V | \Psi_n^{(+)} \rangle P \int_0^\infty dk \frac{2k^2}{k_i^2 - k^2} \int d\Omega_{\vec{k}_i} \langle \alpha | \vec{k}_i \rangle \langle \vec{k}_i | \beta \rangle. \end{aligned} \quad (1.14b)$$

Since the  $L^2$  functions used in the expansion in Eq. 1.14 are typically the same as those used in the expansion of the single particle wavefunctions which comprise the Slater determinants in Eq. 1.9, it is obvious that the resulting  $VG_P^{(+)}V$  term can only have symmetry components already spanned by the Slater determinants, owing to the right-hand most integrals in the residue (1.14a) and principal value (1.14b) parts. However, with the evaluation being directly carried out in  $k$ -space, the residue and principal value terms in Eq. 1.13 can include many symmetry components, depending, in the case of linear molecules, on the  $\phi$  quadrature. As will be described in conjunction with techniques to solve Eq. 1.10, a procedure has been implemented to eliminate possible effects of such terms prior to computation of the scattering amplitude. Hence, a numerical quadrature of these matrix elements should not in itself lead to the appearance of spurious resonances in SMC calculations. It should be noted that this difficulty should not arise in the case of non-linear molecules, or linear molecules not oriented along the  $z$ -axis.

### 1.2.2 Matrix Elements of $A^{(+)}$ and Their Notation

To better interpret the numerical characteristics of  $A^{(+)}$  and its inverse, it is worth examining the various types of matrix elements encountered in multichannel calculations. The notation to be used throughout this work to indicate both particular types of matrix elements and the determinants in Eq. 1.9, is given in Table 1.1 below. The term in brackets indicates the target state on which the  $N + 1$  electron Slater determinant is to be constructed.  $[O]$  indicates the ground state, closed shell wavefunction of the target. The  $[NA \rightarrow NB]$  (hole  $\rightarrow$  particle) notation can denote either the singlet target configuration (1.9b) or triplet (1.9c,d) for an excited state of the target. The letter in parenthesis indicates the type of orbital occupied by the  $N + 1^{th}$  or scattering electron. The use of parenthesis for this latter orbital indicates that it is antisymmetrized with the target electrons. The action of the projector (Eq. 1.3) on one of these configurations is to break this antisymmetrization. In this event, the symbol denoting the scattering function is then set off by brackets, *e.g.*,  $[NA \rightarrow NB][j]$  to show that the scattering electron is no longer antisymmetrized with the target electrons.

Now consider typical values of the matrix elements of  $A^{(+)}$  in atomic units. As would be expected, the on-diagonal terms include the largest elements in absolute magnitude, although quite small values are also present. As indicated in Table 1.2, they range from the order of unity to  $10^{-6}$  for elastic channel elements and from unity to  $10^{-7}$  for inelastic channel elements. Of course, these values will vary somewhat depending on the molecule, especially for elements having nuclear attraction terms. Experience indicates that this range of values is typical for a modest  $\sim 75$  function basis sets.

Off-diagonal terms, which for matrix elements not involving elastic  $\leftrightarrow$  elastic or  $\langle [A \rightarrow B](i) | V | [A \rightarrow B](j) \rangle$  type configurations contain no nuclear terms, are considerably smaller. In general, elastic  $\leftrightarrow$  inelastic terms are about an order of magnitude larger than the inelastic  $\leftrightarrow$  inelastic elements. Matrix elements involving different electronic configurations average to be another order of magnitude smaller. Average values encountered in typical multichannel studies are given in Table 1.2.

Table 1.1. Notation for Matrix Elements of  $A^{(+)}$

Type of term	Notation
elastic $\leftrightarrow$ elastic	$\langle [O](i)   A^{(+)}   [O](j) \rangle$
elastic $\leftrightarrow$ inelastic	$\langle [O](i)   A^{(+)}   [NA \rightarrow NB](j) \rangle$
inelastic $\leftrightarrow$ inelastic	$\langle [NAA \rightarrow NBB](i)   A^{(+)}   [NA \rightarrow NB](j) \rangle$

One important feature to note is the consequence of the very small on-diagonal terms that are encountered, particularly as the basis is enlarged. For those columns having very small on-diagonal elements, one finds that the Euclidean norms for the entire associated rows and columns are very small,  $\sim 10^{-4}$ . Also, in contrast to elastic or typical two state calculations, a large-scale multichannel calculation will involve large numbers of very small on and off diagonal terms which are especially important in describing the coupling of the ground state to excited state channels. As will be seen, this fact is reflected in the extremely poorly conditioned matrices frequently encountered in multichannel studies.

As the Schwinger variational functional (Eq. 1.7) has the useful property that

it is independent of the normalization scheme employed for the scattering wavefunction, one can freely scale these values. This would of course change many of the parameters used to determine the condition of the  $A^{(+)}$  matrix. However the relative ranges would remain unchanged as would the ultimate scattering amplitudes obtained from evaluation of Eq. 1.10.

Table 1.2 Typical Absolute Values of the Matrix Elements of  $A^{(+)}$ .

Matrix Element	Average Value(a.u.)	Max./Min. Value
$\langle [O](i)   A^{(+)}   [O](i) \rangle$	$\sim 0.10$	$\sim 10^0 / \sim 10^{-6}$
$\langle [O](i)   A^{(+)}   [O](j) \rangle$	$\sim 0.01$	—
$\langle [O](i)   A^{(+)}   [NA \rightarrow NB](j) \rangle$	$\sim 0.001$	—
$\langle [NA \rightarrow NB](i)   A^{(+)}   [NA \rightarrow NB](i) \rangle$	$\sim 0.1$	$\sim 10^0 / \sim 10^{-7}$
$\langle [NA \rightarrow NB](i)   A^{(+)}   [NA \rightarrow NB](j) \rangle$	$\sim 0.005$	—
$\langle [NA \rightarrow NB](i)   A^{(+)}   [NAA \rightarrow NBB](j) \rangle$	$\sim 0.0005$	—

### 1.2.3 The Spectrum of $H_{N+1}$

The numerous resonant-like structures observed in multichannel cross sections motivated attempts to assign these features to the eigenvalues in the energy spectrum of the continuum of the short-lived anion formed by the target and scattering electron. Basically, it was hoped that an analysis of the continuum spectrum generated in the space of determinants used in the expansion (Eq. 1.9) of  $\Psi_m^{(+)}$  would

yield possible energy positions of resonant states. This would be analogous to stabilization methods used to determine the positions and widths of resonant complexes, albeit at a rather unsophisticated level [21]. The positions thus found could then be used to interpret the often anomalous features observed in cross sections obtained by evaluation of Eq. 1.7 for multichannel problems. Of course, the shift in a resonance position due to coupling with the continuum is not known, although for the energy resolution ( $\sim 1$  eV) typical of SMC studies, this displacement would be small compared to the interval between the energies at which cross sections are computed. However, correlation between the features observed in the cross sections and eigenvalues computed by diagonalization of  $H_{N+1}$  in the space spanned by the determinants of  $\Psi_m^{(+)}$  usually proved to be weak except at near threshold energies ( $< 5$  eV above threshold). Also, the eigenvalues obtained by this method do not, in general, possess the stability described in studies in which stabilization methods are used [22]. This is most likely due to the size of the basis sets employed in such studies as compared with SMC calculations, the fact that unimproved virtual orbitals are used for the single particle orbitals in Eq. 1.9, and the fact that the energies at which spurious structures appear in SMC cross sections are generally well above the near threshold energies where broad, core-excited resonances are most frequently observed experimentally. Occasionally, however, analysis of the spectrum has proven useful in distinguishing spurious resonances associated with unphysical states in the continuum from what might otherwise be attributed to realistic resonance features. An example of such a state will be considered.

#### 1.2.4 Selection of Determinants

It has been pointed out that the expansion of  $\Psi_m^{(+)}$  in terms of determinants

constructed purely from the triplet states (1.9c,d) of the target and its closed shell, ground state configuration (1.9a) fails to include all components of  $\Psi_m^{(+)}$  in the case of multichannel studies. This becomes quite evident when considering the action of the projector operator as presently formulated. The studies carried out in this work employed the minimum number of closed channel determinants necessary in order to span the entire space of the scattering wavefunction. Failure to limit inclusion of such closed channel singlets to the minimum number required leads to numerous spurious resonances as discussed in connection with the projector operator and seen in Figs. 1.1 and 1.2. As a consequence of this requirement, closed channel singlet configurations (1.9b) generally are included in the expansion of  $\Psi_m^{(+)}$ . Unfortunately, these configurations appear to lead to a significant deterioration in the convergence characteristics of the SMC for scattering symmetries of  $\Psi_m^{(+)}$  in which such "recorrelation" terms are included. Examples of this behavior will be considered later.

In some instances, treating these additional terms as open channels improves the quality of the resulting cross sections, but as the IVO approximation employed in these studies to describe the excited state prevents accurate treatment of both singlet and triplet excitations with the same hole-particle pair, better agreement with experiment is not generally observed. This is especially true for instances in which the singlet and triplet states for a given hole-particle pair are Rydberg and valence-like in character, respectively.

### 1.3 Stability of the SMC Method for Multichannel Studies

#### 1.3.1 Convergence Characteristics

As indicated at the beginning of this chapter, the SMC has yielded satisfactory results for a wide range of static-exchange, polarization, and two-channel inelastic scattering problems. This has been the case even for early studies in which the Green's function term in  $A^{(+)}$  was treated by a less accurate insertion technique. Hence, even with less robust procedures for evaluating Eq. 1.7, converged results could be obtained.

Nonetheless, it has transpired that some two channel and all multichannel prob-

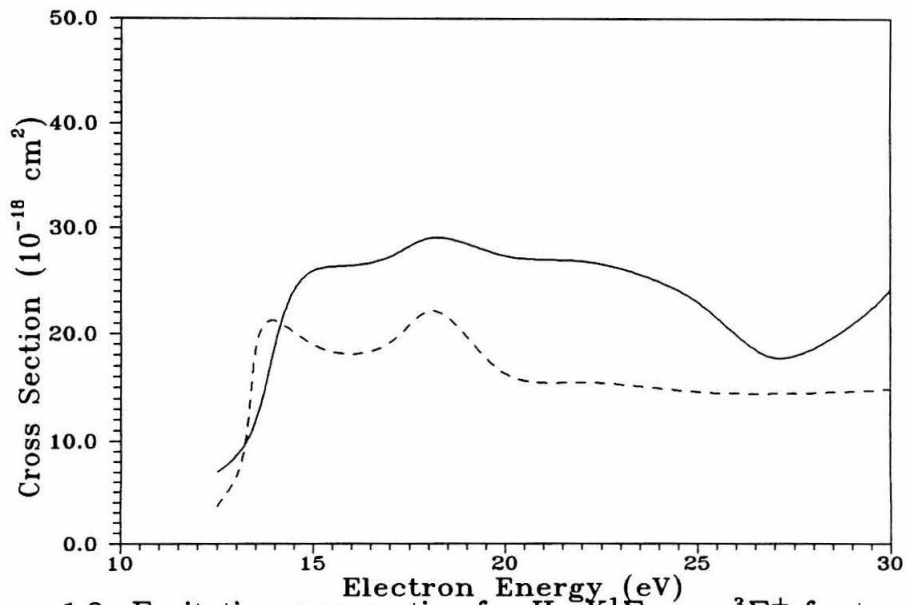


Figure 1.3. Excitation cross section for  $H_2 X^1\Sigma_g^- \rightarrow a^3\Sigma_g^+$  for two basis sets which are identical except for a 20% change in exponents of the  $d$ -type functions used.

lems have proven to be far more difficult to carry out to even a qualitative level of convergence. By convergence, it is meant that modest changes in the choice of basis functions employed to construct the target wavefunction and scattering functions (the  $\phi$  and  $\chi$  of Eq. 1.9, respectively) lead to relatively small ( $\leq 10\%$ ) changes in the resulting cross sections. With a few exceptions, this degree of convergence has not been attainable in this work by direct evaluation of Eq. 1.10 for multichannel calculations. By way of example, Fig. 1.3 shows the results of two calculations of the  $X^1\Sigma_g \rightarrow a^3\Sigma_g^+$  excitation cross section for  $H_2$ . The only difference between the basis functions used in computing the orbitals used in the expansion (Eq. 1.9) is a factor of 20% in the exponents of the  $d$ -type functions. Clearly, quite different results are obtained from Eq. 1.10. Convergence with respect to the number of coupled channels was never expected to occur. However, for a given basis, convergence with respect to the number of quadrature points for evaluation of  $VG_P^{(+)}V$  was readily achievable.

A considerable amount of time has been invested in examining the routines used to construct the numerous additional elements in  $A^{(+)}$  which appear in a multichannel calculation to verify that the software in fact is evaluating these terms consistent with Eq. 1.7. No problems were found which significantly alter the computed scattering amplitudes. Thresholds for the cutoff of the planewave-Gaussian matrix elements ( $\mathbf{b}, \mathbf{b}^\dagger$  in Eq. 1.10) as well as those involving purely  $L^2$  terms were also varied in efforts to improve the SMC results. Algorithms were crafted to reduce the amount of computational work required for linear molecules in an effort to increase the accuracy of the  $VG_P^{(+)}V$  quadrature. None of these changes proved efficacious in improving the behavior of the SMC with respect to the convergence of multichannel studies.

In light of these facts, one must assume that there are either numerical problems unique to multichannel studies or single channel studies employing exceptionally large basis sets; that the approximate description of the target including its discrete and continuum energy spectrum prohibit convergence of multichannel calculations; some portion of the  $A^{(+)}$  operator is especially difficult to treat at the multichannel level; or some aspect of the variational expression (Eq. 1.7) is either incorrect or its present computational implementation is defective with respect to multichannel coupling.

The last of these possibilities will not be considered as the development of some alternate variational expression and code employing it would have been completely out of the scope of this work. Rather, here consideration will be limited to the possibility that purely numerical problems unique to the multichannel case are the source of the problem, that the approximate target description, *i.e.*, the expansion of  $\Psi_m^{(+)}$ , Eq. 1.9) may give rise to the problem, or that the problem lies with some aspect of the multichannel form of  $A^{(+)}$ . Results of numerous calculations made possible by recently available parallel computers indicate that all three problems may potentially arise in multichannel studies as well as some large-scale elastic and two-channel scattering problems.

Evidence for multiple sources for the lack of convergence encountered in these studies includes the fact that test calculations in which the classical problem of linear dependence is intentionally sought lead to results similar to those obtained from calculations in which the problem is scrupulously avoided. In practice this means, for instance, that a simple test for linear dependence like examination of the eigenvalues of the overlap matrix for the single particle basis functions guarantees little about the quality of the SMC results excepting for grossly distorted

basis sets in which one is intentionally introducing linear dependence. The fact that narrow, spurious resonances are observed for many large basis sets – including those in which linear dependence problems are avoided – over the full range of collision energies of interest in this work points to the frequent breakdown of the separable potential approximation (Eq. 1.11). Broad, high energy shape resonances appear in multichannel studies in addition to these narrower structures. Further, the occurrence of these higher energy resonances, and the deterioration of the stability of multichannel calculations above the ionization energy of the target indicate that not all of the instability encountered is due solely to linear dependency of the basis sets or failure of the separable potential approximation. Another observation indicating the nontrivial nature of this problem concerns the behavior of multichannel calculations with respect to convergence as additional scattering functions are added. In particular, it has been found for  $H_2$  that narrow pseudoresonances can be produced at arbitrary impact energies due to the presence of the new states introduced into the continuum of the target by the addition of these functions. This type of resonant structure is also observed, however, in studies employing basis sets where the eigenvalues of the overlap matrix and orbital coefficients indicate that linear dependence must be negligible. An example of this type of structure will be considered in the next section. Hence, it is reasonable to assume that there are several aspects of the multichannel SMC, and in particular, the behavior of the  $A^{(+)}$  matrix that warrant particular consideration.

In what follows, the poor conditioning of the  $A^{(+)}$  matrix and its effects on cross sections obtained by evaluation of Eq. 1.10 are discussed. An estimate of the maximum error that arises purely from numerical round-off is made, as well as the sensitivity of the system of equations 1.10 to such errors. Finally, possible problems with the intrinsic properties of the multichannel  $A^{(+)}$  matrix will also be

considered.

### 1.3.2 Numerical Accuracy and Round – Off Error

The purely numerical characteristics of  $A^{(+)}$  would *prima facia* lead one to suspect that the problem could be purely a problem of numerical instability. Namely, for moderate and large-scale multichannel calculations,  $A^{(+)}$  shows every evidence of being ill-conditioned as defined by the condition numbers given by Fröberg [23]. Of course, as is discussed in numerous texts on linear algebra, the presence of an ill-conditioned matrix does not automatically imply that this condition will be evident in the solutions [24] of the linear equations (1.10). In the case of the SMC, this is borne out by the numerous calculations for elastic and two-state problems where owing to the basis sets employed, the  $A^{(+)}$  matrix undoubtedly was ill-conditioned, yet good convergence and reasonable cross sections were realized.

One effect of ill-conditioning would appear when, as a result of round-off error, the inverse of  $A^{(+)}$  is seriously corrupted. A simple check of the product of  $A^{-1}A^{(+)}$  for multichannel calculations indicates that the inverse is accurate to  $10^{-8}$  to  $10^{-9}$  for most problems considered in this work. Comparison of this number with the range of matrix elements values in Table 1.2 indicates that this error is at most an order of magnitude smaller than most elements. Only for the  $H_2$  molecule, with a single occupied orbital and correspondingly weak potential, is it possible that this may not be true for all significant matrix elements.

An additional study was carried out to investigate the possibility that roundoff error or other source of “noise” is effecting the stability of Eq. 1.10. As noted in [24], a test of the sensitivity of the matrix to minor perturbations is useful in esti-

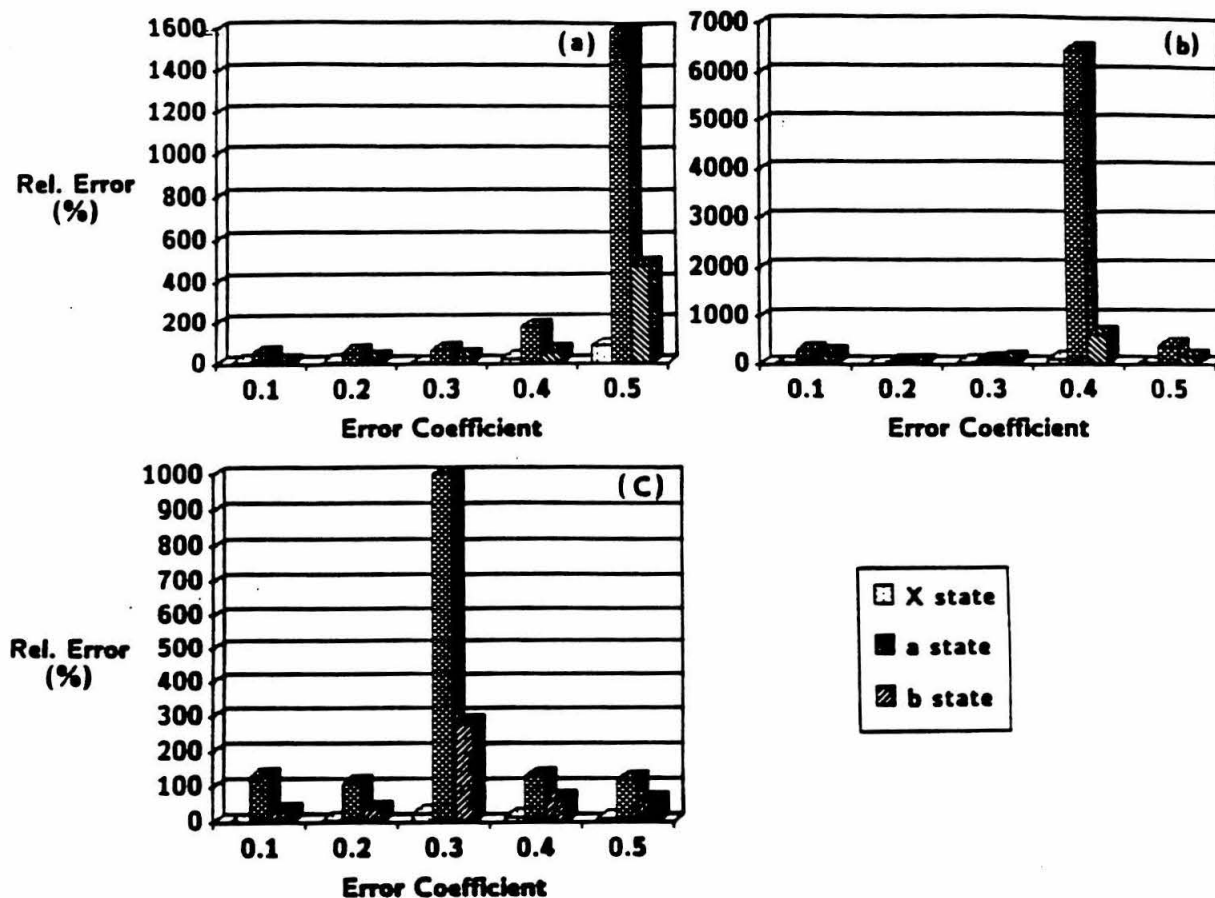


Figure 1.4. Relative error of computed cross sections from  $A^{(+)}$  into which error has been intentionally added. Shown are the cross sections for the  $X^1\Sigma_g \rightarrow X^1\Sigma_g$ ,  $X^1\Sigma_g \rightarrow a^3\Sigma_g^+$ , and  $X^1\Sigma_g \rightarrow b^3\Sigma_u^+$  channels in a seven state calculation for the  $H_2$  molecule at three incident electron energies. Here, 5% of the matrix elements of  $A^{(+)}$  were randomly adjusted by a maximum of  $\pm$  the error coefficient plotted on the  $x$ -axes. The incident electron energies are a) 15 eV, b) 20 eV, and c) 30 eV.

mating to what degree the ill-conditioned nature of  $A^{(+)}$  is actually effecting the calculation of its inverse. The test involved a multichannel study of  $H_2$  including the  $X^1\Sigma_g^+$ ,  $(E, F)^1\Sigma_g^+$ ,  $a^3\Sigma_g^+$ ,  $B^1\Sigma_u^+$ ,  $b^3\Sigma_u^+$ ,  $C^1\Pi_u$ , and  $c^3\Pi_u$  states. A basis selected for its favorable overlap matrix eigenvalues was employed. The  $A^{(+)}$  matrices at 15,

20, and 30 eV were chosen to illustrate the influence that the addition of random error would have on near threshold, intermediate and high energy cross sections, respectively. 5% of the matrix elements were randomly selected and corrupted by factors ranging between  $\pm 10\%$ ,  $\pm 20\%$ ,  $\pm 30\%$ ,  $\pm 40\%$ , and  $\pm 50\%$ . The relative errors in the cross sections computed using these corrupted matrices are depicted in the bar graphs in Fig. 1.4. Only results of the  $X^1\Sigma_g \rightarrow X^1\Sigma_g$ ,  $X^1\Sigma_g \rightarrow a^3\Sigma_g^+$ , and  $X^1\Sigma_g \rightarrow b^3\Sigma_u^+$  are given. The general tendency is for the Rydberg transitions to be more sensitive to injected noise, while the ground state elastic and valence  $X^1\Sigma_g \rightarrow b^3\Sigma_u^+$  inelastic channels are less affected by corruption of the  $A^{(+)}$  matrix.

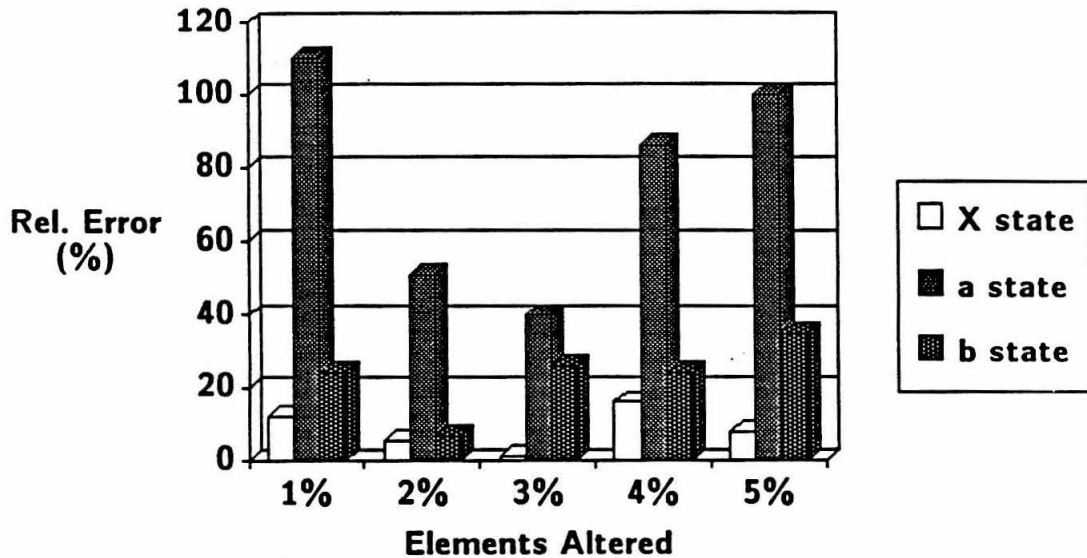


Figure 1.5. Relative error of computed cross sections from  $A^{(+)}$  into which error has been intentionally added. Shown are the cross sections for the  $X^1\Sigma_g \rightarrow X^1\Sigma_g$ ,  $X^1\Sigma_g \rightarrow a^3\Sigma_g^+$ , and  $X^1\Sigma_g \rightarrow b^3\Sigma_u^+$  channels in a seven state calculation for the  $H_2$  molecule at 20 eV incident electron energy. Here, a maximum error of  $\pm 20\%$  was added to 1%, 2%, 3%, 4%, and 5% of the matrix elements of  $A^{(+)}$ .

The stability of the  $A^{(+)}$  matrix was also tested by adding a constant distortion ranging between  $\pm 20\%$  to 1%, 2%, 3%, 4%, and 5% of the matrix elements

of the 15 eV matrix for the same seven-channel calculation of the  $H_2$  molecule. Again, only relative errors in the  $X^1\Sigma_g \rightarrow X^1\Sigma_g$ ,  $X^1\Sigma_g \rightarrow a^3\Sigma_g^+$ , and  $X^1\Sigma_g \rightarrow b^3\Sigma_u^+$  channels are shown in Fig. 1.5. As with the other tests, the Rydberg  $X^1\Sigma_g \rightarrow a^3\Sigma_g^+$  transition is considerably more sensitive to corruption of the  $A^{(+)}$  matrix.

The fact that the relative error in the cross sections is not a monotonic function of noise added, either in terms of the magnitude of the distortion or the number of matrix elements corrupted, would appear to indicate that the particular randomly selected elements which are altered is more important than the degree to which they are distorted. The trend for the Rydberg  $X^1\Sigma_g \rightarrow a^3\Sigma_g^+$  excitation is most relevant to the question of instability. Namely, the near-threshold cross sections are less sensitive to random errors in the  $A^{(+)}$  matrix than at intermediate energies. It can be concluded that although the calculated cross sections are somewhat sensitive to small changes in the  $A^{(+)}$  matrix elements, the totally unstable behavior usually observed in ill-conditioned systems of equations is not present [24]. It would appear rather, that the system of equations (1.10) is neither very stable with respect to such perturbations of  $A^{(+)}$  nor wildly erratic.

Wilkinson [25] has carried out detailed error analyses of a variety of methods for solving systems of linear equations by Gaussian elimination, Given's reduction, Householder's reduction, etc. The method most frequently used in this work to solve Eq. 1.10 makes use of the Householder's reduction to generate a bidiagonal matrix. The subsequent complete diagonalization by a QR procedure contributes much less to the final error and will not be taken into account. Given a particular normalization of the matrix, Wilkinson derived a maximum relative error in computing the matrix inverse by use of this technique, *viz.*

$$\epsilon < 2^{-t} n^2 [a n^{1/2} \|A^{-1}\| + b] \quad (1.15)$$

where  $t = 63$  for a CRAY operating in single precision mode and  $n$  is the order of the  $A^{(+)}$  matrix.  $\|A^{-1}\|$  is the Hilbert norm of the inverse of the  $A^{(+)}$  matrix. For Householder's reduction method,  $a$  and  $b$  are on the order of unity. An analysis of the eigenvalues of  $A^{-1}$  indicates for most moderate and large bases,  $\|A^{-1}\|$  is on the order of  $10^4$  to  $10^5$ . For multichannel studies,  $n$  varies greatly due to the fact that it is the sum of the number of scattering functions in each channel. For the example in Figs. 3 and 4,  $n = 614$ . Hence, given that  $A^{(+)}$  approximately satisfies the normalization assumed for (15), one finds

$$10^{-10} < \epsilon < 10^{-8}$$

depending on  $\|A^{-1}\|$ . Although this is a maximum error, and the author notes that typically much better accuracy is achieved than would be indicated by the analysis, the nature by which the error scales, namely as  $n^{5/2}$  would indicate a potential problem for cases where small off-diagonal coupling terms are important for a particular channel. In addition, as the basis set size increases  $\|A^{-1}\|$  tends to increase, albeit more slowly than the  $n^{5/2}$  factor in Eq. 1.15. The results of Wilkinson's error analysis are consistent with the identity matrix check mentioned earlier where the accuracy of  $A^{-1}A^{(+)} - I$  was on the order of  $10^{-8}$  to  $10^{-9}$ . Again, an examination of the range of magnitudes of the matrix elements in  $A^{(+)}$  for the  $H_2$  molecule shows there tend to be more elements within the range of magnitude of this error limit for large basis sets. However, for larger molecules, there tends to be a more pronounced separation between nonzero matrix elements and those which are zero by symmetry.

It would thus seem that except for cases where the order of  $A^{(+)} \gg 500$ , and matrix elements  $\sim 10^{-8}$  are significant as may be the case in  $H_2$ , purely numerical errors in computing the inverse or solving the equations (10) following computation

of the matrix elements is not significant as a source of error in multichannel problems. Even for  $H_2$ , this should only be important for very large basis sets for which multichannel coupling leads to  $n \gg 500$  in Eq. 1.15.

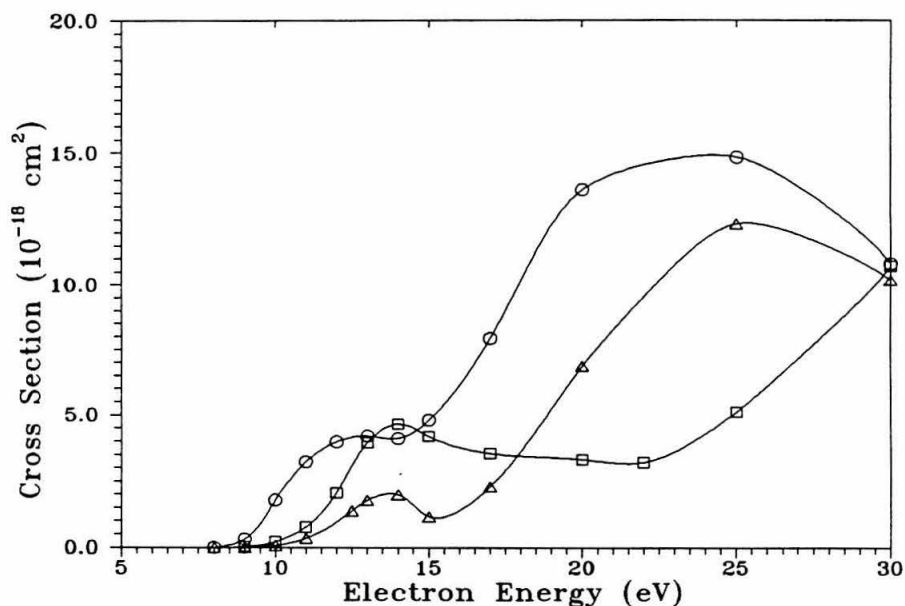


Figure 1.7.  ${}^2\Pi_u$  component of the excitation cross section for  $N_2$  ( $X^1\Sigma_g^+ \rightarrow A^3\Sigma_u^+$  transition for a four-state calculation in which closed channel singlet determinants are included in the expansion of  $\Psi_m^{(+)}$ ). Results for three different basis sets are shown. Good convergence was observed in other symmetry components.

### 1.3.3 Evidence of Other Sources of Instability

Multichannel calculations evince an additional, qualitatively different type of instability the origin of which is not obviously numerical. This is plainly evident upon consideration of results of calculations of excitation cross sections for the  $A^3\Sigma_u^+$  valence state of  $N_2$ . Figure 1.6 shows the  ${}^2\Pi_u$  symmetry compo-

ment of the  $X^1\Sigma_g \rightarrow A^3\Sigma_u^+$  cross section for a calculation involving the minimum number of determinants required in the expansion of  $\Psi_m^{(+)}$  (Eq.1.9) to

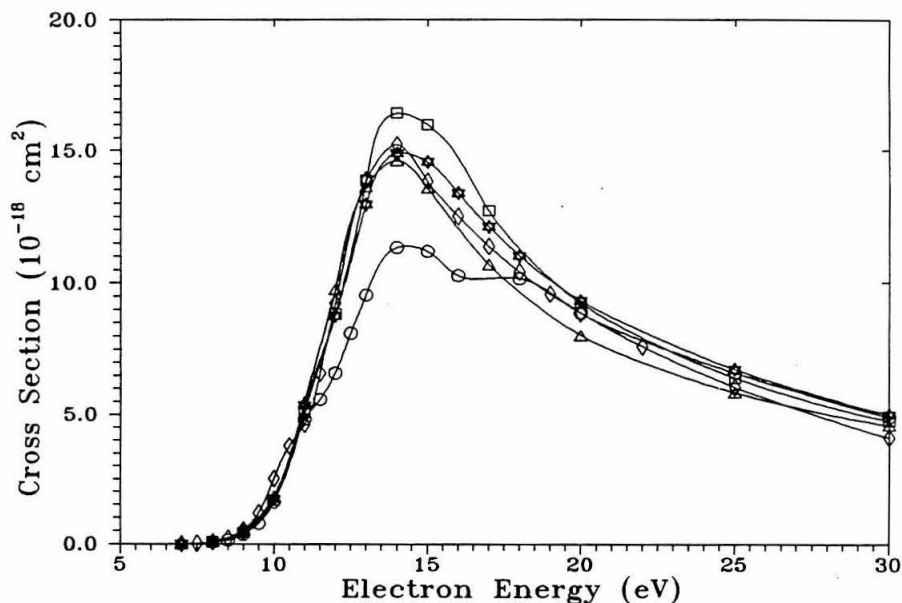


Figure 1.6.  ${}^2\Pi_u$  component of the excitation cross section for  $N_2$  ( $X^1\Sigma_g^+ \rightarrow A^3\Sigma_u^+$  transition at the equivalent of a two-state calculation. Results for four different basis sets are shown. Similar satisfactory convergence was observed in other symmetry components.

compute these cross sections. As with the other symmetry components of this inelastic cross section, the convergence behavior is excellent. Even small valence basis sets yield reasonable cross sections. In this particular case, only one basis set generates somewhat different results over a limited energy range.

Now consider Fig. 1.7 depicting results in which additional channels are coupled with the  $X^1\Sigma_g \rightarrow A^3\Sigma_u^+$  channel. Doing so requires the introduction of previously

mentioned recorrelation terms in the expansion of  $\Psi_m^{(+)}$ .  $N_2$  is useful in this regards; for this particular multichannel coupling scheme, only the  ${}^2\Pi_u$  symmetry has such excitation terms in Eq. 1.9. As is clearly seen, the convergence observed in Fig. 1.6 is completely lost. However, except for narrow resonances of a type to be discussed, the convergence behavior in the other symmetries is quite satisfactory. Figure 1.8 shows results in which the recorrelation terms are not treated as closed channels. The importance of treating such channels as open has been considered in [27]. However, rather than improving results, convergence behavior further deteriorates and a very different energy dependence of the cross sections is observed. Although not specifically considered here, similar deterioration in the quality of cross sections in  $H_2$  and  $CO$  at high (15–30 eV) impact energies has been observed in multichannel studies. In the case of  $H_2$ , this anomalous behavior is observed in all but the  ${}^2\Delta_u$  symmetry component for a five channel calculation including the  $X^1\Sigma_g^+$ ,  $a^3\Sigma_g^+$ ,  $b^3\Sigma_u^+$ , and  $c^3\Pi_u$  states. In these instances, there is effectively no convergence with respect to basis set size.

In these three calculations for the  $X^1\Sigma_g \rightarrow A^3\Sigma_u^+$  transition in  $N_2$ , there are two basic differences. In the first study, no singlet configurations (1.9b) are present in the expansion of  $\Psi_m^{(+)}$  and the projector  $P$  acts in a particularly simple manner in the  ${}^2\Pi_u$  symmetry block. In the second and third sets of calculations, singlet configurations are included as closed and open channels, respectively. Furthermore, the projection operator  $P$  now acts on  $\Psi_m^{(+)}$  in a more complicated way. Note, however, that the projector only has this more complex structure in the  ${}^2\Pi_g$  and  ${}^2\Pi_u$  symmetries. In the third case, the spectrum of  $H_{N+1}$  is also considerably more complex as  $\Psi_m^{(+)}$  consists of more determinants.

One possible source of the poor convergence behavior in these studies is the

presence of coulomb integrals in the potential  $PV + VP$  and  $VG_P^{(+)}V$  terms, owing to singlet $\leftrightarrow$ singlet coupling. At least for the second case, this is not a factor as the singlet transitions are not of a dipole allowed type and are hence relatively short ranged, the convergence of the  $VG_P^{(+)}V$  term with respect to quadrature in  $k$ -space remains satisfactory, and in many cases there is no evidence that the contributions of the higher partial wave components change drastically in going from the first calculation to the others. Such behavior would be expected if long range forces were at least partly responsible for the instability of the cross sections at high energies.

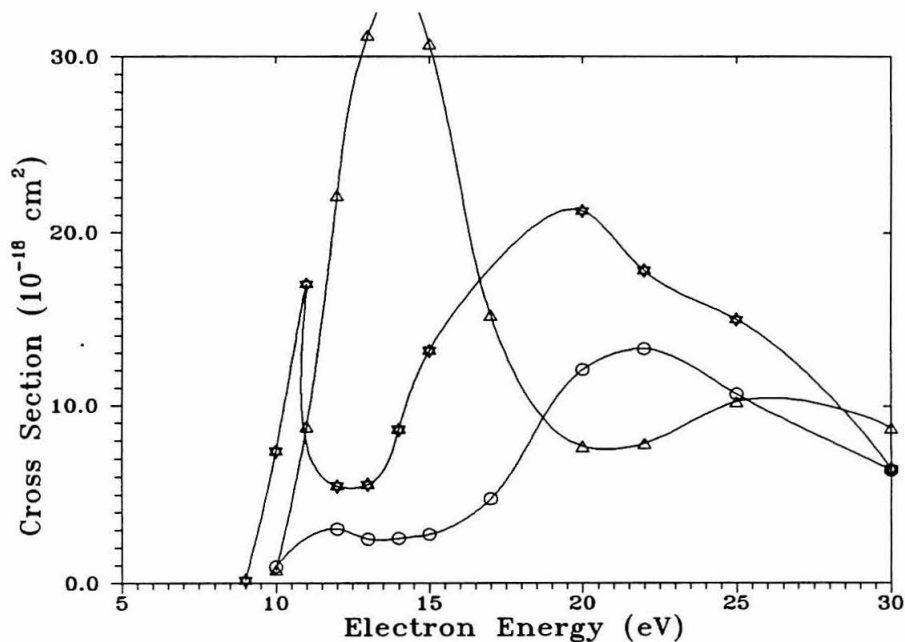


Figure 1.8.  ${}^2\Pi_u$  component of the excitation cross section for  $N_2$  ( $X^1\Sigma_g^+ \rightarrow A^3\Sigma_u^+$ ) transition for a six-state calculation in which the singlet coupled determinants in Fig. 1.7 are now included as open channels in the expansion of  $\Psi_m^{(+)}$ .

The fact that the convergence of the SMC results becomes poorer as the colli-

sion energy and number of highly coupled channels increases seems to point to the  $\hat{H} - a(P\hat{H} + \hat{H}P)$  term, which is manifestly energy dependent, as the more likely source of trouble. Here, it would be helpful to reconsider Eq. 1.9, and instead think of  $\Psi_m^{(+)}$  as consisting of two parts as in the close coupling formulation, *viz.*

$$\Psi_m^{(+)} = \sum_i \sum_j c_{ij}^m \mathcal{A}_{N+1} \Phi_i \phi_{ij} + \sum_\mu d_\mu^m \Theta_\mu, \quad (1.16)$$

where  $\Phi_i$  is the  $i^{\text{th}}$  open channel wavefunction of the target and the  $\phi$  are all orbitals, *i.e.*, scattering functions, orthogonal to all double and singly occupied orbitals of the various target states  $\Phi_i$ . The  $\Theta_\mu$  represent the equivalent to the minimum Hilbert space components of  $\Psi_m^{(+)}$  required in the close coupled equations in order to relax the orthogonality conditions imposed on the  $\phi$ 's. These are the equivalent of the  $\psi$  term in Eq. 2.17 of [2] and are frequently referred to as  $Q$ -space terms. It is useful to consider  $\Psi_m^{(+)}$  in this form as the action of the projector operator is different on the two components. For the first term on the right-hand side of Eq. 1.16, the projector acts on each component of the double sum in a very simple manner,

$$P\mathcal{A}_{N+1}\Phi_i\phi_{ij} = \frac{1}{\sqrt{N+1}} [\mathcal{A}_N\Phi_i] [\phi_{ij}] \quad (1.17)$$

The projector simply acts to break the antisymmetry of the  $N + 1$  electron wave function by selecting only those Slater determinants from Eq. 1.9 in which the  $N + 1^{\text{th}}$  electron is in the scattering orbital. For an elastic, static exchange or polarization calculation, these are the only types of terms appearing in  $P\Psi_m^{(+)}$  as all terms in the rightmost term of Eq. 1.16 are projected out. In this sense, the projector for static exchange or polarization calculations is much like the Feshbach operator as long as one works at collision energies below the first inelastic threshold. This fact was noted by Feshbach in his description of the ‘‘naive’’ projector [Ref. 31, p. 209]. In a two-state calculation, only one recorelation term is present, namely

$||O\rangle(NB)\rangle$  where the inelastic channel involves the  $[NA \rightarrow NB]$  excitation. Even then, the net effect of  $P$  is rather simple as

$$P_{j \rightarrow i} ||O\rangle(i)\rangle = -\frac{1}{\sqrt{N+1}} ||j \rightarrow i\rangle[j]\rangle \quad (1.18)$$

This simple structure persists for calculations involving only the singlet/triplet coupling of a single hole/particle excitation.

With multichannel calculations, however, the continuum spectrum of the  $H_{N+1}$  operator becomes increasingly complex, as does the effect of the projector on the recorelation or  $Q$  space terms. The first of these effects is reflected in Fig. 1.2 in which at the level of a four excitation polarization calculation, the elastic channel exhibits a rich resonance structure above the ionization threshold. The second arises as a consequence of the increasing number of determinants in Eq. 1.9 with multiple parentage with respect to the open channels  $\Phi_i$ .

It should be noted that the action of the projector on such terms has never been explicitly discussed as proofs of the values for  $a$  in Eq. 1.5 have used the orthogonality of the scattering orbitals in the open channel space to the target orbitals (see, for example, Appendix of [1]). However, a close reading of the description of a test case in [2] concerning the static-exchange+polarization elastic  $H \cdot e^-$  scattering is quite interesting in these regards. In this problem, continuum functions were included so that meaningful comparison of convergence properties of the SMC with respect to the Kohn method, for instance, could be made. Otherwise, the problem is not significantly different from present studies except that only two electrons are involved and hence the projector is a one electron operator. Briefly, the basis used in the expansion of  $\Psi_0^{(+)}$  included the following configurations

$$A_2\phi_{1s}\bar{s}\theta_{1,3} \quad \text{and} \quad A_2\phi_{1s}\bar{c}\theta_{1,3}, \quad (1.19a)$$

$$\mathcal{A}_2\phi_{1s}\phi_{1s}\theta_1, \quad (1.19b)$$

$$\mathcal{A}_2\phi_{1s}g_i\theta_{1,3} \quad (i = 1, 2, \dots, M), \quad (1.19c)$$

$$\mathcal{A}_2\phi_t g_j\theta_{1,3} \quad (j = 1, 2, \dots, N_t), \quad (1.19d)$$

where  $\phi_{1s}$  is the  $1s$  state of the  $H$  atom;  $\bar{s}$  and  $\bar{c}$  are appropriately regularized continuum functions orthogonalized to  $\phi_{1s}$ ;  $g_i$  and  $g_j$  are Slater functions also orthogonalized to  $\phi_{1s}$ ; and  $\phi_t$  are pseudostates used to incorporate polarization effects. The most important point here is that, according to the description of the matrix elements in which the kinetic energy operator of  $\hat{H}$  is not canceled in  $[\hat{H} - a(P\hat{H} + \hat{H}P)]$ , the terms (1.19b) and (1.19d) are treated equivalently, *i.e.*,  $P\mathcal{A}\phi_{1s}\phi_{1s}\theta_1 = 0$ . Although it might appear to be trivial, this is quite different from the action of the projector in the  $A^{(+)}$  operator of Eq. 1.5. In the present SMC method, the projector for this problem would be defined as

$$P = \phi_{1s}(\vec{r}_1)\alpha(\vec{r}_1) \quad (1.20)$$

where  $\alpha(\vec{r}_1)$  represents the usual  $m = +1/2$  spin eigenfunction. In this event, there would be an overlap of the projector with the configuration (1.19b). Namely, with

$$\mathcal{A}_2\phi_{1s}\phi_{1s}\theta_1 = \frac{1}{\sqrt{2}}[\phi_{1s}(1)\alpha(1)\phi_{1s}(2)\beta(2) - \phi_{1s}(2)\alpha(2)\phi_{1s}(1)\beta(1)], \quad (1.21a)$$

then

$$\begin{aligned} &\langle \mathcal{A}_2\phi_{1s}\phi_{1s}\theta_1 | \hat{H} - \frac{N+1}{2}(P\hat{H} + \hat{H}P) | \mathcal{A}_2\phi_{1s}\phi_{1s}\theta_1 \rangle = \\ &\langle \phi_{1s}(1)\phi_{1s}(2) | \hat{H} | \phi_{1s}(1)\phi_{1s}(2) \rangle - \langle \phi_{1s}(1)\phi_{1s}(2) | \hat{H} | \phi_{1s}(1)\phi_{1s}(2) \rangle = 0 \end{aligned} \quad (1.21b)$$

and hence (1.19b) would appear to enter into Eq. 1.5 in a manner similar to (1.19a) and (1.19c) rather than the virtual excitation terms (1.19d). In other words, Eqs.

4.1 and 4.2 of [2] imply that in the expansion of  $\Psi_m^{(+)}$  – Eq. 1.19 here or Eqs. 3.1a–d in [2] – both determinants involving virtual excitations and those involving only target orbitals are treated equally, *i.e.*, annihilated by the projector: the projector only returns a nonzero result for those determinants which, in principle, are energetically part of the “open” channel space and are not constituted solely of bound orbitals. This is despite the fact that (1.19b) has a nonzero overlap with the target wavefunction. The present implementation of the SMC projector does not operate on  $\Psi_m^{(+)}$  as described in [2].

The possibility of redefining the projector to act in a manner like that described in [2] was attempted. In one case, overlap terms like Eq. 1.18 were eliminated. A second case was studied in which coupling of inelastic determinants of Eq. 1.9 via the projector were eliminated. Neither yielded physically reasonable results for test  $H_2$  multichannel calculations.

A second series of investigations was carried out to determine the relation between the poor convergence characteristics observed in channels containing  $Q$ -space terms and the various components of the  $A^{(+)}$  matrix elements Eq. 1.5. The basic premise is that since the  $Q$ -space or recorrelation terms involve exclusively orbitals optimized either via an SCF calculation of the ground state wavefunction or IVO calculation of the excited state orbitals, it would be reasonable to assume that the matrix elements involving these configurations would change little from basis to basis. For the purpose of these tests, the five-channel ( $X^1\Sigma_1^+$ ,  $a^3\Sigma_g^+$ ,  $b^3\Sigma_u^+$ ,  $c^3\Pi_{ux}$ ,  $c^3\Pi_{uy}$ ) hydrogen molecule calculation was carried out using five different basis sets.

First, it is useful to note the constituent parts of the matrix elements of  $A^{(+)}$  comprised of  $Q$ -space terms. Consider a three-channel study of the  $H_2$

molecule involving the  $X^1\Sigma_g^+$ ,  $a^3\Sigma_g^+$ , and  $b^3\Sigma_u^+$  states. Then, using the  $\langle [1\sigma_g \rightarrow 2\sigma_g](1\sigma_u) | A^{(+)} | [1\sigma_g \rightarrow 2\sigma_g](1\sigma_u) \rangle$  matrix element as an example, one obtains for the different branches of the projector, the following:

$$\begin{aligned}
\langle [1\sigma_g 2\sigma_g](1\sigma_u) | A^{(+)} | [1\sigma_g 2\sigma_g](1\sigma_u) \rangle &= C_1^2 \theta_{1,2,3} \langle 1\sigma_g 2\sigma_g 1\sigma_u | \hat{H} | 1\sigma_g 2\sigma_g 1\sigma_u \rangle \theta'_{1,2,3} \\
&+ C_1 \left[ \theta_2 \langle [1\sigma_g 2\sigma_g][1\sigma_u] | V | 1\sigma_g 2\sigma_g 1\sigma_u \rangle \theta'_{1,2,3} \right. \\
&\quad \left. + \theta_{1,2,3} \langle 1\sigma_g 2\sigma_g 1\sigma_u | V | [1\sigma_g 2\sigma_g][1\sigma_u] \rangle \theta'_2 \right] \\
&+ C_1 \left[ \theta_3 \langle [1\sigma_g 2\sigma_g][1\sigma_u] | V | 1\sigma_g 2\sigma_g 1\sigma_u \rangle \theta'_{1,2,3} \right. \\
&\quad \left. + \theta_{1,2,3} \langle 1\sigma_g 2\sigma_g 1\sigma_u | V | [1\sigma_g 2\sigma_g][1\sigma_u] \rangle \theta'_3 \right] \\
&- C_2 C_1 \left[ \theta_2 \langle [1\sigma_g 1\sigma_u][2\sigma_g] | V | 1\sigma_g 2\sigma_g 1\sigma_u \rangle \theta'_{1,2,3} \right. \\
&\quad \left. + \theta_{1,2,3} \langle 1\sigma_g 2\sigma_g 1\sigma_u | V | [1\sigma_g 1\sigma_u][2\sigma_g] \rangle \theta'_2 \right] \\
&+ 2C_1^2 \left[ \langle 1\sigma_u | T_e | 1\sigma_u \rangle - (E - E_{1\sigma_g 2\sigma_g}) \right] + C_2^2 C_1^2 \left[ \langle 2\sigma_g | T_e | 2\sigma_g \rangle - (E - E_{1\sigma_g 1\sigma_u}) \right] \\
&- \theta_{1,2,3} \langle 1\sigma_g 2\sigma_g 1\sigma_u | V G_P^{(+)} V | 1\sigma_g 2\sigma_g 1\sigma_u \rangle \theta'_{1,2,3} \tag{1.22}
\end{aligned}$$

where  $C_1 = 1/\sqrt{N+1}$  and  $C_2 = 1/2 + 1/\sqrt{2}$ . For  $H_2$ ,  $N = 2$ .  $T_e$  signifies the kinetic energy operator. The notation for the determinants has been simplified so that those containing no brackets or parenthesis indicate antisymmetrization of all  $N + 1$  electrons.  $\theta$  indicates the target spin configuration: 1– singlet coupling, 2– low spin triplet coupling, and 3–high spin triplet coupling. These correspond to components (1.9b), (1.9c), and (1.9d) of the expansion of  $\Psi_m$ , respectively. For comparison, one finds that for a term such as

$$\langle [1\sigma_g \rightarrow 2\sigma_g](n\sigma_u) | A^{(+)} | [1\sigma_g \rightarrow 1\sigma_u](n\sigma_g) \rangle,$$

one obtains the following contributions –

$$\langle [1\sigma_g 2\sigma_g](n\sigma_u) | A^{(+)} | [1\sigma_g 1\sigma_u](n\sigma_g) \rangle = C_1^2 \theta_{2,3} \langle 1\sigma_g 2\sigma_g n\sigma_u | \hat{H} | 1\sigma_g 1\sigma_u n\sigma_g \rangle \theta'_{2,3}$$

$$\begin{aligned}
& + C_1 \left[ \theta_2 \langle [1\sigma_g 2\sigma_g][n\sigma_u] | V | 1\sigma_g 1\sigma_u n\sigma_g \rangle \theta'_{2,3} + \theta_3 \langle [1\sigma_g 2\sigma_g][n\sigma_u] | V | 1\sigma_g 1\sigma_u n\sigma_g \rangle \theta'_{2,3} \right] \\
& + C_1 \left[ \theta_{2,3} \langle 1\sigma_g 2\sigma_g n\sigma_u | V | [1\sigma_g 1\sigma_u][n\sigma_g] \rangle \theta'_2 + \theta_{2,3} \langle 1\sigma_g 2\sigma_g n\sigma_u | V | [1\sigma_g 1\sigma_u][n\sigma_g] \rangle \theta'_3 \right] \\
& - \theta_{2,3} \langle 1\sigma_g 2\sigma_g n\sigma_u | V G_P^{(+)} V | 1\sigma_g 1\sigma_u n\sigma_g \rangle \theta'_{2,3} \tag{1.23}
\end{aligned}$$

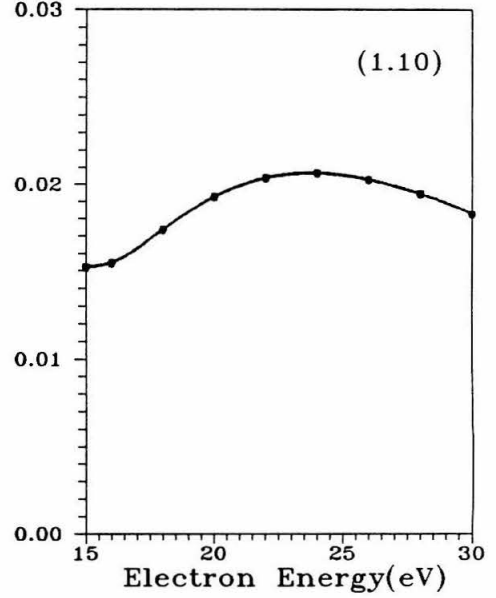
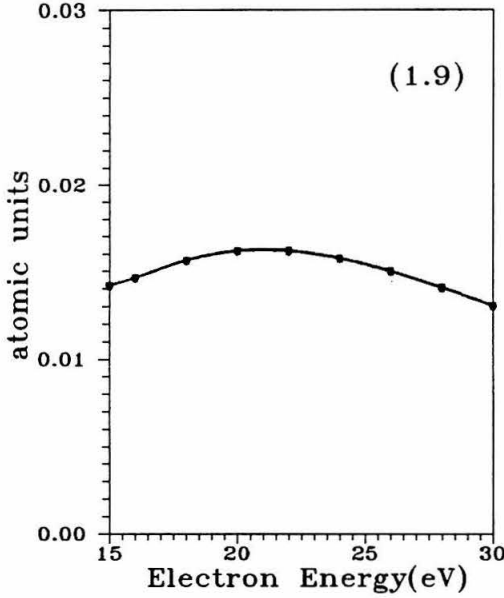


Figure 1.9. Plot of the principal value component of the  $V G_P^{(+)} V$  terms of the  $\langle [1\sigma_g \rightarrow 2\sigma_g](1\sigma_u) | A^{(+)} | [1\sigma_g \rightarrow 2\sigma_g](1\sigma_u) \rangle$  matrix element. Although results of all five basis sets are shown, the scale is not sufficiently fine to reveal the small differences between them.

Figure 1.10. Same as Fig. 1.9, except for matrix elements of the type  $\langle [1\sigma_g \rightarrow 2\sigma_g](1\pi_{ux}) | A^{(+)} | [1\sigma_g \rightarrow 2\sigma_g](1\pi_{ux}) \rangle$ .

It is obvious that the recorrelation terms involve many more elements including kinetic energy terms, excited state energies, and collision energies, in addition to the  $V G_P^{(+)} V$ , unprojected Hamiltonian, and potential terms. The satisfactory con-

vergence characteristics of these latter two components are evident from Tables 1.3 and 1.4. For this multichannel calculation, both components exhibit a variation of no more than  $10^{-3}$  between basis sets. The energy dependent,  $VG_P^{(+)}V$  component of the two recorrelation terms are plotted in Figs. 1.9 and 1.10. Only the real, or principal value part is plotted; similar convergence qualities were observed for the residue terms.

From the tables and figures, it would appear that the  $A^{(+)}$  matrix elements

Table 1.3. Value of Terms Constituting Matrix Elements of the Type  
 $\langle [1\sigma_g \rightarrow 2\sigma_g](1\sigma_u) | A^{(+)} | [1\sigma_g \rightarrow 2\sigma_g](1\sigma_u) \rangle$

Basis	$H_{N+1}$ (a.u.)	$PV + VP$
1	1.3172	-0.1077
2	1.3165	-0.1080
3	1.3162	-0.1083
4	1.3166	-0.1080
5	1.3166	-0.1080

involving recorrelation or  $Q$ -space configurations should vary by no more than  $\sim 10^{-3}$ . However, upon examination of the complete  $A^{(+)}$  matrix element values, differences between basis sets appear. Figures 1.11 and 1.12 indicate that the  $A^{(+)}$  elements converge to at least two significantly different values. These differ by  $\sim 10^{-2}$ , some ten times greater than differences observed for the  $\hat{H}$ ,  $PV + VP$ , and  $VG_P^{(+)}V$  terms alone. It would hence appear, as stated above, that the extra terms associated with matrix elements of the type 1.22 significantly complicate their accurate computation.

It is interesting to note that, considering that the convergence of the  $A^{(+)}$  matrix elements involving recorelation terms is not predictable, as indicated in Figs. 1.11 and 1.12, it is possible that the variation of  $a$  in Eq. 1.8 could fortuitously lead to improved results. Obviously, this would only occur if the  $Q$ -space has a significant number of terms, *i.e.*, highly coupled multiple channels. An optimal value deviating from  $\frac{N+1}{2}$  would be highly indicative of a problem. At any rate, numerous calculations with large basis sets and the results of the studies discussed above

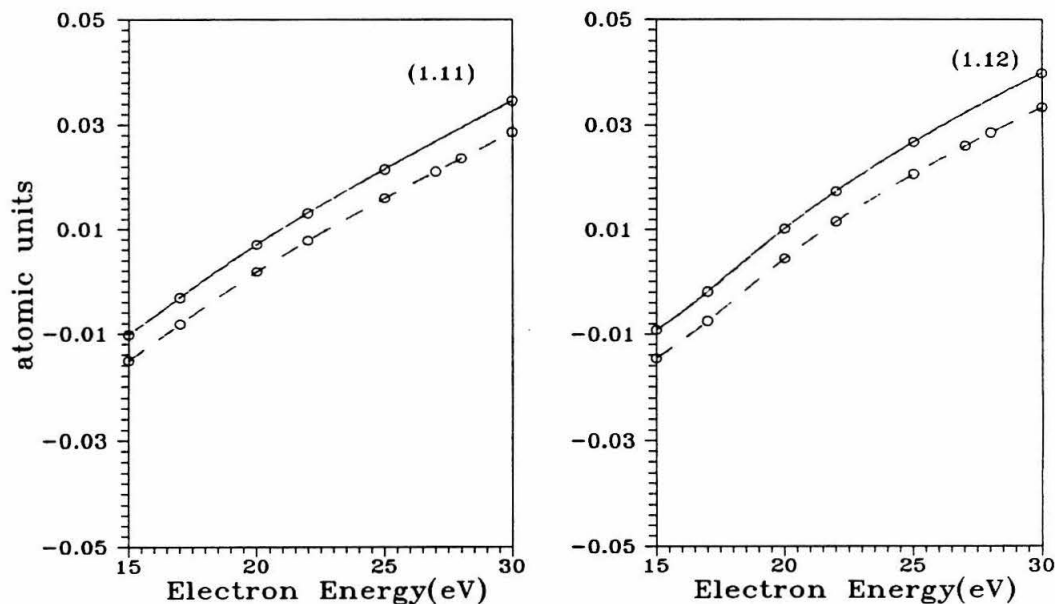


Figure 1.11 Plot of the total  $\langle [1\sigma_g \rightarrow 2\sigma_g](1\sigma_u) | A^{(+)} | [1\sigma_g \rightarrow 2\sigma_g](1\sigma_u) \rangle$  matrix element. Basis set 1, solid line; basis set 2, short dashed line; basis set 3, long dashed line; basis set 4, short dash line plus circles; basis 5, long dash line plus circles.

Figure 1.12 Same as Fig. 1.11 but for matrix elements of the type  $\langle [1\sigma_g \rightarrow 2\sigma_g](1\pi_{ux}) | A^{(+)} | [1\sigma_g \rightarrow 2\sigma_g](1\pi_{ux}) \rangle$

strongly suggest that there are numerical characteristics of the  $\hat{H} - a(P\hat{H} + \hat{H}P)$  component of  $A^{(+)}$  which are difficult to deal with effectively, at least at energies significantly above the ionization threshold for a target.

Table 1.4. Value of Terms Constituting Matrix Elements of the Type  $\langle [1\sigma_g \rightarrow 2\sigma_g](1\pi_{ux}) | A^{(+)} | [1\sigma_g \rightarrow 2\sigma_g](1\pi_{ux}) \rangle$

Basis	$H_{N+1}$ (a.u.)	$PV + VP$
1	1.3004	-0.1109
2	1.2998	-0.1112
3	1.2996	-0.1114
4	1.2999	-0.1112
5	1.2999	-0.1112

The high energy pseudoresonances (Figs. 1.7 and 1.8) apparently introduced by the incorporation of the inelastic channel recorelation terms is suggestively similar to behavior observed in the application of the complex Kohn method to targets described by multiconfiguration wavefunctions [29]. In this case, a simple expansion of the  $Q$ -space of Eq. 1.16 in terms of direct products of all configurations included in the target wavefunction and all partially occupied orbitals leads to spurious high energy resonances. This is attributed to the partial representation of closed channels not explicitly treated in the coupled equations [29]. This consequence of not correctly treating the  $Q$ -space terms in the coupled equations or their equivalent suggests that even for a simple, single determinant description of  $\Phi_i$  in Eq. 1.16, if for some reason elements of the  $Q$ -space terms are unstable with respect to basis sets, then similar features may be observed in the SMC cross sections. Such features

are, in fact, observed in the cross sections for  $N_2$ ,  $H_2$ , and in some instances, for  $H_2O$ .

The net effect of either numerical inaccuracy (which should only occur in extreme cases), poor linear dependency properties of the orbitals constituting the determinants in Eq. 1.9, failure of the separable potential as discussed in [12] and hence nearly singular  $A^{(+)}$ , or poor convergence behavior arising from some as yet undetermined intrinsic properties of the  $A^{(+)}$  operator in Eq. 1.5 connected to the  $\hat{H} - a(P\hat{H} + P\hat{H})$  terms is contamination of the inhomogenous solution of Eq. 1.5 with the homogenous solution, *i.e.*,

$$A^{(+)}\gamma_m^{(+)} = 0 \quad (1.24)$$

The question of the existence of such a solution has been considered in detail. One aspect of the arguments given to prove that in fact there is no non-null  $\gamma^{(+)}$  present in the SMC method concerns the spectrum of  $A^{(+)}$ . Although it is true that in theory the  $A^{(+)}$  operator has a well-defined inverse, experience with multichannel calculations indicates, for the reasons given above, that numerically this is effectively not true in some cases. Further, the anticipated improvement in the behavior of the operator with increasing basis set size and number of elements in the expansion 1.9 has not been realized [1,2]. In fact, the opposite behavior is more commonly observed.

In light of all of the aspects of the application of the SMC to multichannel problems considered above, it must be noted that evaluating Eq. 1.7 for large-scale, multichannel calculations has proven to be much more difficult than could have been foreseen from initial, promising applications of the method. Simply put, convergence of computed cross sections at the multichannel level of approximation

has not been obtainable for most electronic excitations via direct use of Eq. 1.7 despite numerous improvements introduced to evaluate matrix elements of  $A^{(+)}$  more accurately. Indeed, although beneficial in that they removed questions concerning the convergence properties of earlier techniques, the computationally intensive nature of these improvements is such that it was not until high performance parallel computers became available that the extent of the effort needed to obtain reasonable results from Eq. 1.7 was fully appreciated. With vector machines such as CRAYs, the turnaround time for a calculation was such that only a small number of progressively larger basis sets could be realistically considered. Anomalous results were then easy to attribute to lack of flexibility in the basis, explanations for high energy pseudoresonances being sought for instance, in the spectrum of  $H_{N+1}$ . Considering the basis set size requirements of other theoretical methods employing  $L^2$  descriptions of the scattering electron wave function and continuum, this seemed sensible. The much greater computational power of machines such as the INTEL Delta computer have permitted repetition of large-scale multichannel calculations with many basis sets, thus revealing the instability of Eq. 1.7 at the multichannel level, and the fallaciousness of earlier notions concerning basis set size.

#### 1.3.4 Application of SVD

Very fortunately, a procedure has been found [30] that allows for the extraction of physically realistic cross sections from the elements of the variational functional 1.7 via the matrix form, Eq. 1.10. The procedure involves applying singular value decomposition (SVD) to the matrix  $A^{(+)}$ , a technique usually effective for dealing with ill-conditioned sets of linear equations. Given this, the decomposition

algorithm computes matrices  $\mathbf{U}$ ,  $\mathbf{V}$ , and a diagonal weight matrix  $\mathbf{W}$  such that

$$\mathbf{A}^{(+)} = \mathbf{U}\mathbf{W}\mathbf{V}^T \quad (1.25)$$

The steps used in applying the method are discussed in [26]. Basically, the right-most columns of the orthonormal  $\mathbf{V}$  matrix will correspond to the vectors spanning the theoretically nonexistent homogenous solution space  $\gamma^{(+)}$  (Eq. 1.24). By classifying these vectors by symmetry, the spurious resonances appearing in different symmetry components of the cross section can be improved without affecting the other symmetries. Thus, although tedious in practice, one can gradually remove unphysical resonances by judicious selection of the weights in  $\mathbf{W}$  to set to zero. The processed  $A^{-1}$  matrix is then computed by the standard operation [26]

$$\mathbf{A}^{-1} = \mathbf{V}\mathbf{W}^{-1}\mathbf{U}^\dagger \quad (1.26)$$

This classification scheme also permits removal of those vectors which transform in a symmetry not spanned by the set of orbitals  $\phi$  used in Eq. 1.9. This resolves problems discussed earlier concerning the quadrature scheme for the  $VG_P^{(+)}V$  term.

It should be noted that in some instances the SVD fails to converge. It was found that this can be corrected by one of two means. Either the ground state of the target is shifted slightly, or one can compute the column norms of  $A^{(+)}$ , *i.e.*, the norms discussed in connection with typical matrix element values of  $A^{(+)}$  and remove the columns for which these are less than  $\sim 0.001$ . Having removed the corresponding rows of  $A^{(+)}$  and of the vectors  $\mathbf{b}$  in Eq. 1.10, the SVD subroutine works and cross sections can be computed. Note that these two procedures are related in that the first corrects the problems associated with columns and rows with small norms, *i.e.*, columns of zeros, by adding a small constant (but large with

respect to the unaltered matrix element values) to many matrix elements in each column of  $A^{(+)}$ .

The importance of this SVD procedure in obtaining useful cross sections from the SMC at the multichannel level cannot be overemphasized. Its present application in actuality goes beyond the original intent of the method as a means of removing linear dependencies. Namely, for much multichannel work, many more elements of  $\mathbf{W}$  need to be set to zero than the one or two usually so treated in application of SVD to ill-conditioned sets of equations, based on the values of  $\mathbf{W}$  set to zero.

This being the case, in the following section examples of the current use of the SVD procedure are presented in which its application is described in detail. Each of the examples represents either a different type of pseudoresonance observed in cross sections obtained by direct evaluation of the SMC Eq. 1.10, or a situation in which SVD allows physically reasonable cross sections to be recovered from otherwise unsatisfactory SMC cross sections.

### 1.3.5 Examples of Pseudoresonances

As is evident from results such as those given in Figs. 1.3, 1.7, and 1.8, straightforward application of the SMC to multichannel problems has proven to yield unstable cross sections. Although the difficulties encountered in multichannel studies have not been fully resolved, the SVD procedure outlined above has served to mitigate the problem. Four distinct cases have been selected to illustrate both the types of anomalous results obtained by application of the SMC to multichannel problems and the implementation of corrective steps to retrieve physically meaningful cross

sections by use of SVD.

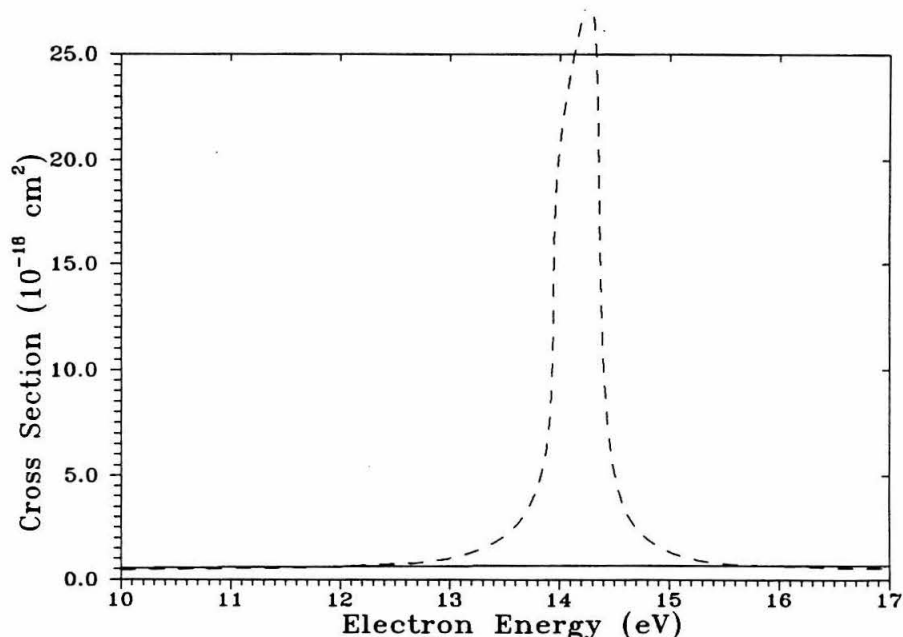


Figure 1.13. Pseudoresonance observed in the  ${}^2\Sigma_g$  component of the excitation cross section for the  $X^1\Sigma_g^+ \rightarrow A^3\Sigma_u^+$  transition of  $N_2$  for one basis set. The solid line indicates the results of application of SVD, dashed line is obtained directly from evaluation of Eq. 1.10.

One of the easiest anomalous resonances to deal with is illustrated in Figs. 1.13–1.15. The feature depicted was observed in the  ${}^2\Sigma_g$  component of the scattering amplitude of a multichannel study of  $N_2$  using a large 83 function basis. As would be expected, the resonance, centered at  $\sim 14.25$  eV appears most prominently in the inelastic  $X^1\Sigma_g^+ \rightarrow A^3\Sigma_u^+$  channel as shown in Fig. 1.13. Nonetheless, the feature also is evident against the large, nonresonant component in the ground state elastic (Fig. 1.14), and the excited state elastic  $A^3\Sigma_u^+ \rightarrow A^3\Sigma_u^+$  (Fig. 1.15) channels. In this latter instance, only the contribution of the doublet space to this cross section is reported. It should be noted that no closed channel excitations were included in

the expansion of  $\Psi_m^{(+)}$  (Eq. 1.9) in these calculations.

As previously discussed, the eigenvalues and eigenvectors of the  $H_{N+1}$  operator spanning the  ${}^2\Sigma_g$  component of  $\Psi_m^{(+)}$  were examined to ascertain whether the feature could possibly be associated with a core excited shape resonance, or other physically

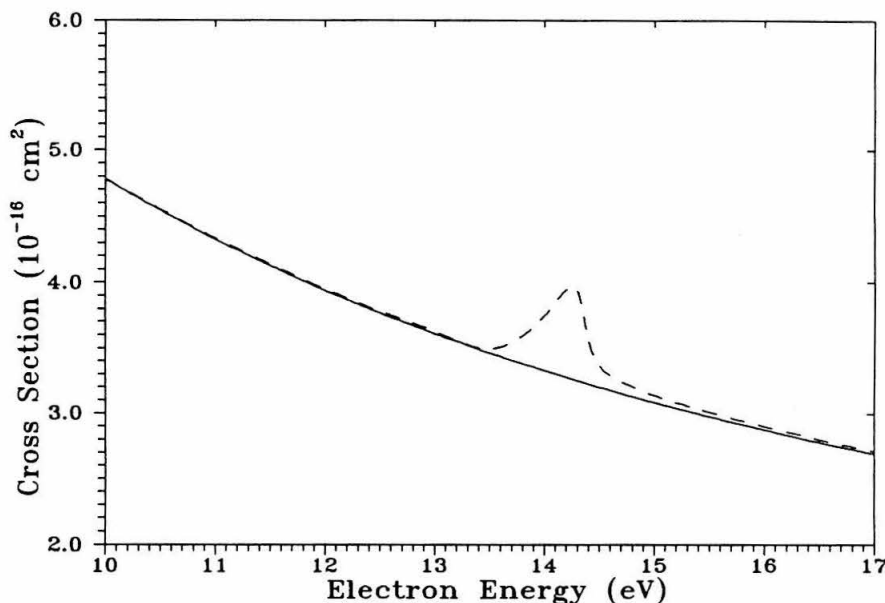


Figure 1.14. Pseudoresonance observed in the  ${}^2\Sigma_g$  component of the excitation cross section for the  $X^1\Sigma_g^+ \rightarrow X^1\Sigma_g^+$  transition of  $N_2$  for the same basis set as in Fig. 1.13. The same notation for the plotted curves as that for Fig. 1.13 is used.

plausible resonance mechanism. In this case, eigenvalues of 10.02, 15.25, and 15.86 eV (with respect to the ground state of  $N_2$ ) were found. The first, upon examination of its corresponding eigenvector, was found to be of  ${}^2\Delta_g$  symmetry and hence could not contribute to a feature present in the  ${}^2\Sigma_g$  symmetry component of the scattering

amplitude. The 15.25 eV eigenvalue was likewise found to be a quartet  $^4\Sigma_g^+$  solution and hence also could play no role in the observed feature. The 15.86 eV eigenvalue was of  $^2\Sigma_g^+$  symmetry and hence could in principle be associated with this feature, although a  $\sim 1.6$  eV energy shift away from the location of the resonance makes this rather implausible. The principle components of the particular vector are the  $[1\pi_{u,x} \rightarrow 1\pi_{g,x}](5\sigma_u)$  and  $[1\pi_{u,y} \rightarrow 1\pi_{g,y}](5\sigma_u)$  excited state determinants.

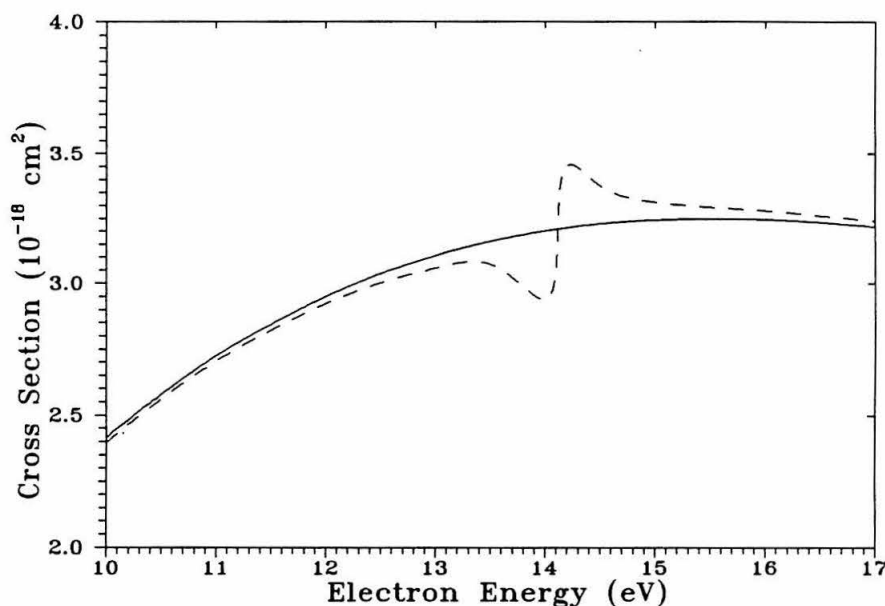


Figure 1.15. Pseudoresonance observed in the  $^2\Sigma_g$  component of the excitation cross section for the  $A^3\Sigma_u^+ \rightarrow A^3\Sigma_u^+$  transition of  $N_2$  for the same basis set as in Figs. 1.13 and 1.14. The same notation for the plotted curves as that for Fig. 1.13 is used.

The source of the resonance is most clearly revealed by tracking the condition number for the  $A^{(+)}$  matrix in Eq. 1.10 as one passes through the resonance region. These are listed in Table 1.5. Clearly, this rapid increase by a factor of  $\sim 20$  indicates a problem. However, verification of the accuracy with which the inverse is computed

results in a matrix not differing significantly (in terms of the accuracy required in these studies indicated earlier) from the unit matrix ( $\sim 10^{-8}$ ) near the 14.25 eV resonance location. Having classified the vectors of  $\mathbf{V}$  (Eq. 1.25) by symmetry, the

Table 1.5. Condition Numbers for  $A^{(+)}$  for the  ${}^2\Sigma_g^+$  Symmetry Block of  $N_2$

Incident Energy	Condition Number( $\times 10^7$ )
10.0	0.12
11.0	0.15
12.0	0.22
13.0	0.39
13.5	0.68
14.0	2.4
14.25	2.8
14.5	1.2
14.75	0.69
15.0	0.49
16.0	0.22

smallest element of  $\mathbf{W}$  corresponding to  ${}^2\Sigma_g$  symmetry was set to zero. Repeated application of this procedure over the scattering energies used results in a cross section indicated by the solid curves in Figs. 1.13-1.15. Removal of a single  ${}^2\Sigma_g^+$  column in  $\mathbf{V}$  thus cleanly removes the pseudoresonance feature in all channels. Examination of this vector shows its composition from 13.0 to 15.0 eV incident electron energy remains unchanged except for a change of phase near the resonance (Table 1.6). Clearly the composition of this column vector is quite different from the 15.86 eV eigenvector of the  $\hat{H}_{N+1}$  operator. Hence, one could assume with reasonable

confidence that this resonance results from a failure of the separable potential approximation (Eq. 1.11) and not as a consequence of a physically realistic, resonant state.

Pseudoresonance features such as this example appear regularly at intermediate (10–20 eV incident electron energy range) energies in multichannel studies of both linear and nonlinear molecules, generally being 1 to 2 eV in width. They are cleanly removed by the SVD procedure as discussed above in which the smallest element of the  $\mathbf{W}$  matrix of Eq. 1.25 corresponding to the symmetry in which the resonance appears is removed. For doubly degenerate symmetries a pair of vectors is removed. The corresponding vectors of  $\mathbf{V}$  in Eq. 1.25 thus removed do not correlate with eigenvectors of  $H_{N+1}$  associated with eigenvalues near the location of the pseudoresonance. Hence, in these instances it would seem the SVD procedure is being employed in a manner for which it is intended, namely to remove those vectors which are numerically indistinguishable from the homogenous solution of Eq. 1.5 or lead to an essentially singular  $\mathbf{V}^{-1}$ .

Table 1.6. Composition of the Column of  $\mathbf{V}$  Removed by SVD

Incident Energy	Principle Components
13.0	-0.8 [O](4 $\sigma_g$ ) +0.5[O](5 $\sigma_g$ ) +0.1[O](6 $\sigma_g$ ) +0.1[O](8 $\sigma_g$ )
14.0	-0.8 [O](4 $\sigma_g$ ) +0.5[O](5 $\sigma_g$ ) +0.1[O](6 $\sigma_g$ ) +0.1[O](8 $\sigma_g$ )
14.25	0.8 [O](4 $\sigma_g$ ) -0.5[O](5 $\sigma_g$ ) -0.1[O](6 $\sigma_g$ ) -0.1[O](8 $\sigma_g$ )
14.5	0.8 [O](4 $\sigma_g$ ) -0.5[O](5 $\sigma_g$ ) -0.1[O](6 $\sigma_g$ ) -0.1[O](8 $\sigma_g$ )
15.0	-0.8 [O](4 $\sigma_g$ ) +0.5[O](5 $\sigma_g$ ) +0.1[O](6 $\sigma_g$ ) +0.1[O](8 $\sigma_g$ )

A second feature frequently encountered in multichannel SMC studies is typi-

fied by the structures seen in Figs. 1.16–1.19. In this example, results of a multi-channel study on  $N_2$  using a 74 function basis indicate a broad, physically implausible resonance-like feature centered near 27 eV incident electron energy in the

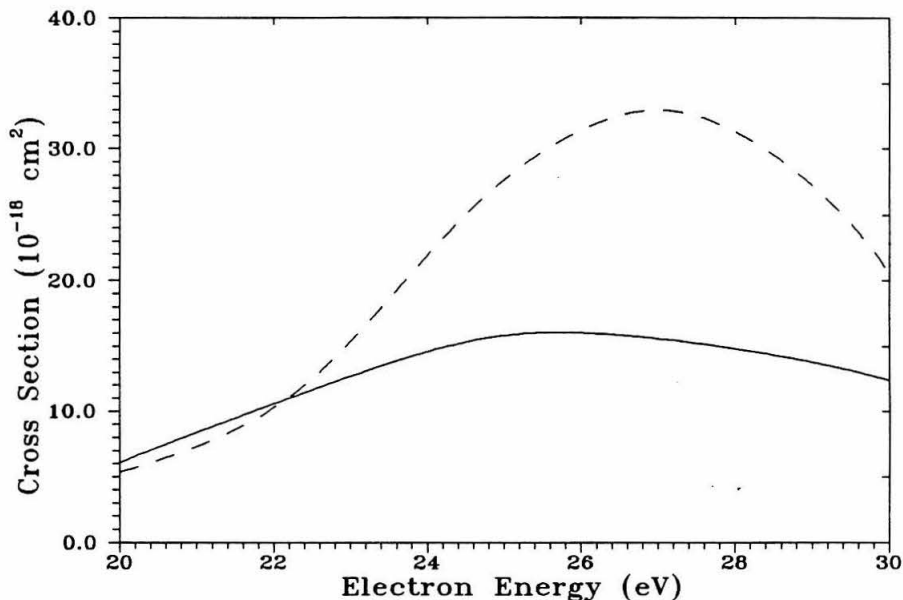


Figure 1.16. High energy pseudoresonance observed in the  ${}^2\Pi_u$  component of the excitation cross section for the  $X^1\Sigma_u^+ \rightarrow W^3\Delta_u$  transition of  $N_2$  for a 74 function basis. The same notation for the plotted curves as that for Fig. 1.13 is used.

$X^1\Sigma_g \rightarrow W^3\Delta_u$  channel (Fig. 1.16). This is associated with the recorelation terms discussed earlier. Less prominent structure is also seen in the  $X^1\Sigma_g \rightarrow A^3\Sigma_u^+$  channel (Fig. 1.17), although a peak is not observed. The elastic scattering in the ground state (Fig. 1.18) and  $W^3\Delta_u \rightarrow W^3\Delta_u$  (Fig. 1.19) channels also reveal weak, broad features around 27 eV. Although one could reason that this behavior is just like that previously discussed, but displaced to higher energies and hence involving

broader peaks, some aspects of these features indicate otherwise.

Unlike the behavior of the condition number for  $A^{(+)}$  cited in the previous example, there is no distinct increase in this parameter in passing through the 25 to 30 eV impact energy range. In addition, in contrast to the  ${}^2\Sigma_g$  resonance, there tend

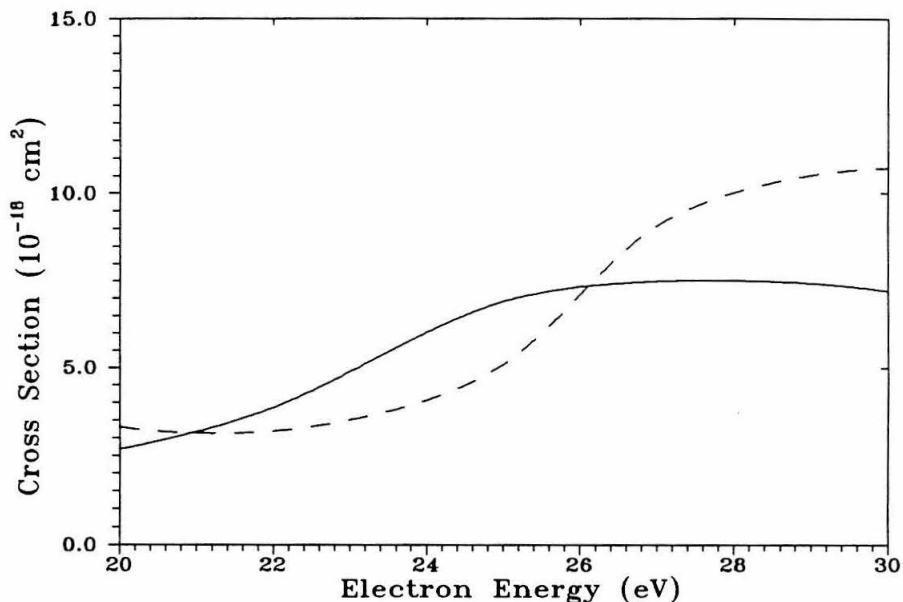


Figure 1.17. High energy behavior observed in the  ${}^2\Pi_u$  component of the excitation cross section for the  $X^1\Sigma_u^+ \rightarrow A^3\Sigma_u^+$  transition of  $N_2$  for a 74 function basis. The same notation for the plotted curves as that for Fig. 1.13 is used.

to be several vectors of  $\mathbf{V}$  in Eq. 1.25 associated with small  $w$  diagonal elements in  $\mathbf{W}$  with the symmetry in which the feature is observed – in this instance  ${}^2\Pi_u$ . Unfortunately, for these broad peaks the spectrum of the  $H_{N+1}$  operator is less informative, especially for modest and large basis sets. The eigenvalues falling in the energy range of interest and their spin and symmetry assignments are presented in

Table 1.7. The null space vectors of  $\mathbf{V}$  removed in order to reduce the highly unphysical resonance, although involving predominately the same type  $[1\pi_u \rightarrow 1\pi_g](n\pi_g)$  determinants as those constituting the eigenvalues of  $\hat{H}_{N+1}$  in the table, are built on  $\pi_g$  orbitals different from those of the Hamiltonian eigenvectors. Again, the correlation between the eigenvectors of  $\hat{H}_{N+1}$  and the null space, although greater than in the first example, is still weak.

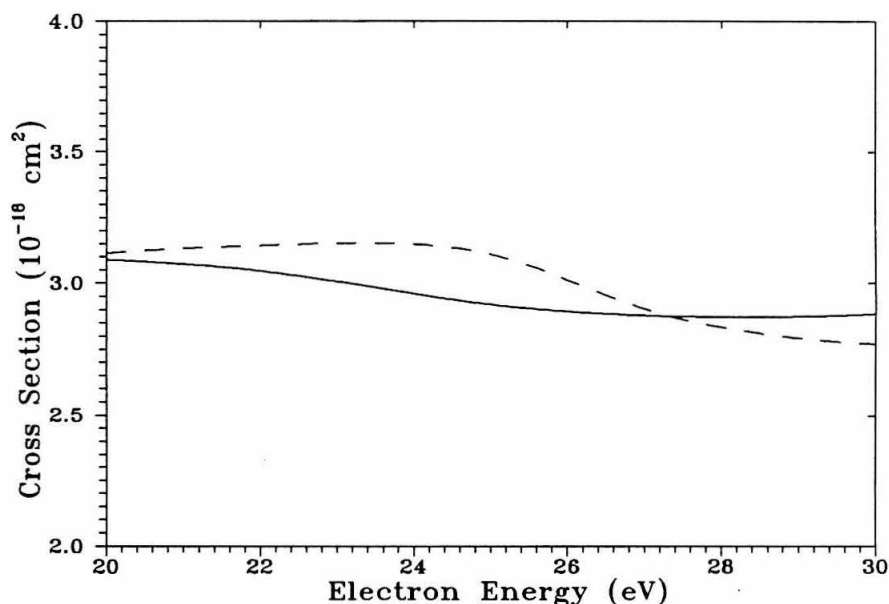


Figure 1.18. High energy behavior observed in the  ${}^2\Pi_u$  component of the elastic cross section for  $\text{N}_2$  using the same 74 function basis set as in Figs. 1.16 and 1.17. The same notation for the plotted curves as that for Fig. 1.13 is used.

Thus, this second application of the SVD procedure seems to be justified on the same grounds as for the narrower peaks observed at lower energies in the inelastic channels, namely the fact that some vectors of  $\mathbf{V}$  are effectively indistinguishable from the homogenous solutions of Eq. 1.5 despite the fact that this is not clearly

indicated by the size of the weights in the  $\mathbf{W}$  matrix. Unfortunately, the resulting cross sections still show rather unusual energy dependencies uncharacteristic of the  $1/E$  behavior of inelastic, optically forbidden transitions.

Table 1.7. Eigenvalues of  $H_{N+1}$  for the  ${}^2\Pi_u$  Symmetry Component of  $N_2^-$

Energy above $X^1\Sigma_g^+$ (eV)	Spin/Symmetry
25.23	${}^4\Pi_u$
26.20	${}^2\Pi_u$
26.42	${}^4\Pi_u$
27.82	${}^4\Pi_u$
28.48	${}^2\Phi_u$
29.92	${}^2\Pi_u$
32.12	${}^2\Pi_u$

A third example of the use of SVD to compensate for the instability inherent in SMC multichannel studies is given by results of a seven-state calculation for  $H_2$  involving coupling of the  $X^1\Sigma_g^+$ ,  $(E, F)^1\Sigma_g^+$ ,  $a^3\Sigma_g^+$ ,  $B^1\Sigma_u^+$ ,  $b^3\Sigma_u^+$ ,  $C^1\Pi_u$ , and  $c^3\Pi_u$  states. In particular, the  ${}^2\Delta_u$  component of the  $X^1\Sigma_g \rightarrow a^3\Sigma_g^+$  is much too large to be physically realistic, *viz.*  $\sim 30$  times greater than for two- and five-state calculations. The cross sections for the other channels, particularly the ground state elastic channel, are also significantly greater. Unlike the previous examples, this behavior is observed for a variety of basis sets indicating convergence to a highly unphysical cross section. No recorelation terms are present in this symmetry block. Figure 1.20 depicts the  $X^1\Sigma_g \rightarrow a^3\Sigma_g^+$  cross section in the  ${}^2\Delta_u$  symmetry for two basis sets. The corresponding cross section in the ground state elastic cross section

is depicted in Fig. 1.21. The long dashed line in both figures indicates results for a five-channel ( $X^1\Sigma_g$ ,  $a^3\Sigma_g^+$ ,  $b^3\Sigma_u^+$ ,  $c^3\Pi_u$ ) calculation. A partial wave analysis indicates that the peak near 15 eV observed in the  $X^1\Sigma_g \rightarrow a^3\Sigma_g^+$  is not due to unphysical contributions from high partial waves.

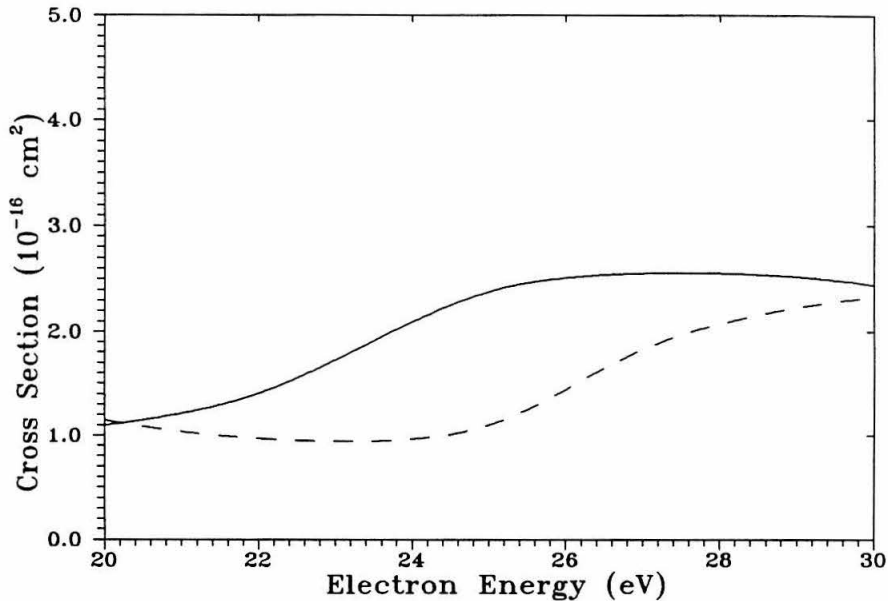


Figure 1.19. High energy behavior observed in the  ${}^2\Pi_u$  component of the excitation cross section for the  $W^3\Delta_u \rightarrow W^3\Delta_u$  transition of  $N_2$  for a 74 function basis. The same notation for the plotted curves as that for Fig. 1.16 is used.

Fortunately, due to the availability of experimental cross sections and reliable theoretical results from the complex Kohn method, we know *a priori* approximately what cross section values to expect. Clearly, the  ${}^2\Delta_u$  component alone greatly exceeds experimental cross sections and theoretical values at all except the highest energies considered.

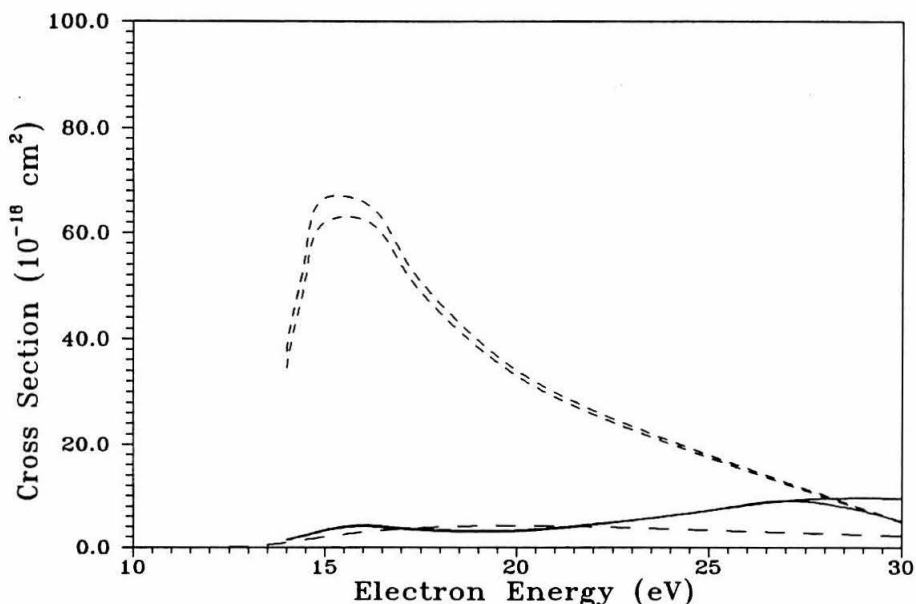


Figure 1.20.  ${}^2\Delta_u$  component of the excitation cross section of the  $X^1\Sigma_g \rightarrow a^3\Sigma_g^+$  transition for  $\text{H}_2$  for a seven state calculation. The short dashed lines indicate results obtained directly from Eq. 1.7, solid lines those with SVD processing. The long dashed line indicates results of a five channel calculation. Results for two basis sets are plotted.

As with previous examples, the computed  $A^{(+)}$  matrix is treated by SVD and the column vectors of  $\mathbf{V}$  labeled by symmetry. In this case, however, the  ${}^2\Delta_u$  component of  $A^{(+)}$  shows no sign of being ill-conditioned (*e.g.*, condition number  $\sim 1.4$ ), hence SVD is technically not warranted. Nonetheless, by selective deletion of columns transforming as  ${}^2\Delta_u$  from  $\mathbf{V}$ , we can recover the original, more physically reasonable results of the five-channel studies. The solid lines in Fig. 1.20 indicate the processed  $X^1\Sigma_g \rightarrow a^3\Sigma_g^+$  cross sections. Likewise, the solid lines in Fig. 1.21 show the improved cross sections for the ground state elastic channel. The well conditioned property of the  ${}^2\Delta_u$  component of  $A^{(+)}$  is apparent in the weights of the  $\mathbf{W}$  matrix being set to zero. For the particular basis set considered here, these

values are 0.30434 and 0.13769. However, for the purposes of this work, as the normalization of the  $A^{(+)}$  matrix can be chosen arbitrarily, these weights are only important in that they are the smallest for the  ${}^2\Delta_u$  component. As the goal is to remove the vectors of  $\mathbf{V}$  most heavily contaminated by the homogenous solution  $\gamma^{(+)}$ , the magnitudes of the weight values of  $\mathbf{W}$  are not directly relevant.

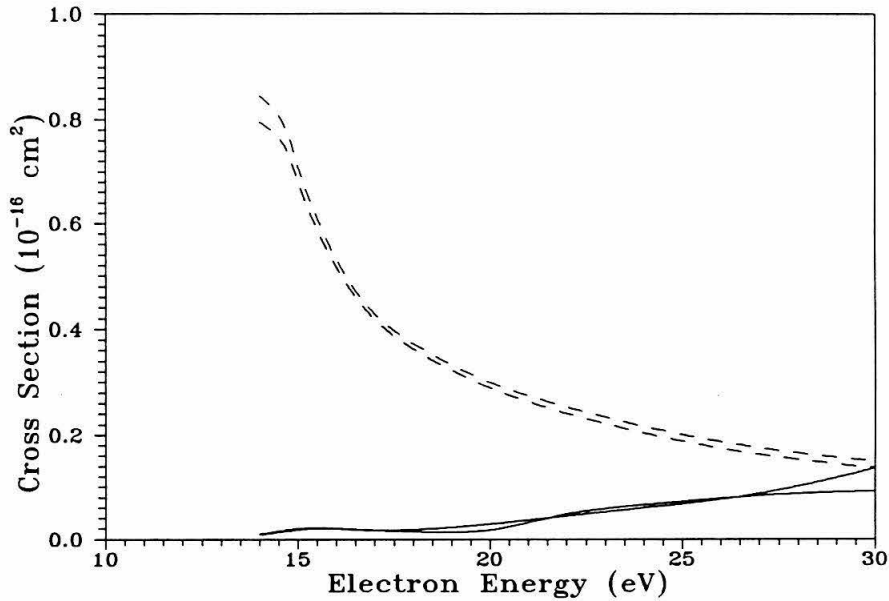


Figure 1.21.  ${}^2\Delta_u$  component of the elastic cross section corresponding to the excitation cross section of Fig. 1.20. Dashed lines indicate results obtained directly from Eq. 1.10, solid lines those with SVD processing.

An examination of the vectors removed from  $\mathbf{V}$  reveals the principle components of the two degenerate pairs of columns removed to be

$$\text{I. } [1\sigma_g \rightarrow 1\sigma_u](1\delta_{g,xy}); [1\sigma_g \rightarrow 1\pi_{ux}](1\pi_{gy}); [1\sigma_g \rightarrow 1\pi_{uy}](1\pi_{gx})$$

$$\text{II. } [1\sigma_g \rightarrow 1\sigma_u](1\delta_{g,x^2-y^2}); [1\sigma_g \rightarrow 1\pi_{ux}](1\pi_{gx}), (2\pi_{gx}); [1\sigma_g \rightarrow 1\pi_{uy}](1\pi_{gy}), (2\pi_{gy})$$

The dominant component of  $I$  is the  $[1\sigma_g \rightarrow 1\sigma_u](1\delta_{g,xy})$  determinant. There is no experimental evidence for a core-excited shape resonance of this structure. Column II is more ambiguous as all of the listed determinants contribute approximately equally. Nonetheless, as the resulting cross sections are so greatly improved by the removal of all four columns of  $V$ , the procedure is justified on physical grounds.

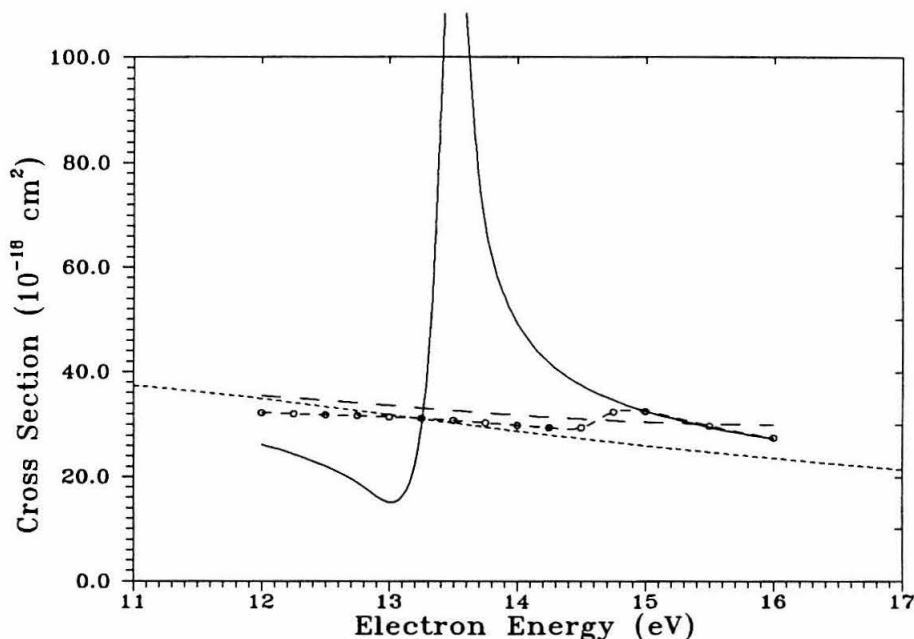


Figure 1.22. Pronounced pseudoresonance in the  ${}^2\Pi_g$  component of the  $X^1\Sigma_g \rightarrow B^3\Pi_g$  excitation cross section for  $N_2$  at the two state approximation. Solid line represents results of directly from Eq. 1.7; dashed line with circles, results when two vectors of  $V$  are deleted; long dashed line, results when six vectors of  $V$  are removed. The short dashed line indicates results for a basis set in which the resonance was not observed.

As a final example, a resonance feature appearing in a variety of basis sets for  $N_2$  is depicted in Figs. 1.22–1.24. The position of this peak varies over a range of 5 eV depending on the basis selected. Unlike the other resonance-like structures

discussed, the nature of this type of behavior is quite different and more difficult to handle.

Figure 1.22 depicts the cross section in the inelastic  $X^1\Sigma_g \rightarrow B^3\Pi_g$  channel. The peak at  $\sim 13.75$  eV is very sharp and almost five times greater than the nonresonant background obtained using other basis sets (short dashed line). There is no experimental evidence for a resonance of this symmetry so high above the  $B^3\Pi_g$  threshold (7.4 eV). Figures 1.22 and 1.23 show the behavior in the elastic  $X^1\Sigma_g \rightarrow X^1\Sigma_g$  and  $B^3\Pi_g \rightarrow B^3\Pi_g$  channels. The resonance is prominent in the former case, while in the latter, the steeply dropping nonresonant background serves to diminish its prominence in the  $B^3\Pi_g \rightarrow B^3\Pi_g$  channel. Included in Fig. 1.24 are both the resonant and nonresonant parts in the  $^2\Pi_g$  component of the cross section. The solid line indicates the resonant  $^2\Pi_g^+$  part while the dashed+square line indicates the much smaller, nonresonant contribution of the  $^2\Pi_g^-$  symmetry. This will be readily understandable in terms of the nature of the resonance, which is characterized by a dominant  $[3\sigma_g \rightarrow 1\pi_g](4\sigma_g)$  electronic configuration.

The appearance of this resonance may at first seem analogous to features observed in a Feshbach resonance study carried out using the SMC method [27]. However, in that study, both open and closed channel excitations were employed to study their effects on the elastic channel and open inelastic channel cross sections. In contrast, the cited example is a simple, two-state calculation involving no closed channel excitations. There are also no closed channel singlet terms (recorrelation terms) present in the dynamically interesting  $^2\Pi_g$  symmetry. Only the  $[O](1\pi_{g(x,y)})$  is present as a recorrelation term. Nonetheless, the SMC consistently “finds” such features in certain symmetries of  $N_2$  and in other molecules. Similar behavior is observed in the cross section for the  $X^1\Sigma_g \rightarrow b^3\Sigma_u^+$  transition in  $H_2$  when additional

scattering functions are included in the scattering basis.

The behavior of the condition number for  $A^{(+)}$  also indicates that this feature is qualitatively different from that observed in the 84 function  ${}^2\Sigma_g$  example first cited. Note that although there is a minimum in the condition number near the location of the resonance ( $\sim 13.5$  eV), the rise is not nearly as rapid nor as pronounced as in the first example. Comparison of the magnitudes of the condition numbers in this table and those in Table 1.5 indicates that the appearance of these resonance features is not dependent on an absolute, but relative, magnitude of the diagonal elements of  $\mathbf{W}$  in Eq. 1.25.

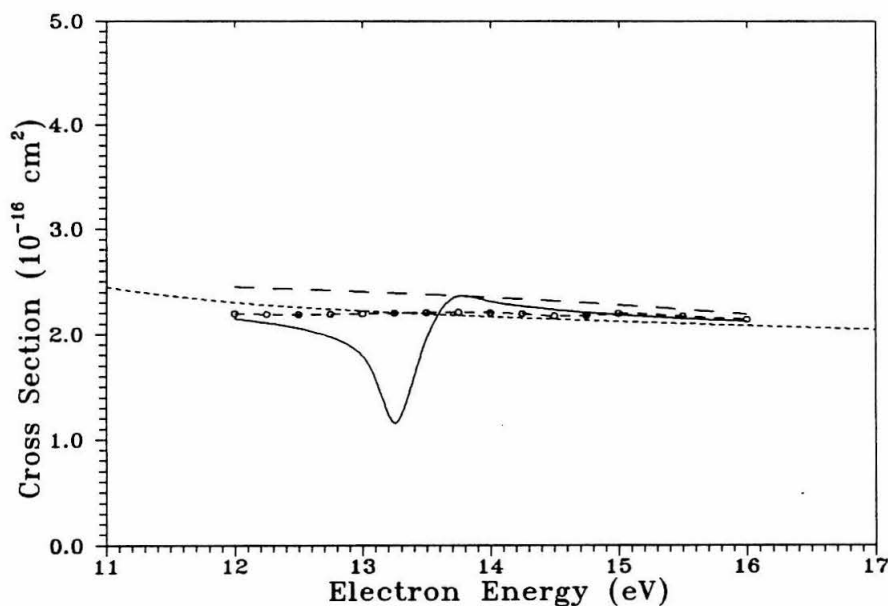


Figure 1.23. Pseudoresonance in the elastic scattering cross section of  $\text{N}_2$  corresponding with the feature depicted in the inelastic channel in Fig. 1.22. The same notation as in Fig. 1.22 is used.

Table 1.8 Condition Numbers for  $A^{(+)}$  for  ${}^2\Pi_g^-$  of  $N_2$ .

Incident Energy	Condition Number( $\times 10^3$ )
12.0	2.8
13.0	6.7
13.25	13.0
13.5	15.0
13.75	6.1
14.0	3.5
15.0	1.5
16.0	1.5

Consideration of the  ${}^2\Pi_g$  component of the  $H_{N+1}$  spectrum for the modest-sized basis used in this example reveals some interesting aspects of the structure observed in all channels. In the energy range of concern there are three eigenvalues of 13.88, 14.16, and 15.33 eV taken with respect to a zero energy ground electronic state. The 14.16 eV level is associated with the  ${}^4\Pi_g$  space and need not be considered further. The 13.88 eV pair of eigenvectors are dominated by contributions from the  $[O](2\pi_{g(x,y)})$  and  $[3\sigma_g \rightarrow 1\pi_{g(x,y)}](4\sigma_g)$  determinants, the elastic component being dominant. The 15.33 eV doublet pair is similar in that its primary components are the configurations  $[O](2\pi_{g(x,y)})$  and  $[3\sigma_g \rightarrow 1\pi_{g(x,y)}](4\sigma_g)$ , this time the latter configuration making the dominant contribution. The possibility that this effect is a consequence of treating the  $3\sigma_g \rightarrow 4\sigma_g$  excitation as a closed channel when it is energetically open was checked by carrying out a SCF calculation using the frozen single particle functions originally optimized for the  $3\sigma_g \rightarrow 1\pi_g$  excitation. Here, the threshold for the triplet  $[3\sigma_g \rightarrow 4\sigma_g]$  excitation is at 15.76 eV, the singlet falling at 16.57 eV. Both values are positioned well above the 13.5 eV position of the

resonance. This arrangement of energies would indicate that if a pseudo-Feshbach resonance were to be responsible for the structure, it would more likely be located near the 15.33 eV eigenvalue. It is this eigenvector which most closely mocks the energetics giving rise to true Feshbach resonances.

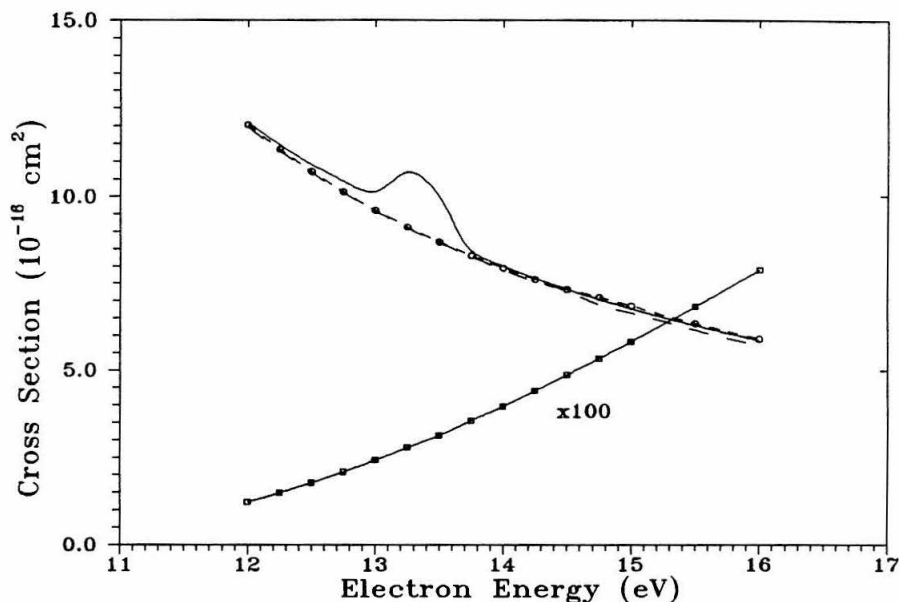


Figure 1.24. Pseudoresonance in the elastic  $B^3\Pi_g \rightarrow B^3\Pi_g$  cross section of  $N_2$  corresponding with the feature depicted in the inelastic channel in Fig. 1.22. Note that here only the doublet space of  $\Psi_m^{(+)}$  is included. Quartet contributions to the cross section are not considered. The small, nonresonant  $^2\Pi_g^-$  contribution is indicated by the solid+squares line, otherwise the same notation as in Fig. 1.22 is used.

It should be noted that the configuration  $[3\sigma_g \rightarrow 1\pi_g](4\sigma_g)$  lacks some important characteristics of those configurations typically associated with Feshbach resonances, as for example the  $[3\sigma_g 4\sigma_g^2]$  configuration responsible for the prominent 11.48 eV resonance observed in the electronic excitation spectrum of  $N_2$  [28]. First, almost all cases of such Feshbach or core-excited resonances involve a Rydberg par-

ent state with the additional electron then occupying a diffuse Rydberg orbital as well. In the case under consideration, however, the  $[\sigma_g \rightarrow 1\pi_g]$  excitation is valence in character. Secondly, there is no experimental evidence for a valence excited state of  $N_2$  supporting (*i.e.*, serving as a parent) a Feshbach resonance. Hence, it would seem unreasonable to attribute the resonance observed in these SMC results to a Feshbach resonance mechanism.

Finally application of SVD to the calculation of  $A^{(+)}$  further distinguishes this structure from that seen in previous examples. Examination of the different curves plotted in Fig. 1.22 corresponding to removal of different numbers of the total of 18 columns of  $\mathbf{V}$  in Eq. 1.26 transforming as  ${}^2\Pi_g$  reveals the problem. Namely, in contrast to the other cases where removal of the smallest vector or pair of columns for nondegenerate symmetries is sufficient, only by zeroing out many elements of  $\mathbf{W}$  is reasonable behavior, *i.e.*, resemblance to the nonresonant cross section for the inelastic channel observed using other basis sets. This is accomplished at the expense of deterioration of the quality of results in other channels. An explanation for this behavior can be found by examining the components of the columns being removed by the SVD procedure. The pair associated with the smallest diagonal elements  $w$  have approximately equal contributions from the  $[O](2\pi_g)$ ,  $[3\sigma_g \rightarrow 1\pi_g](4\sigma_g)$ ,  $[3\sigma_g \rightarrow 1\pi_g](5\sigma_g)$ ,  $[3\sigma_g \rightarrow 1\pi_g](6\sigma_g)$ , and  $[3\sigma_g \rightarrow 1\pi_g](7\sigma_g)$  confirmation. Assuming that this structure is in fact associated with the 13.88 eV state found in diagonalizing the  $H_{N+1}$  operator, it is clear that the SVD procedure is not effective at eliminating its spurious influence on the cross sections in the inelastic channel.

Experience has shown that the best approach to resolving questions concerning spurious resonances such as this is to employ many different basis sets. Over any particular range of energies, most basis sets exhibit nonresonant behavior. The

results of any set yielding such pseudoresonances can then be disregarded over the energy range significantly influenced by the resonance. By averaging the cross sections obtained from several basis sets, the resulting values appear physically reasonable and converged.

#### 1.4 Conclusions

Application of the SMC method to multichannel problems has not been particularly successful. Direct evaluation of the variational functional Eq. 1.7 yields highly unstable cross sections and poor convergence characteristics for most excitation processes. Three possible reasons for this behavior have been explored. The system of linear equations manipulated in the course of computing cross sections do not appear to be sensitive to purely numerical inaccuracy such as round-off error or inaccuracy in matrix inversion procedures. Rather, the two principle sources of instability of the method are 1), the breakdown of the separable potential approximation; and 2), the difficulty in evaluating  $A^{(+)}$  for  $\Psi_m^{(+)}$  matrix elements involving determinants of multiple parentage. The first problem is successfully addressed by application of an SVD procedure. The instability arising from the second problem may eventually be resolved by modification of the action of the projector operator in  $A^{(+)}$ , although its shortcomings can be partially mitigated by use of SVD as well, as demonstrated by the cited examples.

#### References

- [1.] K. Takatsuka and V. McKoy, Phys. Rev. A, **30**(4), 1734 (1984).
- [2.] K. Takatsuka and V. McKoy, Phys. Rev. A, **24**(5), 2473 (1981).

- [3.] K. Takatsuka and V. McKoy, *Phys. Rev. A*, **30**(5), 2799 (1984).
- [4.] K. Takatsuka and V. McKoy, *Phys. Rev. A*, **23**(5), 2352 (1981); *Ibid.*, p. 2359.
- [5.] S. Geltman, *Topics in Atomic Collision Theory* (Academic Press, New York, 1969), pp. 95–103.
- [6.] A. L. Zubarev, *Sov. J. Nucl. Phys.* **23**(1), 40 (1976).
- [7.] D. J. Ernst, C. M. Shakin, R. M. Thaler, and D. L. Weiss, *Phys. Rev. C* **8**(6), 2056 (1973); **8**(1), (1973).
- [8.] A. L. Zubarev, *Sov. J. Nucl. Phys.* **7**(2), 215 (1976); **9**(2), 188 (1978).
- [9.] A. L. Zubarev and M. M. Musakhanov, *Sov. J. Nucl. Phys.* **23**(1), 42 (1976).
- [10.] V. B. Belyaev, A. P. Podkopayev, J. Wrzecionko, and A. L. Zubarev, *J. Phys. B* **12**(7), 1225 (1979).
- [11.] P. Lévy and B. Apagyi, *J. Phys. B* **21**, 3741 (1988).
- [12.] C. Winstead and V. McKoy, *Phys. Rev. A* **41**(1), 49 (1990).
- [13.] M. A. P. Lima, PhD. Thesis, California Institute of Technology (1986).
- [14.] B. H. Bransden, R. Hewitt, and M. Plummer, *J. Phys. B* **21**, 2645 (1988).
- [15.] D. H. Oza, *Phys. Rev. A* **30**, 1101(1984).
- [16.] T. L. Gibson, M. A. P. Lima, K. Takatsuka, and V. McKoy, *Phys. Rev. A* **30**(6), 3005 (1985).

- [17.] D. H. Oza and J. Callaway, *Phys. Rev. A* **27**, 2840 (1983).
- [18.] S. E. Branchett and J. Tennyson, *Phys. Rev. Letts.* **64**(2), 2889 (1990).
- [19.] I. H. Sloan and T. J. Brady, *Phys. Rev. C* **6**(3), 701 (1972).
- [20.] M. A. P. Lima, L. M. Brescansin, A. J. R. da Silva, C. L. Winstead, and V. McKoy, *Phys. Rev. A* **41**, 327 (1990).
- [21.] H. S. Taylor and A. U. Hazi, *Phys. Rev. A* **14**(6), 2071(1976).
- [22.] R. K. Nesbet, *Variational Methods in Electron-Atom Scattering Theory* (Plenum, New York, 1980), pp. 106–112.
- [23.] C. E. Fröberg, *Introduction to Numerical Analysis* (Addison-Wesley, Reading, Mass., 1965), p. 86.
- [24.] R. W. Hornbeck, *Numerical Methods* (Quantum, New York, 1975), pp. 100–101.
- [25.] J. H. Wilkinson, *J. ACM* **8**, 281 (1961).
- [26.] W. H. Press, B. P. Flannery, S. A. Teukolsky, and W. T. Vetterling, *Numerical Recipes* (Cambridge University, Cambridge, 1986), pp. 52–58.
- [27.] A. J. R. Da Silva, M. A. P. Lima, L. M. Brescansin, and V. McKoy, *Phys. Rev. A* **41**(5), 2903 (1990).
- [28.] see, for example G. J. Schulz, *Rev. Mod. Phys.* **45**(3), 423 (1973).
- [29.] B. H. Lengsfeld and T. N. Rescigno, *Phys. Rev. A* **44**(5), 2913 (1991).

- [30.] Q. Sun, C. Winstead, and V. McKoy, *Phys. Rev. A* **46**(11), (1992).
- [31.] H. Feshbach, *Ann. Phys.* **19**, 287 (1962). See also H. Feshbach, *Ann. Phys.* **5**, 357 (1958).

## 2. Computation of the Scattering Amplitude

The purpose of this chapter is to briefly describe the computational procedures used to calculate scattering amplitudes and hence the integral and differential cross sections reported in subsequent chapters. For clarity, several of the equations introduced in the first chapter will be repeated here.

The Hamiltonian for a scattering electron colliding with an  $N$ -electron molecule can be written in the form

$$H = (H_N + T_{N+1}) + V = H_0 + V, \quad (2.1)$$

where  $H_N$  is the Hamiltonian of the molecule;  $T_{N+1}$ , the kinetic energy operator of the scattering electron; and  $V$ , the interaction potential between the scattering electron and the molecule. This is equivalent to  $H_{N+1}$  of the previous chapter.

It can be shown ([1] of chap. 1) that the full scattering wave function satisfies the projected Lippmann–Schwinger equation

$$P\Psi_{\Gamma}^{(+)} = S_{k_{\Gamma}} + G_P^{(+)}V\Psi_{\Gamma}^{(+)}, \quad (2.2)$$

and the following inhomogenous equation:

$$A^{(+)}\Psi_{\Gamma}^{(+)} = VS_{k_{\Gamma}}, \quad (2.3)$$

where

$$A^{(+)} = \frac{1}{2}(PV + VP) - VG_P^{(+)}V + \frac{1}{N+1}[\hat{H} - \frac{N+1}{2}(\hat{H}P + P\hat{H})]. \quad (2.4)$$

To avoid confusion with the labeling for the spherical harmonics,  $\Gamma$  has been substituted for  $m$  of chapter 1 as the channel label.  $S_{\mathbf{k}_\Gamma} = \Phi_\Gamma \exp(i\mathbf{k}_\Gamma \cdot \mathbf{r}_{N+1})$  are eigenfunctions of  $H_0$ ,  $\hat{H} = E - H$ ,  $P$  is the projection operator (Eq. 1.3), and  $G_P^{(+)}$  is the projected Green's function with outgoing-wave boundary conditions.

Using Eqs. (2.2) and (2.3), the body-frame scattering amplitude for a fixed molecular orientation in the linear momentum representation can be constructed:

$$f^b(\mathbf{k}_{\Gamma'}, \mathbf{k}_\Gamma) = -\frac{1}{2\pi} (\langle S_{\mathbf{k}_{\Gamma'}} | V | \Psi_\Gamma^{(+)} \rangle + \langle \Psi_{\Gamma'}^{(-)} | V | S_{\mathbf{k}_\Gamma} \rangle - \langle \Psi_{\Gamma'}^{(-)} | A^{(+)} | \Psi_\Gamma^{(+)} \rangle) \quad (2.5)$$

The trial scattering wave functions used in Eq. (2.5) need not satisfy scattering boundary conditions and can be expanded in  $(N+1)$ -electron Slater determinants:

$$\Psi^{(\pm)} = \sum_i a_i^{(\pm)} \chi_i. \quad (2.6)$$

The stationary value of Eq. (2.5) leads to the fractional form for the scattering amplitude

$$f^b(\mathbf{k}_{\Gamma'}, \mathbf{k}_\Gamma) = -\frac{1}{2\pi} \sum_{i,j} \langle S_{\mathbf{k}_{\Gamma'}} | V | \chi_i \rangle (d^{-1})_{ij} \langle \chi_j | V | S_{\mathbf{k}_\Gamma} \rangle, \quad (2.7)$$

where

$$d_{mn} = \langle \chi_m | A^{(+)} | \chi_n \rangle.$$

These are, of course, the matrix elements of the  $A^{(+)}$  matrix, the numerical properties of which were considered in detail in the previous chapter.

In most of the work reported here, Eq. (2.7) is evaluated at a number of Gauss-Legendre quadrature points. In some instances, a simple trapezoidal quadrature is

employed for the azimuthal angle ( $\phi$ ) in order to maintain symmetry properties concerning  $\pi_x$  and  $\pi_y$  orbitals in linear molecules. Interestingly, little loss in accuracy is noted for this cruder quadrature. Having computed Eq. (2.7) at a number of points, integral cross sections can be obtained,

$$\sigma(k_{\Gamma'}, k_{\Gamma}) = \frac{k_{\Gamma'}}{k_{\Gamma}} \int \int |f^b(\mathbf{k}_{\Gamma'}, \mathbf{k}_{\Gamma})|^2 d\hat{\mathbf{k}}_{\Gamma'} d\hat{\mathbf{k}}_{\Gamma}, \quad (2.8)$$

where  $\hat{\mathbf{k}}_{\Gamma'(\Gamma)}$  are directions of the outgoing(incoming) plane waves. Transformation of the scattering amplitude from the linear momentum to the angular momentum representation leads to the partial-wave amplitude in the body-fixed frame,

$$f_{l'm', lm}^b(k_{\Gamma'}, k_{\Gamma}) = \int \int Y_{l', m'}^*(\hat{\mathbf{k}}_{\Gamma'}) f^b(\mathbf{k}_{\Gamma'}, \mathbf{k}_{\Gamma}) Y_{lm}(\hat{\mathbf{k}}_{\Gamma}) d\hat{\mathbf{k}}_{\Gamma'} d\hat{\mathbf{k}}_{\Gamma}, \quad (2.9)$$

where  $Y_{lm}$  are spherical harmonics.

The transformation to the lab frame is presently accomplished by first expanding (2.7) in spherical harmonics for the outgoing wave,

$$f_{lm}^b(\hat{\mathbf{k}}_{\Gamma}) = \int \int f^b(\hat{\mathbf{k}}_{\Gamma'}, \hat{\mathbf{k}}_{\Gamma}) Y_{lm}^*(\hat{\mathbf{k}}_{\Gamma'}) d\hat{\mathbf{k}}_{\Gamma'}. \quad (2.10)$$

Then, using the fact that  $\hat{\mathbf{k}}_{\Gamma}$  will be the  $z$ -axis in the lab frame,

$$f_{l\mu}^{\text{lab}}(\alpha, \beta) = \sum_m D_{\mu m}^l(-\hat{\mathbf{k}}_{\Gamma}) f_{lm}^b(\hat{\mathbf{k}}_{\Gamma}) \quad (2.11)$$

the lab frame scattering amplitude is found. Here  $\alpha$  and  $\beta$  are equivalent to  $-\hat{\mathbf{k}}_{\Gamma}$ ; they represent the molecular orientation with respect to the incident electron beam.

Differential cross sections are then found by evaluating

$$\sigma(\theta, \phi) = \frac{1}{4\pi} \frac{k_{\Gamma'}}{k_{\Gamma}} \sum_{l, l'} \sum_{\mu, \mu'} Y_{l\mu}(\theta, \phi) Y_{l'\mu'}^*(\theta, \phi) \int f_{l\mu}^{\text{lab}}(\hat{\mathbf{k}}_{\Gamma}) f_{l'\mu'}^{\text{lab}}(\hat{\mathbf{k}}_{\Gamma}) d\hat{\mathbf{k}}_{\Gamma} \quad (2.12)$$

In studies involving the water and nitrogen molecules, some singlet transitions are considered for which the expansion of the scattering wave in  $L^2$  functions alone, Eq. (2.6), is ineffective at treating the contributions of higher partial waves in Eq. (2.9) to the scattering amplitude. To account for this component of the scattering amplitude, the Born Closure method is invoked. The premise is that there is some  $l_{\max}$ ,  $m_{\max}$  in the partial wave representation of the scattering amplitude Eq. (2.9) beyond which a lower order theory such as the First Born Approximation (FBA) is essentially correct. For the energies of interest in this work, and the partial waves treated by this means (typically,  $l_{\max} = 4$ ,  $m_{\max} = 2$ ), this assumption should be valid. In our present implementation, the composite scattering amplitude (body frame) in the linear momentum representation is given by

$$f^{COM}(\mathbf{k}_{\Gamma'}, \mathbf{k}_{\Gamma}) = f^{FBA}(\mathbf{k}_{\Gamma'}, \mathbf{k}_{\Gamma}) + \sum_{l'}^{l_{\max}} \sum_{mm'}^{m_{\max}} [f_{l'm',lm}^{SMC}(k_{\Gamma'}, k_{\Gamma}) - f_{l'm',lm}^{FBA}(k_{\Gamma'}, k_{\Gamma})] Y_{l'm'}(\hat{\mathbf{k}}_{\Gamma'}) Y_{lm}^*(\hat{\mathbf{k}}_{\Gamma}) \quad (2.13)$$

For the dipole-allowed  $\tilde{X}^1A_1 \rightarrow \tilde{A}^1B_1$  transition considered in the study of the water molecule, the point dipole potential was used in computing the FBA scattering amplitude. The procedure is described in greater detail in [2]. In this approximation, the analytical expression for the linear momentum representation of the scattering amplitude is given by

$$f^{FBA}(\mathbf{k}_{\Gamma'}, \mathbf{k}_{\Gamma}) = -2i \frac{\sqrt{k_{\Gamma'} k_{\Gamma}} \mathbf{D} \cdot (\mathbf{k}_{\Gamma'} - \mathbf{k}_{\Gamma})}{|\mathbf{k}_{\Gamma'} - \mathbf{k}_{\Gamma}|^2}. \quad (2.14)$$

The angular momentum representation of the FBA amplitude can also be expressed analytically as

$$f_{l'm',lm}^{FBA}(k_{\Gamma'}, k_{\Gamma}) = (-1)^{m'} [(2l+1)(2l'+1)]^{1/2} (3/4\pi)^{1/2} d_{m'-m} \begin{pmatrix} l & l' & 0 \\ 0 & 0 & 0 \end{pmatrix} \begin{pmatrix} l & l' & 1 \\ m & -m' & m' - m \end{pmatrix} I_{l'l}(k_{\Gamma'}, k_{\Gamma}), \quad (2.15a)$$

where

$$I_{l',l}(k_{\Gamma'}, k_{\Gamma}) = \frac{2^p}{(k_{\Gamma'}, k_{\Gamma})^{1/2}} \kappa^{p+\frac{3}{2}} \sum_{j=0}^{\infty} \frac{(2j+1)!!}{j!} \frac{(p+j)!}{[2(p+j)+3]!!} \kappa^{2j}, \quad (2.15b)$$

with  $p = l$  if  $k_{\Gamma} > k_{\Gamma'}$ ,  $p = l'$  if  $k_{\Gamma'} > k_{\Gamma}$ , and  $\kappa = k_{<}/k_{>}$ , where  $k_{<}(k_{>})$  is the smaller(larger) of  $k_{\Gamma}$  and  $k_{\Gamma'}$ .  $d_{m'-m}$  are the  $d_{\pm 1,0}$  elements of the transition dipole. These can be used directly in (2.13) to provide the body-frame composite scattering amplitude. The analytical expressions facilitate the evaluation of the differential cross section in a more direct manner than Eq. (2.12); averaging over Euler angles  $(\alpha, \beta, \gamma)$  is substituted for transforming using rotation operators  $D_{\mu m}^l$ .

$$\frac{d\sigma^{COM}}{d\Omega} = \frac{k_{\Gamma'}}{k_{\Gamma}} \int \frac{d\alpha \sin \beta d\beta d\gamma}{8\pi^2} |f^{COM}(\mathbf{k}_{\Gamma'}, \mathbf{k}_{\Gamma})|^2 \quad (2.16)$$

This procedure has the advantage of avoiding the expansion in Eq. (2.10) used in the transformation step involving rotation operators Eq. (2.11).

For excitations in  $N_2$  that involve higher order moments of the electronic transitions, we opt to compute the full FBA scattering amplitude in the linear momentum representation. Chung and Lin [3] have shown that for excitation from a closed shell orbital  $\phi_{\nu}$  to an unoccupied orbital  $\phi_{\mu}$ , the direct (no exchange) FBA amplitude is given by

$$f^{FBA}(\mathbf{k}_{\Gamma'}, \mathbf{k}_{\Gamma}) = -\frac{\sqrt{2}}{2\pi} \int \phi_{\mu}^*(\vec{r}_2) e^{-i\mathbf{k}_{\Gamma'} \cdot \vec{r}_1} \frac{1}{r_{12}} e^{i\mathbf{k}_{\Gamma} \cdot \vec{r}_1} \phi_{\nu}(\vec{r}_2) d\vec{r}_1 d\vec{r}_2 \quad (2.17)$$

By expressing the orbitals  $\phi_{\nu}$ ,  $\phi_{\mu}$  as linear combinations of Cartesian Gaussians, the formulae of Watson and McKoy [4] can be used to calculate the matrix elements comprising the scattering amplitude analytically. It should be noted that a more

frequently encountered expression for the FBA scattering amplitude employs the generalized oscillator strength. By means of the Bethe integral

$$\frac{4\pi}{K^2} e^{i\vec{K}\cdot\vec{r}} = \int \frac{e^{i\vec{K}\cdot\vec{r}'}}{|\vec{r}-\vec{r}'|} dr', \quad (2.18)$$

one can convert (2.17) into this form, *i.e.*,

$$f^{\text{FBA}} = -\frac{2\sqrt{2}}{K^2} \int \phi_\nu^*(\vec{r}) e^{i\vec{K}\cdot\vec{r}} \phi_\mu(\vec{r}) d\vec{r} \quad (2.19)$$

with

$$\mathbf{K} = \mathbf{k}_\Gamma - \mathbf{k}_{\Gamma'}$$

One finds that the corresponding matrix elements for Gaussian functions for (2.19) are equivalent to those of Watson and McKoy to within a factor of  $2/K^2$ .

To obtain the combined amplitude (2.13), Eq. 2.17 is evaluated at a large number of Gauss–Legendre quadrature points, and converted to the angular momentum representation via (2.9). The elements of the angular momentum representation  $f_{l'm',lm}^{\text{FBA}}$  are then used with the  $f_{l'm',lm}^{\text{SMC}}$  in (2.13) to compute the new composite amplitude  $f^{\text{COM}}$  at the same quadrature points as used in the original evaluation of  $f^{\text{FBA}}(\mathbf{k}_{\Gamma'}, \mathbf{k}_\Gamma)$ .

In general, for work involving strongly forward peaked transitions, best results are obtained by working to the greatest extent possible in the linear momentum representation. As a consequence, for transitions involving multiple hole→particle excitations, *i.e.*  $X^1\Sigma_g^+ \rightarrow w^1\Delta_u$  in  $N_2$ , best results are obtained by combining amplitudes in the linear momentum representation. The low angle scattering is especially difficult to converge when working with amplitudes in the angular momentum representation.

For continued work on spin allowed transitions, where regardless of the behavior of the scattering at low angles, high partial waves are found to contribute significantly to the cross sections, a more accurate procedure for the body to lab frame transformation may be necessary. One way of avoiding rotation operators would be to use the rotated  $\hat{\mathbf{k}}_{\Gamma'}$  for a given molecular orientation  $(\alpha, \beta)$  to generate a spline fit so as to recompute the amplitude at the Gauss–Legendre quadrature points in the lab frame. In this way, no partial wave expansion of  $f^{COM}$  would be necessary to transform to the lab frame.

### References

- [1.] Q. Sun, C. Winstead, and V. McKoy, Phys. Rev. A **46**(11), (1992).
- [2.] S. Chung and C. C. Lin, Phys. Rev. A **6**, 988(1972).
- [3.] S. Chung and C. C. Lin, Appl. Opt. **10**(8), 1790(1971).
- [4.] D. K. Watson and V. McKoy, Phys. Rev. A **20**, 1474(1979).

### 3. Excitation of the $b^3\Sigma_u^+$ , $a^3\Sigma_g^+$ , and $c^3\Pi_u$ States of $H_2$ by Low-Energy Electrons

Multichannel studies of the differential and integral cross sections for the  $a^3\Sigma_g^+$ ,  $b^3\Sigma_u^+$ , and  $c^3\Pi_u$  states of the hydrogen molecule have been carried out using the Schwinger multichannel(SMC) method. Both integral and differential cross sections for the  $b^3\Sigma_u^+$  and  $c^3\Pi_u$  are in satisfactory agreement with those obtained using the complex Kohn and R-matrix methods, while significant differences are found for the  $a^3\Sigma_g^+$  state. The differential and integral cross sections for the  $b^3\Sigma_u^+$  state are in good agreement with available experimental values, but differences present between experiment and previous two-state calculations persist at the multichannel level for the  $a^3\Sigma_g^+$  and  $c^3\Pi_u$  states.

#### 3.1 Introduction

Electron-impact excitation of molecules is an important process in various physical systems; examples include the upper atmosphere, shock-heated gases, gas lasers, and industrial and laboratory plasmas. More robust modeling of such systems clearly depends on extensive and reliable sets of electron impact excitation cross sections. However, both the experimental and the theoretical determination of such cross sections have proven extremely difficult, and the data base remains limited for even the simplest and most significant molecules. Yet recent progress in the development and application of theoretical methods for studying electron-molecule collisions suggests that the situation may be improving. For instance,

there have been recent *ab initio* studies of the cross sections for electronic excitation of polyatomic molecules such as H<sub>2</sub>O [1], H<sub>2</sub>CO [2,3], and C<sub>2</sub>H<sub>4</sub> [4,5], and of the open-shell, diatomic molecule O<sub>2</sub> [6].

To date, most such electron-impact excitation studies of molecules have been carried out at the two- or three-channel levels of approximation. Comparisons between different theoretical methods at this level have shown reasonably satisfactory agreement for excitations of H<sub>2</sub>CO and C<sub>2</sub>H<sub>4</sub> [2,3]. Good agreement was also found in the most extensively studied case, the prototypical  $X^1\Sigma_g^+ \rightarrow b^3\Sigma_u^+$  transition in H<sub>2</sub>. Excitation of the  $b^3\Sigma_u^+$  state of H<sub>2</sub> has been studied within the two-channel, fixed-nuclei approximation using the linear algebraic [7], R-matrix [8], Schwinger multichannel or SMC [9], and complex Kohn [10] methods, and the results of these calculations agree well both with each other and with the experimental data for the integral and the differential [11–13] excitation cross sections. This agreement is encouraging, and suggests that few-channel studies using these methods may be useful. In particular, such studies would serve to determine to what extent the absence of multichannel coupling in calculations for excitations of the  $a^3\Sigma_g^+$  and  $c^3\Pi_u$  states [14] is responsible for the significant disagreement with measured cross sections [15].

Two multichannel studies of the H<sub>2</sub> molecule have recently been reported. In one [16], the complex Kohn technique was used to study excitation of the  $a^3\Sigma_g^+$ ,  $b^3\Sigma_u^+$ , and  $c^3\Pi_u$  states at the five-channel level. (In our usage, the degenerate  $\Pi$  components are counted as separate channels, and therefore the number of channels can exceed the number of physical states.) In the other study [17–19], the R-matrix method was used to carry out a nine-channel calculation that included not

only the  $a^3\Sigma_g^+$ ,  $b^3\Sigma_u^+$ , and  $c^3\Pi_u$  triplet states, but also the  $B^1\Sigma_u^+$ ,  $(E, F)^1\Sigma_g^+$ , and  $C_u^\Pi$  states. The R-matrix study included target correlation effects, with the ground and excited states of  $H_2$  obtained from a configuration interaction (CI) calculation. While both of these studies showed marked channel-coupling effects, they disagreed with each other in numerous qualitative and quantitative features of the cross sections. Because different representations of the target wavefunctions and channel coupling schemes were used, however, it is difficult to assess the origin and significance of discrepancies between the two sets of results.

In the present work, we have used the SMC method to obtain excitation cross sections for the  $a^3\Sigma_g^+$ ,  $b^3\Sigma_u^+$ , and  $c^3\Pi_u$  states within a five-channel approximation, that is, at the same level of approximation as was used in the earlier complex-Kohn study [16]. We are thus able to compare our results directly to the results of the Kohn calculation. It is also useful to compare with R-matrix results in which the singlet channels have been treated as closed in the R-matrix expression for the scattering wavefunction, but target correlation is retained [19], and to cross sections of the full R-matrix calculation [17,18]. As will be seen, these comparisons allow certain inferences to be drawn but leave many questions unanswered. Specifically, convergence appears easier to achieve for excitation of the valence  $b^3\Sigma_u^+$  state than for the Rydberg  $a^3\Sigma_g^+$  and  $c^3\Pi_u$  states, a not-unexpected result. However, the differential cross section results for the  $b^3\Sigma_u^+$  state of the R-matrix studies are qualitatively different from that of either the complex Kohn or the present SMC calculation. Our results for the  $c^3\Pi_u$  state are in fairly good agreement with the complex Kohn results; however, agreement for the  $a^3\Sigma_g^+$  state is only qualitative.

These observations and tentative explanations for them will be discussed in detail below.

The outline of the remaining sections is as follows. Sec. 3.2 give details of our calculations. Results are presented and discussed in Sec. 3.3. A general discussion and concluding remarks are given in Sec. 3.4.

### 3.2 Computational Details

For this particular study of the  $H_2$  molecule, a large number of basis set were considered to verify convergence of the cross sections in all channels. The cross sections reported in this study were obtained from the basis given in Table 3.1. All

Table 3.1. Exponents of Cartesian Gaussian basis for expansion of the target wavefunctions.

Center	Type	Exponent
hydrogen	<i>s</i>	48.4479, 7.28346, 1.65139, 0.462447, 0.145885
hydrogen	<i>p</i>	4.5, 1.5, 0.5, 0.25, 0.125, 0.0655
hydrogen	<i>d</i>	6.00, 3.00, 1.50, 0.75
c.m. <sup>a</sup>	<i>s</i>	0.083, 0.027
c.m.	<i>p</i>	0.0226, 0.00779
c.m.	<i>d</i>	0.150

<sup>a</sup>center of mass

Gaussian functions were included in the target wavefunction. No additional scattering functions were employed. The excited electronic states included in this study

–  $a^3\Sigma_g^+$ ,  $b^3\Sigma_u^+$ , and  $c^3\Pi_u$  – were approximated by the usual single determinant, IVO description at the equilibrium internuclear distance, 1.40028 a.u. The vertical excitation energies were taken as threshold for the respective states. In addition, the thresholds for the singlet analogs of each triplet state, *i.e.*,  $B^1\Sigma_u^+$ ,  $C^1\Pi_u$ , and  $(E, F)^1\Sigma_g^+$  were computed using the IVO's optimized for the triplet excitations.  $l_{max}=7$  was used in (Eq. 2.10) for all cross sections reported in this study. The thresholds for these states are given in Table 3.2, along with energies obtained from more sophisticated theory [20–24] and experimentally measured threshold excitation energies [25].

Table 3.2. Vertical threshold energies (eV) for open and closed channels.

State	This work	Exact	Experiment
$a^3\Sigma_g^+$	12.03	12.54 <sup>b</sup>	12.28 <sup>g</sup>
$(E, F)^1\Sigma_g^+$	13.14	13.60 <sup>c</sup>	12.35 <sup>a</sup>
$b^3\Sigma_u^+$	9.98	10.62 <sup>d</sup>	10.35 <sup>g</sup>
$B^1\Sigma_u^+$	14.57	12.75 <sup>b</sup>	11.19 <sup>a</sup>
$c^3\Pi_u$	12.31	12.73 <sup>e</sup>	12.60 <sup>g</sup>
$C^1\Pi_u$	13.54	13.23 <sup>f</sup>	12.30 <sup>a</sup>

<sup>a</sup> Ref. 25, <sup>b</sup> Ref. 20, <sup>c</sup> Ref. 21, <sup>d</sup> Ref. 22, <sup>e</sup> Ref. 23, <sup>f</sup> Ref 24, <sup>g</sup> Ref. 14

### 3.3 Results and Discussion

#### 3.3.1 Excitation of the $b^3\Sigma_u^+$ State

Our calculated integral excitation cross sections for the  $b^3\Sigma_u^+$  state are shown in Fig. 3.1 along with results obtained with the R-matrix [18] and complex Kohn [16]

methods and the measured values of Hall and Andric [11], Nishimura and Danjo [12], and Khakoo *et al.* [13]. Our calculated cross sections are in reasonable agreement with the available experimental data for this excitation. Agreement with the results of the complex Kohn calculations is satisfactory over the range of energies con-

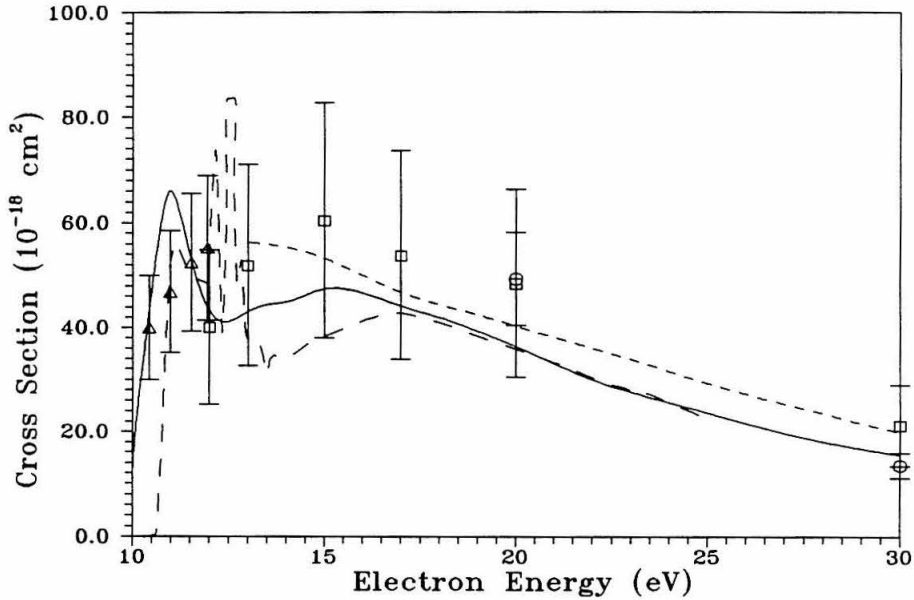


Figure 3.1. Integral cross section for the  $X^1\Sigma_g^+ \rightarrow b^3\Sigma_u^+$  transition: —, present results; - - - -, complex Kohn results of [16]; - · - ·, R-matrix results of [17];  $\square$ , measured cross sections of Nishimura and Danjo [12];  $\circ$ , measured values of Khakoo *et al.* [13];  $\triangle$ , measured values of Hall and Andric [11].

sidered, with the SMC results being somewhat smaller. Differences between the present results and the R-matrix cross sections, in particular from 12.5 to 17 eV, result from the inclusion of open singlet channels in the latter study. Comparison with a more restricted R-matrix calculation[19] in which only triplet channels are included, shows the two methods yield similar cross sections. Both sets of cross

sections show peaks near threshold (11.5 eV) and secondary maxima between 15 and 17 eV. Above 17 eV, all three methods yield similar cross sections as a consequence

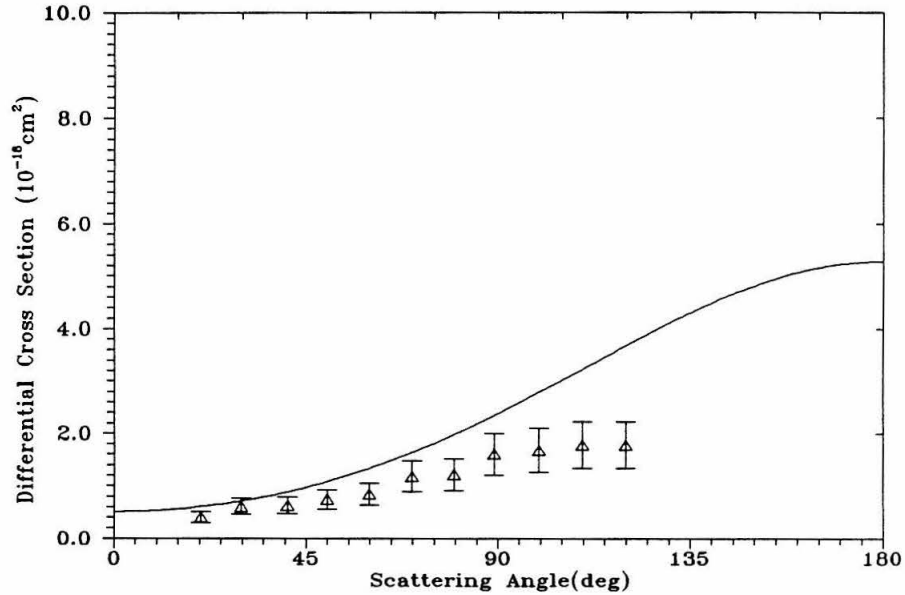


Figure 3.2. Differential cross section for the excitation of the  $b^3\Sigma_u^+$  state at 10.5 eV: —, present results;  $\Delta$ , measured values of Hall and Andric [11].

of the decreasing effects of both target correlation and of the particular channel coupling scheme on the  $X^1\Sigma_g^+ \rightarrow b^3\Sigma_u^+$  channel. The resonance structure seen in the R-matrix cross sections at low energies (12 eV) is not seen in the SMC results due to the simpler target state wave function used in this study. These five-channel excitation cross sections for the valence  $b^3\Sigma_u^+$  state are about 20% to 30% smaller than those of a two-channel calculation, with the most significant differences seen in the  $^2\Pi_g$  symmetry below 20 eV.

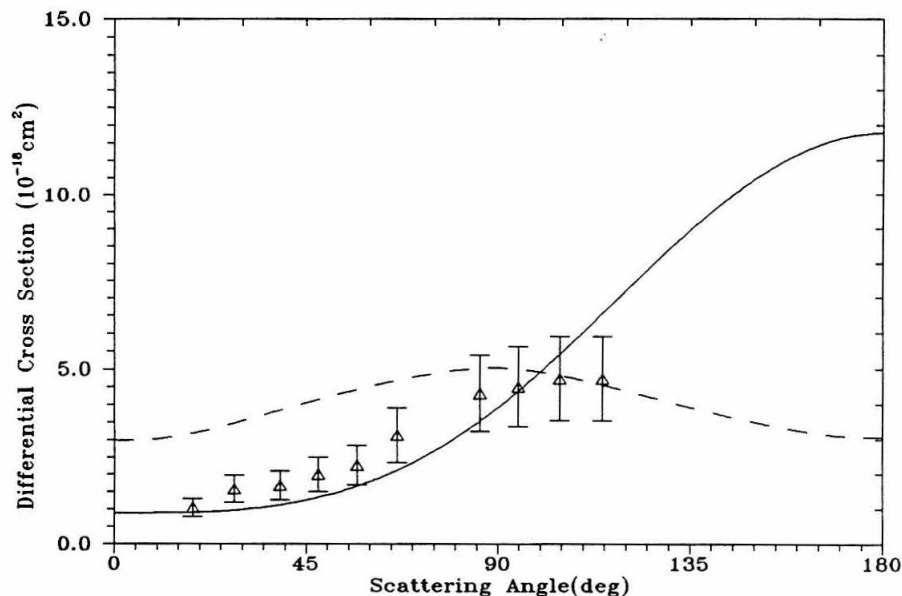


Figure 3.3. Differential cross section for excitation of the  $b^3\Sigma_u^+$  state at 12 eV: —, present results; - - -, R-matrix results of [17].

Our calculated differential cross sections (DCS) for the  $b^3\Sigma_u^+$  state at 10.5 and 12 eV are shown in Figs. 3.2 and 3.3, respectively along with the experimental data of Hall and Andric [11] and R-matrix results [17] at 12 eV. Both the  $c^3\Pi_u$  and  $a^3\Sigma_g^+$  states are closed at these energies, and hence act as polarization-type excitations in the expansion of the scattering wave function. The effect of their inclusion is to enhance the  $^2\Sigma_g$  and  $^2\Sigma_u$  symmetry components of the  $X^1\Sigma_g^+ \rightarrow b^3\Sigma_u^+$  cross section. At both energies, agreement with the measured values of Hall and Andric [11] is good, although the pronounced backward peaking of the calculated cross sections leads to integral cross sections larger than those reported by Hall and Andric. At 12 eV, the R-matrix results are apparently dominated by the near-threshold resonances seen in the corresponding total cross sections.

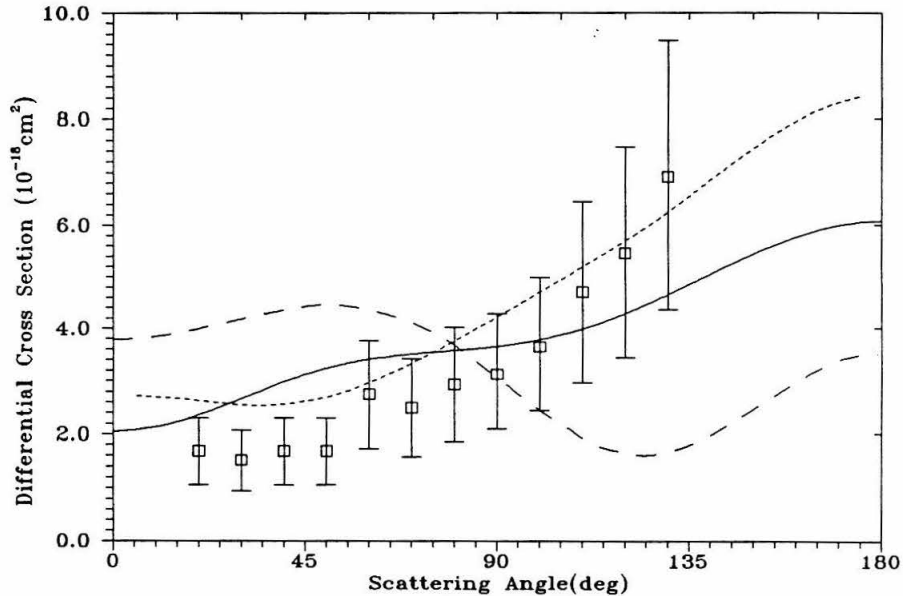


Figure 3.4. Differential cross section for the  $X^1\Sigma_g^+ \rightarrow b^3\Sigma_u^+$  transition at 13 eV: —, present results; - - - -, complex Kohn results [16]; ····, R-matrix results [17]; ( $\square$ ), measured cross sections of Nishimura and Danjo [12].

Figures 3.4 and 3.5 show our calculated DCS's at 13 eV and 15 eV, respectively, along with those of the Kohn and R-matrix studies and the measured values of Nishimura and Danjo [12]. Our calculated DCS's agree qualitatively with those of the Kohn method; both exhibit the significant backward peaking observed experimentally. Agreement with the measured cross sections of Nishimura and Danjo [12] is satisfactory at intermediate and higher angles. The effect of multichannel coupling in the SMC calculations is a reduction of the extent of this backward peaking. The R-matrix DCS's at these energies differ significantly from the present results and from those of the Kohn method, irrespective of the choice of channel coupling schemes.

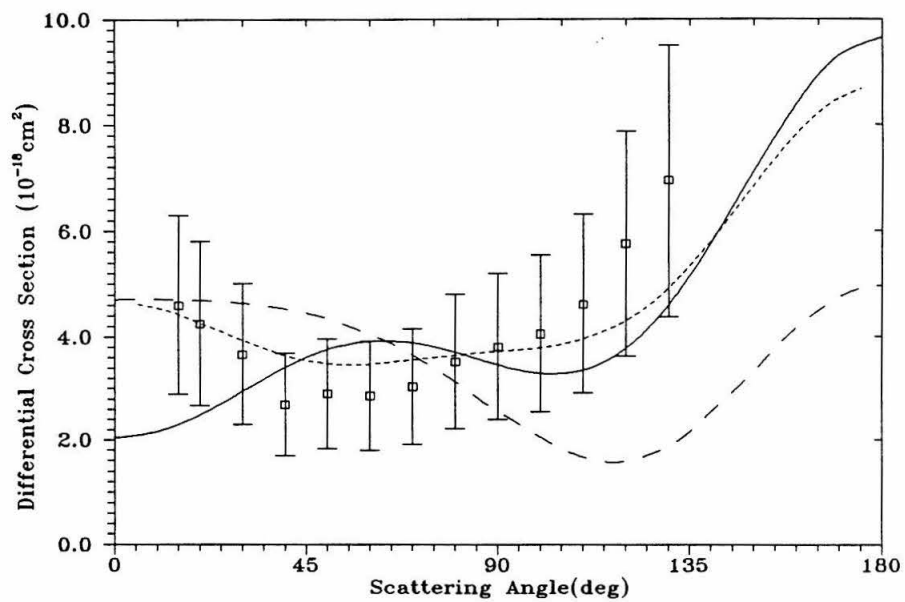


Figure 3.5. Same as Figure 3.4 at 15 eV.

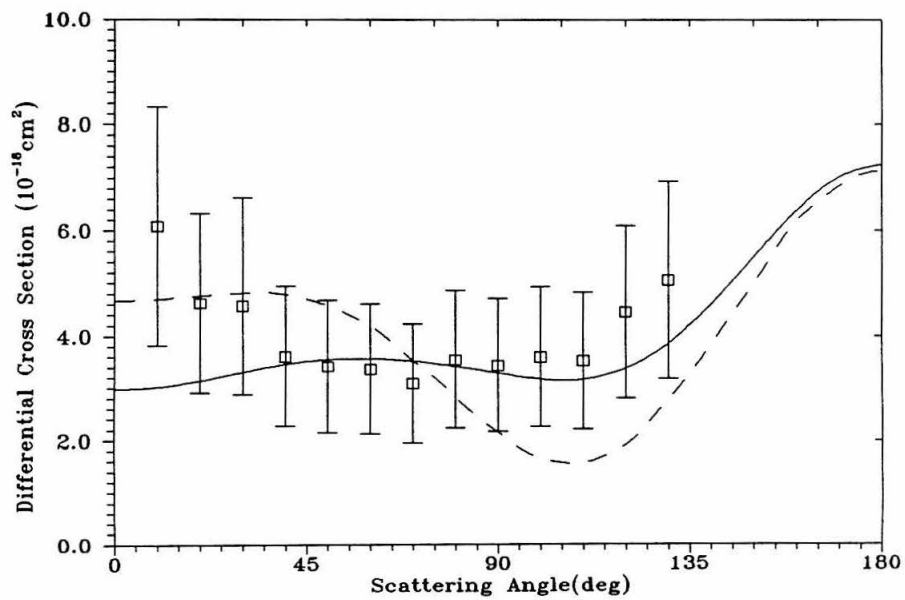


Figure 3.6. Same as Figure 3.5 at 17 eV.

Figures 3.6, 3.7 and 3.8 show the differential cross sections for excitation of the  $b^3\Sigma_u^+$  state at 17 eV, 20 eV, and 30 eV, respectively. Agreement between our calculated DCS's and the measured values at 17 and 30 eV is quite good, but poor at 20 eV. In contrast to the DCS's at lower energies, the SMC and R-matrix results are in better agreement for low and intermediate angles at 17 and 20 eV (Figs. 3.6 and 3.7). The DCS at 30 eV (Fig. 3.8) shows that multichannel effects have little influence at these energies: two and multichannel results are almost identical and in good agreement with experiment.

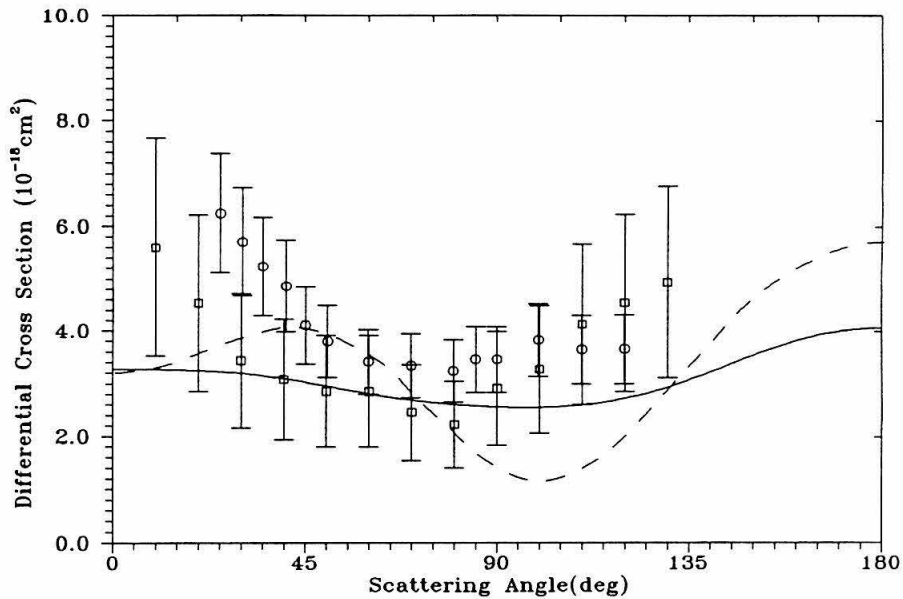


Figure 3.7. Differential cross section for excitation of the  $b^3\Sigma_u^+$  state at 20 eV: —, present results; - - -, R-matrix results [17];  $\square$ , measured cross sections of Nishimura and Danjo[12];  $\circ$ , measured cross sections of Khakoo *et al.* [13].

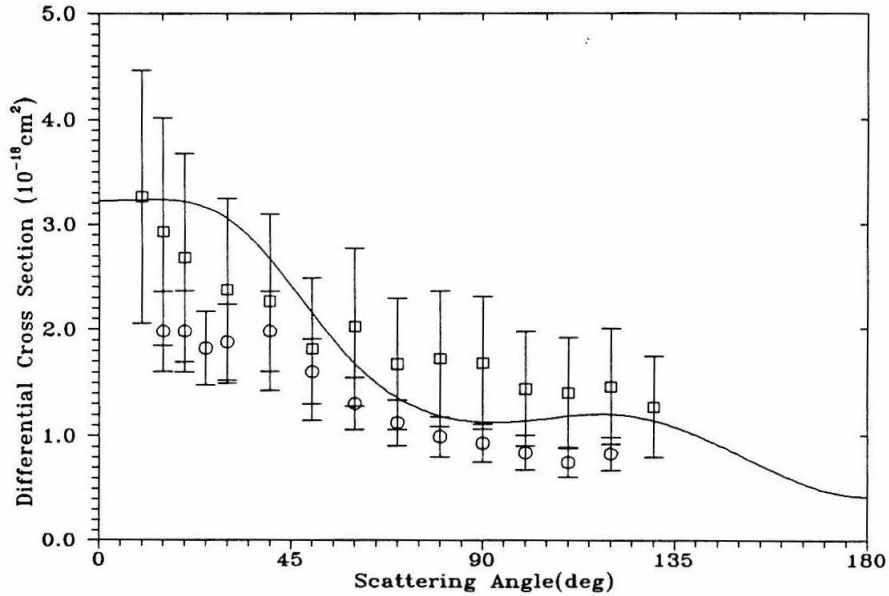


Figure 3.8. Same as Figure 3.7 at 30 eV.

### 3.3.2 Excitation of the $a^3\Sigma_g^+$ State

Our calculated cross sections for excitation of the  $a^3\Sigma_g^+$  state are shown in Fig. 3.9. Also shown are the experimental values of Khakoo and Trajmar [15] at 20 eV and 30 eV and the calculated values of the R-matrix [17] and complex Kohn studies [16]. The SMC  $X^1\Sigma_g^+ \rightarrow a^3\Sigma_g^+$  cross sections share some qualitative features with those of the R-matrix studies, which, in addition to including singlet open channels, also used a correlated target wave function. In particular, both show a near threshold peak at about 13 eV. A partial-wave analysis of these SMC cross sections reveals that the primary contribution to this peak comes from the  $^2\Sigma_g$  symmetry, as expected, with significant  $^2\Pi_u$  and  $^2\Delta_g$  components as well. The

symmetry composition of the near-threshold peak in the R-matrix cross section was not discussed in [17]. It should be noted that similar qualitative agreement was

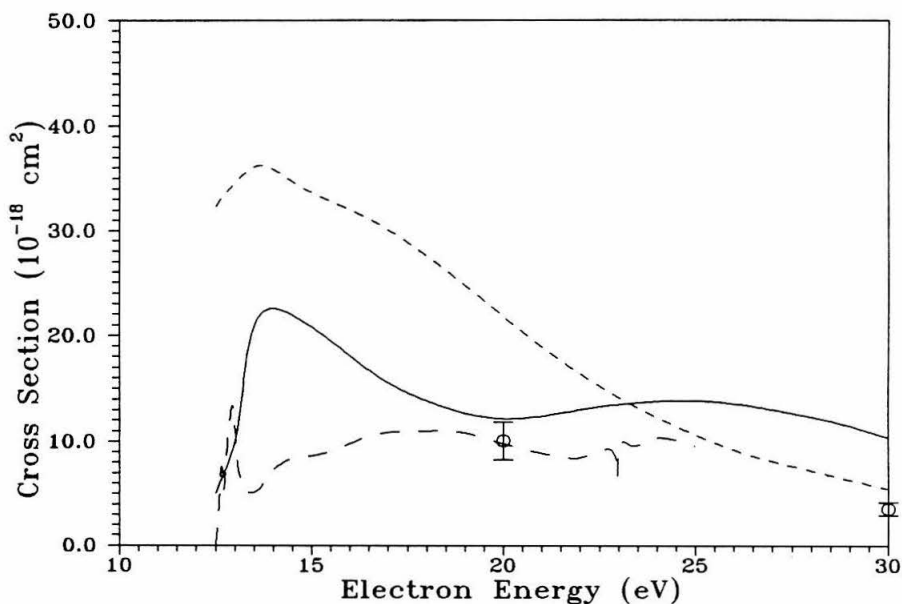


Figure 3.9. Integral cross section for excitation of the  $a^3\Sigma_g^+$  state: —, present results; - - - - -, complex Kohn results [16]; - · - · - ·, R-matrix results [17] (see text); ○, measured cross sections of Khakoo and Trajmar [15].

observed between the SMC cross sections and the R-matrix values calculated without inclusion of singlet open channels. Agreement between the SMC cross sections and those of the complex Kohn study is poor. The source of this disagreement is not clear. Comparison of the differential cross sections in Fig. 3.10 shows that the Kohn results are much more strongly peaked in both the forward and backward direction than those of the present and R-matrix studies at 20 eV. This behavior

arises from the  ${}^2\Delta_g$  contribution to the cross sections and suggests that this component is more dominant in the Kohn results than in either the SMC or R-matrix

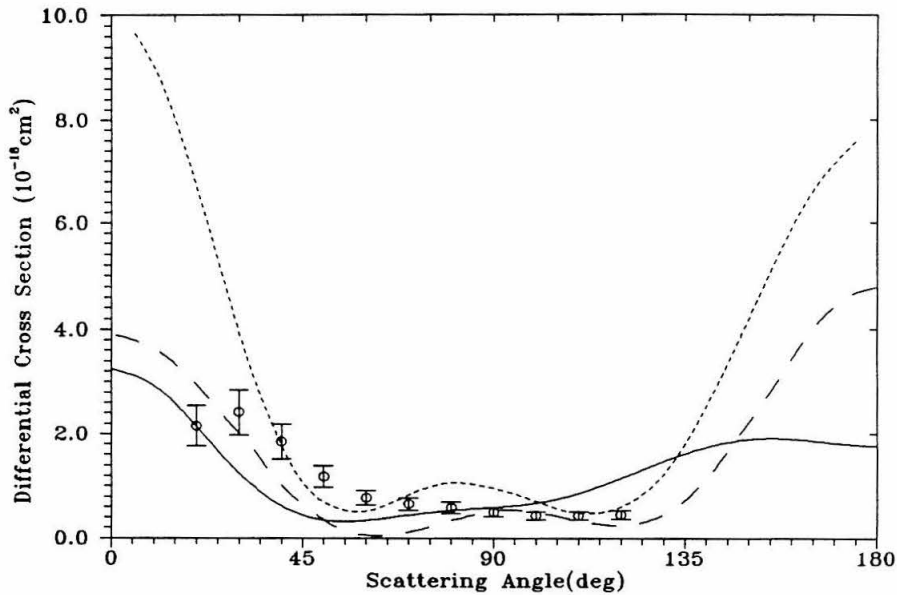


Figure 3.10. Differential cross section for excitation of the  $a^3\Sigma_g^+$  state at 20 eV: —, present results; - - -, complex Kohn results [16]; - · - ·, R-matrix results [17]; ○, measured cross sections of Khakoo and Trajmar [15].

studies at this energy. However, all three theoretical results are in good agreement with the data of Khakoo and Trajmar [15], which does not extend into the forward and backward directions. At 30 eV, the SMC differential cross sections of Fig. 3.11 show a pronounced backward and forward peaking quite similar to the behavior seen in the complex Kohn cross sections at 20 eV. Agreement between these calculated cross sections and the measured values of Khakoo and Trajmar is fair, particularly for angles above approximately  $40^\circ$  where such measurements can be expected to be most reliable.

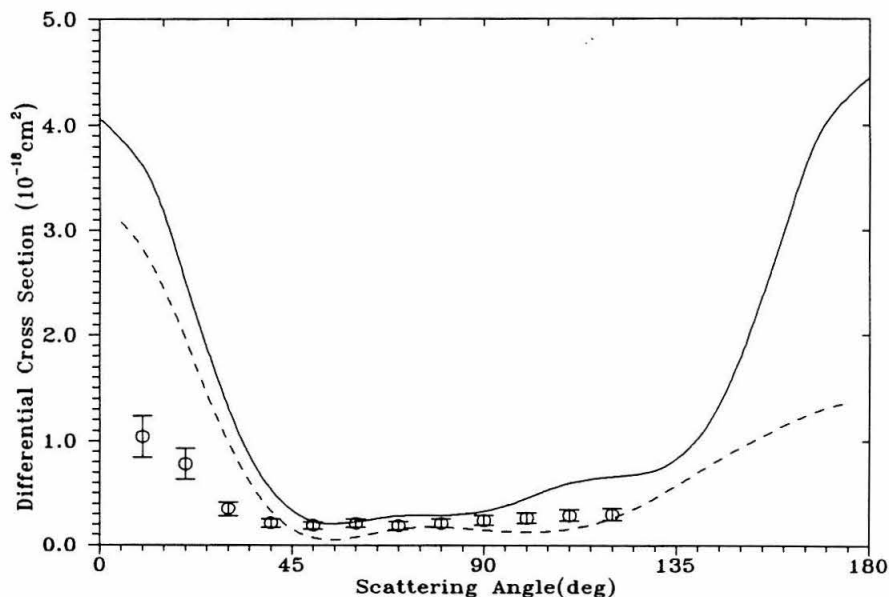


Figure 3.11. Differential cross section for excitation of the  $a^3\Sigma_g^+$  state at 30 eV: —, present results; - - -, complex Kohn results [16];  $\circ$ , measured cross sections of Khakoo and Trajmar [15].

### 3.3.3 Excitation of the $c^3\Pi_u$ State

Our calculated integral cross sections for this state are given in Fig. 3.12 along with the R-matrix results of Branchett *et al.* [17], the complex Kohn results of Parker *et al.* [16], and the measurements of Khakoo and Trajmar [15] at 20 and 30 eV. All three sets of calculated cross sections show qualitatively similar features. For example, all show a near-threshold peak, which is most pronounced in the R-matrix results. This peak falls near 13.5 eV in the SMC cross section and arises from the  $^2\Pi_u$  component. The complex Kohn results show a less prominent feature

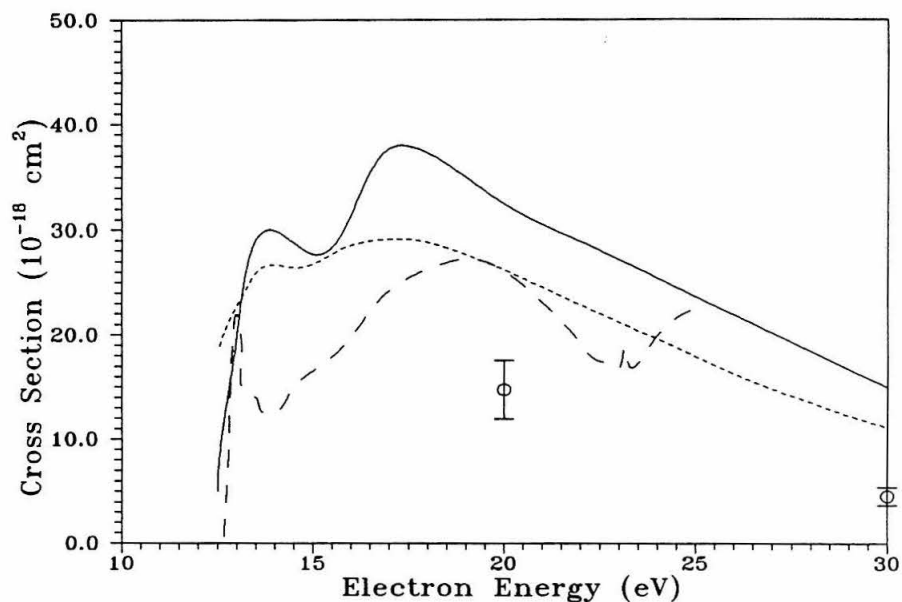


Figure 3.12. Integral cross section for excitation of the  $c^3\Pi_u$  state: —, present results; - - - -, complex Kohn results [16]; - - - -, R-matrix results [17];  $\circ$ , measured cross sections of [15].

at this same energy. This feature is also seen in R-matrix calculations in which the singlet channels were treated as closed[19]. All three sets of cross sections also show a broader secondary maximum at higher energies, and the SMC and Kohn methods yield fairly similar cross sections above 17 eV. It should be noted that agreement with experiment improves somewhat upon coupling the  $c^3\Pi_u$  state with the  $a^3\Sigma_g^+$  and  $b^3\Sigma_u^+$  states, although the cross sections for all three theories remain about twice as large the experimental value at 20 eV and 30 eV.

As with the  $a^3\Sigma_g^+$  state, application of the SMC to a multichannel treatment of the  $c^3\Pi_u$  excitation reveals significant changes in the contributions of different

symmetry components to the total cross section. In contrast with the  $a^3\Sigma_g^+$  state,

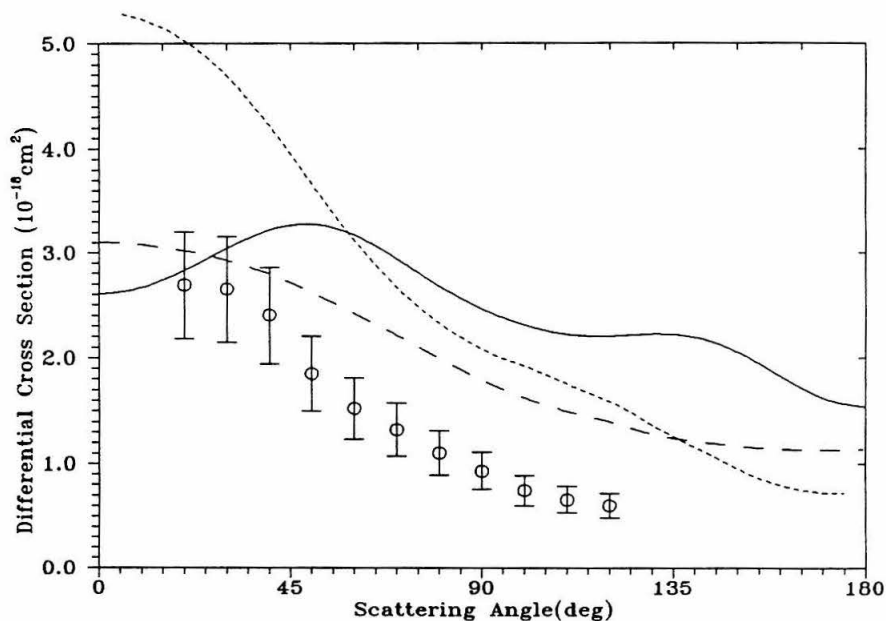


Figure 3.13. Differential cross section for the  $c^3\Pi_u$  state at 20 eV: —, present results; - - -, complex Kohn results [16]; - · - ·, R-matrix results [17]; ○, measured cross sections of [15].

however, the total magnitude also changes substantially. In fact, comparison with previous two-state applications of the SMC to this excitation shows a twofold or greater drop in the cross section below 20 eV. The greatest change is in the  $^2\Pi_g$  symmetry, where, due to coupling with the  $b^3\Sigma_u^+$  state through the  $[1\sigma_g 1\sigma_u 1\pi_u]$  configuration in the expansion of  $\Psi_m$  (Eq. 1.9), the  $c^3\Pi_u$  state cross section drops by a factor of 20 or more between threshold and 20 eV. A narrow peak at 13.5 eV replaces a broad peak of similar height observed in the  $^2\Pi_u$  symmetry at the two-state approximation, leading to the peak observed at threshold in this channel.

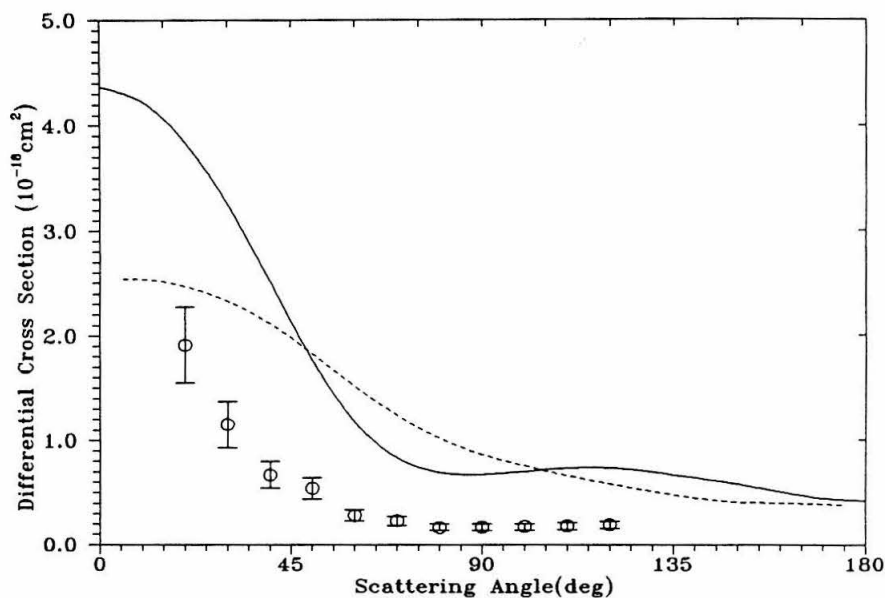


Figure 3.14. Differential cross section for the  $c^3\Pi_u$  state at 30 eV:——, present results; - - -, complex Kohn results of [16];  $\circ$ , measured cross sections of [15].

The differential cross sections at 20 and 30 eV incident electron energies are shown in Figs. 3.13 and 3.14. Although the three sets of calculated differential cross sections show some qualitative similarities, significant differences remain. At 20 eV, the R-matrix results in which the singlet analogs of these triplet channels were included are in better agreement with the experimental values of Khakoo and Trajmar [15].

### 3.4 Observations and Conclusions

The reported SMC integral cross sections are in qualitative agreement with those obtained using the complex Kohn and R-matrix methods for the  $b^3\Sigma_u^+$  state.

Above 17eV the SMC and R-matrix results are comparable for the  $c^3\Pi_u$  and  $a^3\Sigma_g^+$  states; discrepancies at lower energies are not explained by the inclusion of singlet open channels in the latter study. The complex Kohn and SMC yield quite different results for the  $a^3\Sigma_g^+$  state at all energies, the source of these differences at higher energies being evident in the DCS. Differential cross sections for the Kohn and SMC methods are in good agreement for the  $b^3\Sigma_u^+$  and  $c^3\Pi_u$ , but not for the  $a^3\Sigma_g^+$  state, due to differences in the energy dependence and magnitude of the  $m = 2$  partial wave contribution to the scattering amplitude. Agreement with DCS of the R-matrix method is good for the  $c^3\Pi_u$  state but poor for the  $b^3\Sigma_u^+$  state except at 20 eV.

Based on this study, several observations can be made concerning the ability of multichannel coupling to improve agreement of theory with experiment. Multichannel coupling for the  $H_2$  molecule in the context of the SMC method most strongly influences the cross sections for different channels near threshold, *e.g.*, the peaks in the  $a^3\Sigma_g^+$  and  $c^3\Pi_u$  channels, and changes the underlying symmetry contribution to the cross section in a specific channel, again near threshold. In this study, the  $^2\Sigma_u$  symmetry component in the  $a^3\Sigma_g^+$  state and  $^2\Pi_u$  symmetry component in the  $c^3\Pi_u$  state are the clearest examples of the latter behavior. The energy dependence of this type of coupling is such that it is not likely to alter results of two-state calculations significantly at the highest energies considered. Inclusion of correlation in the target, in light of the R-matrix results [17,18] and studies using the distorted wave approximation (DWA) method in which both correlated and uncorrelated targets were considered [26,27], does not appear to improve agreement either. These

observations seem to indicate that, as in close-coupling studies of electronic excitation of atoms by low energy electrons [28], many more channels including members of the Rydberg series corresponding to these excitations and ionization need to be opened to improve higher energy cross sections for Rydberg-type excitations.

### 3.5 References

- [ 1.] H. P. Pritchard, V. McKoy, and M. A. P. Lima, *Phys. Rev. A* **41**(1), 546–549(1990).
- [ 2.] Q. Sun, C. Winstead, V. McKoy, and M. A. P. Lima, *Phys. Rev. A*, **46**, 2462 (1992).
- [ 3.] T. N. Rescigno, B. H. Lengsfeld, and C. W. McCurdy, *Phys. Rev. A* **41**, 2462(1990).
- [ 4.] Q. Sun, C. Winstead, V. McKoy, and M. A. P. Lima, *J. Chem. Phys.* **96**(5), 3531–3535(1992).
- [ 5.] T. N. Rescigno and B. I. Schneider, *Phys. Rev. A* **45**, 2894 (1992).
- [ 6.] C. J. Noble and P. G. Burke, *Phys. Rev. Lett.* **68**(3), 2011–2014(1992).
- [ 7.] B. I. Schneider and L. A. Collins, *J. Phys. B* **18**, L857 (1985).
- [ 8.] K. L. Baluja, C. J. Noble, and J. Tennyson, *J. Phys. B* **18**, L851 (1985).

- [ 9.] M. A. P. Lima, T. L. Gibson, W. M. Huo, and V. McKoy, *J. Phys. B* **18**, L865 (1985).
- [ 10.] T. N. Rescigno and B. I. Schneider, *J. Phys. B* **21**, L691–695(1988).
- [ 11.] R. I. Hall and L. Andric, *J. Phys. B* **17**, 3815(1984).
- [ 12.] H. Nishimura and A. Danjo, *J. Phys. Soc. Jpn.* **55**, 3031(1986).
- [ 13.] M. A. Khakoo, S. Trajmar, R. McAdams, and T. W. Shyn, *Phys. Rev. A* **35**, 2832(1987).
- [ 14.] M. A. P. Lima, T. L. Gibson, V. McKoy, and W. M. Huo, *Phys. Rev. A* **38**, 4527(1988); T. L. Gibson, M. A. P. Lima, V. McKoy, and W. M. Huo, *Phys. Rev. A* **35**, 2473 (1987).
- [ 15.] M. A. Khakoo and S. Trajmar, *Phys. Rev. A* **34**, 146(1986).
- [ 16.] S. D. Parker, C. W. McCurdy, T. N. Rescigno, and B. H. Lengsfeld, *Phys. Rev. A* **43**, 3514 (1991).
- [ 17.] S. E. Branchett, J. Tennyson, and L. A. Morgan, *J. Phys. B* **23**, 4625(1990); *Ibid.* **24**, 3479 (1991).
- [ 18.] S. E. Branchett and J. Tennyson, *Phys. Rev. Lett.* **64**, 2889 (1990).
- [ 19.] S. E. Branchett and J. Tennyson, private communication.
- [ 20.] W. Kołos and L. Wolniewicz, *J. Chem. Phys.* **48**, 3672(1968).
- [ 21.] W. Kołos and K. Dessler, *J. Chem. Phys.* **82**, 3292 (1985).

- [ 22.] W. Kołos and L. Wolniewicz, *J. Chem. Phys.* **43**, 2429(1965).
- [ 23.] W. Kołos and J. Rychlewski, *J. Mol. Spectrosc.* **66**, 428(1977).
- [ 24.] S. Rothenberg and E. R. Davidson, *J. Chem. Phys.* **44**, 730(1966).
- [ 25.] T. E. Sharp, *At. Data* **2**, 119(1971).
- [ 26.] Lee Mu-Tao, R. R. Lucchese, and V. McKoy, *Phys. Rev. A* **26**, 3240 (1982).
- [ 27.] Lee Mu-Tao, L. E. Machado, E. P. Leal, L. M. Brescansin, M. A. P. Lima, and F. B. C. Machado, *J. Phys. B*, **23**, L233 (1990).
- [ 28.] P. M. J. Sawey, K. A. Berrington, and P. G. Burke, *J. Phys. B* **23**, 4321 (1990).

## 4. Electronic Excitation of H<sub>2</sub>O by Electron Impact

We report results of a multichannel application of the Schwinger Multichannel (SMC) method to the electronic excitation of water by low energy electron impact. Differential and integral cross sections for electronic excitation of several low-lying Rydberg states of the water molecule are reported in addition to the momentum transfer cross section and differential cross sections for the elastic channel. Cross sections for excitation of the  $\tilde{A}^1B_1, \tilde{a}^3B_1(1b_1 \rightarrow 3sa_1)$ ,  $\tilde{d}^3A_1(1b_1 \rightarrow 3pb_1)$ ,  $^3A_2(1b_1 \rightarrow 3pb_2)$ , and  $\tilde{b}^3A_1(3a_1 \rightarrow 3sa_1)$  states are given from threshold up to 30eV incident electron energy. Differential cross sections for these excitations are reported at 11, 15, and 20 eV. Agreement with available elastic channel differential and momentum transfer cross section data is satisfactory. Qualitative agreement is also found with relevant observations from electron impact-induced dissociation experiments.

### 4.1 Introduction

Electron impact excitation of electronically excited states of the water molecule and its subsequent dissociation are known to play a significant role in the radiation chemistry of water and a variety of space physics phenomena [1,2]. Due to the large energy transfer associated with such electronically inelastic collisions, these cross sections are also relevant to studies of subexcitation electron degradation spectra and to modeling of radiation damage in biological materials [3]. Nonetheless, there exist relatively few measurements of the cross sections for electronic excitation of

water by low-energy electrons. Skerbele *et al.* [4] have reported results of electron-energy-loss (EEL) experiments at energies of 30 and 60 eV for small angle scattering. Tam and Brion [5] have reported EEL spectra of H<sub>2</sub>O using 50 and 100 eV beams. Trajmar *et al.* [8] have also measured relative differential cross sections for singlet and triplet excitations of H<sub>2</sub>O at 15, 20, and 53 eV as well as at 20° and 90° for impact energies ranging from 4.2 to 12 eV [9]. Reviews of available cross section data for electron-water collisions, including estimated electronic excitation cross sections, have been prepared by Hayashi [10] and Shimamura [11].

Emission cross sections for various products resulting from electron impact dissociation of water have also been measured [12–16]. Such measurement can provide useful estimates of the cross sections for excitation of dissociative electronic states. For example, using measurements of the ( $A^2\Sigma \rightarrow X^2\Pi$ ) OH emission bands, Becker *et al.* [15] estimated the relative contributions of singlet and triplet excitation processes to the production of the excited OH by comparing the dependence of the P<sub>1</sub>(21) and Q<sub>1</sub>(3) rotational line intensities in the (0–0) band on electron impact energy. Similar studies involving the Q<sub>1</sub>(2) and P<sub>1</sub>(27) lines yielded results supporting these observations[16].

On the theoretical side there have been few studies of the cross sections for electronic excitation of water by low-energy electrons. We have previously used the Schwinger multichannel (SMC) formulation to study the cross sections for excitation of the  $\tilde{b}^3A_1(3a_1 \rightarrow 3sa_1)$  excited state of water [17]. These calculations, in which only two open electronic channels were included, represented the first application of this method to electronic excitation of a nonlinear molecule by low-energy electrons. Here we present results of further applications of the SMC method to obtain the

cross sections for other triplet and singlet states at the two-state approximation. We have also carried out calculations of these cross sections with three to five open channels so as to gain some insight on multichannel effects on these cross sections. To do so, we consider several of these multichannel coupling schemes.

In the following sections, a brief description of our calculations and details of the application of the SMC method to the water molecule will be given. In section 4.3, results of the calculations will be presented and compared with available experimental data including fluorescence measurements of the OH ( $A^2\Sigma^+$ ) dissociation product. We also discuss the nature and importance of multichannel coupling effects.

## 4.2 Computational Details

The difficulties associated with obtaining converged results by use of the SMC were discussed in chapter 1. In this case, in order to assess convergence of the scattering amplitude (Eq. 1.7), a large number of basis sets was used in the expansion of the trial scattering functions and target functions constituting the Slater determinants used to describe the  $N + 1$  electron wavefunction (Eq. 1.16). The final results were obtained using the basis set listed in Table 4.1. This set of Cartesian Gaussian functions was used both in the expansion of the target wavefunction and the scattering functions. The basis was constructed from a (9s5p/4s2p) oxygen basis and a (4s) hydrogen basis of Poirier *et al.* [22]. The contraction scheme was partially relaxed for the  $s$  and  $p$  functions on the oxygen in order to increase the flexibility of the basis. Three additional  $s$  and three additional  $p$ -functions supplemented the

Table 4.1 Cartesian Gaussians Used in the Target and Scattering Basis Sets

Center		Exponent	Contraction Coefficient
oxygen	<i>s-type</i>	10662.285	0.001907
		1599.710	0.014678
		364.7253	0.074327
		103.6518	0.275762
		33.905805	0.719361
		12.287469	1.00000
		4.7568030	1.00000
		1.0042710	1.00000
		0.3006860	1.00000
		0.0800000	1.00000
		0.0200000	1.00000
		0.0040000	1.00000
		oxygen	<i>p-type</i>
7.843131	0.256398		
2.308269	0.803598		
0.7231640	1.00000		
0.2148820	1.00000		
0.0500000	1.00000		
0.0125000	1.00000		
oxygen	<i>d-type</i>	0.0025000	1.00000
		1.21880	1.00000
		0.3610000	1.00000
hydrogen	<i>s-type</i>	0.0363580	1.00000
		13.3615	1.00000
		2.01330	1.00000
		0.45380	1.00000
		0.12330	1.00000
hydrogen	<i>p-type</i>	0.02000	1.00000
		1.1838380	1.00000
		0.5919191	1.00000

oxygen basis. The inclusion of  $p$ -functions in the hydrogen basis was found to be particularly important, especially for collision energies near the inelastic thresholds. Throughout these calculations, the nuclei were held fixed at the experimental geometry for the ground state [17].

The SCF energy of the ground state using the basis of Table 4.1 was -76.055 a.u. The associated dipole moment was 2.04D, compared with the experimental value of 1.86. For computational convenience, the molecule was oriented with the two-fold rotation axis along the  $y$ -axis; the hydrogens were located in the  $yz$  plane. The IVO procedure of Hunt and Goddard [23] was used to approximate the wavefunctions of the Rydberg states considered in this study. For the case of the ( $1b_1 \rightarrow 3sa_1$ ) excitation, the IVO orbital was optimized for the  $\tilde{a}^3B_1$  state, except in the case of a two-state calculation involving the  $X^1A_1$  and  $\tilde{A}^1B_1$  states exclusively. Vertical excitation energies were derived using the experimental ionization energies of 12.62 eV for the  $1b_1$  orbital and 14.68 eV for the  $3a_1$  orbital [24]. In actual application

Table 4.2 Vertical threshold energies used for the open channels.

Excitation	Excited State	Vert. Exc. <sup>a</sup> Energy(eV)	IVO <sup>b</sup>	CI Results <sup>c</sup>	Experiment <sup>d</sup>
$1b_1 \rightarrow 3sa_1$	$\tilde{a}^3B_1$	6.85	6.68	7.26	7.0
$1b_1 \rightarrow 3sa_1$	$\tilde{A}^1B_1$	7.58	7.30	7.61	7.49
$1b_1 \rightarrow 3pb_2$	$^3A_2$	8.81	8.68	9.34	8.9
$1b_1 \rightarrow 3pb_1$	$\tilde{d}^3A_1$	9.58	9.70	9.74	9.81
$3a_1 \rightarrow 3sa_1$	$\tilde{b}^3A_1$	8.91	9.02	9.44	9.3

*a*, this work; *b*, Ref. 23; *c*, Ref. 24; *d*, Ref. 8.

of these approximate excited states to the SMC method, the difference between the total electronic energies of a given excited state and the ground state was used for the threshold energy. Tables 4.2 and 4.3 give the vertical excitation energies for the various transitions of interest here as well as expectation values of  $\langle x^2 \rangle$ ,  $\langle y^2 \rangle$ , and  $\langle z^2 \rangle$  for the Rydberg orbitals of these states. For the dipole allowed  $\tilde{A}^1B_1$  excitation, the oscillator strength, computed using the length form, was found to be 0.027. Although smaller than the experimental value of 0.04–0.06, this value is in reasonable agreement with oscillator strengths obtained in similar SCF calculations[25].

The body-fixed scattering amplitude was computed in the linear momentum representation and then transformed into the angular momentum representation. Integral and differential cross sections were obtained by transforming the body-fixed partial wave amplitude to the lab-frame and then averaging over the Euler angles. In the partial wave expansion of the scattering amplitude,  $l_{max} = 7$  was used for the triplet excitations, whilst for the dipole allowed transition, the SMC contribution to the scattering amplitude was limited to  $l_{max}=6$ . The procedure is straightforward and details are given elsewhere [18].

Table 4.3 Characterization of the Rydberg Orbitals for Excited States of Water

Orbital	$\langle x^2 \rangle$	$\langle y^2 \rangle$	$\langle z^2 \rangle$
$3s_{a_1}$	4.20	6.86	6.55
$3p_{b_2}$	4.35	6.36	14.38
$3p_{b_1}$	25.74	8.98	8.59

For dipole-allowed excitations such as the  $\tilde{X}^1A_1 \rightarrow \tilde{A}^1B_1$  transition here, a purely  $L^2$  expansion of the scattering wave function in the SMC variation expression is inadequate due to the significant contribution expected from higher partial waves to the scattering amplitude in these cases. In these studies, the higher partial wave contribution to the scattering amplitude is included via a Born-closure procedure (see Chapter 2). This approach is identical to that used in a recent application of the SMC method to electronic excitation of CO [20] as well as in applications of the complex Kohn method to electronic excitation of the  $V(\pi \rightarrow \pi^*)$  state of ethylene [21]. For the purposes of this study, the long-range interaction was approximated by the point dipole potential in the First Born approximation (FBA). Further details are given in [20] and Chapter 2. Note, as these calculations were carried out in the fixed nuclei approximation, this procedure does not correctly treat the long range dipole potential in the elastic channel. This would require taking nuclear motion and rotational excitation of the target into account. Inclusion of such effects is of little relevance to the electronically inelastic processes which are the primary focus of interest in this paper.

In these multichannel studies, we found that it was important to monitor the condition number of the matrix  $A^{(+)}$  of Eq. (1.7). Numerical techniques previously described by Winstead and McKoy [19], based on singular-value decomposition, were used to eliminate instabilities associated with poor conditioning. Extensive calculations with several basis sets indicate that the cross sections presented below are well converged.

Two-channel calculations were carried out for all five excitations. Although a large number of different channel coupling schemes were investigated, only three

multichannel coupling schemes will be considered in this paper. In the first of these schemes the ground state and the triplet states, *i.e.*, the  $\tilde{X}^1A_1$ ,  $\tilde{a}^3B_1$ ,  $\tilde{d}^3A_1$ ,  $^3A_2(1b_1 \rightarrow 3pb_2)$ , and  $\tilde{b}^3A_1$  states, were included. The second calculation couples the  $\tilde{A}^1B_1$ ,  $\tilde{a}^3B_1$ ,  $\tilde{d}^3A_1$ , and  $^3A_2(1b_1 \rightarrow 3pb_2)^3$  states with the ground state. These excitations are all related in that they involve promotion of a lone pair  $1b_1$  electron to one of several Rydberg orbitals. In the third calculation, only the  $\tilde{A}^1B_1$  and  $\tilde{a}^3B_1$  are coupled with the elastic channel.

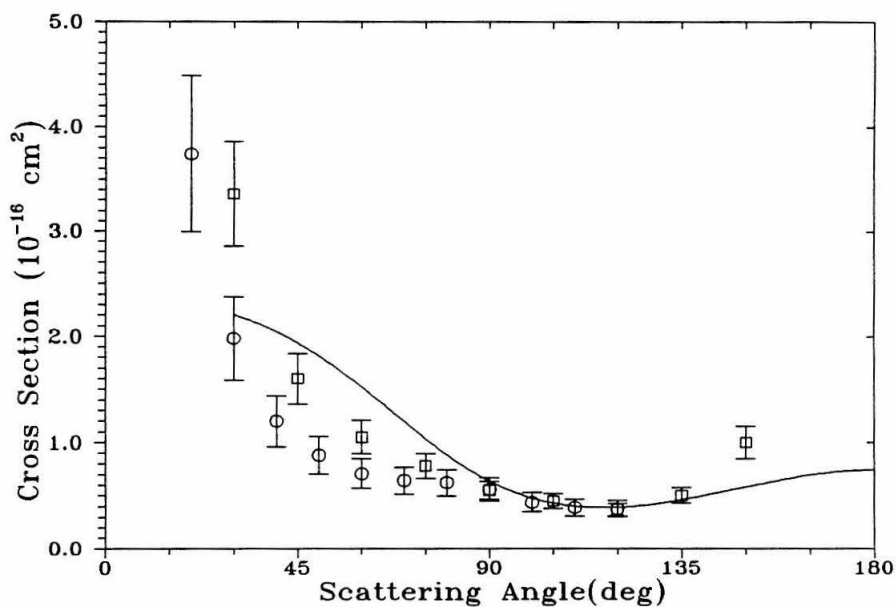


Figure 4.1. Elastic differential cross sections(DCS) at 6 eV: The solid line are present SMC results; (O) are measured values of [30]. (□) are measured values of [27].

### 4.3 Results and Discussion

#### 4.3.1 The Elastic Channel

Although the cross sections for electronic excitation of water are the main objective of these studies, it is useful to report the elastic cross sections resulting from these calculations. Since the same expansion of the total scattering wave function was used below and above the inelastic thresholds, these elastic cross sections do include some effects of target polarization due to “closed” channel determinants in Eq. 1.16.

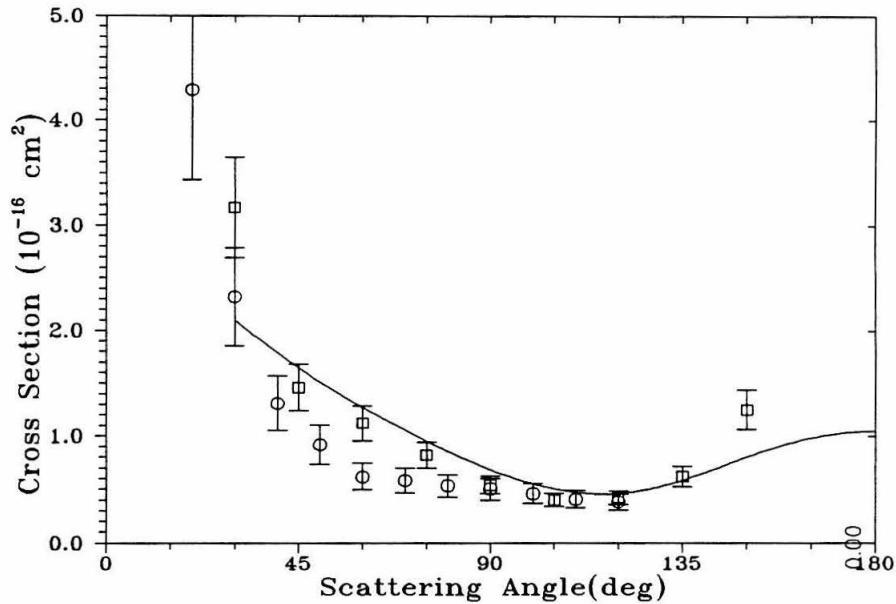


Figure 4.2. Same as Figure 4.1 at 8 eV.

Figures 4.1 to 4.6 show the elastic differential cross sections (DCS) along with the experimental data of [27] and [30], and the calculated values of Sato *et al.* [29] at impact energies ranging from 6 to 30 eV. Since these fixed nuclei DCS are well known

to be divergent as the scattering angle approaches zero, we show our calculated cross sections only down to  $20^\circ$ . Agreement with the measured values is satisfactory at all energies, although the cross section at the highest angle reported by Shyn *et al.* [30] is consistently higher than the SMC results.

Figure 4.7 shows the momentum transfer cross sections derived from the calculated differential cross sections of Figs. 4.1 to 4.6 along with values calculated from measured DCS's and results of other calculations. Below 8 eV the SMC results are in relatively good agreement with both the experimental results of Danjo and Nishimura [27] and the calculated cross sections of Jain and Thompson [28] using

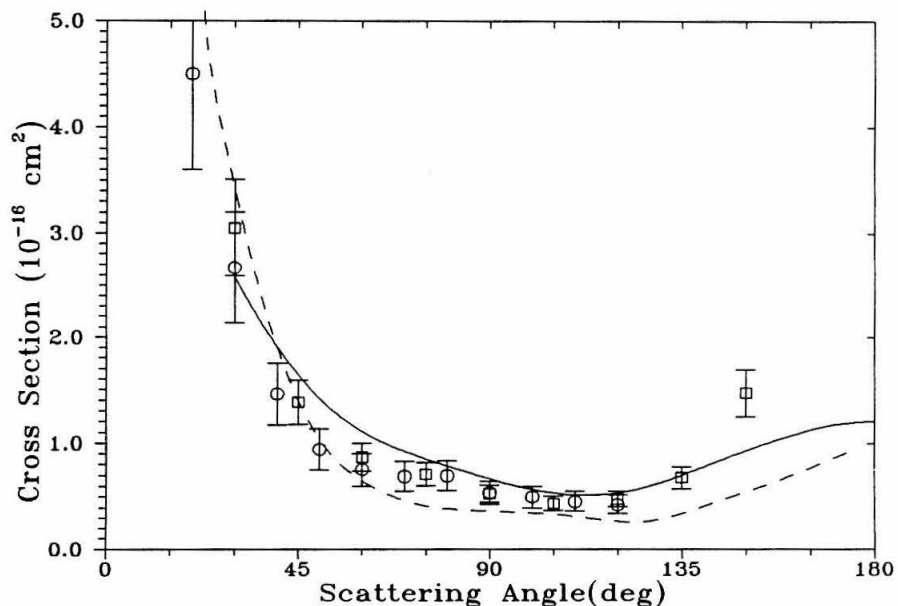


Figure 4.3. Elastic channel DCS at 10 eV: The solid line are present SMC results; (○) are measured values of [30]; (□) are measured values of [27]; the long-dash line is the calculated result of [29].

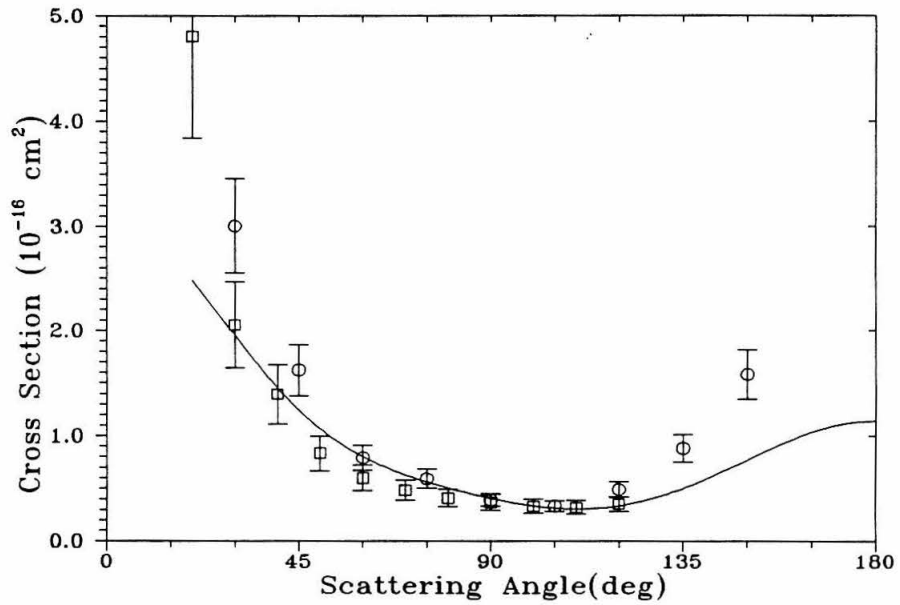


Figure 4.4. Same as Figure 4.1 at 15 eV.

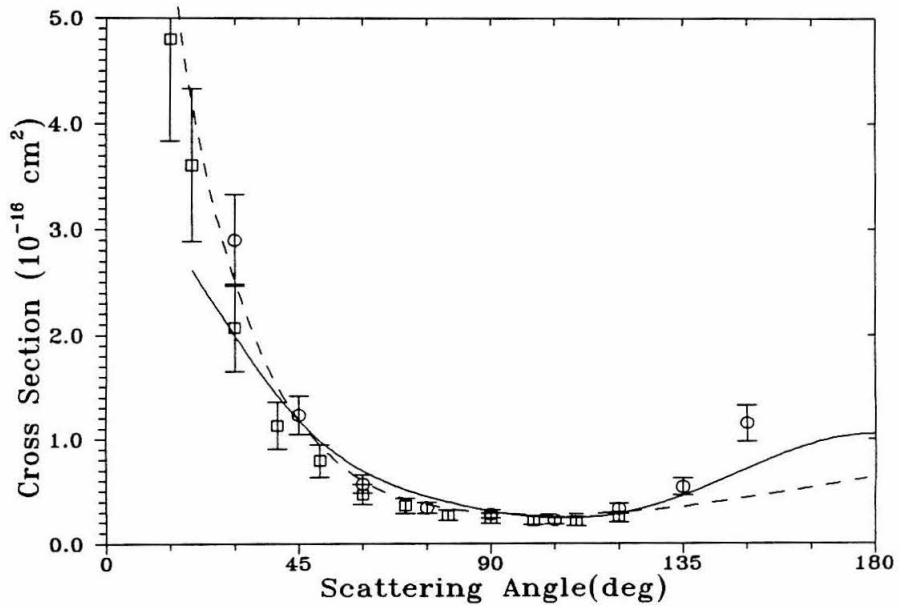


Figure 4.5. Same as Figure 4.3 at 20 eV.

a static-plus-model-exchange potential, and static, model exchange plus polarization potential [38]. The values derived from the measured DCS of Shyn and Cho [30] are considerably larger than our calculated values due to the larger high-angle scattering seen in their measured DCS.

#### 4.3.2. The $\tilde{A}^1B_1(1b_1 \rightarrow 3sa_1)$ State

The cross section for excitation of this optically allowed transition, which appears prominently in EEL spectra [4–8] as a well separated peak at  $\sim 7.4$  eV, are shown in Figs. 4.8 and 4.9. Figure 4.8 shows total cross sections obtained from calculations with two channels, three channels ( $\tilde{X}^1A_1$ ,  $\tilde{A}^1B_1$ ,  $\tilde{a}^3B_1$ ) and five channels ( $\tilde{X}^1A_1$ ,  $\tilde{A}^1B_1$ ,  $\tilde{a}^3B_1$ ,  $\tilde{d}^3A_1$ , and  ${}^3A_2(1b_1 \rightarrow 3pb_2)$ ) open. Only near threshold do

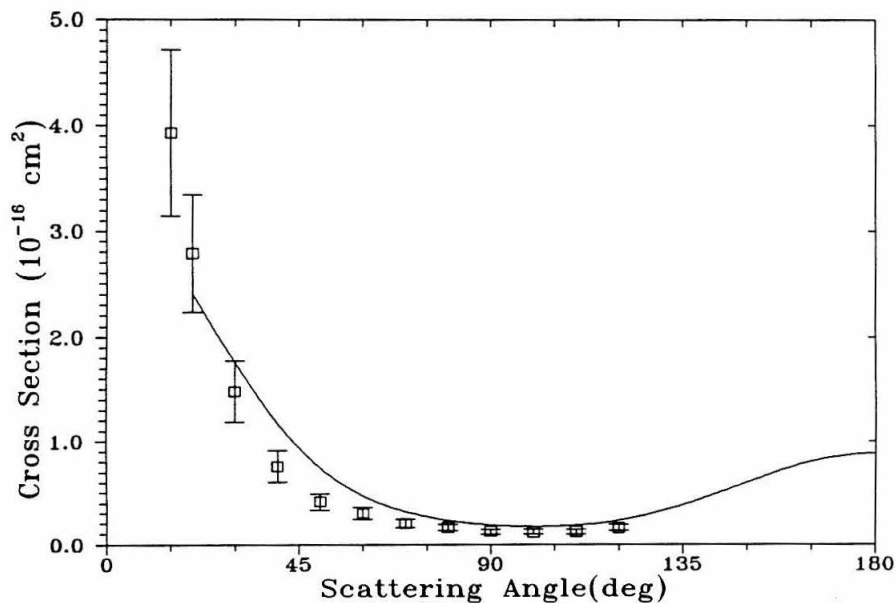


Figure 4.6. Same as Figure 4.3 at 30 eV.

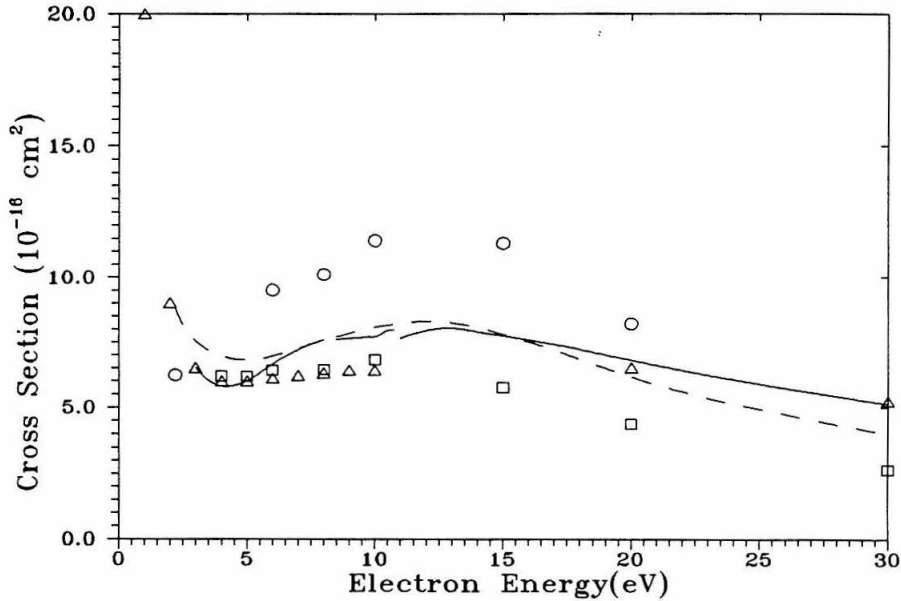


Figure 4.7. Momentum transfer cross sections for the elastic channel: the solid line shows the present SMC results; long dash line is the continuum multiple-scattering cross section [29]; (○) values are derived from measured DCS of Shyn and Cho [30]; (△) are calculated cross sections of Jain and Thompson [28] and Jain[38]; (□) are derived from DCS measurements of Danjo and Nishimura [27].

these cross sections exhibit significant sensitivity to the channel coupling scheme. For the two- and three-channel cases, the  $^2B_1$  and  $^2A_2$  symmetries are the dominant components of the peak near threshold. In the five-channel calculation, however, the  $^2A_2$  component of the cross section is reduced considerably between 11 and 15 eV. This leads to the substantial reduction of the cross sections in this energy range. This reduction in the  $^2A_2$  component to the cross section in this channel is accompanied by an enhancement of the contribution of this symmetry component to the cross section for the  $^3A_2(1b_1 \rightarrow 3pb_2)$  state.

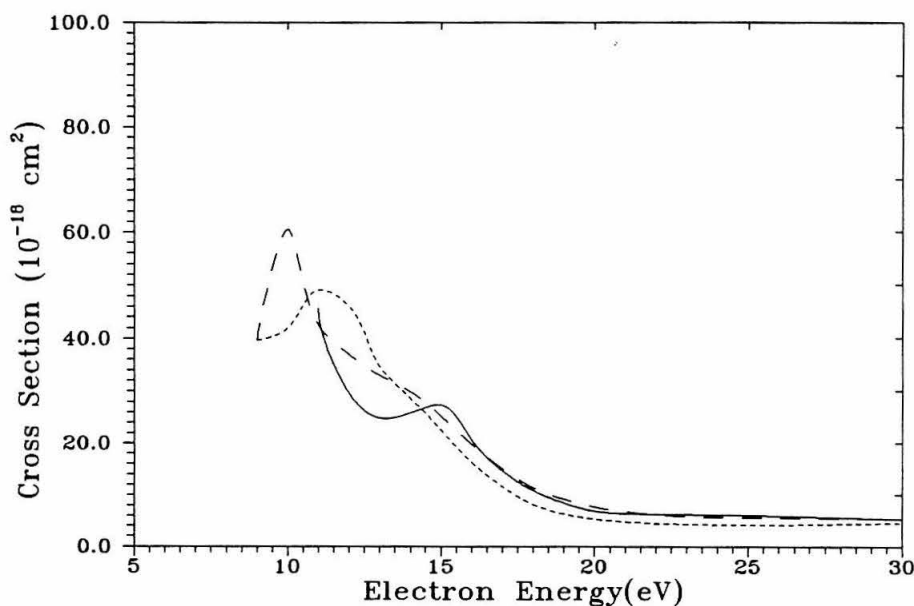


Figure 4.8. Integral excitation cross sections for excitation of the  $\tilde{A}^1B_1$  state: (- - - -) two channel results; (- . - .), three channel( $\tilde{X}^1A_1, \tilde{A}^1B_1, \tilde{a}^3B_1$ ) results; (—), five open channels(see text).

Figure 4.9 shows differential cross sections for excitation of this state. The Born term does not contribute significantly to the integral cross section below 20 eV, although it does increase the differential cross section at small scattering angles considerably, even at 15 eV. The relative measurements of these DCS by Trajmar, *et al.* [8] at 15 and 20 eV are also shown. These cross sections are normalized to the SMC results at 30°. Agreement between the calculated and measured cross sections is good at 20 eV but larger differences are seen at 15 eV.

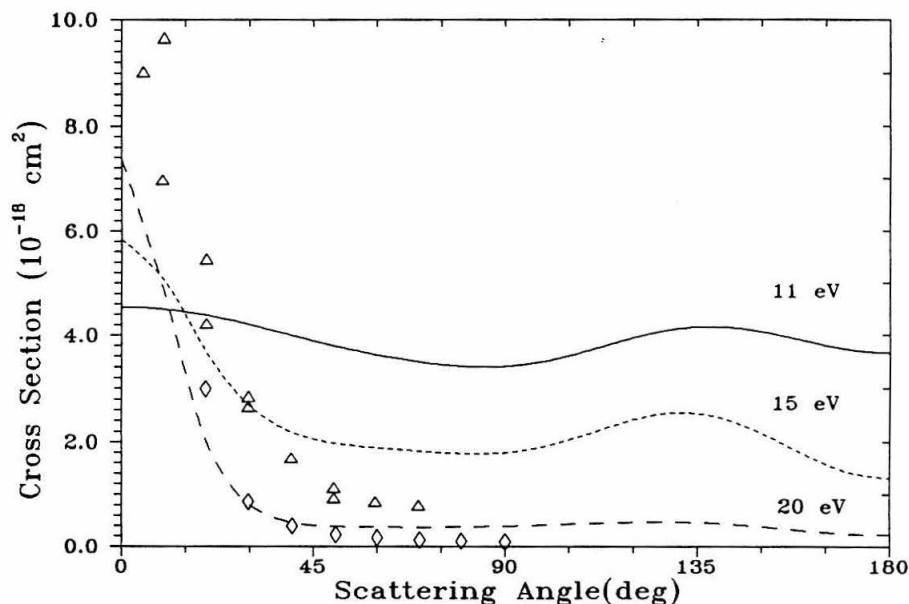


Figure 4.9. Differential cross sections for excitation of the  $\tilde{A}^1B_1$  state obtained with five open channels(see text): (—), 11 eV results; (- - -), DCS at 15 eV; (- · - ·), DCS at 20 eV; ( $\Delta$ ) are relative DCS measurements of Trajmar *et al.* [8] at 15 eV normalized to the calculated results at  $30^\circ$ ; ( $\diamond$ ), same at 20 eV.

### 4.3.3 The $\tilde{a}^3B_1$ ( $1b_1 \rightarrow 3sa_1$ ) State

Excitation of this state is evident in high-angle EEL measurements of water as a broadening of the  $\tilde{X}^1A_1 \rightarrow \tilde{A}^1B_1$  peak [8]. Figure 4.10 shows the excitation cross section for this state obtained from two-state, three-state ( $\tilde{X}^1A_1$ ,  $\tilde{A}^1B_1$ ,  $\tilde{a}^3B_1$ ), and two five-channel ( $\tilde{X}^1A_1$ ,  $\tilde{a}^3B_1$ ,  $\tilde{d}^3A_1$ ,  ${}^3A_2(1b_1 \rightarrow 3pb_2)$ ,  $\tilde{b}^3A_1$ ); ( $\tilde{X}^1A_1$ ,  $\tilde{a}^3B_1$ ,  $\tilde{A}^1B_1$ ,  $\tilde{d}^3A_1$ ,  ${}^3A_2(1b_1 \rightarrow 3pb_2)$ ) calculations. The opening of the  $\tilde{A}^1B_1$  channel in

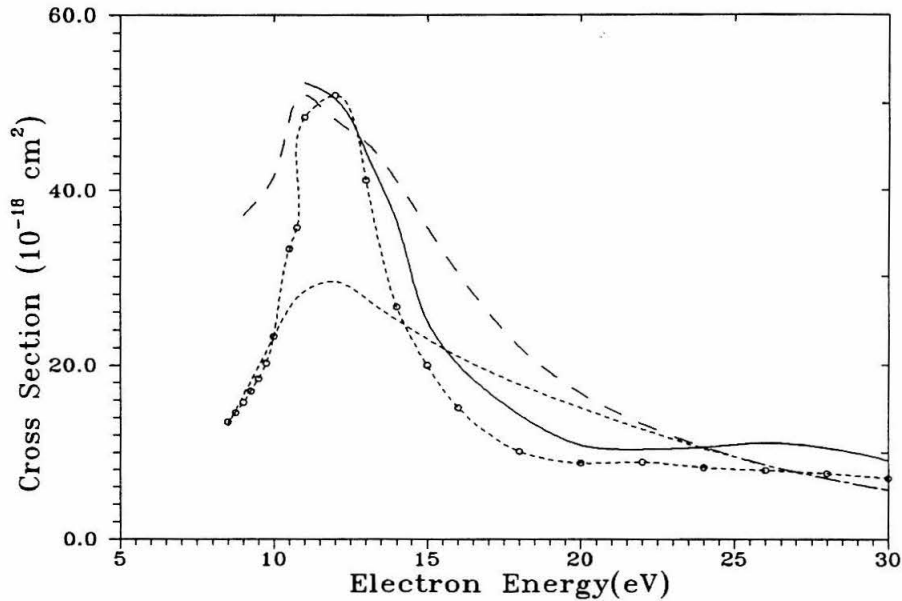


Figure 4.10. Integral cross sections for excitation of the  $\tilde{a}^3B_1$  state: (---), two channel results; (----), three-channel ( $\tilde{X}^1A_1, \tilde{A}^1B_1, \tilde{a}^3B_1$ ) calculation; (-o-o-o-), results of a five channel ( $\tilde{X}^1A_1, \tilde{a}^3B_1, \tilde{d}^3A_1, {}^3A_2(1b_1 \rightarrow 3pb_2), \tilde{b}^3A_1$ ) calculation; (—), results of a five channel calculation involving the ( $\tilde{X}^1A_1, \tilde{a}^3B_1, \tilde{A}^1B_1, \tilde{d}^3A_1, {}^3A_2(1b_1 \rightarrow 3pb_2)$ ) states.

the three-state calculation clearly leads to a significant deviation from the two-state results. However, at the five-channel level, the opening of this channel does not influence the cross section substantially. Our calculated differential cross sections are shown in Fig. 4.11. They exhibit the lack of forward peaking typical of intercombination singlet  $\leftrightarrow$  triplet excitations. The differential cross sections of our other five-channel calculations are similar to those of Fig. 4.11 and are not shown here. Unlike the singlet transition, the cross section for excitation of the  $\tilde{a}^3B_1$  state is dominated ( $\sim 60\%$ ) by the  ${}^2A_1$  symmetry component for all energies.

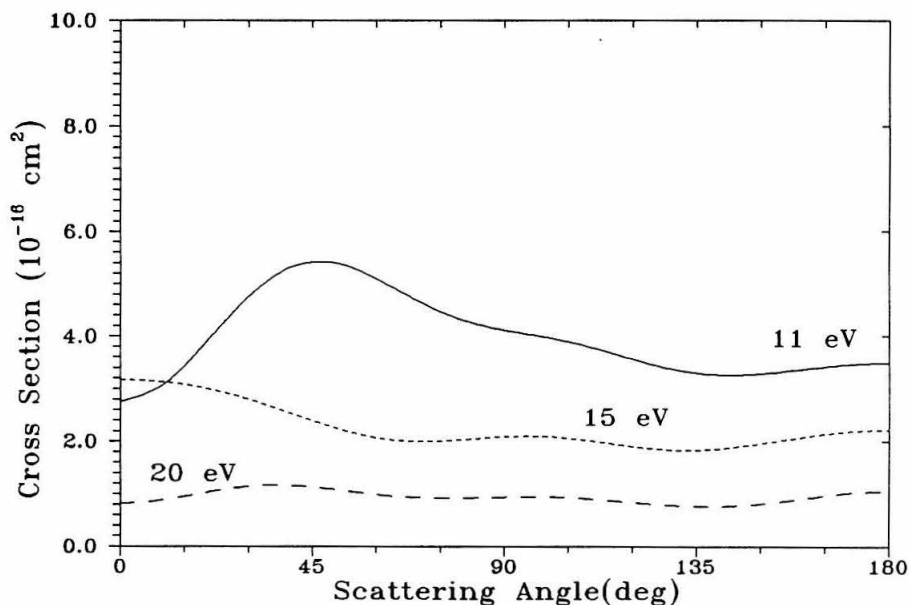


Figure 4.11. Differential cross sections for excitation of the  $\tilde{a}^3B_1$  state from the  $(\tilde{X}^1A_1, \tilde{a}^3B_1, \tilde{A}^1B_1, \tilde{d}^3A_1, {}^3A_2(1b_1 \rightarrow 3pb_2))$  five channel calculation: (—), 11eV; (- - - - -), 15 eV; (- · - · - ·), 20 eV.

#### 4.3.4 The $\tilde{b}^3A_1$ ( $3a_1 \rightarrow 3sa_1$ ) State

This state was considered previously in our earlier two-channel studies [17]. Figure 4.12 shows our integral excitation cross sections for this state obtained from the present two- and five-channel  $(\tilde{X}^1A_1, \tilde{a}^3B_1, \tilde{d}^3A_1, {}^3A_2(1b_1 \rightarrow 3pb_2), \tilde{b}^3A_1)$  calculations. The two-state cross sections in Fig. 4.12 differ somewhat from those of Ref. 17 due to the finer numerical quadratures of the  $VG_P^{(+)}V$  matrix elements, which are now practical on the Intel parallel computers being used in these calculations.

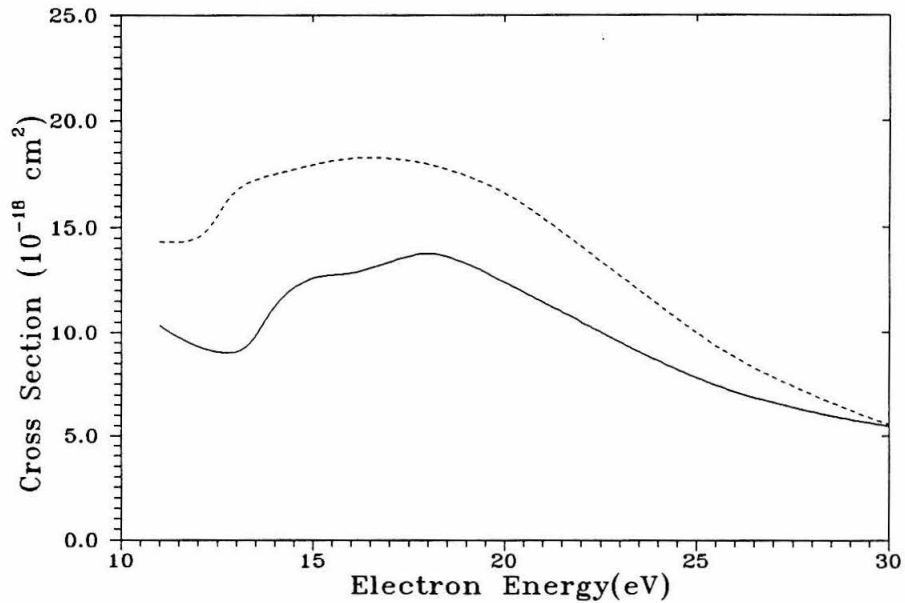


Figure 4.12. Integral cross sections for excitation of the  $\tilde{b}^3A_1$  state: (—), five channel results; (- - - -) two-channel coupling.

Comparison of the two and five-state cross sections indicates that multichannel coupling does not change the underlying symmetry composition of these cross sections, but uniformly reduces their magnitudes. The  $^2A_1$  symmetry component is the dominant contributor to these cross sections.

The DCS's for excitation of this state obtained from our five-channel calculation are shown in Fig. 4.13.

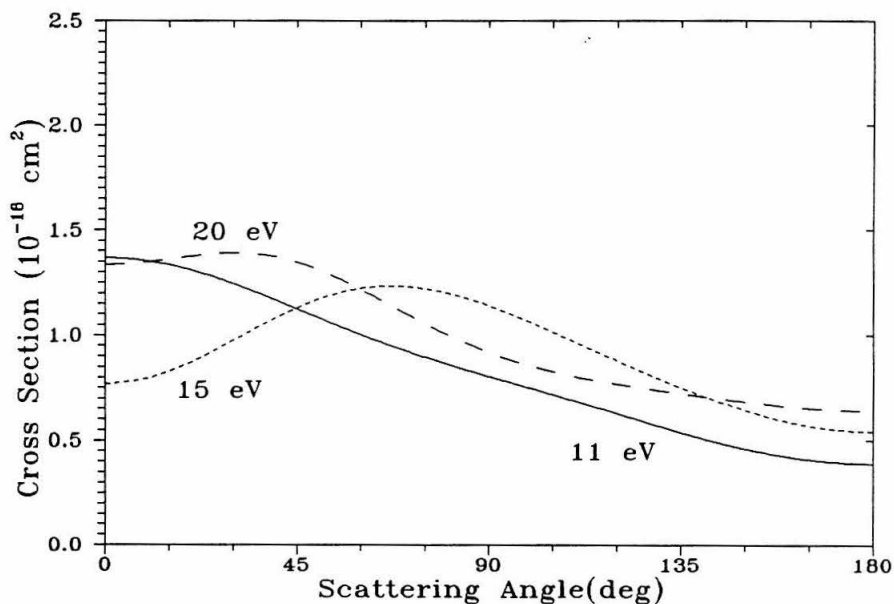


Figure 4.13. Differential cross sections for excitation of the  $\tilde{d}^3A_1$  state: (—), 11 eV results; (- - - -), 15 eV; (- · - · -), 20 eV.

#### 4.3.5 The $\tilde{d}^3A_1$ ( $1b_1 \rightarrow 3pb_1$ ) State

Our calculated two- and five-channel excitation cross sections for this state, the highest lying of those considered in this study, are shown in Fig. 4.14. These results show that channel coupling leads to a substantial reduction in the two-state cross sections near threshold. Above 15 eV, the dominant  $^2A_1$  and  $^2B_1$  contributions to the total cross section are comparable in both the two-channel and multichannel calculations.

Figure 4.15 shows our calculated five-channel ( $\tilde{X}^1A_1$ ,  $\tilde{a}^3B_1$ ,  $\tilde{A}^1B_1$ ,  $\tilde{d}^3A_1$ ,  $^3A_2(1b_1 \rightarrow 3pb_2)$ ) excitation cross sections of Fig. 4.14 for the  $X^1A_1 \rightarrow \tilde{d}^3A_1$  transition along with data of Becker *et al.* [15] and Möhlmann *et al.* [16]. These

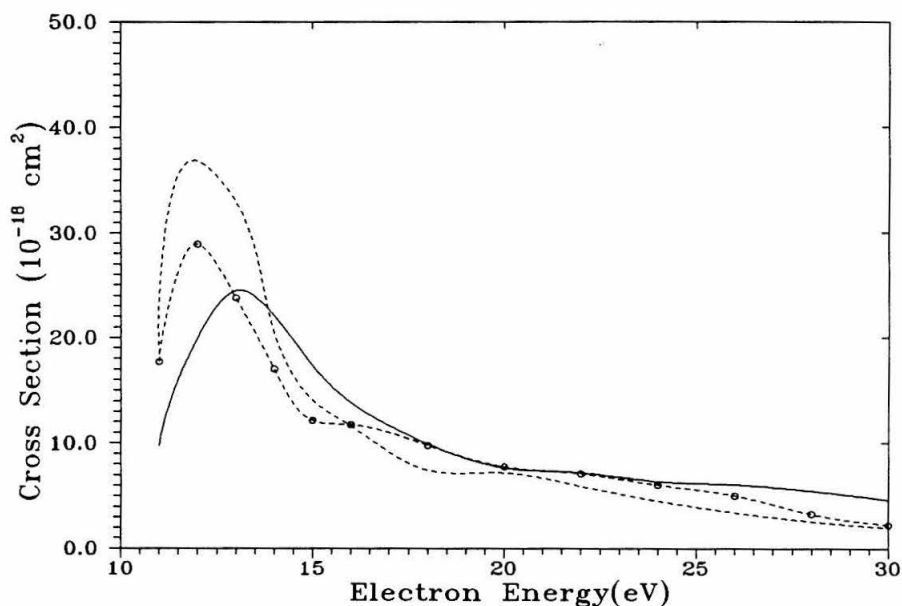


Figure 4.14. Integral cross sections for excitation of the  $\tilde{d}^3A_1$  state: (- - - - -), two channel results; (-o-o-o-), five channel ( $\tilde{X}^1A_1, \tilde{a}^3B_1, \tilde{d}^3A_1, {}^3A_2(1b_1 \rightarrow 3pb_2), \tilde{b}^3A_1$ ) coupling; (—) five-channel calculation coupling the ( $\tilde{X}^1A_1, \tilde{a}^3B_1, \tilde{A}^1B_1, \tilde{d}^3A_1, {}^3A_2(1b_1 \rightarrow 3pb_2)$ ) states.

data are derived from measurements of  $\text{OH}(A^2\Sigma^+ \rightarrow X^2\Pi)$  UV fluorescence radiation generated by electron impact dissociation of  $\text{H}_2\text{O}$ . In both experiments, the contribution of triplet excitations to the final fluorescence yield was estimated by monitoring rotationally cool  $Q_1(2), Q_1(3)$  and rotationally hot  $P_1(21), P_1(27)$  lines. Electronic structure studies [25] and the energy dependence of the two different lines indicate that only singlet excitations contribute to the rotationally hot lines ( $T=13800$  K), while the rotationally cool lines are produced by both triplet ( $T=4000$  K) and singlet excitations ( $T=2900$  K). By assuming that the energy dependence of the singlet excitation rate is similar for both the hot and cool lines, the singlet

contribution to the cool line can be approximately removed [15,16]. With these assumptions, the data of Möhlmann *et al.* lead to a maximum near 12.6 eV while Becker *et al.* found a maximum at 14.2 eV.

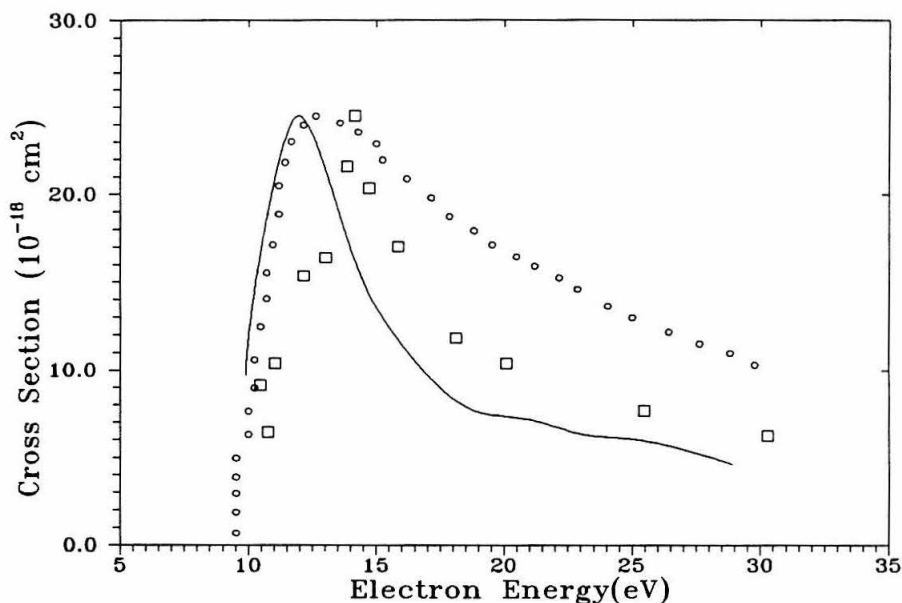


Figure 4.15. Cross sections for excitation of the  $\tilde{d}^3 A_1$  state of  $H_2O$ : (—), calculated values; (o) are derived from  $OH(A^2\Sigma^+)$  fluorescence measurements by Becker *et al.* [15]; ( $\square$ ), analogous measurements of Möhlmann *et al.* [16]. Note that both sets of results are normalized to the maximum in the calculated cross sections and that the calculated cross sections have been shifted by 1.5 eV to match the experimentally observed threshold for OH fluorescence (9.3 eV).

Symmetry considerations restrict the state leading to dissociation into  $OH(A^2\Sigma^+) + H(n=1)$  to either  $^1,^3A_1$  or  $^1,^3B_2$  symmetries. Energy considerations (a threshold of  $\sim 9.3$  eV) and electronic structure calculations of excited states of water suggest that the  $\tilde{X}^1A_1 \rightarrow \tilde{d}^3A_1$  ( $1b_1 \rightarrow 3pb_1$ ) transition is most likely the main triplet contributor to the measured fluorescence. In earlier work Beenakker

*et al.* [33] suggested that the  $\tilde{d}^3A_1(3a_1 \rightarrow 3sa_1)$  state may also contribute to the triplet component of the fluorescence excitation cross section.

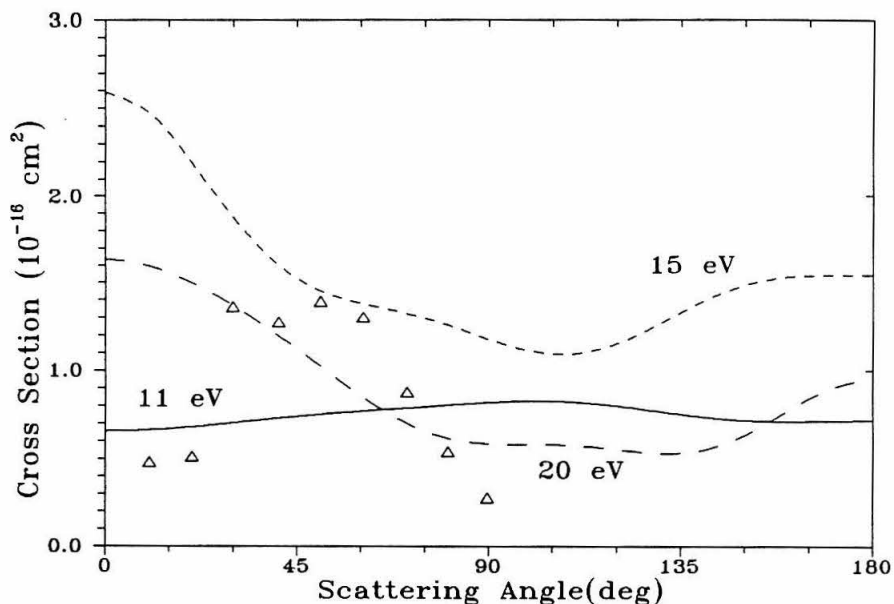


Figure 4.16. Differential cross sections for excitation of the  $\tilde{d}^3A_1$  state: (—), 11 eV results; (- - - -), 15 eV; (- · - · -), 20 eV;  $\Delta$ , measured relative values of [8]. The ( $\Delta$ ) indicate relative DCS measurements of Trajmar *et al.* [8] normalized to the present results at  $30^\circ$ .

In Fig. 4.15 the calculated cross sections have been shifted by 1.5 eV to bring the threshold for the  $X^1A_1 \rightarrow \tilde{d}^3A_1$  excitation used in these calculations into agreement with the experimentally observed threshold for generation of  $\text{OH}(A^2\Sigma^+ \rightarrow X^2\Pi)$  fluorescence. The measured relative data were also scaled to have their maximum values equal to the calculated values. The calculated cross sections show a rapid rise near threshold and agree quite well with the measurements of Becker *et al.* in this region. The calculated cross sections, however, decrease more rapidly with increasing energy than the cross sections attributed to triplet

state excitations in analysis of the fluorescence data [15,16]. This behavior and the fact that the measured cross sections of Möhlmann *et al.* peak at energies higher than that for the SMC could be due to assumptions concerning the contribution of singlet states to the rotationally “normal” OH molecules. In fact, Becker *et al.* suggest that a dissociation channel available to the  $\tilde{B}^1A_1$  state above 10.2 eV which leads to rotationally “normal” OH, may contribute significantly to the population of rotationally cool OH. This is supported by the observation that in photodissociation experiments, in which the triplet contribution is negligible, such a “normal” rotational population is not seen when a Ly $\alpha$  or Kr resonance line light source is used [39,40]. Furthermore, predissociation of higher Rydberg states by the  $\tilde{b}^3A_1$  state at these higher impact energies also leads to “normal” OH populations [32]. In either case, the analysis used to extract the triplet contribution in the studies of refs. 15 and 16 can lead to underestimation of the singlet contribution to the rotationally cool OH( $A^2\Sigma^+$ ) population.

The corresponding DCS’s for excitation of the  $\tilde{d}^3A_1$  state obtained in these five-state calculations are shown in Fig. 4.16. Also shown are the relative differential cross sections of Trajmar *et al.* [8] for excitation of an electronic state of water at 9.81 eV by 20 eV electrons. These values have been normalized to the calculated cross sections at 30°. On the basis of energy level calculations, Hunt and Goddard [23] assigned this energy loss feature at 9.81 eV to the  $\tilde{d}^3A_1$  state of water. Agreement between the measured values and the calculated cross sections is fair for angles above 30° but poor at lower angles where the measured values fall off rapidly.

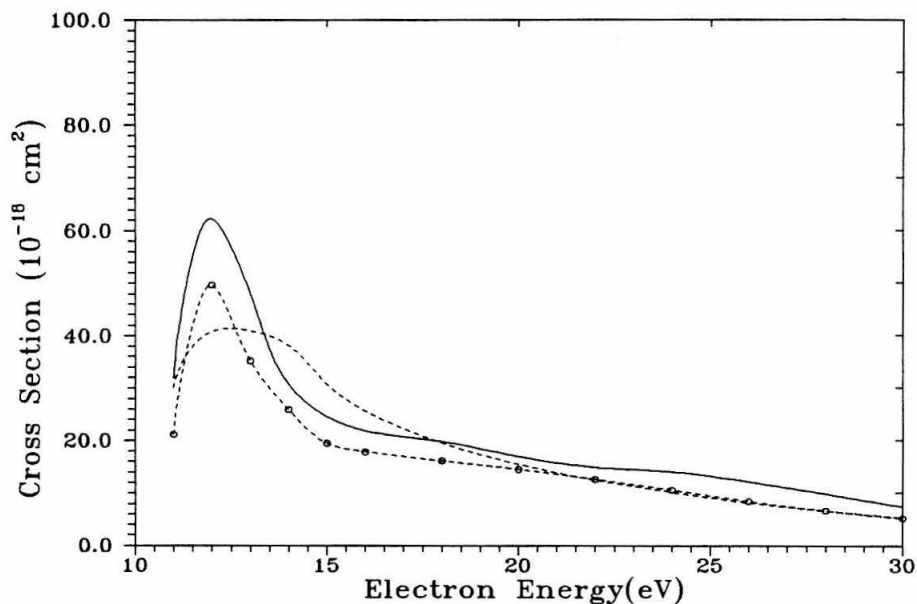


Figure 4.17. Integral cross sections for excitation of the  $(1b_1 \rightarrow 3pb_2)^3A_2$  state: (- - -), two-channel results, (-o-o-o-), five-channel ( $\tilde{X}^1A_1, \tilde{a}^3B_1, \tilde{d}^3A_1, {}^3A_2(1b_1 \rightarrow 3pb_2), \tilde{b}^3A_1$ ) results; (—), five-channel coupling ( $\tilde{X}^1A_1, \tilde{a}^3B_1, \tilde{A}^1B_1, \tilde{d}^3A_1, {}^3A_2(1b_1 \rightarrow 3pb_2)$ ).

#### 4.3.6 The ${}^3A_2(1b_1 \rightarrow 3pb_2)$ State

Integral cross sections for excitation of this state obtained from calculations with two and five open channels are shown in Fig. 4.17. As with the  $\tilde{d}^3A_1$  and  $\tilde{A}^1B_1$  transitions, channel coupling is seen to be important only near threshold.

Our calculated five-channel ( $\tilde{X}^1A_1, \tilde{a}^3B_1, \tilde{A}^1B_1, \tilde{d}^3A_1$ , and  ${}^3A_2(1b_1 \rightarrow 3pb_2)$ ) differential cross sections for excitation of this state are shown in Fig. 4.18. The 11 and 15 eV results are qualitatively similar to differential cross sections calculated for the  ${}^3A_2(n \rightarrow \pi^*)$  transition in formaldehyde using the complex Kohn [36] and

SMC [37] methods. A generalization of a symmetry property of  $\Sigma^+ \leftrightarrow \Sigma^-$  type transitions [35] to nonlinear molecules in order explain the relatively weak forward and backward scattering of the  ${}^3A_2$  type transitions has been discussed [36]. This effect is less pronounced at 20 eV for the water molecule.

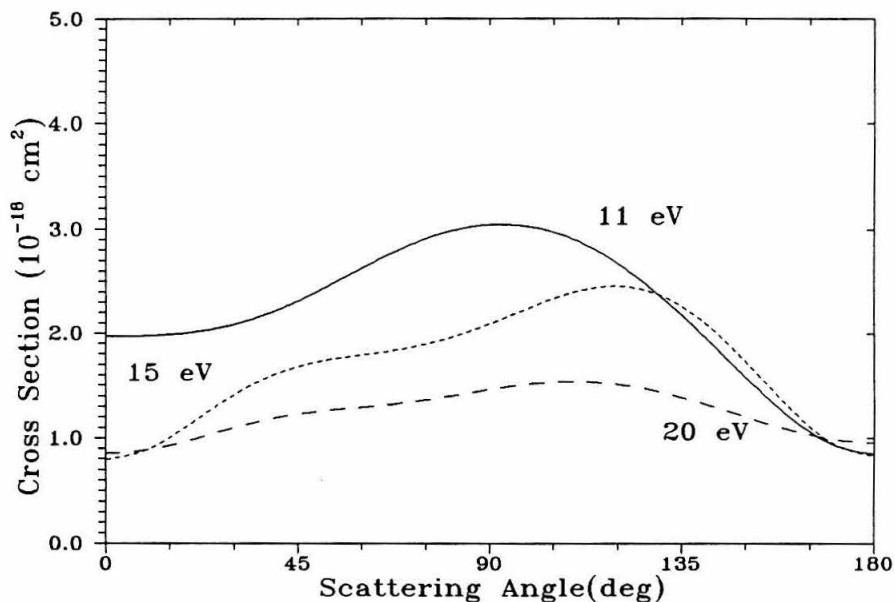


Figure 4.18. Differential excitation cross sections for excitation of the  $(1b_1 \rightarrow 3pb_2) {}^3A_2$  state: (—), (---), and (- - -), calculated five-channel ( $\tilde{X}^1A_1, \tilde{a}^3B_1, \tilde{A}^1B_1, \tilde{d}^3A_1, {}^3A_2(1b_1 \rightarrow 3pb_2)$ ) values at 11 eV, 15 eV, and 20 eV, respectively.

#### 4.3.7 Threshold Excitation Cross Sections

The relevance of the electronic transitions considered in this study, particularly to the  $\tilde{A}^1B_1$  and  $\tilde{a}^3B_1$ , to the modeling of radiation damage in biological materials has been discussed previously. The best available data for such electronically

inelastic transition, estimated from measured Townsend ionization coefficients and ionization cross sections, have been compiled by Hayashi[10]. The present studies can clearly provide useful estimates of the cross sections for excitation of the  $\tilde{A}^1B_1$  and  $\tilde{a}^3B_1$  dissociative states near threshold. The sum of these two cross sections as obtained from the five-channel ( $\tilde{X}^1A_1, \tilde{a}^3B_1, \tilde{A}^1B_1, \tilde{d}^3A_1, {}^3A_2(1b_1 \rightarrow 3pb_2)$ ) calculation are plotted in Fig. 4.19 along with the recommended values of Hayashi [10]. Our calculated cross sections have been shifted to match the experimental thresholds for the singlet (7.49 eV) and triplet (7.0 eV) excitations. The calculated values of these cross sections are significantly larger than the estimates of Hayashi near threshold. These more reliable, near-threshold cross sections could be of particular relevance to the calculation of electron degradation spectra [3] and similar quantities used in modeling radiation energy absorption in biological materials.

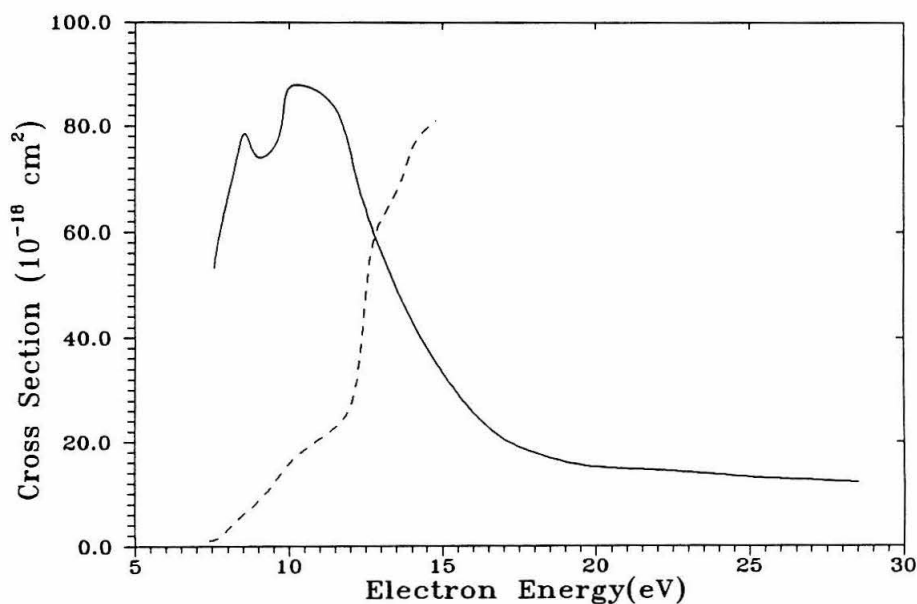


Figure 19. Sum of integral cross sections for excitation of the  $\tilde{a}^3B_1$  and  $\tilde{A}^1B_1$  states of water: (—), calculated values; (---), recommended values of [10]. See text.

#### 4.4 Conclusions

A multichannel study of the electron impact excitation of the water molecule to the  $\tilde{A}^1B_1$ ,  $\tilde{a}^3B_1$ ,  $\tilde{b}^3A_1$ ,  $\tilde{d}^3A_1$ , and  $^3A_2(1pb_1 \rightarrow 3pb_2)$  Rydberg states was carried out using several two and multichannel coupling schemes. Although multichannel effects were significant for all of the states excepting the  $\tilde{d}^3A_1$ , the effect is especially prominent in the  $^2A_2$  component of the  $\tilde{X}^1A_1 \rightarrow \tilde{A}^1B_1$  and  $\tilde{X}^1A_1 \rightarrow ^3A_2(1b_1 \rightarrow 3pb_2)$  cross sections. The  $\tilde{a}^3B_1$  cross section near the thresholds of the higher lying states is also observed to be more sensitive to the channel coupling scheme than its singlet analog. Although coupling via the potential led to modest changes in cross sections in some channels, the strongest effects are observed between channels coupled via the projection operator in Eq. 1.5, *i.e.*, connected by a shared recorelation term. This suggests that the most important multichannel effects are accounted for by coupling channels sharing a common hole, at least for the case of Rydberg excitations considered in this study.

In addition to multichannel features observed, the DCS for the  $\tilde{X}^1A_1 \rightarrow (1b_1 \rightarrow 3pb_2)^3A_2$  transition are found to be similar to those previously noted for symmetry equivalent transitions in other molecules. The integral cross section for the  $\tilde{X}^1A_1 \rightarrow \tilde{d}^3A_1$  qualitatively match the experimentally observed energy dependence of the yield of  $\text{OH}(A^2\Sigma^+)$  attributed to dissociation of this state when possible cascade contributions from higher lying states are taken into account.

The SMC derived cross sections for the  $\tilde{A}^1B_1$  and  $\tilde{a}^3B_1$  states point to the need for better estimates of these quantities either by experiment or other theoretical methods owing to the lack of reliable excitation cross section data, especially

considering their importance to the modeling of ionizing energy deposition in biological materials.

### References

- [1.] M. Singh, *Astrophys. Space Sci.* **141**, 75 (1988); M. Inokuti, in *Applied Atomic Collision Physics*, edited by C. F. Barnett, M. F. A. Harrison, H. S. W. Massey, E. W. McDaniel, and B. Bederson (Academic Press, New York, 1983), Vol. IV, pp. 179–236.
- [2.] J. J. Olivero, R. W. Stagat, and A. E. Green, *J. Geophys. Res.* **77**, 4797 (1972).
- [3.] M. A. Ishii, M. Kimura, and M. Inokuti, *Phys. Rev.* **42**, No. 11, 6486 (1990).
- [4.] A. Skerbele, M. A. Dillon, and E. N. Lassetre, *J. Chem. Phys.* **48**, 5042 (1968).
- [5.] W. C. Tam and C. E. Brion, *J. Elec. Spectros. Rel. Phenom.* **3**, 263 (1974).
- [6.] T. Pradeep and M. S. Hedge, *Spectrochimica Acta.* **44A**, No. 9, 883 (1988).
- [7.] K. H. Tan, C. E. Brion, Ph. E. Van Der Leeuw, and M. J. Van der Wiel, *Chem. Phys.* **29**, 299(1978).
- [8.] S. Trajmar, W. Williams, and A. Kuppermann, *J. Chem. Phys.* **58**, No. 6, 2521 (1973).

- [9.] A. Chutijian, R. I. Hall, and S. Trajmar, *J. Chem. Phys.* **63**, No. 2, 892 (1975).
- [10.] M. Hayashi, *Atomic and Molecular Data for Radiotherapy, Proceedings of an IAEA Advisory Group meeting, Vienna, June 1988, Report No. IAEA-TECDOC-506*, (International Atomic Energy Agency, Vienna, 1989).
- [11.] I. Shimamura, *Sci. Papers Inst. Phys. Chem. Res. (Rikagaku Kenkyusho)*, **82**, 1 (1989).
- [12.] T. Horie, T. Nagura, and M. Otsuka, *J. Phys. Soc. Japan* **11**, No. 1, 1157 (1956).
- [13.] I. V. Sushanin and S. M. Kishko, *Opt. Spectrosk.* **30**, 315 (1971).
- [14.] S. Tsurubuchi, T. Iwai, and T. Horie, *J. Phys. Soc. Japan* **36**, 537 (1974).
- [15.] K. Becker, B. Stumpf, and G. Schulz, *Chem. Phys. Letts.* **73**, No. 1, 102 (1980).
- [16.] G. R. Möhlmann, C. I. M. Beenakker, and F. J. De Heer, *Chem. Phys.* **13**, 375 (1976).
- [17.] H. Pritchard, V. McKoy, and M. A. P. Lima, *Phys. Rev. A* **41**, 546 (1990).
- [18.] W. M. Huo, T. L. Gibson, M. A. P. Lima, and V. McKoy, *Phys. Rev. A* **36**, 1632(1987); W. M. Huo, M.A.P. Lima, T. L. Gibson, and V. McKoy, *Phys. Rev. A* **36**, 1642(1987).
- [19.] C. L. Winstead and V. McKoy, *Phys. Rev. A* **41**(1), 49(1990).

- [20.] Q. Sun, C. Winstead, V. McKoy, Phys. Rev. A (in press).
- [21.] T. N. Rescigno and B. I. Schneider, Phys. Rev. A **45**(5), 2894 (1992).
- [22.] R. Poirier, R. Kari, and I. G. Csizmadia, *Handbook of Gaussian Basis Sets* (Elsevier, Amsterdam, 1985).
- [23.] W. A. Goddard and W. J. Hunt, Chem. Phys. Lett. **24**, 464 (1974).
- [24.] N. W. Winter, W. A. Goddard, and F. W. Bobrowicz, J. Chem. Phys. **62**, 4325 (1975).
- [25.] V. Staemmler, R. Jaquet, and M. Jungen, J. Chem. Phys. **74**(2), 1285(1981).
- [26.] J. Yuan and Z. Zhang, Phys. Rev. A **45**(7), 4565(1992).
- [27.] A. Danjo and H. Nishimura, J. Phys. Soc. Japan **54**, 1224 (1985).
- [28.] A. Jain and D. G. Thompson, J. Phys. B **15**, L631 (1982).
- [29.] H. Sato, M. Kimura, and K. Fujima, Chem. Phys. Lett. **145**, 21 (1988).
- [30.] T. W. Shyn and S. Y. Cho, Phys. Rev. A **36**, 5138 (1987).
- [31.] L. M. Brescansin, M. A. P. Lima, T. L. Gibson, and V. McKoy, J. Chem. Phys. **85**, 1854 (1986).
- [32.] S. Tsurubuchi, Chem. Phys. **10**, 335 (1975).
- [33.] C. I. M. Beenakker, F. J. De Heer, H. B. Krop, and G. R. Möhlmann, Chem. Phys. **6**, 445 (1974).

- [34.] N. Böse, H. Hertz, W. Sroka, R. Zietz, J. Harms, H. Oertel, and H. Schenk, *Verh. Dtsch. Physik. Ges.* **2**, 170(1976).
- [35.] D. C. Cartwright, S. Trajmar, W. Williams, and D. L. Huestis, *Phys. Rev. Letts.* **27**, 704 (1971).
- [36.] T. N. Rescigno, B. H. Lengsfeld, and C. W. McCurdy, *Phys. Rev. A* **41**, 2462 (1990).
- [37.] Q. Sun, C. Winstead, V. McKoy, and M. A. P. Lima, *Phys. Rev. A* (in press).
- [38.] A. Jain, *J. Phys. B* **21**, 905(1988).
- [39.] I. Yamashita, *J. Phys. Soc. Japan* **39**, 205(1975); T. Carrington, *J. Chem. Phys.* **41**, 2012(1964).
- [40.] R. E. Winters, J. H. Collins, and W. L. Courchene, *J. Chem. Phys.* **45**, 1931(1966).

## 5. Electronic Excitation of $N_2$ by Electron Impact

We report results of an application of the Schwinger Multichannel (SMC) method to the excitation of triplet and singlet valence states of nitrogen by low energy electron impact. Differential and integral cross sections for electronic excitation of the  $a^1\Pi_g$ ,  $B^3\Pi_g$ ,  $A^3\Sigma_u^+$ ,  $W^3\Delta_u$ ,  $w^1\Delta_u$ ,  $B'^3\Sigma_u^-$ , and  $a'^1\Sigma_u^-$  states are presented for impact energies above 10 eV. The behavior of cross sections for the  $A^3\Sigma_u^+$  state near threshold is also examined. Comparison is made with available experimental data and results of R-matrix calculations. Good agreement is found between the SMC cross sections and experimental values for most states. However, agreement with results of R-matrix calculations is fair for the  $A^3\Sigma_u^+$  and  $W^3\Delta_u$  states, but poor for the  $B^3\Pi_g$  state.

### 5.1 Introduction

Cross sections for electronic excitation of the nitrogen molecule are of considerable importance to our understanding of a wide range of natural phenomena and industrial processes. These include, for instance, the excitation conditions present in aurora, the dayglow of the Earth's atmosphere [1], Titan's dayside emissions [2], modeling of the spectral and radiative properties in bow shocks of reentry vehicles [3], the modeling of UV and IR band systems in  $N_2$  lasers [4], and the control of species present in silane -  $N_2$  discharges used in nitriding semiconductor surfaces [5]. In most of these cases, the most relevant parameter derived from these cross sections is the excitation rate coefficient. The importance of using accurate cross

sections to compute this coefficient and errors resulting from the use of unreliable values of these cross sections has been discussed [6].

In view of such need for accurate excitation rate coefficients, there have been several experimental studies of the cross sections for excitation of low-lying valence and Rydberg states of  $N_2$ . Earlier work, emphasizing resonant scattering processes, has been reviewed by Schulz [7]. A comprehensive review of experimental data on electronic excitation cross sections has been compiled by Trajmar *et al.* [8]. In fact, of all molecular systems except  $H_2$ , the  $N_2$  molecule has the largest data base of such cross sections. This system hence serves as a particularly good test of theoretical methods.

In contrast, relatively little theoretical work on the cross sections for non-resonant, electronic excitation of  $N_2$  by electron impact has been published. Early work includes that of Chung and Lin in which the First Born Approximation (FBA) was used in conjunction with the Ochkur and Rudge approximations to calculate cross sections for excitation of the  $a^1\Pi_g$ ,  $c'^1\Sigma_u^+$ ,  $a''^1\Sigma_g^+$ ,  $w^1\Delta_u$ ,  $b'^1\Sigma_u^+$ ,  $b^1\Pi_u$ ,  $A^3\Sigma_u^+$ ,  $B^3\Pi_g$ ,  $C^3\Pi_u$ ,  $D^3\Sigma_u^+$ ,  $W^3\Delta_u$ , and  $E^3\Sigma_g^+$  states of  $N_2$ [9]. References to earlier theoretical work are included in ref. [9]. Holley *et al.* have carried out a two-state, close-coupling calculation for excitation of the  $a^1\Pi_g$  state [10]. The Distorted Wave (DW) method has also been applied to the calculation of cross sections for some of these transitions [11,12]. More recently, the R-matrix method has been used to calculate integral cross sections for excitation of the  $A^3\Sigma_u^+$ ,  $W^3\Delta_u$ , and  $B^3\Pi_g$  states [13]. In this study, a multiconfiguration description of the target was employed.

The SMC method has been applied to the study of a number of molecular targets including H<sub>2</sub> [14,15], H<sub>2</sub>CO [16], C<sub>2</sub>H<sub>4</sub> [17], CO [18], CH<sub>4</sub> [19], H<sub>2</sub>O [20], and O<sub>2</sub> [21]. However, except for recent studies [15,18,20], these have included relatively few open electronic channels. Here, we report results of multichannel studies of the cross sections for excitation of the  $a^1\Pi_g$ ,  $B^3\Pi_g$ ,  $A^3\Sigma_u^+$ ,  $W^3\Delta_u$ ,  $w^1\Delta_u$ ,  $a'^1\Sigma_u^-$ , and  $B'^3\Sigma_u^-$  states using the SMC method. One of the goals of this study is to assess the importance of channel coupling on these cross sections. To this end, several channel coupling schemes are examined. In particular, we chose to consider a three-channel calculation in which only the  $3\sigma_g \rightarrow 1\pi_g$  type excitations are included ( $X^1\Sigma_g^+$ ,  $a^1\Pi_g$ ,  $B^3\Pi_g$ ), a six-channel calculation in which only the  $1\pi_u \rightarrow 1\pi_g$  type excitations are coupled to the ground state elastic channel ( $A^3\Sigma_u^+$ ,  $W^3\Delta_u$ ,  $w^1\Delta_u$ ,  $a'^1\Sigma_u^-$ , and  $B'^3\Sigma_u^-$ ), and a eight-channel calculation in which both types of excitations are coupled. The mixed valence-Rydberg  $b'^1\Sigma_u^+$  state at 12.9 eV was not included in these studies. The resulting cross sections are compared with the available, measured integral and differential cross sections and with results of close-coupling and R-matrix studies [10,13].

## 5.2 Computational Details

A large number of basis sets was used in the expansion of the target wavefunction and trial scattering functions (Eq. 1.9) so as to assess the convergence of our calculated cross sections. Final results are reported for the basis set given in Tables

Table 5.1a. Exponents of  $sp$ -type Cartesian Gaussians used in the target and scattering wavefunctions [22].

Center		Exponent	Contraction Coefficient
nitrogen	<i>s-type</i>	7476.7150	0.0000500
		1112.3654	0.0003940
		2512.6857	0.0020880
		703.77729	0.0089060
		225.47879	0.0320810
		79.615810	0.0974240
		30.237283	0.2317280
		12.263622	0.3775400
		5.2850860	1.0000000
		2.3334710	1.0000000
		0.9018560	1.0000000
		0.3583360	1.0000000
		0.1410930	1.0000000
nitrogen	<i>p-type</i>	126.66657	0.0011520
		29.837389	0.0090160
		9.3940380	0.0408140
		3.4051040	0.1301010
		1.3500000	0.2776790
		0.5576960	0.3807360
		0.2324490	1.0000000
		0.0942640	1.0000000

5.1a,b. The [13s8p/7s4p] set of  $sp$  functions (Table 5.1a) centered on the nitrogen atoms were taken from [22]. The set of  $d$  functions centered on the nitrogen atoms was chosen such that the smallest eigenvalues of the overlap matrix was greater

Table 5.1b. Additional uncontracted Cartesian Gaussians used in the target and scattering wavefunctions

Center		Exponents
nitrogen	<i>d-type</i>	1.520, 0.600
c.m.	<i>s-type</i>	0.05548, 0.021869, 0.00861
c.m.	<i>p-type</i>	0.038319, 0.001558
c.m.	<i>d-type</i>	0.150, 0.032

than  $10^{-5}$ . An additional [3s2p2d] set of functions was centered at the center of mass in order to increase the flexibility of the scattering basis (Table 5.1b). These exponents were selected largely by experimentation.

Table 5.2. Vertical threshold energies used for open channels. The IVO energies used for the present SMC calculations are given along with experimental values taken from Lofthus and Krupenie [40], SCF energies from Rose and McKoy [24], and CI energies of Ermler *et al.* [25].

Target State	Exp(eV)	IVO	SCF	MRD CI
$a^1\Pi_g$	9.39	10.47	9.44	9.72
$B^3\Pi_g$	8.12	8.45	7.66	8.50
$A^3\Sigma_u^+$	7.86	6.76	6.16	8.00
$W^3\Delta_u$	9.13–9.30	8.36	7.26	9.34
$w^1\Delta_u$	10.45–10.60	9.16	9.01	10.72
$B'^3\Sigma_u^-$	9.79	8.81	8.34	10.13
$a'^1\Sigma_u^-$	10.15–10.45	8.81	8.34	10.60

For the target state wavefunctions we used the improved virtual orbital (IVO) approximation [23]. The nuclei were held fixed at the experimental ground state internuclear distance of 2.068 a.u. In most cases, the  $1\pi_g$  IVO orbital was optimized for the  $B^3\Pi_g$  state. The electronic energies for the states of interest in this paper are listed in Table 5.2 along with *ab initio* calculations [24,25] and experiment [43]. Although the issue of threshold energies has been the object of considerable attention [13], our experience has shown that the cross sections for the  $N_2$  molecule for impact energies above 10 eV are negligibly affected by changes in threshold energies  $\leq 0.5$  eV for a given state. This behavior would not be expected to remain true for detailed studies very near the threshold ( $\sim 1$ eV) for a particular channel. In cases where the threshold region for a state is of interest, we use the experimentally observed excitation energies for given vibrational levels of the particular excited state. In calculations involving extensive channel coupling, the thresholds for the  $W^3\Delta_u$  and  $w^1\Delta_u$  states were used for the  $[1\pi_u \rightarrow 1\pi_g]$  triplet and singlet excitations respectively, while the thresholds for the  $B^3\Pi_g$  and  $a^1\Pi_g$  states were used for the  $[3\sigma_g \rightarrow 1\pi_g]$  triplet and singlet excitations.

The following channel coupling schemes were investigated using basis sets ranging from a minimal *sp* basis to the one listed in Tables 5.1a,b. Here the electronically elastic channel is always assumed to be open. Two-state calculations were carried out on the  $a^1\Pi_g$ ,  $B^3\Pi_g$ , and  $A^3\Sigma_u^+$  states. A three-state calculation involving coupling of the  $a^1\Pi_g$ , and  $B^3\Pi_g$  states was also done. For the  $[1\pi_u \rightarrow 1\pi_g]$  excitations, a study including only triplet excitations ( $X^1\Sigma_g^+$ ,  $A^3\Sigma_u^+$ ,  $W^3\Delta_u$ ,  $B'^3\Sigma_u^-$ ) was carried out, in addition to one coupling both singlets and triplets ( $X^1\Sigma_g^+$ ,  $A^3\Sigma_u^+$ ,  $W^3\Delta_u$ ,  $w^1\Delta_u$ ,  $B'^3\Sigma_u^-$ , and  $a'^1\Sigma_u^-$ ). A final set of calculations was carried out

in which all eight channels, counting the ground state were coupled. In the discussions of the individual excitations below, particular attention will be paid to the ( $X^1\Sigma_g^+, a^1\Pi_g, B^3\Pi_g$ ) three state; ( $X^1\Sigma_g^+, A^3\Sigma_u^+, W^3\Delta_u, w^1\Delta_u, B'^3\Sigma_u^-, a'^1\Sigma_u^-$ ) six state; and ( $X^1\Sigma_g^+, A^3\Sigma_u^+, W^3\Delta_u, w^1\Delta_u, B'^3\Sigma_u^-, a'^1\Sigma_u^-, B^3\Pi_g, a^1\Pi_g$ ) eight-state coupling calculations.

For convenience, tabulated values of the differential and integral cross sections reported in this paper for the eight-channel calculation, except where noted, are given in Tables 5.3–9 at the end of the text.

## 5.3 Results and Discussion

### 5.3.1 The $a^1\Pi_g$ State.

The importance of the Lyman–Birge–Hopfield (LBH)  $a^1\Pi_g \rightarrow X^1\Sigma_g^+$  emission system as a probe of the aurora and the dayglow [26,27] has served to motivate the accurate measurement of these excitation cross sections at low incident electron energies. Consequently there is a relatively large set of data obtained using a variety of experimental procedures with which to compare theoretical values. For example, the differential cross sections (DCS) for this excitation have been measured by Finn and Doering [31], Cartwright *et al.* [8,32], and Brunger and Teubner [33]. Furthermore, since cascade contributions via the various components of the Gaydon–Herman system and from other, higher-lying states are expected to contribute less than 5% to the measured emission cross sections [32,34], the fluorescence

excitation measurements of the cross sections by Ajello and Shemansky [30] are expected to be more reliable than for most states for which cascade contributions are typically difficult to estimate. Furthermore, the effect of predissociation of the

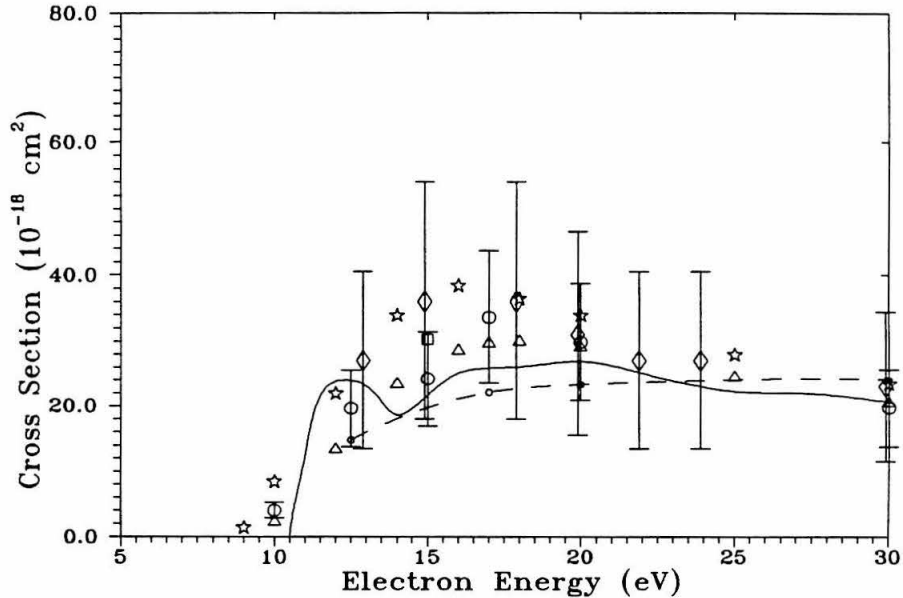


Figure 5.1. Integral cross sections for excitation of the  $a^1\Pi_g$  state. The present SMC+FBA results are indicated by the solid line. The close-coupling, two-state results of Holley *et al.* [10] are indicated by the short dashed line. Measured values of Borst [29] are indicated by ( $\star$ ), those of Finn and Doering [31] by ( $\diamond$ ), those of Shemansky and Ajello [30] ( $\triangle$ ), and those of Cartwright *et al.* [8,32] by ( $\circ$ ). Measurements of Trajmar [42] are marked by ( $\square$ ).

$a^1\Pi_g(v > 6)$  levels on the resulting fluorescence excitation cross section is known and can be accounted for. Exploiting the state's relatively long lifetime, Borst [29] has measured the excitation cross section using a metastable detection technique. The available data for this excitation generally suggests that the cross section rises rapidly from threshold (9.4 eV) to a maximum of  $\sim 35 \times 10^{-18} \text{ cm}^2$  near 17 eV

followed by a decrease whose  $1/E$  energy dependence at high energies is consistent with that anticipated for a dipole forbidden transition.

In contrast to numerous experimental studies, the most recent theoretical treatment of the excitation of this state is a close-coupling, two channel calculation of Holley *et al.* [10] in which integral cross sections were reported. Earlier work includes studies of Chung and Lin [9] which made use of the Born-Ochkur approximation.

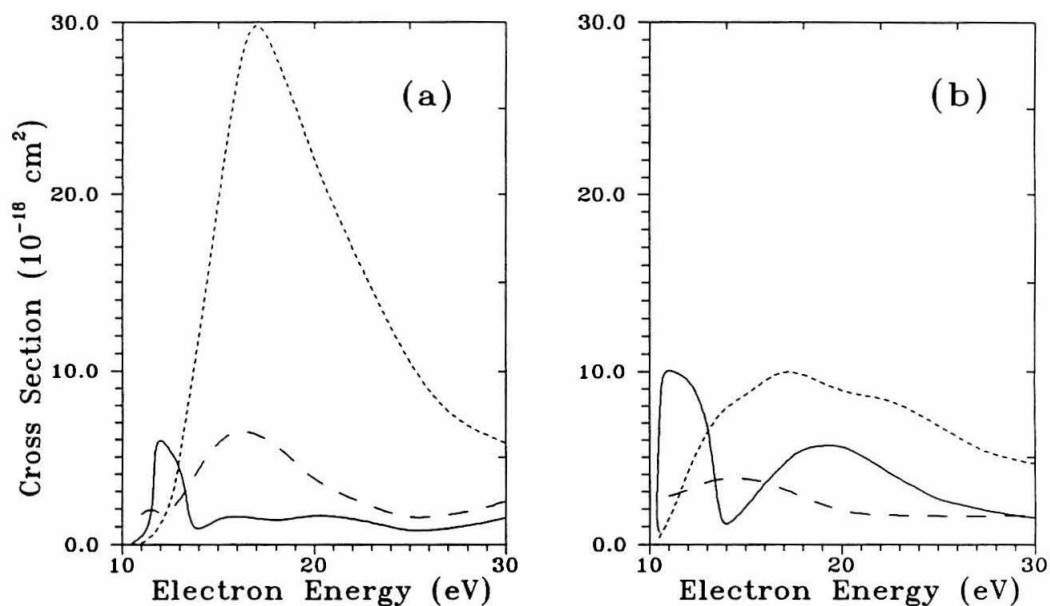


Figure 5.2. The  ${}^2\Pi_g$  component of the integral excitation cross section (SMC only) for excitation of the  $a^1\Pi_g$  state for  $\lambda = -1$  subcomponent (a), and  $\lambda = +1$  subcomponent (b). The short dashed line indicates results of a two-state ( $X^1\Sigma_g^+$ ,  $a^1\Pi_g$ ) calculation; long dashed line, results of a three-state ( $X^1\Sigma_g^+$ ,  $a^1\Pi_g$ ,  $B^3\Pi_g$ ) calculation; and solid line, results of the eight-channel calculation.

Fig. 5.1 shows our calculated results for the eight-channel coupling scheme along with computed cross sections of Holley *et al.* [10] and the measured values of the studies described above. The figure clearly indicates the very good agreement of

the SMC cross sections both with experiment, and with the close-coupling calculation at higher energies. The broad peak around 12 eV in our calculated cross sections is due to a resonance-like feature in the  ${}^2\Pi_g$  symmetry component. At higher energies, the quadrupole component of the  $X^1\Sigma_g^+ \rightarrow a^1\Pi_g$  transition grows increasingly important. This contribution was treated using the Born Closure method discussed in Chapter 2. It was found that retaining the SMC partial wave amplitude up to  $l_{max} = 4, m_{max} = 2$ , with the remaining partial waves ( $l \leq 10$ ) being computed in the FBA, yielded stable results. The contribution of these higher partial waves was found to be substantial, *e.g.*, at 20 eV constituting about 30% of the total excitation cross section.

Channel coupling was found to be important for this transition. Although the three-state ( $X^1\Sigma_g^+, a^1\Pi_g, B^3\Pi_g$ ) calculations yield cross sections similar to our eight channel results, the two-state coupling scheme leads to much larger (a factor of almost two) values than the multichannel cross sections. An additional two-state calculation carried out using an IVO optimized for the  $a^1\Pi_g$  state showed that this effect is not due to use of the  $B^3\Pi_g$  optimized IVO to approximate the singlet state. The dynamically important effects of multichannel coupling for this transition occur in the  ${}^2\Pi_g$  symmetry component, as shown in Figs. 5.2a,b, where excitation to the  $a^1\Pi_g(3\sigma_g \rightarrow 1\pi_g^+)$  state is considered. Here, the two components of the  ${}^2\Pi_g$  symmetry block ( $\lambda = \pm 1$  of [10]) are considered separately for the three coupling schemes.  $\lambda$  represents the projection of the electronic angular momentum on the molecular axis. In particular, the most significant change is noted in the  $\lambda = -1$  component in going from the two state to three- and eight-channel results. The broad resonance-like feature centered at 17 eV in the two-state approximation

is greatly reduced when coupling to the  $B^3\Pi_g$  state is allowed. Further coupling of the  $\pi_u \rightarrow \pi_g$  type excitations present in the eight-channel approximation leads to only minor changes, except for the enhancement of the resonance feature at 12 eV. The changes in the  $\lambda = +1$  component (Fig. 5.2b) are less dramatic, except for the near-threshold resonance. It would appear based on these observations that the

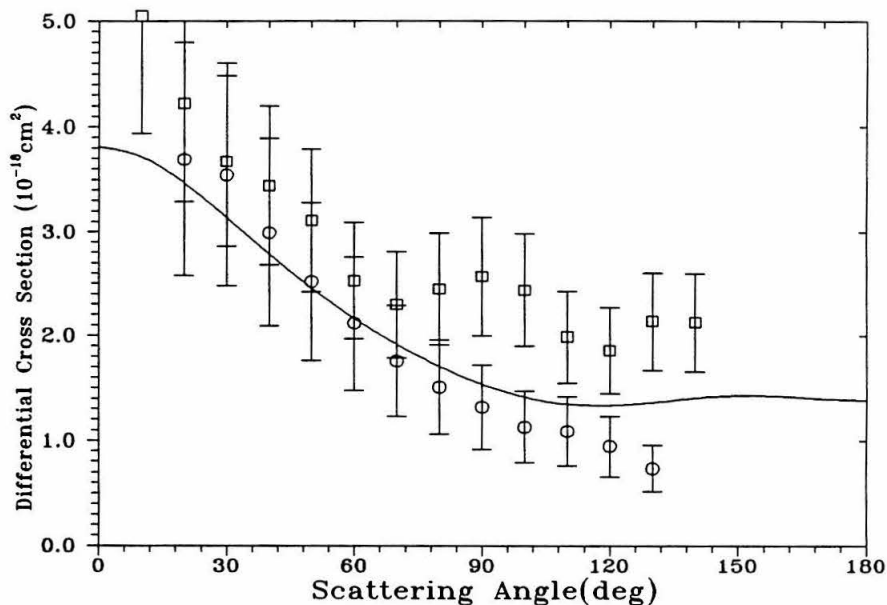


Figure 5.3. DCS for the  $a^1\Pi_g$  state at 12.5 eV. The solid line are present SMC+FBA results for the eight channel coupling scheme. (○) are measured values of Cartwright *et al.* [32]. (□) are measured values of Trajmar [42].

choice of channel coupling for the symmetry component of  $\Psi_m$  (Eq. 1.9) containing the correlation term involving the  $1\pi_g$  orbital has a substantial effect on at least the  $a^1\Pi_g$  channel, although we observe that the elastic channel cross section itself significantly changes when all eight channels are coupled. It should be noted that our two-state results are expected to differ substantially from those of Holley *et*

*al.* as they constrained the scattering wavefunction to be orthogonal to all occupied orbitals. Effects introduced by such constraints have been discussed in the context of excitation of the  $b^3\Sigma_u^+$  state of  $H_2$  [14].

Figures 5.3–5.7 show our calculated differential cross sections for excitation of the  $a^1\Pi_g$  state at 12.5, 15, 17, 20, and 30 eV along with measured values of Cartwright *et al.* [32], Brunger and Teubner [33], and Finn and Doering [31]. The electric quadrupole contribution to these differential cross sections is substantial below about  $60^\circ$  and inclusion of the higher partial-wave components of the scattering amplitude via Born-Closure is essential in accounting for this behavior. The strong forward peaking combined with the isotropic DCS at intermediate and high

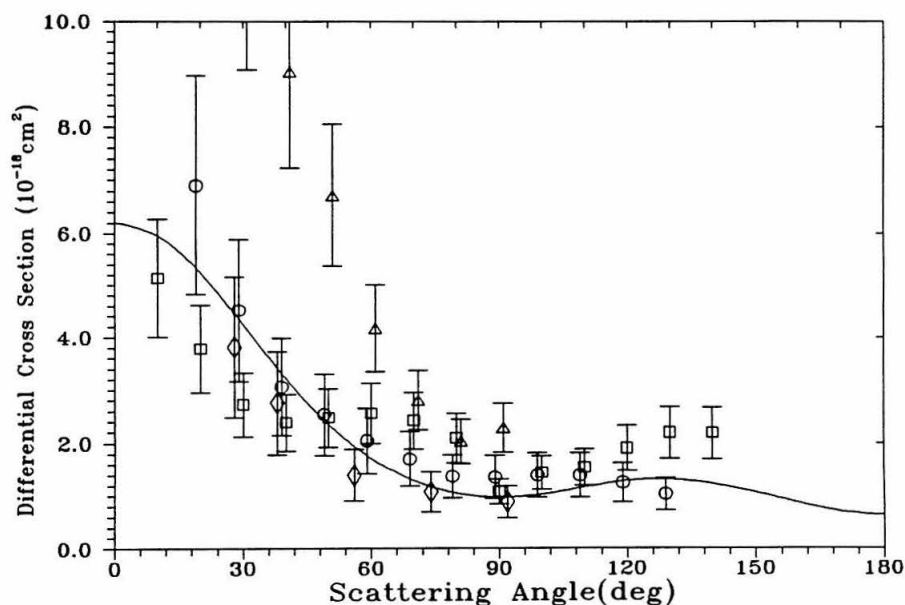


Figure 5.4 Same as Fig. 5.3 at 15.0 eV. The solid line indicates present SMC+FBA eight channel results. ( $\Delta$ ) indicate measured DCS values of Brunger and Teubner [33]. Relative values of Finn and Doering normalized to SMC results at  $90^\circ$  are indicated by ( $\diamond$ ).

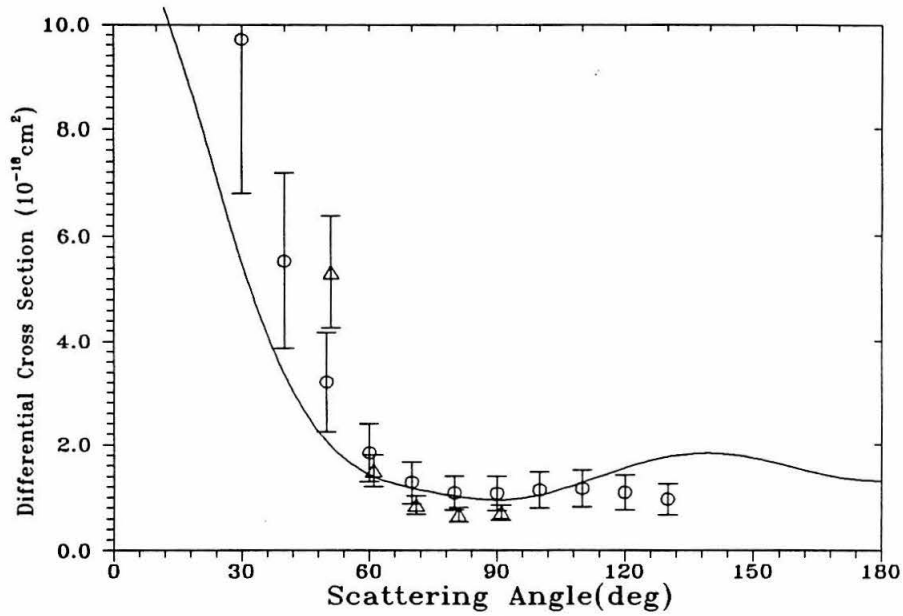


Figure 5.5. Same as Fig. 5.4 at 17.0 eV.

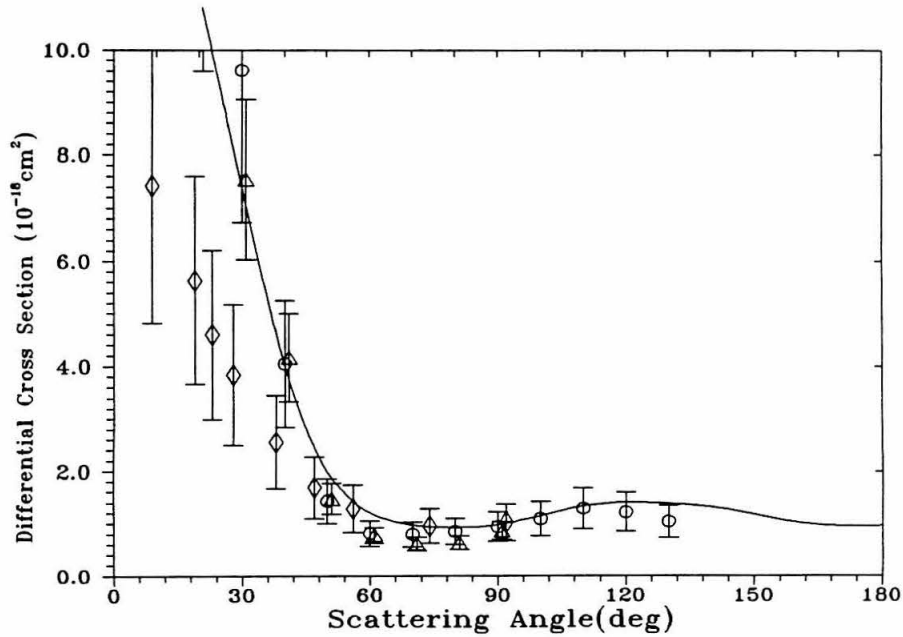


Figure 5.6. Same as Figure 5.4 at 20.0 eV.

scattering angles has been described by Finn and Doering [31] as an intermediate situation between a dipole-allowed, singlet transition and a triplet, dipole forbidden one. At intermediate and higher scattering angles the SMC cross sections without inclusion of the Born term are in good agreement with experiment, especially at higher energies. It should be noted that the high angle behavior of the SMC derived DCS indicates the assumption of Finn and Doering concerning the DCS at high angles used in their calculation of integral cross sections is valid. Thus, for this transition at least, approximation of the DCS from  $90^\circ$  to  $180^\circ$  as a constant is sufficiently accurate for computing integral cross sections when using DCS measurements restricted to scattering angles below  $90^\circ$ .

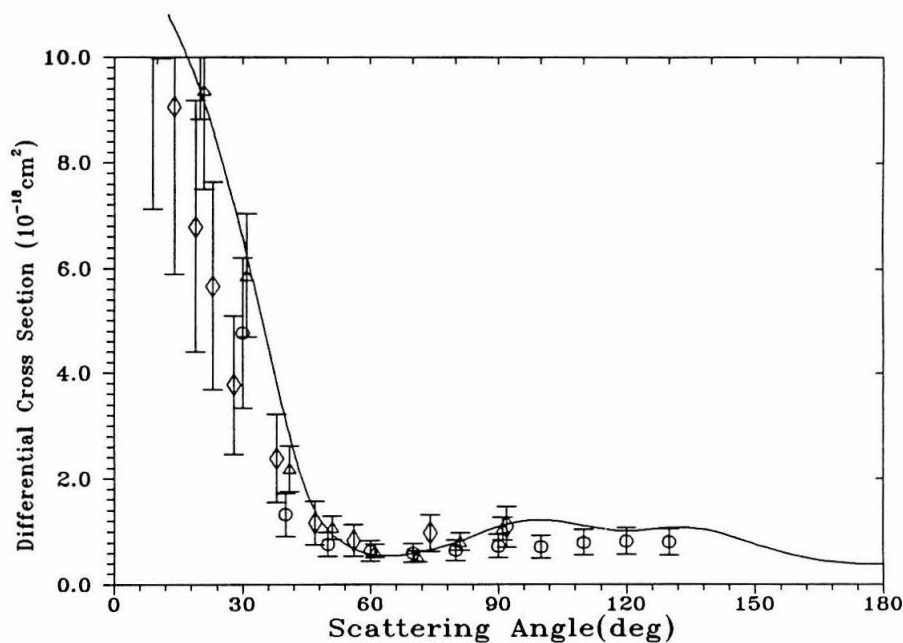


Figure 5.7. Same as Fig. 5.4 at 30.0 eV.

### 5.3.2 The $B^3\Pi_g$ State.

Interest in the excitation cross sections for the  $X^1\Sigma_g^+ \rightarrow B^3\Pi_g$  transition stems partly from use of emission lines of the First Positive System ( $B^3\Pi_g \rightarrow A^3\Sigma_u^+$ ) in plasma diagnostics and studies of the aurora [36–40]. The relatively short lifetime of this state precludes the use of a metastable detection scheme, while for energies above 15 eV, large cascade contributions via the  $C^3\Pi_u \rightarrow B^3\Pi_g$  Second Positive (2PG) system complicate the interpretation of optical fluorescence measurements

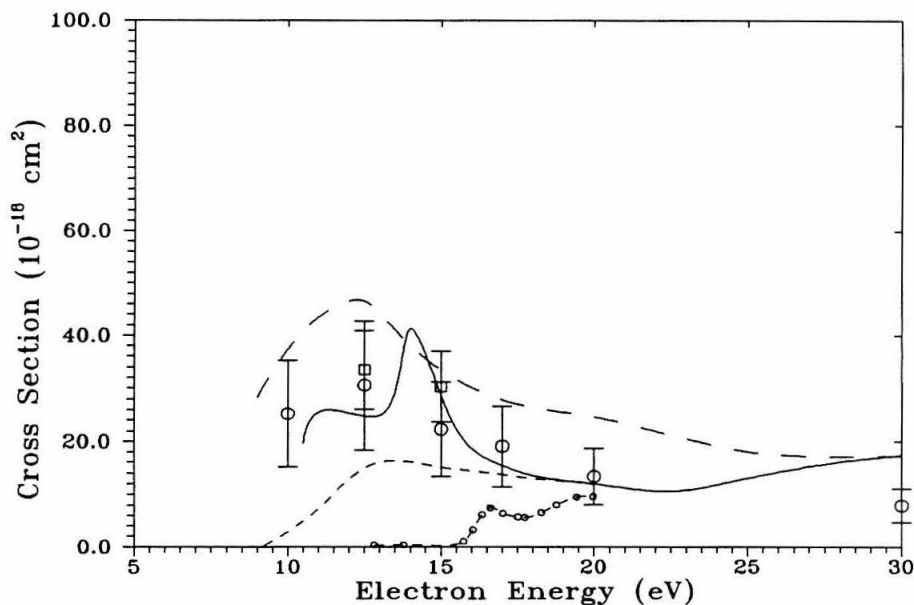


Figure 5.8. Integral cross sections for excitation of the  $B^3\Pi_g$  state. The SMC results of the eight-channel coupling calculation are indicated by the solid line and long dashed line, those from a two-channel ( $X^1\Sigma_g^+$ ,  $B^3\Pi_g$ ) calculation. Two-state (short dashed line) and multichannel (short dashed line + circles) R-matrix results of Gillan *et al.* [13]. Experimental values of Cartwright *et al.* [32] are denoted by (O). (□) are results of Trajmar [42].

[*e.g.*, 28,41]. However, there have been direct measurements of the cross sections for electron impact excitation of the state by Cartwright *et al.* [32] and Brunger and Teubner [33] with which our calculated values can be compared.

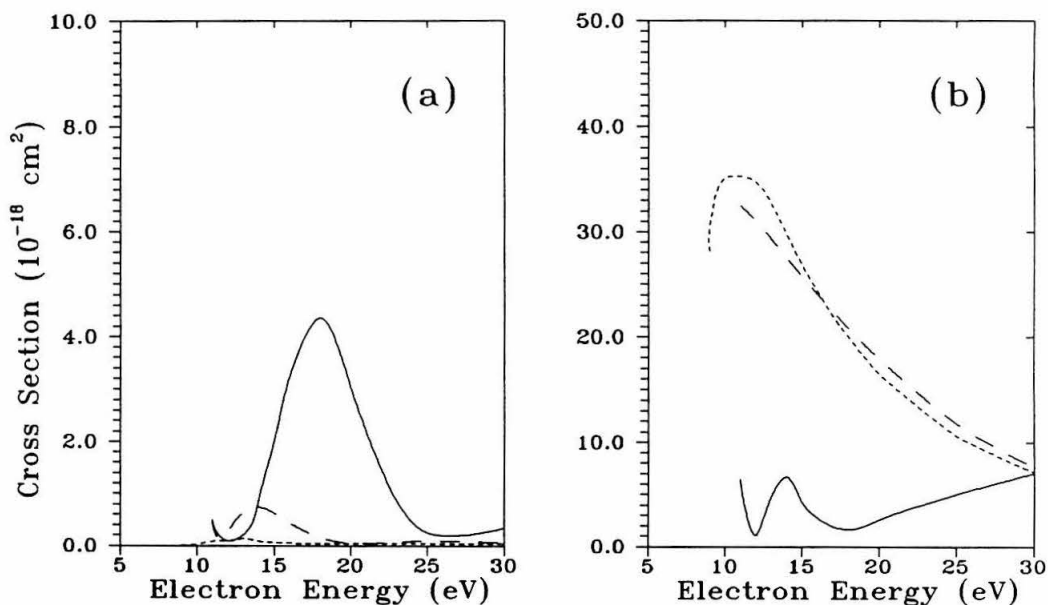


Figure 5.9. The  ${}^2\Pi_g$  component of the integral excitation cross section for excitation of the  $B^3\Pi_g$  state for the  $\lambda = -1$  subcomponent (a), and the  $\lambda = +1$  subcomponent (b). The short dashed line indicates results of a two-state ( $X^1\Sigma_g^+$ ,  $B^3\Pi_g$ ) calculation; long dashed line, results of a three-state ( $X^1\Sigma_g^+$ ,  $a^1\Pi_g$ ,  $B^3\Pi_g$ ) calculation; and solid line, results of the eight-channel coupling calculation.

In contrast to the  $a^1\Pi_g$  state, for which little theoretical work beyond FBA and two-state close-coupling calculations has been reported, excitation of the  $B^3\Pi_g$  state has been recently studied by Gillan *et al.* using the R-matrix method and a four-channel ( $X^1\Sigma_g^+$ ,  $A^3\Sigma_u^+$ ,  $W^3\Delta_u$ ,  $B^3\Pi_g$ ) coupling scheme [13]. The most significant difference between their study and the present calculation is their use of a

more sophisticated, restricted valence configuration interaction(VCI) description of the target wavefunction.

Figure 5.8 shows our calculated cross sections for excitation of the  $B^3\Pi_g$  state at the two-state, three-state ( $X^1\Sigma_g^+$ ,  $B^3\Pi_g$ ,  $a^1\Pi_g$ ), and eight-state ( $X^1\Sigma_g^+$ ,  $B^3\Pi_g$ ,  $a^1\Pi_g$ ,  $W^3\Delta_u$ ,  $w^1\Delta_u$ ,  $a'^1\Sigma_u^-$ ,  $B'^3\Sigma_u^-$ ) levels along with the two- and multichannel R-matrix results of Gillan *et al.* [13]. The total cross sections derived from DCS measurements of Cartwright *et al.* [32] and more recent measurements of Trajmar [42] at 12.5 and 15 eV are also shown. Agreement between our calculated eight-state cross sections and the measured values of [32] and [42] is reasonable. Unlike the  $a^1\Pi_g$  state, our calculated cross section for the  $B^3\Pi_g$  state is virtually unaffected by coupling with the  $a^1\Pi_g$  state alone. However, coupling with the  $[\pi_u \rightarrow \pi_g]$  type excitations included in the eight-channel calculation results in substantial changes in both the magnitude and energy dependence of the cross sections. This is a consequence primarily of a significant reduction in the  $^2\Pi_g$  component of the scattering amplitude. It should be noted that Gillan *et al.* [13] observed qualitatively similar behavior in their R-matrix studies, although as indicated in the Fig. 5.8, the effect of multichannel coupling was much more dramatic in their case. The R-matrix two-channel results for this transition are also much smaller than analogous SMC two-channel cross sections. The authors note that the  $^2\Pi_g$  contribution is dominant in the two-state calculation, which is also the case for the SMC two-state results. As is true for the  $a^1\Pi_g$  state at the three-channel level of approximation, the correlation term involving the  $1\pi_g$  virtual orbital and the ground state electronic configuration apparently plays an important role in the multichannel dynamics exhibited in this symmetry component of the scattering amplitude. Evidence for this

is the substantial change in the  ${}^2\Pi_g$  component of the elastic channel. Figures 5.9a and 5.9b, which are the equivalent of Figs. 5.2a and 5.2b for the  $B^3\Pi_g$  state, indicate that the dominant  $\lambda = +1$  subcomponent of the  ${}^2\Pi_g$  symmetry is virtually

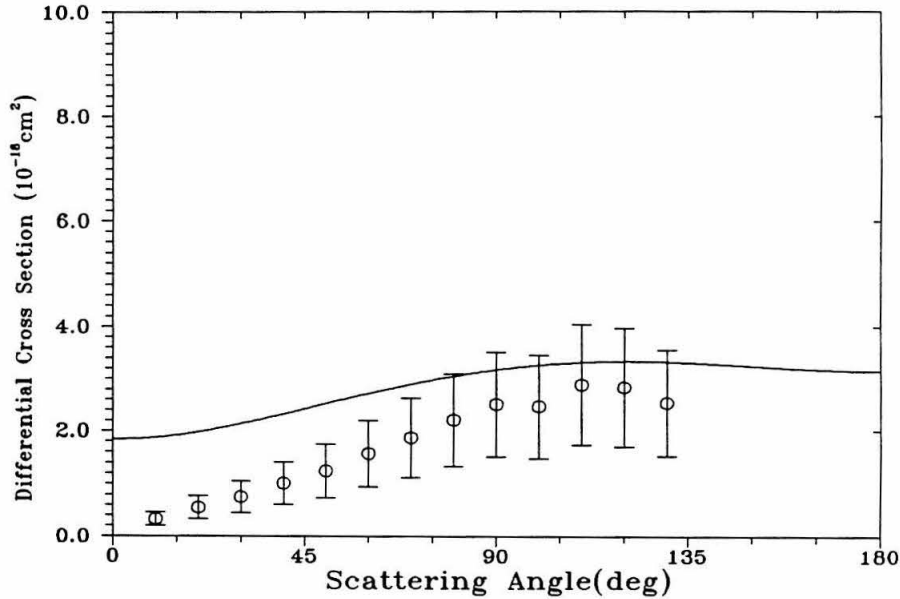


Figure 5.10. DCS for the  $B^3\Pi_g$  state at 10 eV. Present SMC results are indicated by the solid line. Measured values of Cartwright, *et al.* are given by the ( $\circ$ ).

unchanged upon coupling with the  $a^1\Pi_g$  state. However, coupling with the  $[\pi_u \rightarrow \pi_g]$  type excitations significantly reduces the cross sections and complicates their energy dependence. The  $\lambda = -1$  component is very small for the two- and three-channel coupling schemes, but is somewhat enhanced for the eight-channel coupling scheme. The net effect of the reduction in the  ${}^2\Pi_g$  cross section is a modest improvement in agreement with experiment. The resonance-like feature peaking at 14 eV is primarily a consequence of a peak in the  ${}^2\Delta_g$  symmetry component at this

energy. The  ${}^2\Pi_g$  symmetry component also exhibits a modest peak at this energy (Fig. 5.9b). More closely spaced experimental points could aid in resolving whether this feature is physically real or whether it is an artifact of our approximation of the target states. Note that in the R-matrix study, the  ${}^2\Delta_g$  symmetry was not considered [13].

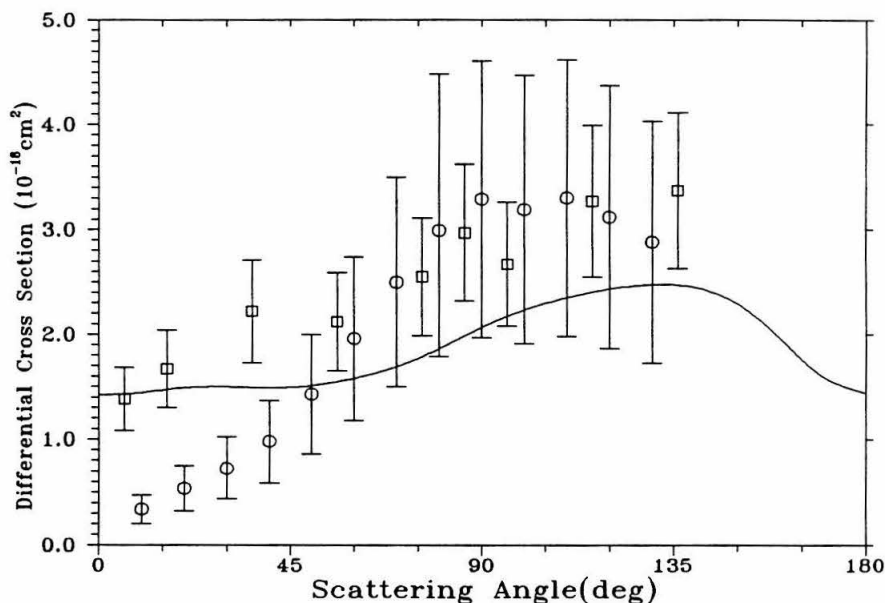


Figure 5.11. Same as Fig. 5.10 at 12.5 eV. Present SMC results are indicated by the solid line. Values of Trajmar[42] are indicated by ( $\square$ ).

Our calculated differential cross sections for impact energies of 10, 12.5, 15, 17, 20, and 30 eV are compared with the measurements of Cartwright *et al.* [32], Brunger and Teubner [33], and of Trajmar [42] in Figs. 5.10–5.15. The calculated cross sections shown in Fig. 5.10 are those of a two-state calculation, while results of the eight-channel ( $X^1\Sigma_g^+$ ,  $B^3\Pi_g$ ,  $a^1\Pi_g$ ,  $W^3\Delta_u$ ,  $w^1\Delta_u$ ,  $a'^1\Sigma_u^-$ ,  $B'^3\Sigma_u^-$ ) studies are shown at other energies. Agreement between our calculated cross sections and the

measured values of Cartwright *et al.* and Trajmar is generally encouraging. At 15 and 17 eV, the measurements of Brunger and Teubner, however, differ substantially from both our calculated values and the experimental results of Cartwright *et al.* and Trajmar. The rapidly increasing  $^2\Pi_u$  component at higher energies results in SMC DCS values somewhat larger than experiment at 30 eV, although the observed angular dependence of the cross sections is qualitatively similar.

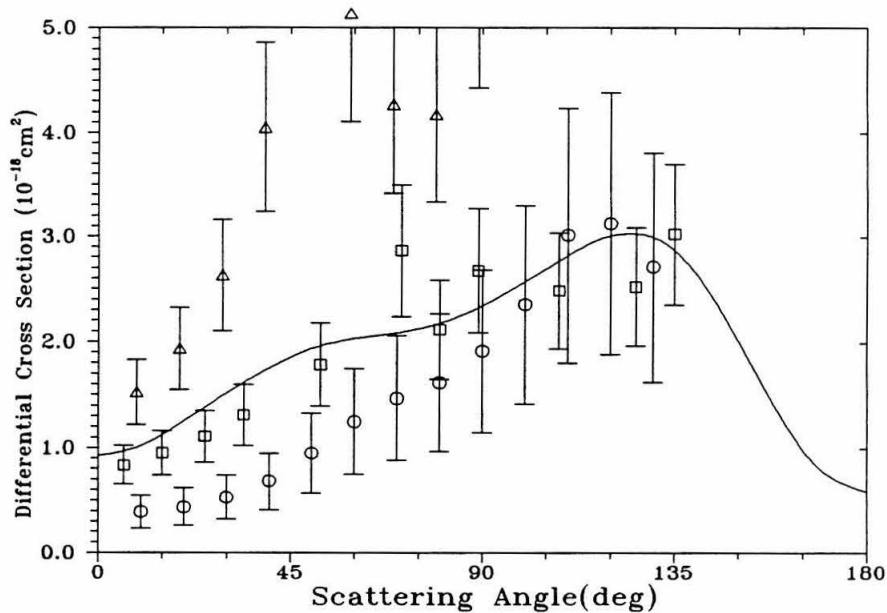


Figure 5.12. Same as Fig. 5.11 at 15.0 eV. Measured DCS of Brunger and Teubner [33] are given by ( $\Delta$ ).

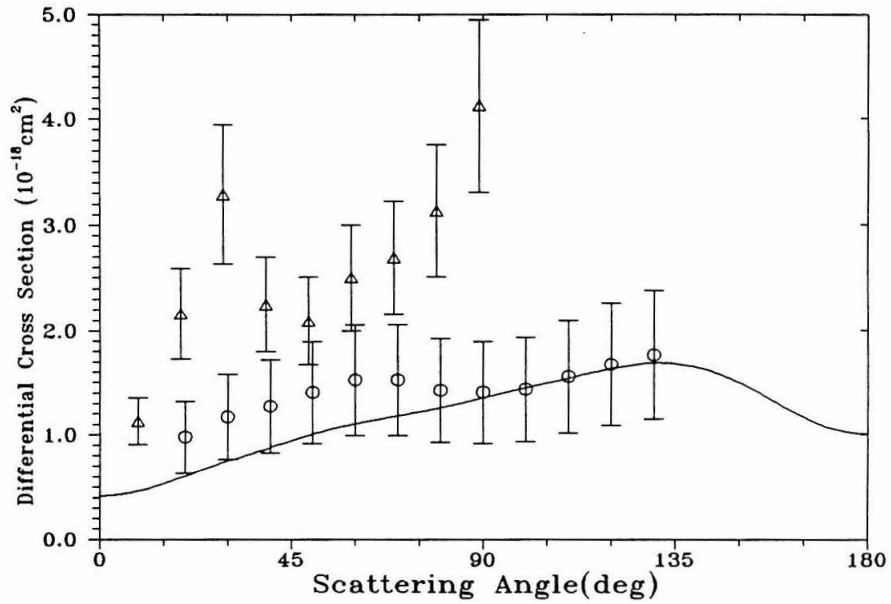


Figure 5.13. Same as Fig. 5.12 at 17.0 eV.

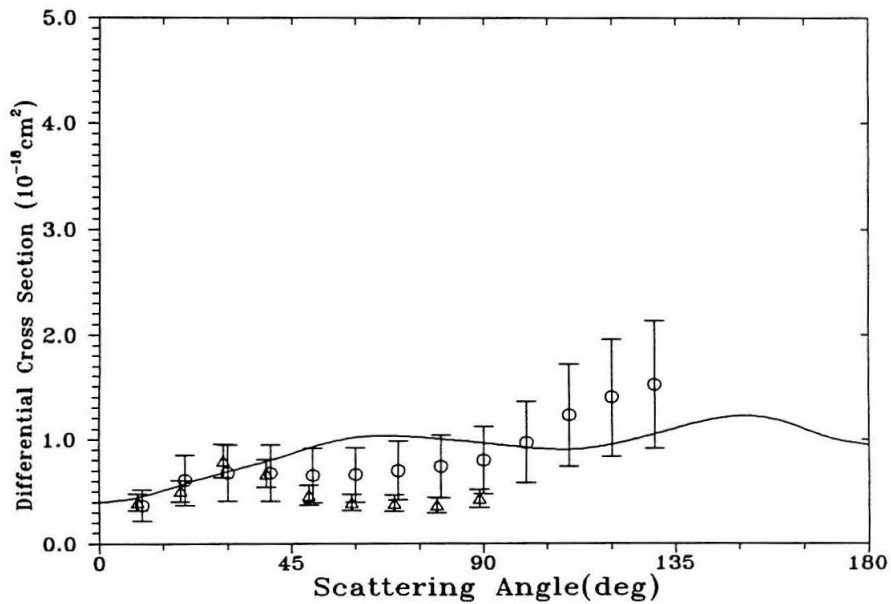


Figure 5.14. Same as Fig. 5.12 at 20.0 eV.

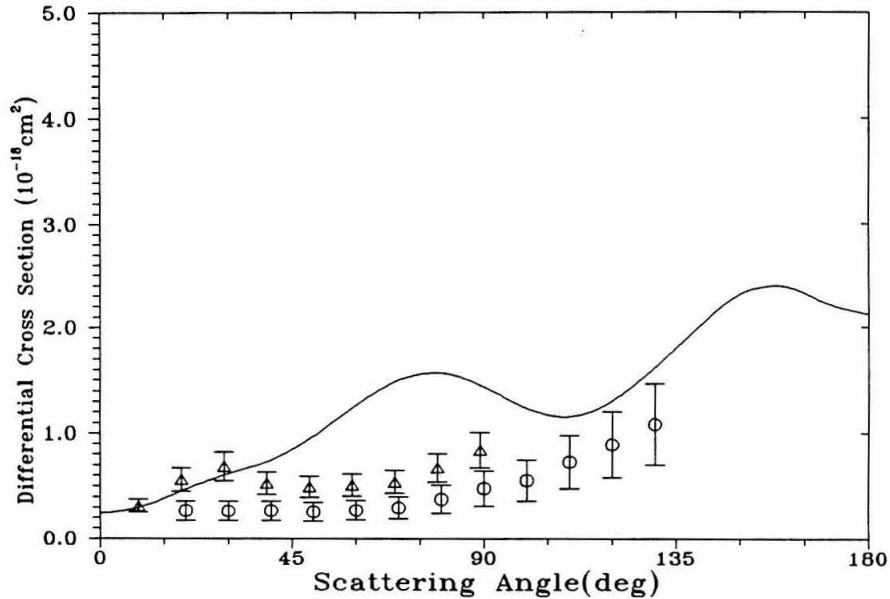


Figure 5.15. Same as Fig. 5.12 at 30.0 eV.

### C. The $A^3\Sigma_u^+$ State.

With its very long lifetime ( $\sim 1$  sec), this metastable state [43] can play an important role in the modeling of shock-heated airflows [3], where the near-threshold cross sections are particularly relevant. Fig. 5.16 shows our calculated cross sections for excitation out of the ground vibrational state of  $X^1\Sigma_g^+$  to the  $A^3\Sigma_u^+$  state over this important range of energies (threshold to 10 eV). These were obtained from a four-state ( $X^1\Sigma_g^+$ ,  $A^3\Sigma_u^+$ ,  $W^3\Delta_u$ ,  $w^1\Delta_u$ ,  $B'^3\Sigma_u^-$ ,  $a'^1\Sigma_u^-$ ) calculation. The different thresholds for the first 19 vibrational levels of the  $A^3\Sigma_u^+$  were taken from Lofthus and Krupnie [43], along with Franck-Condon factors provided by Cartwright [44]. The plotted results were obtained by assuming that the energy dependence of the

cross section was the same for each open vibrational channel with respect to its threshold, *i.e.*,

$$\sigma_{X \rightarrow A}(E) = \sum_{v=0}^{N_{open}(E)} f_{0v} \sigma_v(E).$$

The figure shows that the resulting cross sections obtained by the SMC fall below the metastable results of Borst [29] and above the measurement at 10 eV of Cartwright *et al.* [32]. Considering the experimental difficulties associated with measurements over this range of energies, such agreement is quite encouraging. A study of the dependence of these cross sections on internuclear distance would be of particular interest.

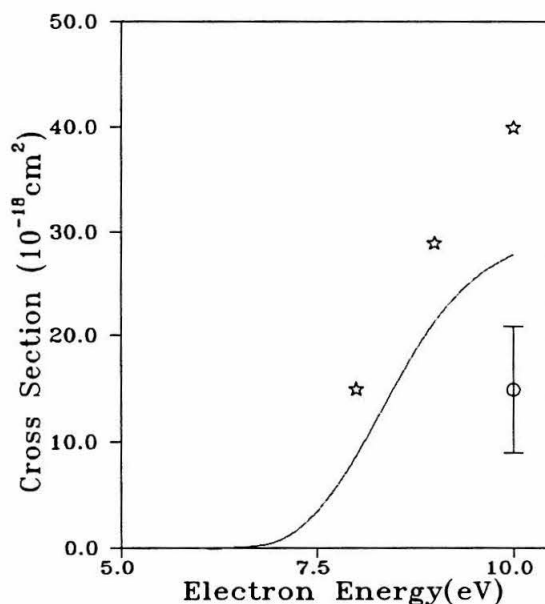


Figure 5.16. Integral cross sections for excitation of the  $A^3\Sigma_u^+$  state near threshold. The SMC four channel results are given by the solid line, measured values of Borst [29] are indicated by ( $\star$ ), and the measurement of Cartwright *et al.* [32] at 10 eV by ( $\circ$ ). See text for a description of the computational procedure used to obtain the SMC values.

Fig. 5.17 shows our calculated integral cross sections for the six- and eight-channel calculations over a wider range of impact energies along with the experimental values of Cartwright *et al.* [32], Trajmar [42], and Borst [29] and the multichannel R-matrix cross sections of Gillan *et al.* [13]. No two-state R-matrix results for this transition were reported.

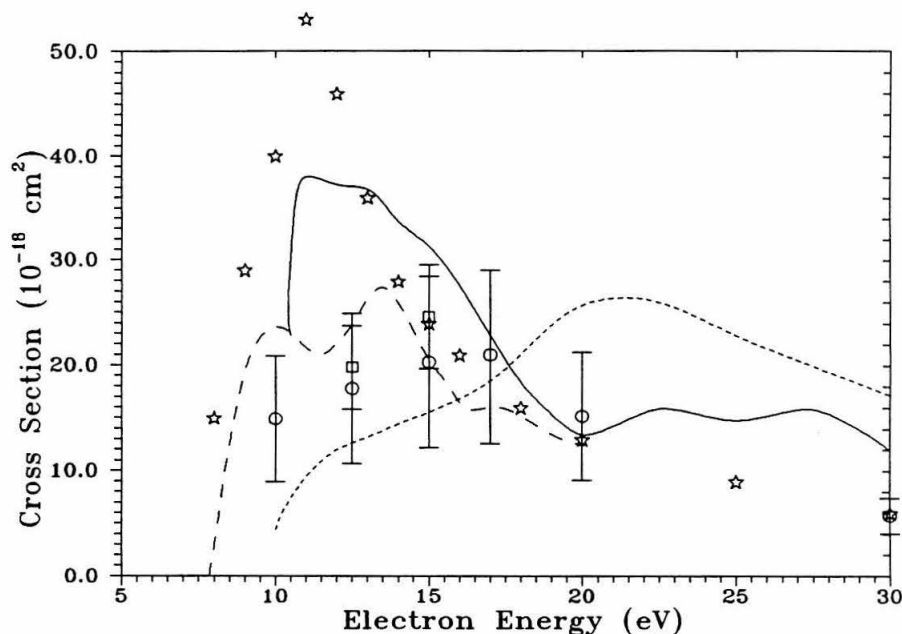


Figure 5.17. Integral cross sections for excitation of the  $A^3\Sigma_u^+$  state. The SMC results are given by the solid line (eight channel coupling) and short dashed line (six channel coupling). Calculated R-matrix cross sections of Gillan, *et al.* [13] are indicated by the long dashed curve. Measured values of Borst [29] are denoted by ( $\star$ ); those of Cartwright *et al.* [32], by ( $\circ$ ); those of Trajmar [42], by ( $\square$ ).

It is evident from the figure that at energies above 10 eV, coupling the  $[\pi_u \rightarrow \pi_g]$  excitations constituting the  $A^3\Sigma_u^+$  state to the  $[3\sigma_g \rightarrow 1\pi_g]$  excitations of the  $a^1\Pi_g$  and  $B^3\Pi_g$  states substantially alters the SMC results. The cross sections computed

at the eight-channel level of approximation, although differing substantially from the results of Cartwright *et al.* at 10 and 12.5 eV, appear to be in better qualitative agreement with the R-matrix cross sections and the measurements of Borst. The features at higher energies present in the eight-channel results arise from features in the  $^2\Pi_u$  symmetry component. The resonance observed by Gillan *et al.* in this symmetry at 13.7 eV is qualitatively similar to a broad peak observed in the SMC cross section for this symmetry component at 14 eV. It is unlikely that this is related to the resonance in this symmetry investigated by Mazeau *et al.* [45] due to the large difference between the energies at which these features are observed. The  $^2\Pi_u$  resonance they observed was at a much lower energy, 9.8 eV. The multichannel effects observed in the  $[\pi_u \rightarrow \pi_g]$  type excitations will be discussed in greater detail below.

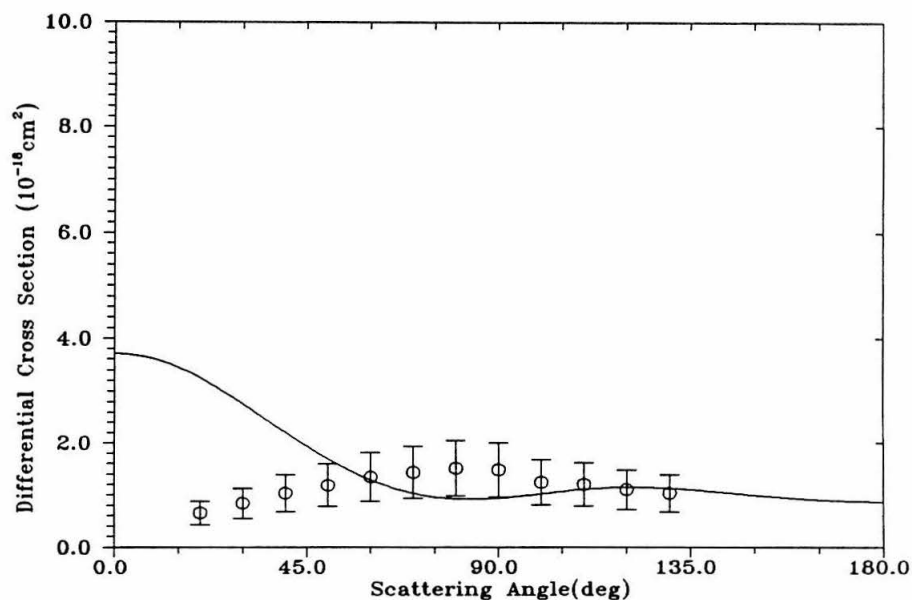


Figure 5.18. DCS for the  $A^3\Sigma_g^+$  state at 10.0 eV. SMC four channel coupling results are indicated by the solid curve. Measured DCS of Cartwright *et al.* [32] are given by (○).

Our calculated differential cross sections for excitation of the  $A^3\Sigma_u^+$  state at 12.5, 15, 17, 20, and 30 eV are compared with available measured values of Cartwright *et al.* [32], Trajmar [42], and Brunger and Teubner [42] in Figs. 5.18 to 5.23. The four-state results used in calculating the integral cross sections of Fig. 16 are shown for 10 eV. While the calculated differential cross sections show significant forward peaking at 10 and 12.5 eV, the cross sections are strongly backward peaked at the higher energies. This behavior at small angles in the calculated cross sections at 10 and 12.5 eV is not seen in the measured values. In contrast, the behavior of the differential cross sections at the higher angles, where measured values are available, seems consistent with the backward peaking seen in the calculated cross sections at impact energies above 15 eV. Although similar in shape, the magnitudes of the calculated and measured cross sections at 30 eV differ significantly.

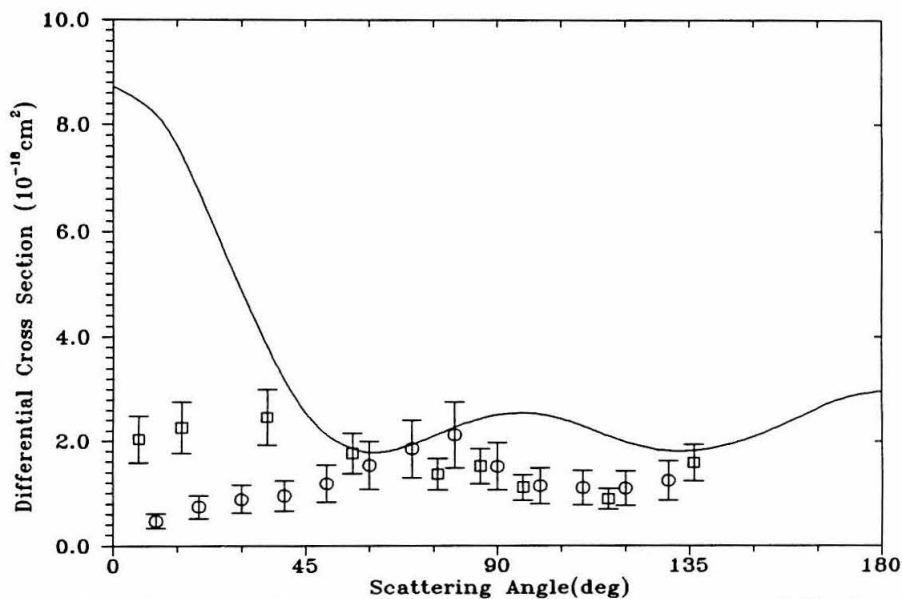


Figure 5.19. Same as Fig. 18 at 12.5 eV. Measurements of Trajmar [42] are denoted by (□).

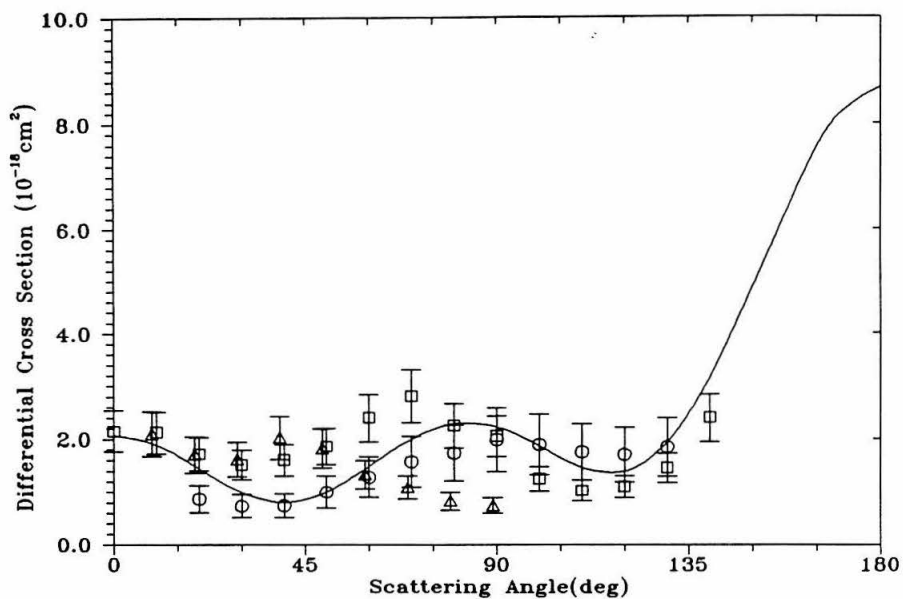


Figure 5.20. Same as Figure 5.19 at 15.0 eV. Values of Brunger and Teubner [33] are given by ( $\Delta$ ).

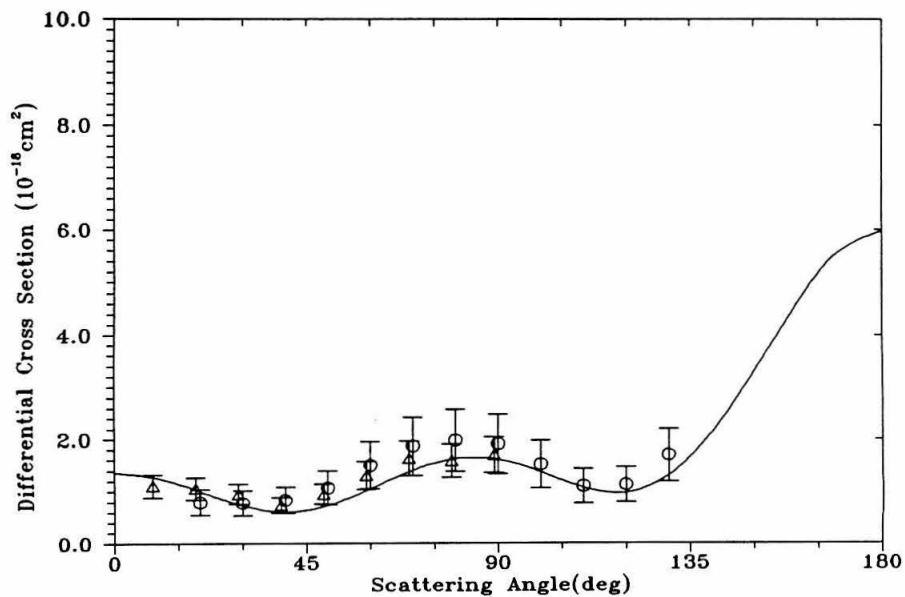


Figure 5.21. Same as Figure 5.18 at 17.0 eV.

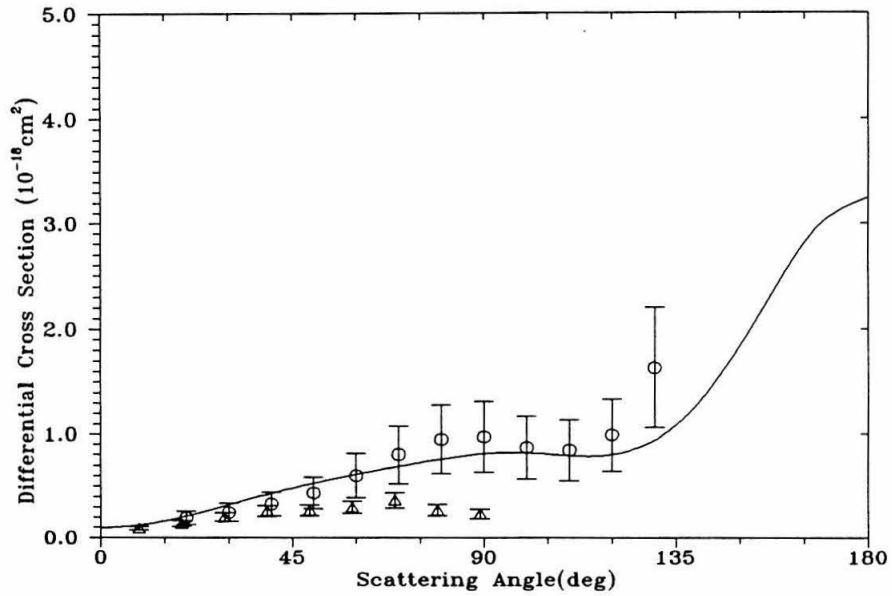


Figure 5.22. Same as Fig. 5.18 at 20.0 eV.

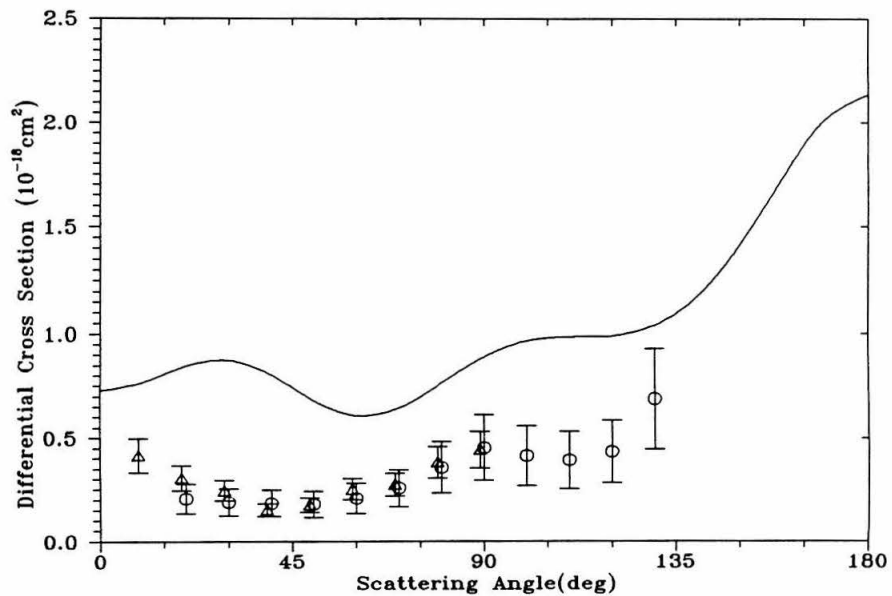


Figure 5.23. Same as Fig. 5.18 at 30.0 eV.

### 5.3.4 The $W^3\Delta_u$ State.

Integral cross sections for excitation of the  $X^1\Sigma_g^+ \rightarrow W^3\Delta_u$  transition are shown in Fig. 5.24. As with the  $A^3\Sigma_u^+$  state, the six- and eight-state cross sections show some significant differences. These differences, which reflect the importance of channel coupling to the  $3\sigma_g \rightarrow 1\pi_g$  states, are qualitatively similar to those seen for the  $A^3\Sigma_u^+$  state in Fig. 5.17. The eight-state cross

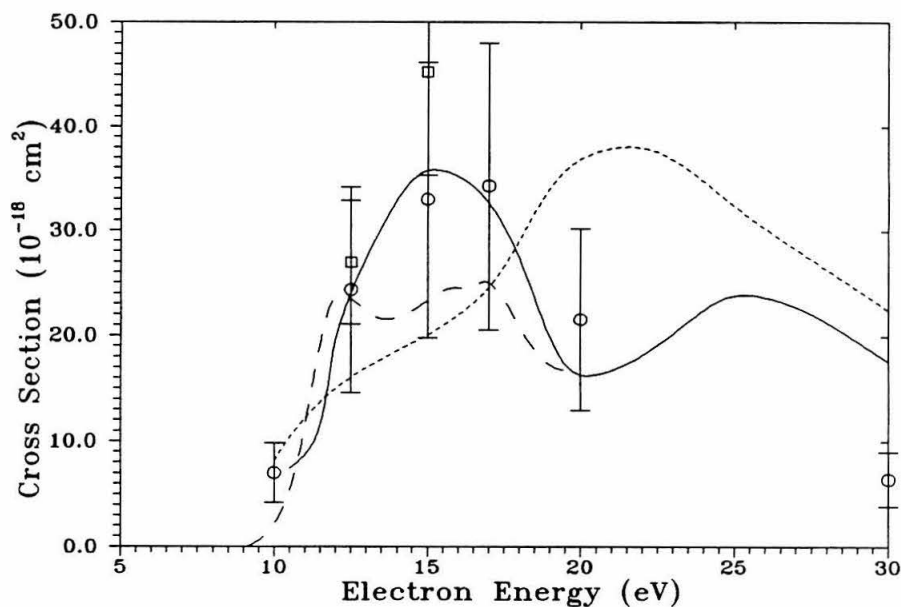


Figure 5.24. Integral excitation cross sections for the excitation of the  $W^3\Delta_u$  state. The SMC results are given by the solid line (eight-channel coupling) and short dashed line (six-channel coupling). Calculated R-matrix cross sections of Gillan *et al.* [13] are indicated by the long dashed curve. Measured values of Cartwright *et al.* [32] are given by (O); those of Trajmar [42], by (□).

sections agree quite well with the measured values of Cartwright *et al.* [32] and of Trajmar [42], except at 30 eV, and with the multichannel R-matrix results of Gillan *et al.* [13]. The broad feature in these calculated cross sections between 20 and 30 eV arises from the  ${}^2\Pi_u$  symmetry component. The enhancement in the cross sections at 15 eV also arises from the  ${}^2\Pi_u$  component; a similar feature was reported by Gillan *et al.* [13] at 18.1 eV in the  ${}^2\Pi_u$  symmetry.

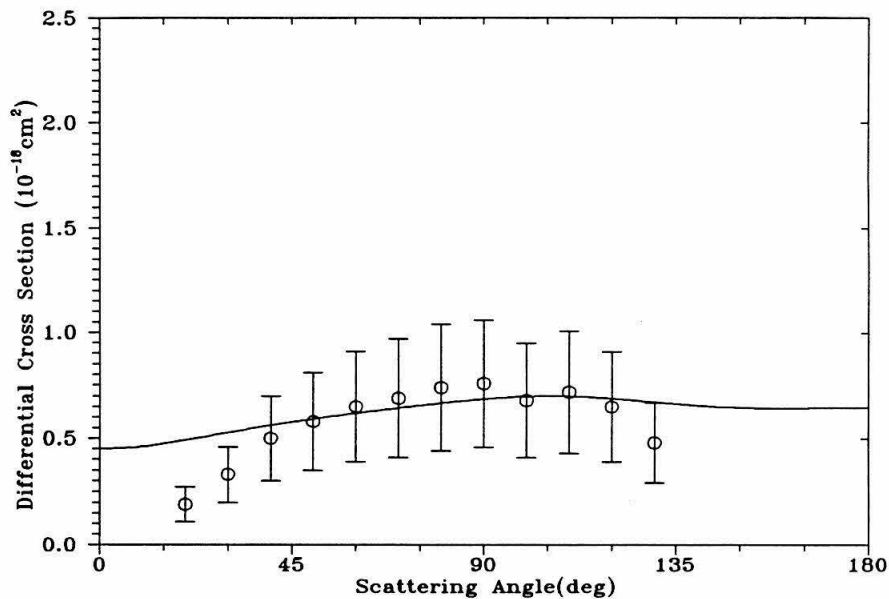


Figure 5.25. DCS for the  $W^3\Delta_u$  state at 10.0 eV. Results of an SMC six-channel coupling calculation are indicated by the solid curve. Measured DCS of Cartwright *et al.* [32] are given by (O).

Figures 5.25 through 5.30 show the our calculated differential cross sections for the eight-channel coupling scheme and the measured values of Cartwright *et al.* [32], Trajmar [42], and Brunger and Teubner [33]. At 10 eV, only results of the six-channel coupling calculation are given as the

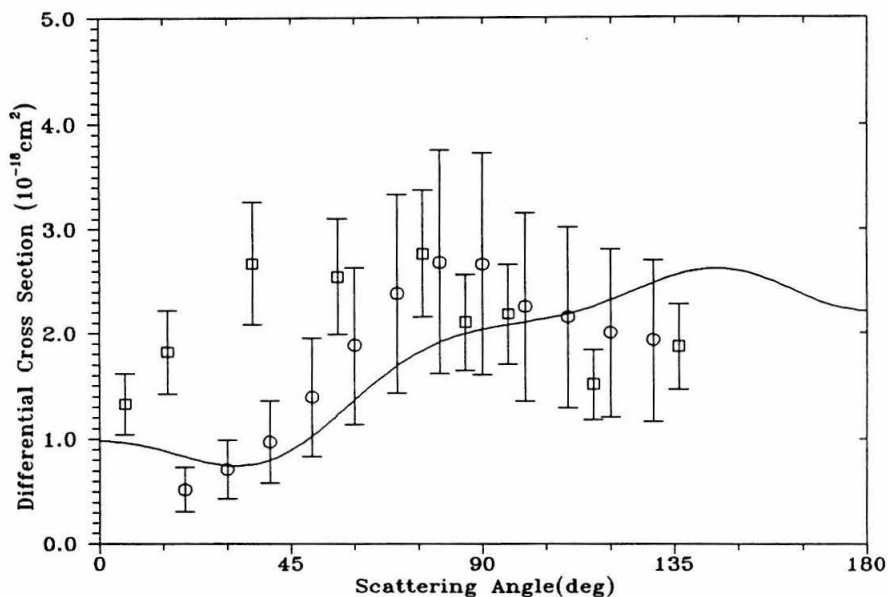


Figure 5.26. DCS for the  $W^3\Delta_u$  state at 12.5 eV. SMC eight channel coupling results are indicated by the solid line. Measurements of Trajmar [42] are denoted by ( $\square$ ).

$a^1\Pi_g$  channel is closed at this energy within our approximation of the excited states. Agreement between the calculated and measured values at 10, 12.5, 15, and 17 eV is quite reasonable. However, at the higher energies of 20 and 30 eV, there are significant differences between the calculated values and available measurements. Calculations with more extensive channel coupling schemes and more sophisticated target wavefunctions could be helpful in identifying reasons for these differences.

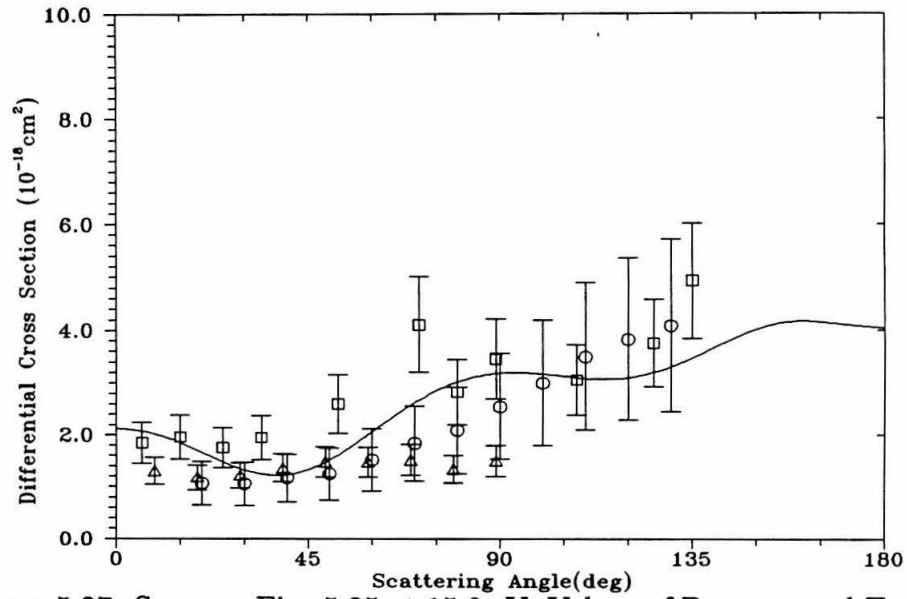


Figure 5.27. Same as Fig. 5.25 at 15.0 eV. Values of Brunger and Teubner [33] are given by ( $\Delta$ ).

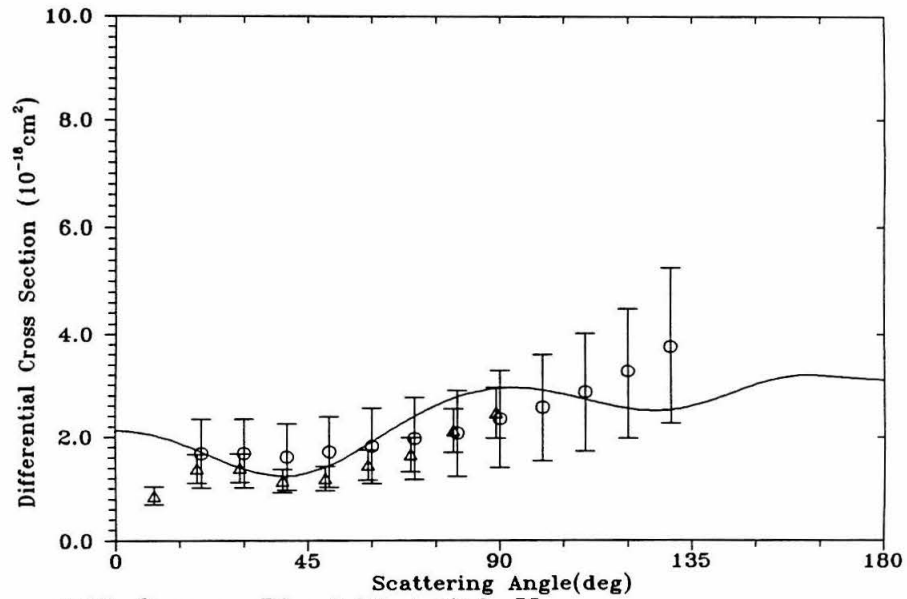


Figure 5.28. Same as Fig. 5.26 at 17.0 eV.

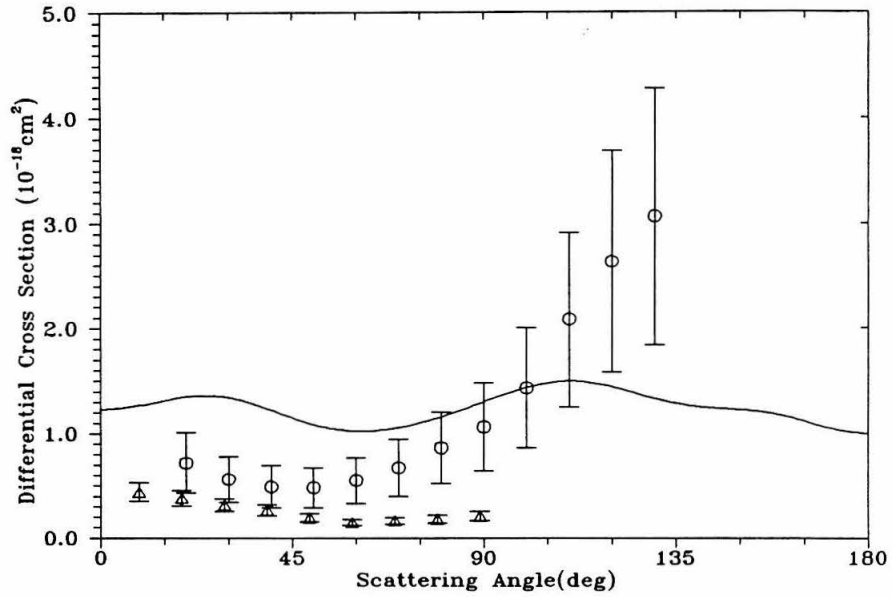


Figure 5.29. Same as Fig. 5.26 at 20.0 eV.

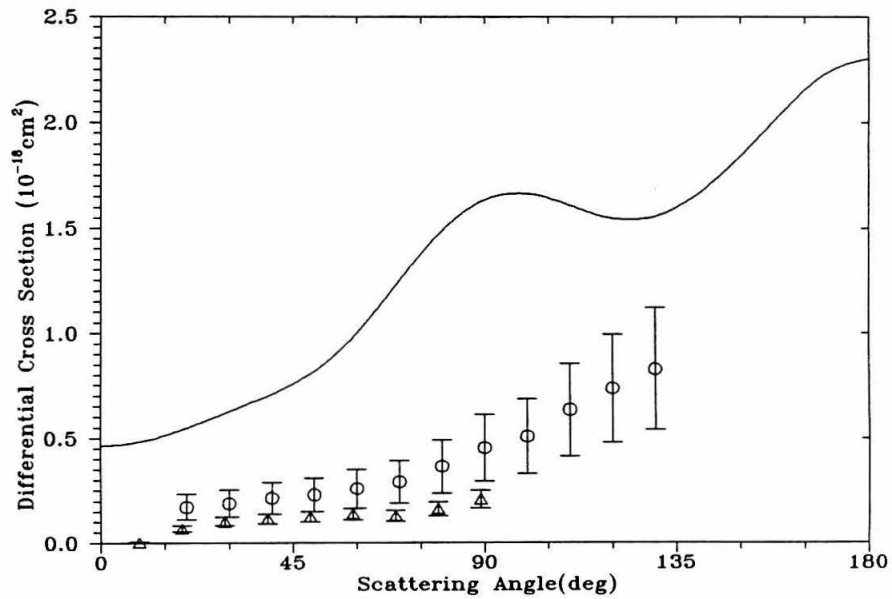


Figure 5.30. Same as Fig. 5.26 at 30.0 eV.

### E. The $w^1\Delta_u$ State.

Fig. 5.31 shows our calculated integral cross sections for the  $w^1\Delta_u$  state along with measured values of Cartwright *et al.* [32]. The calculated cross sections show a sharp peak near threshold (11 eV) due to a rapid rise and fall of the  $^2\Pi_g$  symmetry component between threshold and 12 eV. Otherwise, the  $^2\Pi_u$  symmetry is the dominant part of the cross section at these energies. Although agreement is satisfactory at 12.5 and 15 eV, our cross sections at higher energies lie above experiment. As with the  $X^1\Sigma_g^+ \rightarrow a^1\Pi_g$  transition, we took into account the contribution of higher partial waves to the cross section by use of the Born closure method. Here  $l_{max} = 6$

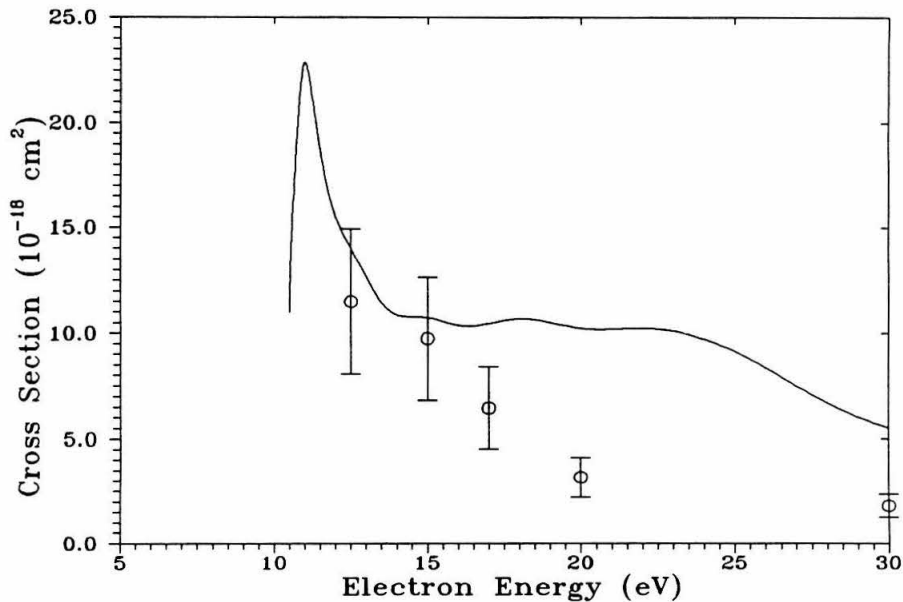


Figure 5.31. Integral cross sections for the excitation of the  $w^1\Delta_u$  state. The SMC+FBA eight channel results are given by the solid line. Measured values of Cartwright *et al.* [32] are given by (○).

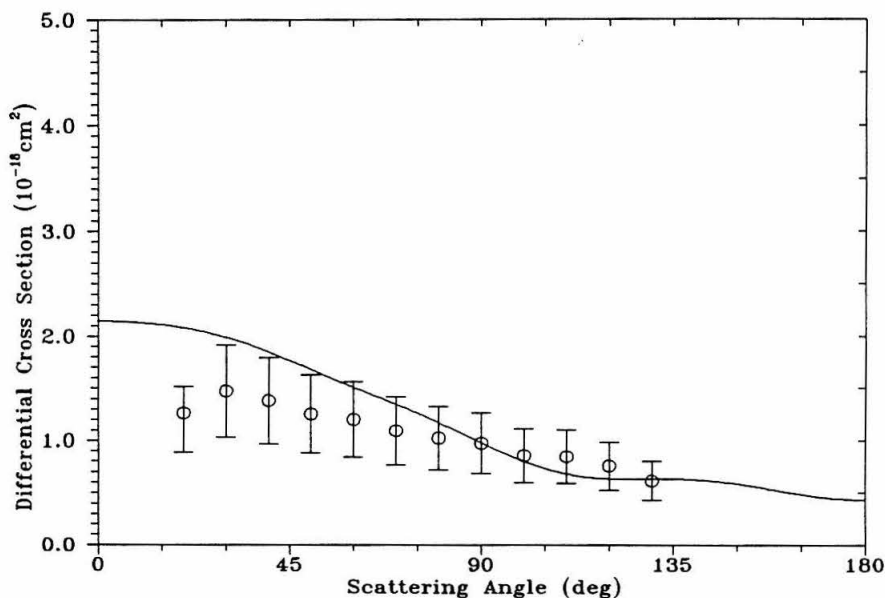


Figure 5.32. DCS for the  $w^1\Delta_u$  state at 12.5 eV. SMC+FBA eight-channel results are indicated by the solid curve. Measured DCS of Cartwright *et al.* are given by (O).

(Eq. 2.13) was used at all energies. As would be expected, the Born contribution to the excitation cross section increases as incident electron energy increases. However, in contrast to the  $a^1\Pi_g$  state, the Born component is substantially smaller than the SMC component ( $\sim 20\%$  even at 30 eV).

Our DCS values are presented in Figs. 5.32–5.36. Except at 12.5 eV, agreement with Cartwright *et al.* [32] and Brunger and Teubner's [33] measurements is not as satisfactory as for the states discussed previously. Although at 15 and 17 eV, our computed DCS are of the same magnitude as experiment, the angular dependence is markedly different. The maxima observed in our DCS between 30 and 60° result

from the contribution of the high partial waves of the FBA amplitude. In this regards, it is worth noting that the observed forward peaking of the DCS of Brunger and Teubner and Cartwright *et al.* cannot be due to the long range nature of this spin-allowed transition. The angular dependence of the FBA differential cross sections has been considered by Klump and Lassette [48]. Based on their expansion of the generalized oscillator strength in terms of moments of the electronic transition,

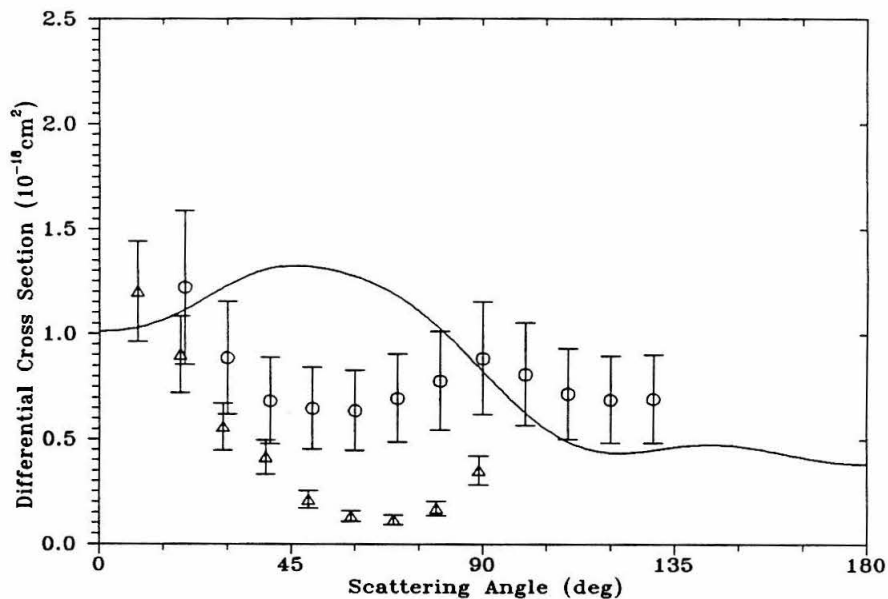


Figure 5.33. Same as Fig. 5.32 at 15.0 eV. Values of Brunger and Teubner [33] are given by ( $\Delta$ ).

an octupole type transition such as  $X^1\Sigma_g^+ \rightarrow w^1\Delta_u$  should exhibit a DCS which increases with increasing scattering angle for low-angle scattering. Hence, inclusion of the FBA amplitude does not lead to improved agreement with experiment at low scattering angles, particular at higher energies ( $> 15$  eV). It should be noted that forward peaking was not observed in the DCS computed using the DW method [11].

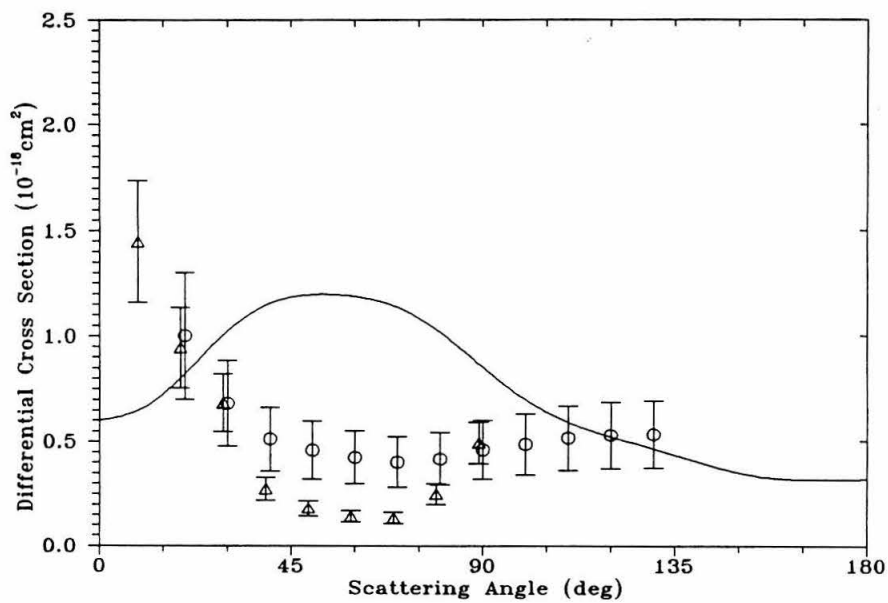


Figure 5.34. Same as Fig. 5.33 at 17.0 eV.

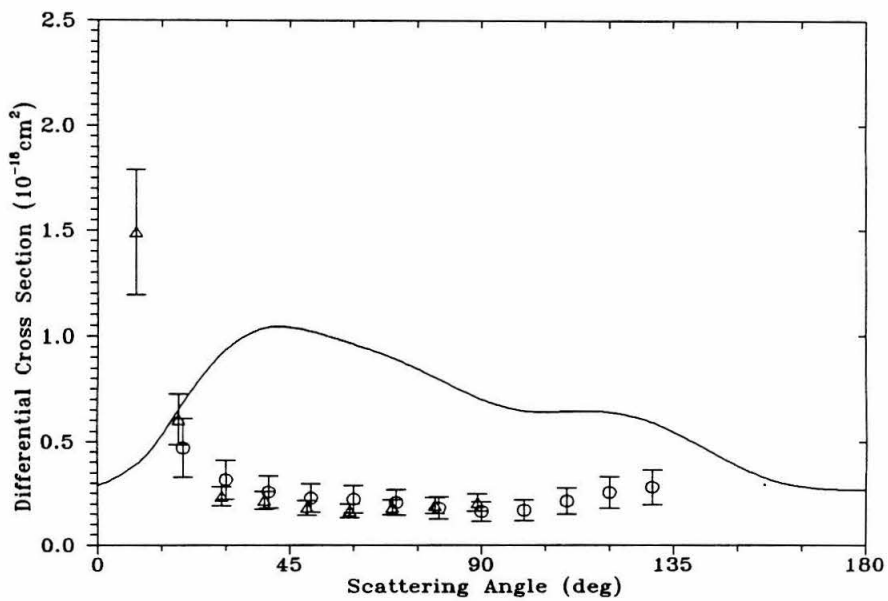


Figure 5.35. Same as Fig. 5.33 at 20.0 eV.

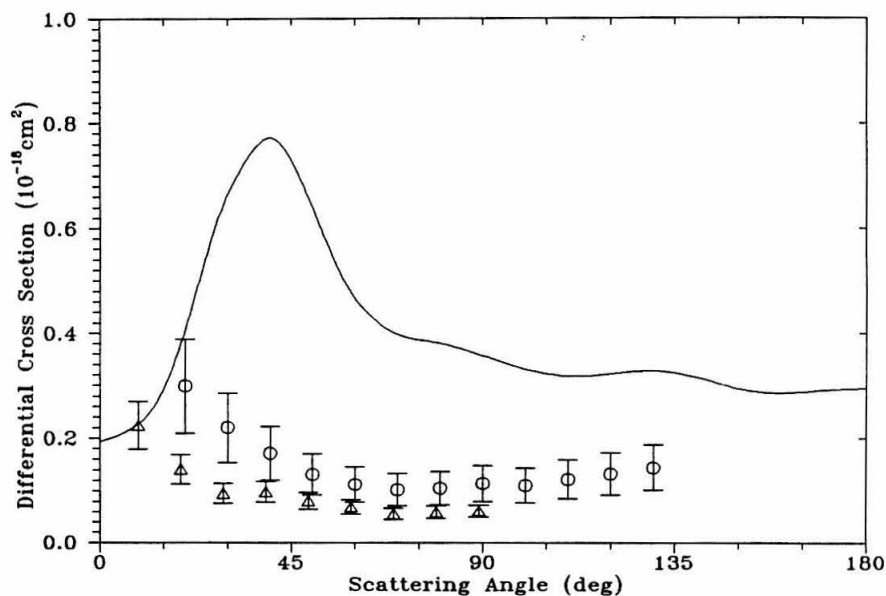


Figure 5.36. Same as Fig. 5.33 at 30.0 eV.

### 5.3.6 The $a'^1\Sigma_u^-$ State.

The integral cross sections for excitation of this state obtained from six- and eight-channel calculations are shown in Fig. 5.37. Differences in these cross sections again show that channel coupling is important in describing the dynamics of electron impact excitation of this state. The eight-state results are in reasonable agreement with the limited experimental data of Cartwright *et al.* [32]. The near threshold peak is associated with a resonance-like feature in the  $^2\Pi_u$  symmetry while the broader peak between 14 and 15 eV is associated with the  $^2\Pi_g$  symmetry component.

Differential cross sections for the  $X^1\Sigma_g^+ \rightarrow a'^1\Sigma_u^-$  excitation are presented in Figs. 5.38 to 5.41. The zero DCS values at  $0^\circ$  and  $180^\circ$  predicted for  $\Sigma^- \leftrightarrow \Sigma^+$

transitions based on symmetry arguments and discussed by Cartwright *et al.* [46] are evident in the figures. Note that this symmetry requirement extends to the symmetry components of the integral cross sections: the  $^2\Sigma_g$  and  $^2\Sigma_u$  components are identically zero for this class of transitions. The asymmetric (with respect to  $90^\circ$ ) appearance of the experimental DCS values of Cartwright *et al.* at 15 and 17 eV is not observed in the SMC. At 20 eV, however, the six-channel SMC results more accurately reflect the prominent peak at  $130^\circ$  observed experimentally (Fig.

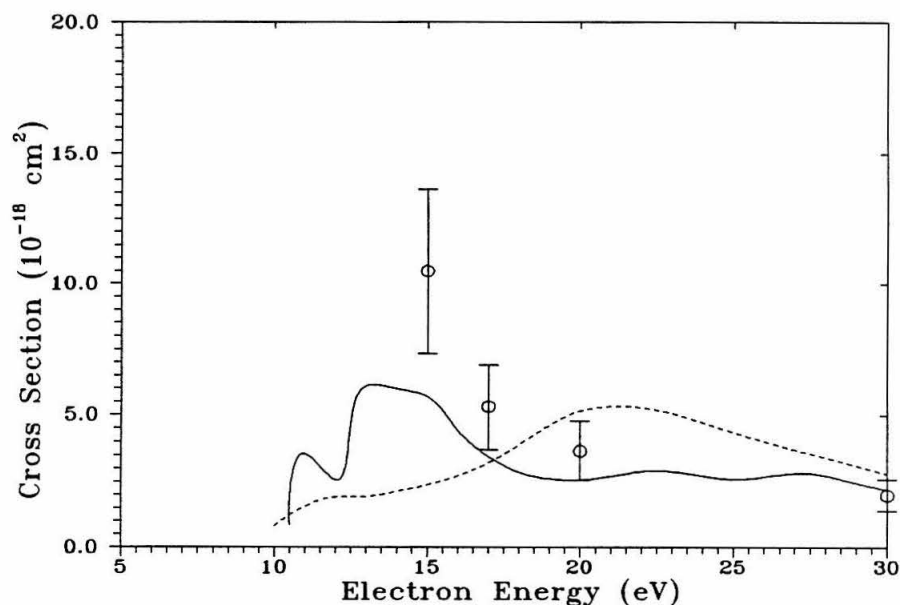


Figure 5.37. Integral cross sections for the excitation of the  $a'^1\Sigma_u^-$  state. The SMC results are given by the solid line (eight-channel coupling) and short dashed line (six-channel coupling). Measured values of Cartwright *et al.* [32] are given by (○).

5.40). As with the  $w^1\Delta_u$  state, the increasing DCS values measured by Brunger and Teubner [33] and Cartwright *et al.* toward lower angles at 30 eV is not evident in the SMC cross sections.

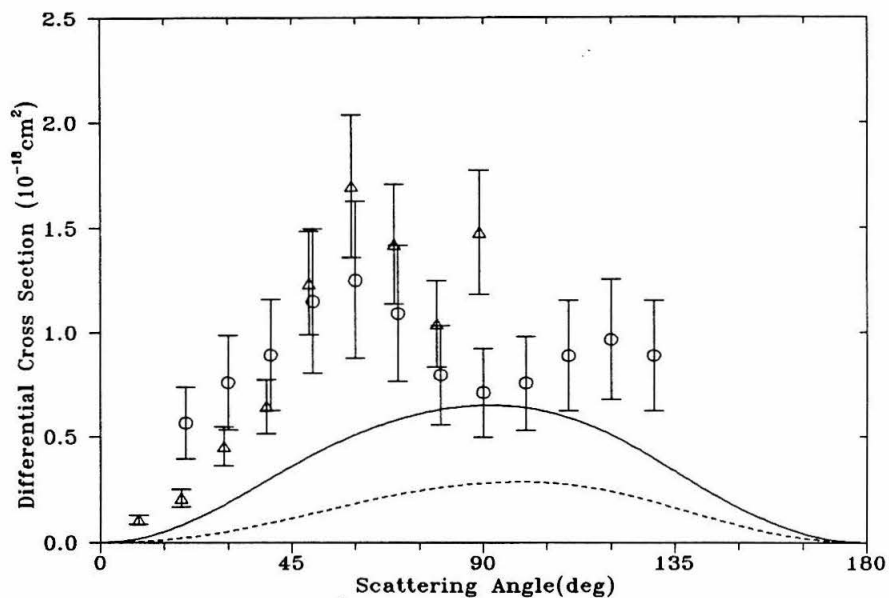


Figure 5.38. DCS for the  $a'^1\Sigma_u^-$  state at 15.0 eV. SMC six channel coupling results are indicated by the dashed curve, eight channel by the solid curve. Measured DCS of Cartwright *et al.* [32] are given by (O). Values of Brunger and Teubner [33] are given by ( $\Delta$ ).

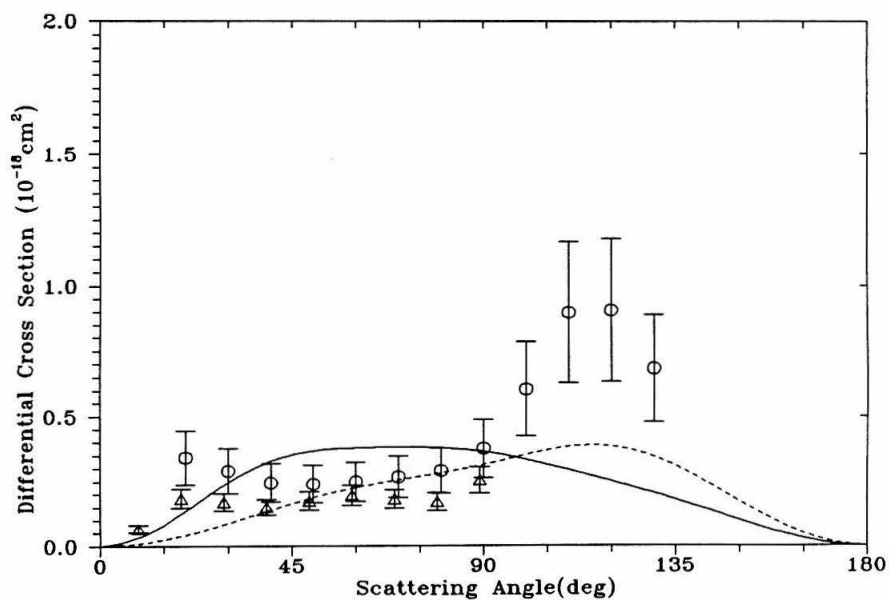


Figure 5.39. Same as Fig. 5.38 at 17.0 eV.

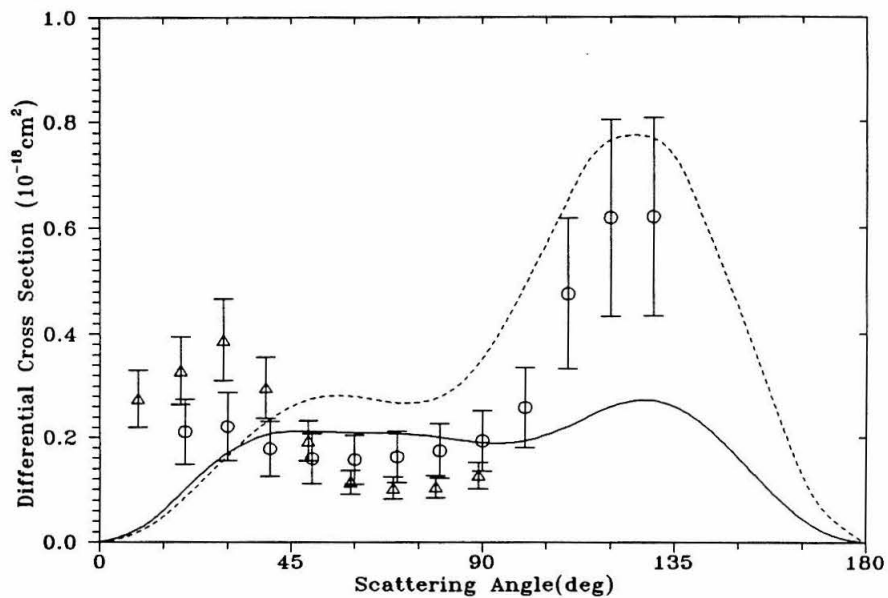


Figure 5.40. Same as Fig. 5.38 at 20.0 eV.

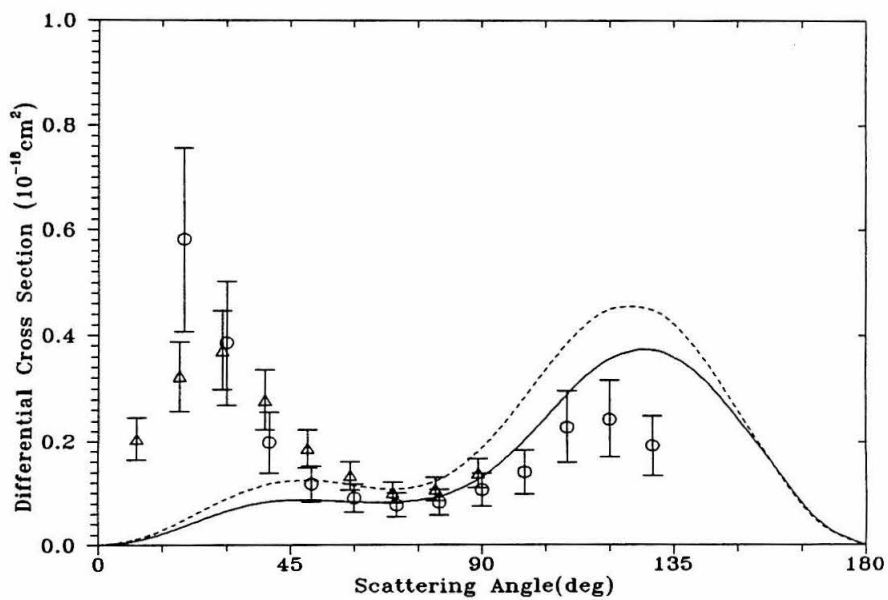


Figure 5.41. Same as Fig. 5.38 at 30.0 eV.

### 5.3.7 The $B'^3\Sigma_u^-$ State.

Figure 5.42 shows our integral cross sections for excitation of the  $B'^3\Sigma_u^-$  state obtained from both six- and eight-state studies along with measured values of Cartwright *et al.* [32]. As in the case of the  $a'^1\Sigma_u^-$  state, resonant-like features in the  ${}^2\Pi_u$  symmetry component of the eight-channel calculation at 11 eV and in the  ${}^2\Pi_g$  component at 15 eV result in the double peak structure in the SMC cross sections. As observed in the other transitions considered, the eight-channel cross sections are in consistently better agreement with the experimental values than those obtained for the six-channel coupling scheme.

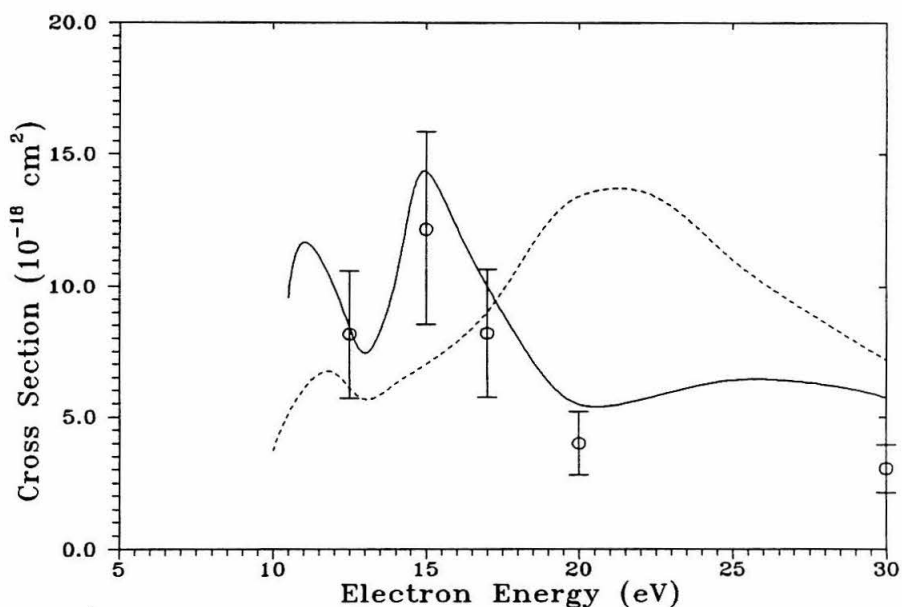


Figure 5.42. Integral cross sections for the excitation of the  $B'^3\Sigma_u^-$  state. The SMC results are given by the solid line (eight-channel coupling) and dashed line (six-channel coupling). Measured values of Cartwright *et al.* [32] are given by (○).

The DCS data plotted in Figs. 5.43 through 5.47 are similar qualitatively to those for the  $a'^1\Sigma_u^-$  state. Measured values for this transition have been reported by Brunger and Teubner [33], in addition to Cartwright *et al.* Like the  $a'^1\Sigma_u^-$  state, the results of the six-channel coupling scheme exhibits more prominently the asymmetry observed in the data of Cartwright *et al.*, especially at 20 eV, although the magnitudes of the cross sections are significantly greater than the experimental cross sections. Again, the low angle behavior at 30 eV (Fig. 5.47) of the experimental cross sections reported by all three groups is not reflected by results of either SMC multichannel coupling calculation, nor expected theoretically [46].

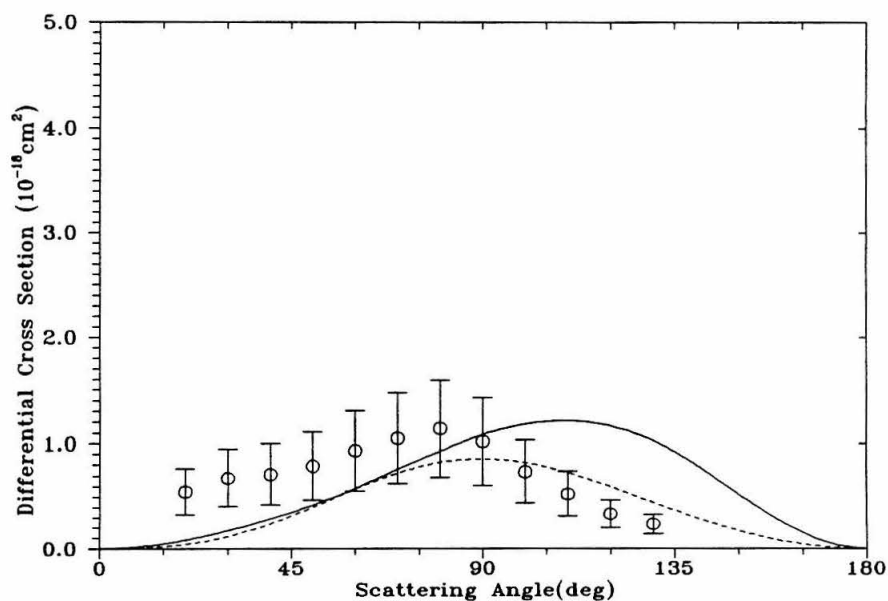


Figure 5.43. DCS for the  $B'^3\Sigma_u^-$  state at 12.5 eV. SMC six-channel coupling results are indicated by the dashed curve, eight-channel by the solid curve. Measured DCS of Cartwright *et al.* [32] are given by (○).

### 5.3.8 Multichannel Effects Involving the $[\pi_u \rightarrow \pi_g]$ Excitations

In contrast to other molecules investigated using the SMC method, the excitations considered in this study exhibit very distinctive multichannel effects, particularly in the case of states involving the singlet and triplet coupled  $[\pi_u \rightarrow \pi_g]$

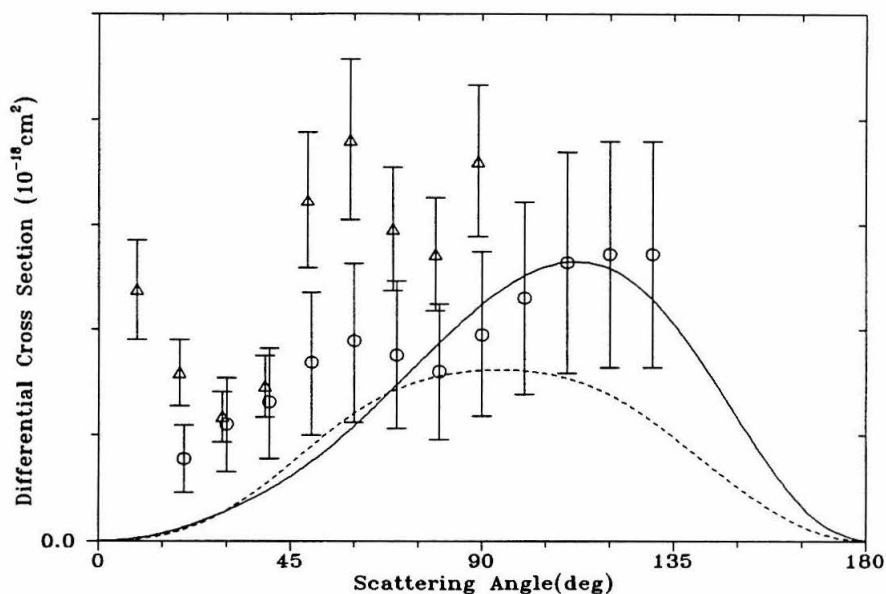


Figure 5.44. Same as Fig. 5.43 at 15.0 eV. Values of Brunger and Teubner [33] are given by ( $\Delta$ ).

excitations. The relatively simple, single configuration target description used for the target wavefunction is helpful in studying such effects. In light of results obtained using more sophisticated target wavefunctions [13], a clear understanding of multichannel coupling is evidently needed before attempting to analyze results of studies where the inclusion of multiconfiguration target wavefunctions complicates

interpretation of multichannel effects. What one observes is that the recorelation terms present in the total wavefunction in Eq. (1.9) play an essential role in the multichannel dynamics. Here, recorelation terms are considered to be those configurations in Eq. (1.9) required to compensate for the orthogonality of the continuum

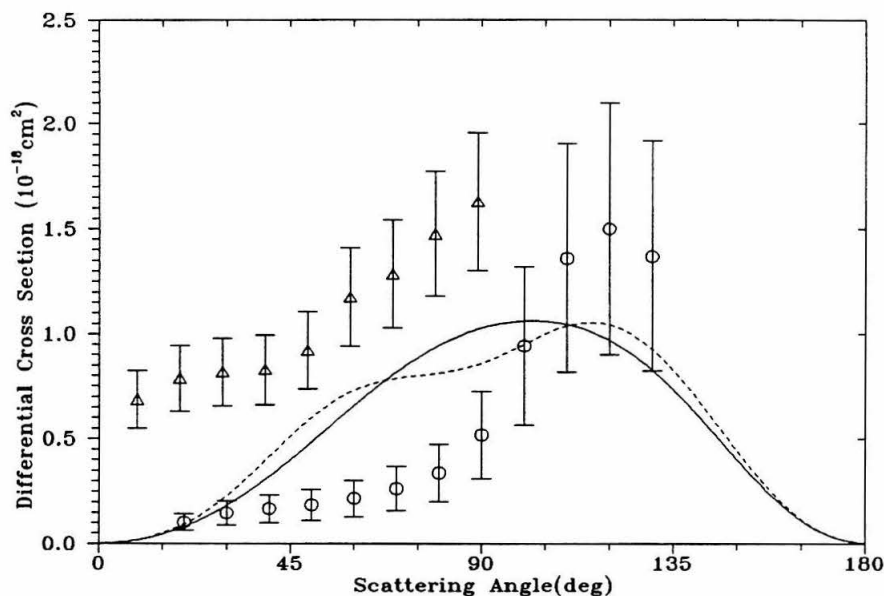


Figure 5.45. Same as Figure 5.44 at 17.0 eV.

functions with the occupied orbitals included in the description of the ground and excited states of the target which is imposed in most procedures. Although there are no continuum functions included in the present SMC expansion of the scattering wavefunction, it is still convenient to consider it as consisting of open channel and closed space or recorelation terms, *i.e.*, Eq. (1.16). Difficulties associated with these latter terms ( the  $\Theta_\mu$  in 1.16) when employing multiconfiguration target wavefunctions have been discussed in the context of the complex Kohn-method [47].

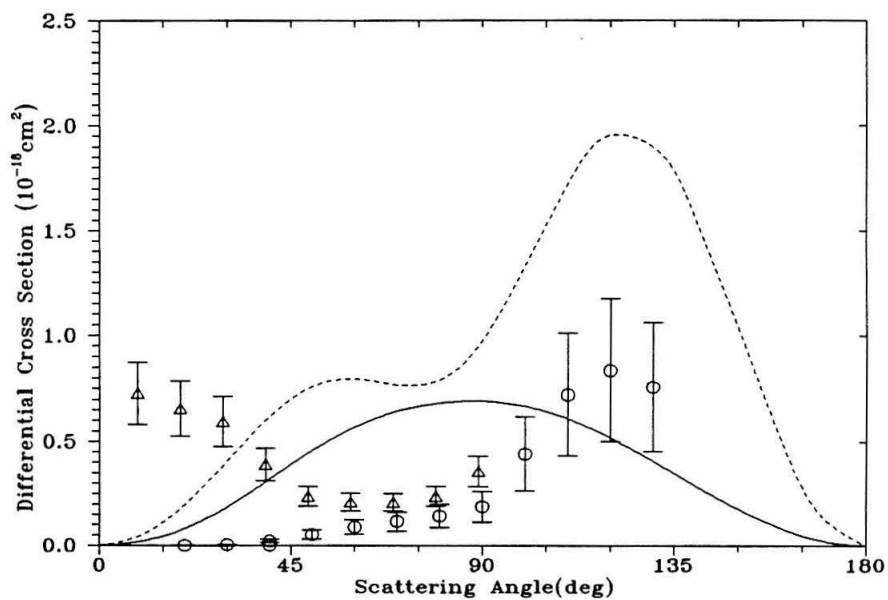


Figure 5.46. Same as Fig. 5.44 at 20.0 eV.

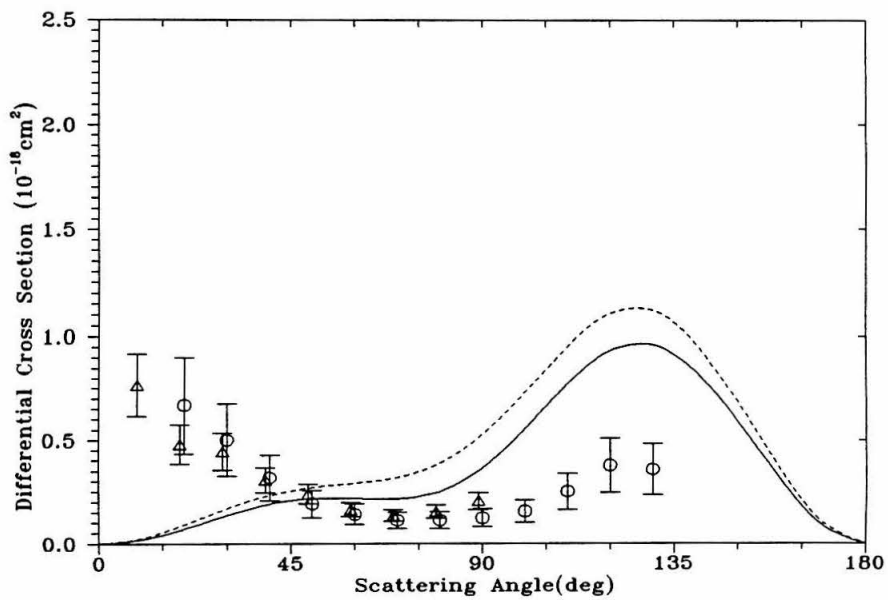


Figure 5.47. Same as Fig. 5.44 at 30.0 eV.

Studies of the  $\text{H}_2\text{O}$  molecule have indicated that for the SMC, there are two types of multichannel coupling effects. For excitations involving configurations with different holes (*e.g.*, the  $[3\sigma_g \rightarrow 1\pi_{g(x,y)}]$  and  $[1\pi_{ux} \rightarrow 1\pi_{gy}]$  excitations in  $\text{N}_2$ , see 1.2.2 concerning notation), coupling occurs only via the potential  $\mathbf{V}$  in the expression for  $A^{(+)}$ , Eq. (1.8). The other type of coupling involves excitations from the same hole. These excitations are coupled by the projector  $\mathbf{P}$  in addition to the potential, and are closely related to the recorrelation terms discussed Lengsfeld and Rescigno [47]. Although the subject of considerable speculation [13], it was found that the SMC results are relatively insensitive to excitation thresholds for impact energies above 10 eV in the case of the  $\text{N}_2$  molecule. Even the relative order of threshold energies was found to be unimportant for the collision energies of interest in this study.

The consequences of coupling via the projector  $\mathbf{P}$  are quite dramatic for the  $[\pi_u \rightarrow \pi_g]$  transitions in  $\text{N}_2$ . For the symmetry components of the total cross section lacking recorrelation terms, namely the  ${}^2\Sigma_g$ ,  ${}^2\Sigma_u$ ,  ${}^2\Delta_g$ , and  ${}^2\Delta_u$  symmetries for coupling involving  $[\pi_u \rightarrow \pi_g]$  transitions exclusively, convergence with respect to basis set choice is very rapid. Small, valence basis sets including a set of  $d$ -functions yield results almost identical with the large basis set employed in this study. The case of the  ${}^2\Pi_g$  symmetry is similar in that the only recorrelation term present is the  $[O](1\pi_{g(x,y)})$  configuration (see 1.2.2). For this symmetry, excellent convergence characteristics are observed regardless of the coupling schemes chosen, as long as the  $[\pi_u \rightarrow \pi_g]$  transitions alone are considered. For the  ${}^2\Pi_u$  symmetry however, the effects of channel coupling are dramatic and lead to instability with respect to basis set selection. Only for restricted, two-state calculations in which there

are no recorelation terms in the  ${}^2\Pi_u$  symmetry is convergence also observed to be rapid. It is in this symmetry that all of the inelastic recorelation or closed channel terms (*e.g.*,  $[1\pi_{ux} \rightarrow 1\pi_{gx}](1\pi_{gy})$ ) are present. Large shifts ( $> 5$  eV) in the peak cross sections of this symmetry component are observed, the positions of the peaks being highly dependent on the choice of basis set. The singlet coupled, and hence optically allowed nature of some of these recorelation terms is undoubtedly partly responsible for this behavior, although their influence on the scattering amplitude does not include a substantial increase in the contribution of higher partial waves to the triplet excitation cross sections. The SVD procedure discussed in chapter 1 is used to smooth out the high energy resonances resulting from the presence of these terms (see 1.3.5), while the FBA amplitude is used to treat the higher partial-wave components of the amplitudes for the singlet transitions.

Coupling of the  $[3\sigma_g \rightarrow 1\pi_{g(x,y)}]$  excitations with the  $[1\pi_{u(x,y)} \rightarrow 1\pi_{g(x,y)}]$  type might not initially seem to be important. However, for the  $N_2$  molecule, at least, it appears that the elastic channel  $[O](1\pi_{g(x,y)})$  configuration in the  ${}^2\Pi_g$  symmetry component plays an important role in the dynamics of multichannel coupling. Thus, it is necessary to couple both types of excitations. This leads to significant reductions in the  ${}^2\Pi_g$  symmetry contribution to all of the transitions considered in this study.

The need to consider all energetically open channels whose respective components of the projector  $\mathbf{P}$  have a nonzero overlap with elastic channel configurations of this type has important consequences. Namely, it implies that limited channel coupling schemes are unlikely to account for some significant multichannel effects. The fact that the computational effort required for evaluation of  $A^{(+)}$  and the

onshell integrals in Eq. (1.7) grows rapidly as additional channels are opened underscores the need for fast, parallel computers such as the Intel Touchstone Delta machine to make these studies feasible.

## 5.4 Conclusions

Results of application of the SMC method to electronic excitation of  $N_2$  have been presented and compared with the extensive set of available experimental data. Integral excitation cross sections for the  $A^3\Sigma_u^+$ ,  $B^3\Pi_g$ , and  $W^3\Delta_u$  states have also been compared with those of recent R-matrix calculations. Coupling of all possible excitations out of the  $3\sigma_g$  and  $1\pi_u$  orbitals to the  $1\pi_g$  orbitals was found to be necessary for the  $B^3\Pi_g$ ,  $A^3\Sigma_u^+$ ,  $W^3\Delta_u$ ,  $w^1\Delta_u$ ,  $B'^3\Sigma_u^-$ , and  $a'^1\Sigma_u^-$  states. In most instances, this leads to improved agreement with experiment and R-matrix cross sections compared to less extensive coupling schemes. Inclusion of First Born terms with multichannel SMC results was found to yield cross sections in very good agreement with experiment for the  $a^1\Pi_g$  state. Considering the consistently better agreement with experiment for the most extensive channel coupling schemes, our results clearly indicate the need to treat electronic excitation of molecules by low energy electrons as a multichannel problem in order to obtain reliable cross sections.

## 5.5 References

- [1.] A. V. Jones, *Aurora* (Reidel, Boston, 1974).
- [2.] D. E. Strobel and D. E. Shemansky, *J. Geophys. Res.* **87**, 1361 (1982).
- [3.] C. Park, *Nonequilibrium Hypersonic Aerothermodynamics* (Wiley, New York, 1990).
- [4.] O. S. Heavens, *Contemp. Phys.* **17**, 529 (1976).
- [5.] L. G. Piper and G. E. Caledonia, *J. Phys. Chem.* **95**, 698 (1991).
- [6.] D. C. Cartwright, *J. Appl. Phys.* **49**, 3855 (1978).
- [7.] G. J. Schulz, *Rev. Mod. Phys.* **45**, 378 (1973).
- [8.] S. Trajmar, D. F. Register, and A. Chutjian, *Phys. Rep.* **97**, 219 (1983).
- [9.] S. Chung and C. C. Lin, *Phys. Rev. A* **6**, 988 (1972); *Appl. Opt.* **10**, 1790 (1971).
- [10.] T. K. Holley, S. Chung, C. C. Lin, and E. T. P. Lee, *Phys. Rev. A* **24**, 2946 (1981).
- [11.] A. W. Fliflet, V. McKoy, and T. N. Rescigno, *J. Phys. B* **12**, 3281 (1979).
- [12.] Lee Mu-Tao and V. McKoy, *Phys. Rev. A* **28**, 6971 (1983).
- [13.] C. J. Gillan, C. J. Noble, and P. G. Burke, *J. Phys. B* **23**, L407 (1990).

- [14.] M. A. P. Lima, T. L. Gibson, V. McKoy, and W. M. Huo, *Phys. Rev. A* **38**, 4527 (1988); T. L. Gibson, M. A. P. Lima, V. McKoy, and W. M. Huo, *Phys. Rev. A* **35**, 2473 (1987).
- [15.] H. Pritchard, C. L. Winstead, V. McKoy, and M. A. P. Lima, in preparation.
- [16.] Q. Sun, C. Winstead, V. McKoy, and M. A. P. Lima, *Phys. Rev. A*, **46**, 2462 (1992).
- [17.] Q. Sun, C. L. Winstead, V. McKoy, and M. A. P. Lima, *J. Chem. Phys.* **96**(5), 3531(1992).
- [18.] Q. Sun, C. L. Winstead, and V. McKoy, *Phys. Rev. A* (in press).
- [19.] C. L. Winstead and V. McKoy, *Phys. Rev. A* (in preparation).
- [20.] H. Pritchard and V. McKoy (in preparation).
- [21.] F. J. Da Paixo, M. A. P. Lima, and V. McKoy, *Phys. Rev. Lett.* **68**(11), 1658 (1992).
- [22.] R. Poirier, R. Kari, and I. G. Csizmadia, *Handbook of Gaussian Basis Sets* (Elsevier, Amsterdam, 1985), p. 262.
- [23.] W. A. Goddard and W. J. Hunt, *Chem. Phys. Lett.* **24**, 464 (1974).
- [24.] J. B. Rose and V. McKoy, *J. Chem. Phys.* **55**, 5435 (1971).
- [25.] W. C. Ermler, A. D. McLean, and R. S. Mulliken, *J. Phys. Chem* **86**, 1305 (1982).

- [26.] R. R. Meier, *et al.*, J. Geophys. Res. **90**(A7), 6608 (1985).
- [27.] R. R. Meier, D. J. Strickland, P. D. Feldman, and E. P. Gentieu, J. Geophys. Res. **85**, 2177 (1980).
- [28.] M. Imami and W. L. Borst, J. Chem. Phys. **61**, 1115 (1974).
- [29.] W. L. Borst, Phys. Rev. A **5**, 648 (1972).
- [30.] J. M. Ajello and D. E. Shemansky, J. Geophys. Res. **90**(A10), 9845 (1985).
- [31.] T. G. Finn and J. P. Doering, J. Chem. Phys. **64**(11), 4490 (1976).
- [32.] D. C. Cartwright, A. Chutjian, S. Trajmar, and W. Williams, Phys. Rev. A **16**(3), 1013 (1977); *Ibid.* p. 4041.
- [33.] M. J. Brunger and P. J. O. Teubner, Phys. Rev. A **41**(3), 1413 (1990); M. J. Brunger, Thesis Report, Flinders University of South Australia, (1988).
- [34.] A. R. Filippelli, S. Chung, and C. C. Lin, Phys. Rev. A **29**, 1709 (1984).
- [35.] J. T. Vanderslice, P. G. Wilkinson, and S. G. Tilford, J. Chem. Phys. **42**, 2681 (1965).
- [36.] W. Benesch and D. Fraedrich, J. Chem. Phys. **81**, 5367 (1984).
- [37.] R. Nagpal and P. K. Ghosh, J. Phys. B **24**, 3295 (1991).
- [38.] D. Neuschäfer, Ch. Ottinger, and A. Sharma, Chem. Phys. **117**, 113 (1987).
- [39.] W. Benesch, J. Geophys. Res. **86**, 9065 (1981).

- [40.] J. S. Morrill, W. M. Benesch, and K. G. Widing, *J. Chem. Phys.* **94**, 262 (1991).
- [41.] P. N. Stanton and R. M. St. John, *J. Opt. Soc. Am.* **59**(3), 252 (1968).
- [42.] S. Trajmar, private communication.
- [43.] A. Lofthus and P. H. Krupenie, *J. Phys. Chem. Ref. Data* **6**(1), 113 (1977).
- [44.] D. C. Cartwright, private communication.
- [45.] J. Mazeau, F. Gresteau, R. I. Hall, G. Joyez, and J. Reinhardt, *J. Phys. B* **6**, 862 (1973).
- [46.] D. C. Cartwright, S. Trajmar, W. Williams, and D. L. Huestis, *Phys. Rev. Letts.* **27**, 704 (1971).
- [47.] B. H. Lengsfeld and T. N. Rescigno, *Phys. Rev. A* **44**(5), 2913 (1991).
- [48.] K. N. Klump and E. N. Lassettre, *J. Chem. Phys.* **68**(3), 886 (1978).

Table 5.3. Differential and Integral Excitation Cross Sections for the  $a^1\Pi_g$  State of  $N_2$ ,  $10^{-18}$  ( $\text{cm}^2/\text{sr}$ ).

$\theta(\text{deg})$	12.5 eV	15.0	17.0	20.0	30.0
0	3.81	6.21	11.8	15.1	12.1
10	3.72	5.95	10.8	14.0	11.2
20	3.46	5.24	8.24	11.1	9.39
30	3.14	4.25	5.50	7.38	6.58
40	2.79	3.21	3.35	4.01	3.14
50	2.46	2.35	2.05	1.99	1.04
60	2.16	1.72	1.42	1.20	0.578
70	1.92	1.30	1.17	0.974	0.595
80	1.71	1.06	1.02	0.924	0.801
90	1.54	0.973	0.948	0.980	1.09
100	1.42	1.03	1.03	1.15	1.22
110	1.35	1.17	1.27	1.33	1.11
120	1.34	1.30	1.55	1.41	1.01
130	1.36	1.32	1.76	1.38	1.07
140	1.41	1.24	1.83	1.32	1.01
150	1.43	1.07	1.74	1.18	0.772
160	1.42	0.876	1.54	1.02	0.544
170	1.40	0.709	1.37	0.961	0.418
180	1.39	0.642	1.30	0.966	0.390
$\sigma_{\text{int}}$	23.4	21.6	25.5	26.9	20.6

Table 5.4. Differential and Integral Excitation Cross Sections for the  $B^3\Pi_g$  State of  $N_2$ ,  $10^{-18}$  ( $\text{cm}^2/\text{sr}$ ).

$\theta(\text{deg})$	10.0 eV	12.5	15.0	17.0	20.0	30.0
0	1.84	1.42	0.922	0.414	0.401	0.242
10	1.87	1.44	1.02	0.472	0.455	0.308
20	1.98	1.49	1.25	0.607	0.576	0.469
30	2.13	1.50	1.52	0.745	0.690	0.614
40	2.32	1.49	1.76	0.874	0.800	0.743
50	2.52	1.51	1.94	1.00	0.928	0.970
60	2.71	1.58	2.04	1.10	1.02	1.26
70	2.89	1.69	2.09	1.18	1.03	1.50
80	3.05	1.87	2.18	1.25	1.00	1.56
90	3.18	2.07	2.34	1.35	0.963	1.43
100	3.27	2.23	2.57	1.44	0.921	1.23
110	3.32	2.34	2.82	1.53	0.903	1.15
120	3.34	2.43	3.01	1.63	0.951	1.30
130	3.33	2.48	3.00	1.68	1.05	1.62
140	3.30	2.45	2.66	1.64	1.16	1.99
150	3.25	2.29	2.02	1.49	1.22	2.31
160	3.20	1.96	1.30	1.27	1.17	2.39
170	3.17	1.60	0.770	1.08	1.03	2.23
180	3.15	1.44	0.586	1.00	0.949	2.12
$\sigma_{\text{int}}$	37.3*	25.2	28.7	16.1	12.0	17.3

\*From a two-state calculation.

Table 5.5. Differential and Integral Excitation Cross Sections for the  $A^3\Sigma_u^+$  State of  $N_2$ , ( $10^{-18}$  cm<sup>2</sup>/sr).

$\theta$ (deg)	10.0 eV	12.5	15.0	17.0	20.0	30.0
0	3.71	8.72	2.07	1.36	0.095	0.728
10	3.59	8.18	1.89	1.26	0.126	0.769
20	3.25	6.74	1.45	1.00	0.209	0.847
30	2.75	4.88	0.996	0.732	0.319	0.875
40	2.20	3.18	0.806	0.607	0.428	0.804
50	1.69	2.12	1.00	0.731	0.525	0.681
60	1.28	1.78	1.48	1.05	0.610	0.607
70	1.23	1.93	1.99	1.40	0.686	0.645
80	0.920	2.26	2.28	1.62	0.756	0.765
90	0.941	2.51	2.21	1.61	0.805	0.892
100	1.02	2.52	1.86	1.37	0.813	0.967
110	1.10	2.29	1.47	1.07	0.788	0.986
120	1.14	1.98	1.39	0.973	0.796	0.990
130	1.12	1.81	1.93	1.30	0.936	1.04
140	1.06	1.86	3.16	2.12	1.28	1.17
150	0.988	2.09	4.88	3.31	1.84	1.41
160	0.926	2.44	6.72	4.58	2.50	1.73
170	0.884	2.81	8.14	5.58	3.03	2.02
180	0.869	2.97	8.68	5.96	3.24	2.14
$\sigma_{\text{int}}$	16.9*	37.1	31.3	23.0	13.4	11.9

\*Taken from a four-( $X^1\Sigma_g^+$ ,  $A^3\Sigma_u^+$ ,  $W^3\Delta_u$ ,  $B'^3\Sigma_u^-$ ) state calculation.

Table 5.6. Differential and Integral Excitation Cross Sections for the  $W^3\Delta_u$  State of  $N_2$ , ( $10^{-18}$  cm<sup>2</sup>/sr).

$\theta$ (deg)	10.0 eV	12.5	15.0	17.0	20.0	30.0
0	0.450	0.983	2.12	2.12	1.23	0.463
10	0.461	0.938	1.99	2.01	1.27	0.486
20	0.491	0.832	1.65	1.71	1.35	0.547
30	0.527	0.749	1.316	1.38	1.34	0.625
40	0.562	0.796	1.22	1.24	1.22	0.707
50	0.592	1.02	1.50	1.44	1.08	0.819
60	0.619	1.36	2.06	1.91	1.02	1.00
70	0.644	1.69	2.62	2.40	1.05	1.25
80	0.668	1.91	3.01	2.78	1.15	1.49
90	0.687	2.03	3.18	2.95	1.30	1.64
100	0.700	2.10	3.16	2.91	1.43	1.66
110	0.701	2.18	3.08	2.73	1.49	1.61
120	0.690	2.31	3.09	2.55	1.44	1.55
130	0.673	2.48	3.30	2.52	1.33	1.56
140	0.657	2.60	3.66	2.72	1.25	1.66
150	0.647	2.60	4.01	3.02	1.22	2.84
160	0.645	2.46	4.17	3.20	1.17	2.05
170	0.646	2.29	4.11	3.16	1.06	2.23
180	0.647	2.21	4.04	3.10	0.996	2.30
$\sigma_{\text{int}}$	4.17*	23.5	35.7	31.2	16.3	17.5

\*From a six-channel calculation.

Table 5.7. Differential and Integral Excitation Cross Sections for the  $w^1\Delta_u$  State of  $N_2$ , ( $10^{-18}$  cm<sup>2</sup>/sr).

$\theta$ (deg)	12.5 eV	15.0	17.0	20.0	30.0
0	2.14	1.01	0.600	0.282	0.193
10	2.13	1.03	0.657	0.405	0.234
20	2.08	1.11	0.820	0.683	0.406
30	1.99	1.23	1.02	0.937	0.664
40	1.85	1.31	1.15	1.04	0.772
50	1.67	1.32	1.19	1.02	0.639
60	1.50	1.27	1.18	0.962	0.465
70	1.34	1.18	1.13	0.891	0.397
80	1.17	1.03	1.01	0.850	0.380
90	0.974	0.825	0.850	0.699	0.356
100	0.797	0.629	0.696	0.646	0.331
110	0.678	0.490	0.589	0.643	0.318
120	0.630	0.436	0.520	0.640	0.322
130	0.628	0.450	0.463	0.589	0.328
140	0.622	0.475	0.403	0.492	0.315
150	0.583	0.469	0.349	0.382	0.294
160	0.517	0.434	0.321	0.303	0.286
170	0.456	0.398	0.317	0.273	0.291
180	0.431	0.383	0.320	0.269	0.294
$\sigma_{\text{int}}$	14.1	10.8	10.5	10.2	5.52

Table 5.8. Differential and Integral Excitation Cross Sections for the  $a' \ ^1\Sigma_u^-$  State of  $N_2$  ( $10^{-18}$  cm<sup>2</sup>/sr).

$\theta$ (deg)	15.0 eV	17.0	20.0	30.0
0	0.000	0.000	0.000	0.000
10	0.023	0.038	0.030	0.010
20	0.090	0.135	0.100	0.036
30	0.190	0.246	0.170	0.065
40	0.305	0.328	0.206	0.084
50	0.416	0.367	0.211	0.087
60	0.509	0.378	0.208	0.083
70	0.581	0.381	0.207	0.083
80	0.628	0.378	0.200	0.094
90	0.647	0.363	0.190	0.131
100	0.636	0.333	0.193	0.203
110	0.590	0.294	0.221	0.289
120	0.508	0.250	0.259	0.355
130	0.397	0.204	0.271	0.373
140	0.276	0.153	0.235	0.332
150	0.163	0.100	0.160	0.245
160	0.744	0.050	0.078	0.135
170	0.019	0.013	0.020	0.039
180	0.000	0.000	0.000	0.000
$\sigma_{\text{int}}$	5.69	3.64	2.57	2.21

Table 5.9. Differential and Integral Excitation Cross Sections for the  $B' \ ^3\Sigma_u^-$  State of  $N_2$  ( $10^{-18}$  cm<sup>2</sup>/sr).

$\theta$ (deg)	12.5 eV	15.0	17.0	20.0	30.0
0	0.000	0.000	0.000	0.000	0.000
10	0.021	0.017	0.020	0.020	0.019
20	0.082	0.066	0.081	0.081	0.071
30	0.172	0.142	0.183	0.186	0.135
40	0.286	0.245	0.321	0.321	0.188
50	0.424	0.376	0.485	0.458	0.215
60	0.585	0.542	0.658	0.568	0.215
70	0.764	0.736	0.819	0.643	0.214
80	0.928	0.937	0.946	0.683	0.250
90	1.08	1.12	1.03	0.692	363
100	1.18	1.25	1.06	0.668	0.553
110	1.21	1.32	1.04	0.609	0.771
120	1.17	1.29	0.971	0.519	0.932
130	1.03	1.14	0.828	0.407	0.962
140	0.804	0.889	0.627	0.288	0.835
150	0.530	0.580	0.401	0.176	0.589
160	0.264	0.285	0.194	0.084	0.306
170	0.071	0.075	0.051	0.022	0.084
180	0.000	0.000	0.000	0.000	0.000
$\sigma_{\text{int}}$	8.69	14.4	10.2	5.47	5.73